UiO : University of Oslo

Matthias Rauter

Multiphase Navier–Stokes Equations applied to landslide tsunamis

Numerical simulations of granular flows and their interaction with water bodies

Thesis submitted for the degree of Philosophiae Doctor

Department of Mathematics
Faculty of Mathematics and Natural Sciences

Norwegian Geotechnical Institute

2021

Series of dissertations submitted to the
Faculty of Mathematics and Natural Sciences, University of Oslo
No. 2405

ISSN 1501-7710

Cover: Hanne Baadsgaard Utigard.
Print production: Reprosentralen, University of Oslo.

Funded by the Horizon 2020 Framework
Programme of the European Union

Preface

This thesis is submitted in partial fulfilment of the requirements for the degree of *Philosophiae Doctor* at the University of Oslo. The research presented here was conducted at the Norwegian Geotechnical Institute. This project has received funding from the European Union's Horizon 2020 research and innovation programme under the Marie Skłodowska-Curie grant agreement No. 721403 (SLATE). The computational results presented have been achieved (in part) using the HPC infrastructure LEO of the University of Innsbruck.

The thesis is a collection of four papers. The common theme is the numerical simulation of granular flows and their potential to generate tsunamis with Navier-Stokes type models.

Acknowledgements

I gratefully acknowledge the support from my supervisors, Finn Løvholt, Geir Pedersen, Mickael Mortensen, Carl Harbitz, the whole SLATE team, especially Katrin Huhn-Frehers, Jannis Kuhlmann, Peter Talling and Michael Strasser, as well as Biljana Dragisic from UiO. I am very grateful for the contributions of many co-authors, Thomas Barker, Wolfgang Fellin, Sigríður Sif Gylfadóttir, Luisa Hoße, Finn Løvholt, Ryan Mulligan, Andy Take and Sylvain Viroulet, for the help of many great researchers, especially Nico Gray, Chris Johnson, Eoin Maguire, Gertaud Medicus, and Magdalena Schreter and for the review and valuable comments from Anne Mangeney, Valentin Heller and numerous anonymous referees. I further thank the HPC group from the University of Innsbruck for their great support without which this work would not have been possible. I would like to thank all my colleges that accompanied me during my PhD, especially my office mates Iman Bathaeian, Andreas Huber, Andreas Kofler, Thomas Morris-Zengaffinen and Fabian Schranz. I would like to thank all my flatmates in Norway, Harald and Maja, in Innsbruck, Ulisse and Sebi and in Durham, Sam and Steven for their hospitality and a great time.

Mein größter Dank gebührt meiner Familie und meinen Freunden, welche mich während diesem Abenteuer und meinem Umzug nach Norwegen unterstützt haben, vor allem meinen Eltern Brigitte und Karl, meiner Schwester Lissi und ihrer Familie, sowie meiner Cousine Judith und ihrer Familie für die Rundreise durch Norwegen. Endelig vil jeg takke kjæresten min Sol for sterk støtte og for a gjøre tiden min i Norge sa mye bedre.

Matthias Rauter
Oslo, May 2021

List of Papers

Paper I

Rauter, M. and Barker, T. and Fellin, W. “Granular viscosity from plastic yield surfaces: The role of the deformation type in granular flows”. In: *Computers and Geotechnics*. Vol. 122 (2020), pp. 103492. DOI: 10.1016/j.compgeo.2020.103492.

Paper II

Rauter, M. “The compressible granular collapse in a fluid as a continuum: validity of a Navier–Stokes model with $\mu(J)$,$\phi(J)$-rheology”. In: *Journal of Fluid Mechanics*. Vol. 915 (2021), pp. A87. DOI: 10.1017/jfm.2021.107.

Paper III

Rauter M. and Hoße L. and Mulligan R. P. and Take W. A. and Løvholt F. “Numerical simulation of impulse wave generation by idealized landslides with OpenFOAM”. In: *Coastal Engineering*. Vol. 165 (2021), pp. 103815. DOI: 10.1016/j.coastaleng.2020.103815.

Paper IV

Rauter, M. and Viroulet, S. and Gylfadóttir, S. S. and Fellin, W. and Løvholt, F. “Porous granular flow models can predict full-scale landslide tsunamis”. In preparation.

Contents

List of Figures

List of Tables

Chapter 1

Introduction

1.1 Landslides, tsunamis and landslide tsunamis

Landslides and similar gravity driven mass flows (e.g. snow avalanches, debris flows, mud slides, rock falls) are common events with high socioeconomic impact (Pudasaini and Hutter, 2007). They occur primarily in steep, mountainous terrain but also in lakes and the ocean. Landslides can travel over long distances and unleash high forces and destruction on obstacles in their flow path. Between 1998 and 2017, 4.8 million people have been affected by landslides and they caused more than 18 000 fatalities (Wallemacq *et al.*, 2018).

The prediction of landslides is a complex and multidisciplinary problem (Pudasaini and Hutter, 2007). Various factors influence the formation of landslides, e.g. geology, meteorology, or hydrology. Triggers can be manifold, ranging from earthquakes, over strong precipitation to human activities. All factors are affected by a high level of uncertainty and a similar level of uncertainty has to be expected for landslides. This is an important aspect that should be accounted for in all decisions and models. The dynamic evolution of the landslides from the initial release to the final deposition is equally complex. Landslides consist of a mixture of water (sometimes ice or snow), air and granular particles in various sizes, from fine sediment particles to large rocks, that again, depend strongly on geology, meteorology and hydrology. Various phenomena emerge from this complex mixture, e.g. Coulomb friction, dilatancy, liquefaction, fluidisation, cohesion or segregation. Many of these phenomena are barely described in an isolated context, yet in a unified manner considering all the interactions.

Nevertheless, a large variety of mathematical models and methods were developed in the last century to investigate, understand and predict landslides. The simplest class of models can be described as block models, where kinematic equations are integrated over the whole landslide volume. These models idealize the landslide or avalanche as a mass point which is subject to gravity and friction. The resulting acceleration, velocity and deceleration allows an estimation of the runout and the destructive impact at a certain point in the path. Notable examples are the model of Voellmy (1955) or the α-β model (Bakkehoi *et al.*, 1983). Many of these models can be solved analytically and applied on a regional scale.

Further developments extended the early mass point models to continuum-mechanical models. The first step were depth-integrated flow models, incorporating variations and the extension of the slide, first in longitudinal direction (one-dimensional) and further in transversal direction (two-dimensional) (Grigorian *et al.*, 1967; Savage and Hutter, 1989, 1991). Notably, these models were highly influenced by the depth-integrated Shallow Water Equations, well known for the application of water waves. Depth-integrated models are well-established and applied on a regular basis (Pitman *et al.*, 2003; Sampl and Zwinger, 2004; Hungr, 1995, 2008; Christen *et al.*, 2010; Pudasaini, 2012; Mergili *et al.*, 2012; Bouchut *et al.*, 2017; Kim *et al.*, 2019), see also Tab. 1.1.

The next natural step incorporates a complete removal of integration (except for numerical approximations of the exact solution). This results in complete three-dimensional continuum mechanical models, e.g. the Navier–Stokes Equations. Many studies with such models have been conducted in recent years, among others by Crosta *et al.* (2009); Meruane *et al.* (2010); Lagrée *et al.* (2011); Staron *et al.* (2012); Domnik *et al.* (2013); Savage *et al.* (2014); Zhang *et al.* (2014); Ionescu *et al.* (2015); Peng *et al.* (2015); Mast *et al.* (2015); Dunatunga and Kamrin (2015); von Boetticher *et al.* (2016, 2017); Martin *et al.* (2017); Wang *et al.* (2017a,b); Si *et al.* (2018a); Baumgarten and Kamrin (2019); Gesenhues *et al.* (2019). The various approaches differ by their numerical solution method (Finite Element Method (FEM), Particle Finite Element Method (PFEM), Finite Volume Method (FVM), Smoothed Particle Hydrodynamics (SPH) or Material Point Method (MPM)), the number of considered phases (single-phase or multi-phase), the constitutive framework (elasto-pastic, visco-plastic, plastic, hypoplastic) and the constitutive relations (Drucker–Prager, Mohr–Couloumb, Matsuoka–Nakai, Critical State Theory (CST); $\mu(I)$-rheology or $\mu(I), \phi(I)$-rheology, Granular Kinetic Theory (GKT)), see Tab. 1.1 for some examples. All of the mentioned models consider granular flows and slides as continua, which can be interpreted as a simplification in itself, as these flows are composed of many discrete bodies, i.e. grains. The discrete element method (DEM) (e.g. Lacaze *et al.*, 2008; Guo and Curtis, 2015) takes advantage of this fact and simulates all grains and the respective contact or impact forces individually. The complexity of granular flows can be reduced to simple contact problems, however, for a high computational effort, required to track individual particles and all possible contacts and interactions. It should be noted that some effects cannot be covered by the DEM and that additional models are required for e.g. the interaction with the surrounding fluid or for non-spherical particles (Shan and Zhao, 2014; Guo and Curtis, 2015; Xu *et al.*, 2019). Despite this manifold attempts, three-dimensional models are still falling behind depth-integrated models for most applications. There are multiple reasons for the dominance of depth-integrated models, e.g. efficiency but also technical and conceptual problems of three-dimensional models. Furthermore, the simplifications and assumptions of depth-integrated models fit well to most naturally occurring landslides and an extension to full three-dimensional models is rarely advantageous.

The interaction of landslides with lakes and oceans can generate large impulse waves, i.e. tsunamis, which represent a substantial secondary hazard. In fact, landslides are the second most frequent tsunami source, only surpassed by earthquakes (Ward, 2001; Harbitz *et al.*, 2014). Respective events are mainly distinguished by the origin of the landslide, either as subaerial (landslide is released above the water level) or subaquatic landslides tsunamis (landslide is released below the water level). Subaquatic landslides can reach much larger volumes than subaerial landslides, however, the latter are more efficient in terms

Table 1.1: Examples for landslide and granular flow models, their numerical solution method and constitutive relations.

Type	Model name	Solution method	Const. relations	References
Savage–Hutter	TITAN2D	FVM	Voellmy-like	Pitman *et al.* (2003); Patra *et al.* (2005)
	DAN	Lagrangian solver	Voellmy-like	Hungr (1995, 2008)
	SamosAT	SPH	Voellmy-like	Sampl and Zwinger (2004)
	Shaltop	FVM	Voellmy-like/$\mu(I)$-rheology	Mangeney *et al.* (2007)
	FLATModel	FVM	Voellmy-like	Medina *et al.* (2008)
	RAMMS	FVM	Voellmy/GKT	Christen *et al.* (2010)
	Avaflow	FVM	two-phase Voellmy-like/CST	Mergili *et al.* (2012, 2017)
	-	FVM/FDM	CST	Bouchut *et al.* (2017)
	OpenFOAM	FVM	Voellmy-like/$\mu(I)$-rheology	Rauter and Tuković (2018); Rauter *et al.* (2018)
	BingClaw	FVM	Herschel–Bulkley	Kim *et al.* (2019)
Navier–Stokes	-	FEM	elasto-plastic/Mohr–Coulomb	Crosta *et al.* (2009)
	-	FVM	visco-plastic/CST-like	Meruane *et al.* (2010)
	Gerris	FVM	visco-plastic/$\mu(I)$-rheology	Lagrée *et al.* (2011); Staron *et al.* (2012)
	COMSOL	FEM	visco-plastic/Drucker–Prager	Savage *et al.* (2014)
	-	PFEM	elasto-plastic/Drucker–Prager	Zhang *et al.* (2014)
	-	FEM	visco-plastic/$\mu(I)$-rheology	Ionescu *et al.* (2015); Martin *et al.* (2017)
	-	SPH	hypoplastic/Drucker–Prager	Peng *et al.* (2015)
	-	MPM	elasto-plastic/Matsuoka–Nakai	Mast *et al.* (2015)
	-	MPM	elasto-plastic/$\mu(I)$-rheology	Dunatunga and Kamrin (2015)
	OpenFOAM	FVM	visco-plastic/Drucker–Prager	von Boetticher *et al.* (2016)
	-	SPH	two-phase CST/$\mu(I)$-rheology	Wang *et al.* (2017b,a)
	OpenFOAM	FVM	two-phase visco-plastic/KT	Si *et al.* (2018a)
	-	MPM	two-phase CST/$\mu(I)$-rheology	Baumgarten and Kamrin (2019)
	-	FEM	visco-plastic/$\mu(I)$-rheology	Gesenhues *et al.* (2019)
DEM	varous models	DEM	contact model	see review of Lacaze *et al.* (2008)

of wave generation and both represent a substantial hazard. It should be noted that most subaquatic landslides are triggered by earthquakes and that these earthquakes might play a role in the generation of the tsunami (Harbitz *et al.*, 2006).

Notable examples of subaquatic landslide tsunamis include

- the prehistoric (about 11 500 BP) BIG'95 slide in the mediterranean sea that generated waves up to 10 m on the continental shores (Iglesias *et al.*, 2012),
- the prehistoric (about 8 000 BP) extremely large Storrega landslide (slide volume 10^{12} m^3) and the following tsunami which led to inundation heights of up to 20 m at the Faeroes Islands, 15 m in Norway, and 6 m in Scotland (Bondevik *et al.*, 2005),
- the 1929 Grand Banks landslide and the following tsunami, causing 28 fatalities at the coast of Newfoundland (Løvholt *et al.*, 2019),
- the 1992 Flores Island tsunami that caused more than 1000 fatalities (Yeh *et al.*, 1993), or
- the 1998 Papua New Guinea slump and tsunami causing over 2100 fatalities (Synolakis *et al.*, 2002).

Notable examples of subaerial landslide tsunamis include

- the 563 lake Geneva (Switzerland) rockfall induced tsunami with inundation heights of 13 m in Lausanne and 8 m in Geneva (Kremer *et al.*, 2012),
- the 1784 earthquake induced rockfall and tsunami in Calabria (Italy) that caused more than 1 500 fatalities in the village Scilla,
- the 1792 Mount Unzen landslide tsunami that caused more than 15 000 fatalities (Sassa *et al.*, 2016)
- the 1888 Ritter Island Volcano (Papua New Guinea) collapse, generating a $10-15$ m high wave at neighbouring islands (Ward and Day, 2003),
- the 1905 and 1936 rockfall generated tsunamis in lake Loen (Norway), destroying nearby villages and killing most inhabitants (Grimstad, 2006),
- the 1934 Tafjord (Norway) rockfall and tsunami with inundation heights of up to 60 m that caused 41 fatalities (Harbitz *et al.*, 1993),
- the 1958 Lituya Bay (Alaska) landslide that generated a tsunami with a maximum inundation height of 500 m (Franco *et al.*, 2019),
- the 1963 Vajont landslide that hit an artificial reservoir (Italy), generating a 200 m high wave that destroyed the village of Longarone and caused about 2 000 fatalities (Panizzo *et al.*, 2005),

- the 1964 Alaska earthquake, leading to landslides and further on to a tsunami that caused 13 fatalities and destroyed the village Seward (Lee *et al.*, 2003),
- the 1979, Lembata Island (Indonesia) landslide and tsunami that caused 539 fatalities (Yudhicara *et al.*, 2015),
- the 1979 Nice accident, where a landslide was released during building operations, generating a tsunami (Assier-Rzadkieaicz *et al.*, 2000),
- the 1994 Skagway (Alaska) harbour accident, where a collapsing dock generated a tsunami with up to 10 m high waves (Rabinovich *et al.*, 1999),
- the 2007 earthquake induced landslide in the Aisén Fjord (Chile) that caused ten fatalities (Sepúlveda and Serey, 2009),
- the 2007 landslide and tsunami in lake Chehalis (Canada) that generated inundation heights of 38 m on the opposite shore (Wang *et al.*, 2015),
- the 2010 Haiti earthquake that triggered a coastal tsunamigenic landslide in the Bay of Grand Goâve, killing at least three people (Fritz *et al.*, 2013),
- the 2014 lake Askja landslide that generated $10 - 15$ m high waves and inundation heights up to 70 m (see Paper IV),
- the 2015 Tyndall Glacier landslide and the following tsunami in Taan Fjord with 5 m high waves in the far field (George *et al.*, 2017),
- the 2015 Hongyanzi landslide that generated a tsunami in the Three Gorges reservoir (China) with up to 6 m inundation height on the opposite shore (Xiao *et al.*, 2018),
- the 2017 Karrat Fjord landslide tsunami, killing four people and destroying eleven houses in the village of Nuugaatsiaq (Paris *et al.*, 2019),
- the 2018 Sulawesi earthquake that was accompanied by a large amount of landslides and a tsunami wave with up to 10 m inundation height (Takagi *et al.*, 2019), or
- the 2018 flank collapse of Anak Krakatoa (Indonesia), generating a tsunami that caused several hundred fatalities (Grilli *et al.*, 2019).

Pictures of the 1963 Vajont landslide and the caused destruction are shown in Fig. 1.1 [1].

Three major approaches are currently used to model and predict landslide generated tsunamis (Heller, 2020). Semi-empirical scaling relations (i) that are

---

[1] Picture sources: (a) public domain, taken from commons.wikimedia.org/wiki/File:Valle_del_Vajont_1960.jpg on 20.01.21, (b) public domain, taken from it.wikipedia.org/wiki/File:Disastro_Vajont.jpg on 20.01.21, (c,d) public domain, taken from commons.wikimedia.org/wiki/File:Longarone_disastro.jpg on 20.01.21.

Figure 1.1: The Vajont reservoir before (a) and after the 1963 landslide (b). The landslide displaced large parts of the water and generated a tsunami that destroyed the village of Longarone, shown before (c) and after the event (d).

derived from a large set of experiments (e.g. Fritz, 2002), physical laboratory scale models (ii) (e.g. Lindstrøm *et al.*, 2014) and mathematical-mechanical models (iii), on which we will focus in the following.

A tsunami event can be split into three major phases (Fritz, 2002). In the generation phase (i), a water reservoir at rest is disturbed by an earthquake, a volcanic eruption, a landslide or a similar event. The water wave travels widely undisturbed during the propagation phase (ii) where it is only affected by the water body geometry and its depth i.e. the bathymetry. The wave will eventually reach a shore in the inundation phase (iii) and areas that are located above the water level will be flooded.

The simulation of tsunamis is, similar to landslides, dominated by depth-integrated models, such as the Shallow Water Equations or the Boussinesq Equations. Some models are listed in Tab. 1.2, for a comprehensive list, the reader is refereed to the excellent review of Yavari-Ramshe and Ataie-Ashtiani

(2016). These models have substantial advantages in comparison to full three-dimensional models. Most notably, the wave elevation can be described by a scalar function (the wave or water height) and the models conserve energy. This is an important property, especially in the propagation phase. In fact, it has been shown that three-dimensional models are dissipating wave energy, which might lead to an underestimation of the respective hazard (Løvholt *et al.*, 2008).

However, the assumptions of depth-integration might not hold during the generation or inundation phase. This is especially the case for subaerial landslides that penetrate the water surface in a violent, chaotic, and turbulent process. Furthermore, these stages require special treatment in depth-integrated models, either coupling with a landslide/earthquake model (generation) or special treatment of dry regions (inundation). Three-dimensional models might solve some of these problems and are thus studied with increasing interest (Liu *et al.*, 2005; Gisler *et al.*, 2006; Biscarini, 2010; Abadie *et al.*, 2010; Horrillo *et al.*, 2013; Shan and Zhao, 2014; Si *et al.*, 2018b; Clous and Abadie, 2019; Abadie *et al.*, 2020; Romano *et al.*, 2020; Mulligan *et al.*, 2020; Chen *et al.*, 2020; Franco *et al.*, 2019). In particular, three-dimensional models allow a unified treatment of the landslide and the tsunami and a direct numerical simulation of the interaction and the tsunami genesis process. Further, three-dimensional models allow complex and realistic constitutive models for the landslide material. These properties give three-dimensional methods a strong potential to substantially improve the understanding and prediction of landslide tsunamis. The methods and flow models are the same as for granular flows and landslides (see above), however, complicated by the additional water-air surface, where the wave is generated and propagated.

Table 1.2: Examples for tsunami models, their solution method and source (i.e. landslide) modelling.

Type	Model name	Solution	Source modelling	References
depth-averaged	Avalanche	FVM	variable bathymetry	Heinrich *et al.* (2001)
	NHWAVE	FVM	variable bathymetry	Ma *et al.* (2012, 2015)
	GloBouss	FDM	variable bathymetry	Løvholt *et al.* (2008)
	HYSEA	FVM	variable bathymetry	Fernández-Nieto *et al.* (2008)
	GeoClaw	FVM	variable bathymetry	Berger *et al.* (2011)
	D-Claw	FVM	mixture model	George *et al.* (2017)
	FUNWAVE	FDM	variable bathymetry	Kirby *et al.* (1998)
	SWASH	SPH	variable bathymetry	Tan *et al.* (2018)
Navier–Stokes	-	FVM	block slide	Liu *et al.* (2005)
	SAGE	FVM	inviscid/plastic slide	Gisler *et al.* (2006)
	THETIS	FVM	block/plastic slide	Abadie *et al.* (2010, 2020)
	Fluent	FVM	block/viscous slide	Biscarini (2010)
	TSUNAMI3D	FDM	inviscid slide	Horrillo *et al.* (2013)
	CFDEM	FVM	DEM	Shan and Zhao (2014)
	OpenFOAM	FVM	granular porous slide	Si *et al.* (2018b)
	THETIS	FVM	granular slide	Clous and Abadie (2019)
	OpenFOAM	FVM	block/solid slide	Romano *et al.* (2020)
	-	PFEM	viscous slide	Mulligan *et al.* (2020)
	Flow3D	FVM	viscous slide	Franco *et al.* (2019)

1.2 Goal and methodology of the thesis

This thesis aims to pick up three-dimensional models for landslides and water waves and combine them in a unified model to directly simulate the process of wave generation. Further, the model should be solved numerically to include arbitrary and complex geometries and properties. Analytical solutions, although desirable, can not be expected from the complex model and complex geometries. Considerable emphasis was placed on the efficiency and scalability of the numerical method to allow the application to full scale events. Further, it was the goal to develop a model with real predictive power, that does not rely on the fitting of empirical parameters.

The thesis project is embedded into the Marie Skłodowska-Curie international training network SLATE, with the overarching goal to understand and quantify the hazard of submarine landslides.

Three-dimensional models for water surface waves are well established in the field of Computational Fluid Dynamics (CFD) (Ferziger and Perić, 2002). The vast majority of models relies on the incompressible Navier–Stokes Equations (see section 1.3), which describe a fluid with good accuracy. The description of the water surface and the respective waves can be included with different approaches, e.g. with a moving boundary condition (e.g. Tuković and Jasak, 2012) or with the application of a multi-phase or multi-component model (e.g. Hirt and Nichols, 1981). The latter is chosen in this work, as this approach promises flexibility and a simple implementation of multiple interacting phases for water, landslide and air.

Fluids are defined by Ferziger and Perić (2002) as „[...] substances whose molecular structure offers no resistance to external shear forces: even the smallest force causes deformation of a fluid [...]" and the Navier–Stokes Equations reflect this property. It is clear that granular material, i.e. soil, sand or marine sediments, do not follow this description and large shear forces can be sustained for long periods. The application of the Navier–Stokes Equations to granular material is thus problematic and not without restrictions.

However, landslides are first and foremost a flow of granular material, with limiting states (i.e. release and deposition) resembling the behaviour of a solid. It has been shown, that this flow regime can be described well as a fluid with a non-Newtonian viscosity (see section 1.4). The very influential work of Jop *et al.* (2006) popularized this approach, although the idea is much older (e.g. Schaeffer, 1987). Solid material can be expressed as a fluid with infinite or very high viscosity and represents the limit of the approach, matching the process of a granular flow with peripheral solid regions (i.e. a landslide) well. Most notable, this model is consistent with the Navier–Stokes Equations and the surface wave model and was thus chosen in this work. This allows a seamless integration of granular flows into the CFD model and a direct numerical simulation of the wave generation.

The resulting mathematical system is solved with OpenFOAM (see section 1.5), an open source library for the solution of partial differential equations (OpenCFD, 2018; Weller *et al.*, 1998). OpenFOAM was chosen because of the simple high level syntax, good support of multiphase systems, complex geometries, and parallelisation (via MPI), and theoretical scalability up to real case scenarios. The implementation and/or validation of new models and existing components is presented in four publications (see section 1.6). An introduction to the basic methods and tools in this thesis is given in sections 1.3, 1.4 and 1.5.

1.3 The incompressible Navier–Stokes Equations and other conservation laws

The Navier–Stokes Equations are (in this work) understood as the continuum-mechanical expression of conservation of mass

$$\frac{\mathrm{d}\,m}{\mathrm{d}t} = 0, \tag{1.1}$$

and momentum (Newtons' second law)

$$\frac{\mathrm{d}\,m\,\mathbf{u}}{\mathrm{d}t} = \mathbf{f}, \tag{1.2}$$

for a fluid (Moukalled *et al.*, 2016; Ferziger and Perić, 2002). Here, m is a control mass, $\mathbf{u}$ its velocity and $\mathbf{f}$ the sum of all forces acting on it.

The *Reynolds' transport theorem* is central for the development of continuum-mechanical models, based on conservation laws (Ferziger and Perić, 2002). It is given as

$$\frac{\mathrm{d}\Psi}{\mathrm{d}t} = \frac{\mathrm{d}}{\mathrm{d}t}\int\limits_{\Omega_{\mathrm{CM}}} \psi\,\mathrm{d}V = \frac{\partial}{\partial t}\int\limits_{\Omega_{\mathrm{CV}}} \psi\,\mathrm{d}V + \oint\limits_{\partial\Omega_{\mathrm{CV}}} \psi\,\mathbf{u}\cdot\mathbf{n}\,\mathrm{d}S, \tag{1.3}$$

with the conservative property (mass, momentum, energy) Ψ and its respective density $\psi(\mathbf{x}, t)$ at position $\mathbf{x}$ and time t. Ω_{CM} is the volume occupied by the control mass, Ω_{CV} is the matching but stationary control volume and $\partial\Omega_{\mathrm{CV}}$ its boundary with the outward pointing normal unit vector $\mathbf{n}$.

Introducing the mass conservation equation (1.1) and the respective density ρ into Eq. (1.3) yields the integral form of the mass conservation equation

$$\frac{\partial}{\partial t}\int\limits_{\Omega_{\mathrm{CV}}} \rho\,\mathrm{d}V + \oint\limits_{\partial\Omega_{\mathrm{CV}}} \rho\,\mathbf{u}\cdot\mathbf{n}\,\mathrm{d}S = 0. \tag{1.4}$$

Gauss' divergence theorem, given as,

$$\int\limits_{\Omega_{\mathrm{CV}}} \boldsymbol{\nabla}\cdot(\rho\,\mathbf{u})\;\mathrm{d}V = \oint\limits_{\partial\Omega_{\mathrm{CV}}} (\rho\,\mathbf{u})\cdot\mathbf{n}\,\mathrm{d}S, \tag{1.5}$$

with the divergence operator "$\boldsymbol{\nabla}\cdot$" can be applied to transform the surface integral into a volume integral to get

$$\int\limits_{\Omega_{\mathrm{CV}}} \frac{\partial\,\rho}{\partial t} + \boldsymbol{\nabla}\cdot(\rho\,\mathbf{u})\;\mathrm{d}V = 0. \tag{1.6}$$

The control volume Ω_{CV} is arbitrary and it follows that the integrand in Eq. (1.6) has to be zero. The differential form of the mass conservation equation (Ferziger and Perić, 2002) follows as

$$\frac{\partial \rho}{\partial t} + \boldsymbol{\nabla} \cdot (\rho \, \mathbf{u}) = 0. \tag{1.7}$$

The same procedure can be conducted with Newtons' second law. The forces on the control volume are specified at this point and we distinguish between volume forces such as gravity and forces on the boundary such as stresses,

$$\mathbf{f} = \int\limits_{\Omega_{\mathrm{CV}}} \rho \, \mathbf{g} \, \mathrm{d}V + \oint\limits_{\partial\Omega_{\mathrm{CV}}} \boldsymbol{\sigma} \, \mathbf{n} \, \mathrm{d}S, \tag{1.8}$$

with the gravitational acceleration $\mathbf{g}$ and *Cauchy's stress tensor* of rank two $\boldsymbol{\sigma}$ (Irgens, 2008). The differential form of Newtons' second law follows as (Ferziger and Perić, 2002)

$$\frac{\partial \rho \, \mathbf{u}}{\partial t} + \boldsymbol{\nabla} \cdot (\rho \, \mathbf{u} \otimes \mathbf{u}) = \rho \, \mathbf{g} + \boldsymbol{\nabla} \cdot \boldsymbol{\sigma}, \tag{1.9}$$

and is called *Cauchy Equations of Motion* (Irgens, 2008). Notably, this equation holds not only for fluids, but also for solids and any other matter.

The limitation to fluids is introduced with the assumption of a specific form of the stress tensor (Ferziger and Perić, 2002),

$$\boldsymbol{\sigma} = -p \, \mathbf{I} + \mathbf{T}^{\mathrm{dev}} = -p \, \mathbf{I} + 2 \, \eta \, \mathbf{D}^{\mathrm{dev}}, \tag{1.10}$$

with the pressure p, the dynamic viscosity η and the deviatoric strain rate tensor,

$$\mathbf{D}^{\mathrm{dev}} = \frac{1}{2} \left(\boldsymbol{\nabla} \, \mathbf{u} + (\boldsymbol{\nabla} \, \mathbf{u})^{T} \right) - \frac{1}{3} \boldsymbol{\nabla} \cdot \mathbf{u} \, \mathbf{I}, \tag{1.11}$$

where "$\boldsymbol{\nabla}$" is the gradient operator. $\mathbf{I}$ is the identity matrix of rank two. The factor 2 in Eq. (1.10) is related to the historic definition of the viscosity. This assumption states that shear stresses $\mathbf{T}^{\mathrm{dev}}$ can only be present in the material if there is a respective strain rate $\mathbf{D}^{\mathrm{dev}}$, following the definition of a fluid (Ferziger and Perić, 2002). The final momentum conservation equation of the Navier–Stokes Equations follows as

$$\frac{\partial \rho \, \mathbf{u}}{\partial t} + \boldsymbol{\nabla} \cdot (\rho \, \mathbf{u} \otimes \mathbf{u}) = \rho \, \mathbf{g} - \boldsymbol{\nabla} \, p + \boldsymbol{\nabla} \cdot \left(2 \, \eta \, \mathbf{D}^{\mathrm{dev}} \right), \tag{1.12}$$

In many cases, we can assume that fluids are incompressible, i.e.

$$\frac{\mathrm{d}\rho}{\mathrm{d}t} = 0 \tag{1.13}$$

and the incompressible Navier–Stokes Equations follow as

$$\boldsymbol{\nabla} \cdot \mathbf{u} = 0, \tag{1.14}$$

$$\frac{\partial \rho \mathbf{u}}{\partial t} + \boldsymbol{\nabla} \cdot (\rho \, \mathbf{u} \otimes \mathbf{u}) = \rho \, \mathbf{g} - \boldsymbol{\nabla} \, p + \boldsymbol{\nabla} \cdot \left(2 \, \eta \, \mathbf{D}^{\text{dev}}\right) . \tag{1.15}$$

Note, that the density can not be removed from the first two terms of the momentum conservation equation, because we want to retain the possibility for spatially varying densities ($\boldsymbol{\nabla} \rho \neq \mathbf{0}$) as present in e.g. multiphase systems.

The presented procedure including *Reynold's transport theorem* and *Gauss' divergence theorem* can be conducted with all conservative properties to find the respective differential forms. This is one of the central tools of this thesis and was applied to a large variety of conservative properties, e.g. volumetric phase fractions, phase momentum or component indicators. More details can be found in the respective papers of this thesis.

1.4 Constitutive modelling

The very specific form for the stress tensor in the Navier–Stokes Equations (see Eq. 1.10) has strong implications for complex fluids such as landslides, as shown in Paper I. Here, a short introduction to one-dimensional conceptual material models and their extension to three dimensions is given to facilitate a better understanding of the respective parts of this thesis.

Basic constitutive models can be classified as either elastic, viscous or plastic (see Fig. 1.2 and Liingaard *et al.* (2004)).

Elastic models describe a unique relationship between the (one-dimensional) stress σ and the (one-dimensional) strain ε, the stress is proportional to the deformation. In the simplest case the relationship is linear, as shown in Fig. 1.2, and the model is described by *Hook's law*,

$$\sigma = E \, \varepsilon, \tag{1.16}$$

with the elastic modulus E. The schematic representation of an elastic model is a spring.

Viscous models describe a unique relationship between the (one-dimensional) stress σ and the (one-dimensional) strain rate $\dot{\varepsilon} = \partial\varepsilon/\partial t$, the stress is proportional to the velocity at which the deformation occurs. The linear case is called a Newtonian fluid and is described by

$$\sigma = \eta \, \dot{\varepsilon}, \tag{1.17}$$

similar as in the Navier–Stokes Equations. The schematic representation is a viscous damper.

Plastic models are formulated in terms of a yield stress σ_{y}, that has to be reached to allow a deformation or deformation rate $\dot{\varepsilon}$ and which cannot be exceeded. The model describes two cases,

$$\dot{\varepsilon} = \begin{cases} 0 & \text{for} \quad \sigma < \sigma_{\text{y}}, \\ \text{undefined} & \text{for} \quad \sigma = \sigma_{\text{y}}. \end{cases} \tag{1.18}$$

The schematic representation is a (frictional) slider.

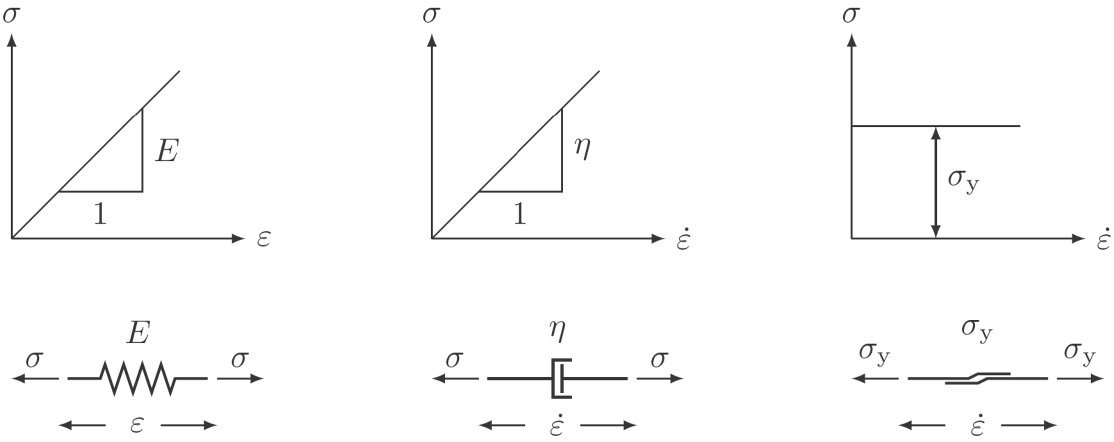

Figure 1.2: Basic one-dimensional constitutive models: (a) linear elasticity, (b) linear (Newtonian) viscosity and (c) plasticity and the respective schematic representations (a) spring, (b) damper and (c) slider. Redrawn after Liingaard *et al.* (2004).

The three basic constitutive models can be combined in various ways to model complex material behaviour. Models can be combined in a parallel manner, adding respective stresses and matching strain and strain rate or in a serial manner, matching stresses and adding strain and strain rate. Simple examples of such combinations include elasto-plastic models (elastic and plastic model in series) or the elasto-visco-plastic Bingham model (Liingaard *et al.*, 2004), as shown in Fig. 1.3. This model predicts an initial elastic deformation until the stress σ exceeds the yield stress σ_y. Stresses that exceed the yield stress are absorbed by the viscous damper and a flow at a rate of $\dot{\varepsilon}$ occurs. Note that the elastic part is often excluded in the Bingham model.

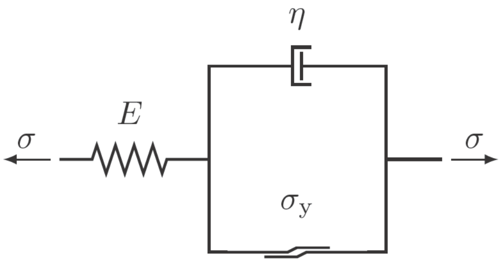

Figure 1.3: The Bingham model is a popular example for a combined elasto-visco-plastic model for ice or granular material. Redrawn after Liingaard *et al.* (2004).

For realistic applications it is required to extend these models to three-dimensional stress and deformation states, defined by the rank two stress and strain or strain rate tensors. Interestingly, different strategies are applied to extend elastic, viscous and plastic models. Elasticity shows a very general approach and uses linear algebra to define the three-dimensional *Hook's law* as

$$\boldsymbol{\sigma} = \mathbf{C}\,\boldsymbol{\varepsilon}, \tag{1.19}$$

where $\mathbf{C}$ is a tensor of rank four and 81 entries. Notably, many assumptions on the structure of $\mathbf{C}$ can be made and a simplified notation, exploiting the symmetry of the stress and strain tensor is given as

$$\begin{pmatrix} \varepsilon_{11} \\ \varepsilon_{22} \\ \varepsilon_{33} \\ \varepsilon_{12} \\ \varepsilon_{13} \\ \varepsilon_{21} \end{pmatrix} = \begin{pmatrix} \frac{1}{E} & \frac{1}{E} - \frac{1}{2\,G} & \frac{1}{E} - \frac{1}{2\,G} & 0 & 0 & 0 \\ \frac{1}{E} - \frac{1}{2\,G} & \frac{1}{E} & \frac{1}{E} - \frac{1}{2\,G} & 0 & 0 & 0 \\ \frac{1}{E} - \frac{1}{2\,G} & \frac{1}{E} - \frac{1}{2\,G} & \frac{1}{E} & 0 & 0 & 0 \\ 0 & 0 & 0 & \frac{1}{G} & 0 & 0 \\ 0 & 0 & 0 & 0 & \frac{1}{G} & 0 \\ 0 & 0 & 0 & 0 & 0 & \frac{1}{G} \end{pmatrix} \begin{pmatrix} \sigma_{11} \\ \sigma_{22} \\ \sigma_{33} \\ \sigma_{12} \\ \sigma_{13} \\ \sigma_{21} \end{pmatrix}, \tag{1.20}$$

with the shear modulus G. Further, the stress and strain tensors have been reassembled into a vector and the reciprocal of $\mathbf{C}$ is shown to simplify the notation.

The three-dimensional extension of viscous models was already introduced in the context of the Navier–Stokes Equations as

$$\boldsymbol{\sigma} = -p\,\mathbf{I} + 2\,\eta\,\mathbf{D}^{\mathrm{dev}}. \tag{1.21}$$

The viscosity is a scalar, which is a strong contrast to the elastic material model, where the factor of proportion is a tensor of rank four. This approach introduces a specific assumption about the form of the stress tensor and its consistency with non-Newtonian fluids is not guaranteed. Notably, the hydrostatic part of the stress tensor, p, is not resolved by the viscous model and has to be established in a different way (i.e. the divergence constraint on the velocity).

In plasticity, the simple inequality $\sigma < \sigma_{\mathrm{y}}$ is replaced by a complex yield criterion,

$$f(\boldsymbol{\sigma}) < 0, \tag{1.22}$$

taking into account all components of the stress tensor. Examples for the yield surface $f(\boldsymbol{\sigma})$ are given in Paper I. As for elastic models, this approach is very flexible and a large variety of material properties can be expressed.

Granular materials behave elastic at small deformations and are described best by a plastic model at large deformations. Implementing this complex behaviour in a viscous framework, like the Navier–Stokes Equations, is problematic. However, it has been shown, first by Jop *et al.* (2006) but also by many other researchers (e.g. Lagrée *et al.*, 2011; Barker and Gray, 2017), that the decisive behaviour of granular flows can be encoded in a single scalar viscosity. This is done by neglecting the elastic behaviour at small deformations and by defining a non-linear viscosity that mimics plastic behaviour. The closest match is achieved if the viscosity tends to infinity for $\sigma < \sigma_{\mathrm{y}}$ (and thus $\dot{\varepsilon} \to 0$) and results in the stress $\sigma = \sigma_{\mathrm{y}}$ for $\dot{\varepsilon} > 0$. This is fulfilled by a viscosity of the form

$$\eta = \frac{\sigma_{\mathrm{y}}}{\dot{\varepsilon}}. \tag{1.23}$$

It is easy to recognize in Eq. (1.23) that solid material $\dot{\varepsilon} \to 0$ is only included as a limit state and that the asymptote of the viscosity at $\dot{\varepsilon} = 0$ introduces numerical problems. This issue is solved in this work by truncating the viscosity and the solid material is basically modelled as a highly viscous fluid. Further issues appear in the three-dimensional extension because three-dimensional viscous models are much more limited than their elastic or plastic equivalents (compare Eqs. (1.20), (1.21) and Eqs. (1.22)). Paper I investigates the consistency of this approach with known granular behaviour in three dimensions. The consequence of truncating the viscosity is investigated in paper II.

1.5 The Finite Volume Method and OpenFOAM

The models developed in this thesis lead to non-linear partial differential equations. An analytical solution is not achievable, except for trivial cases and we have to rely on numerical solutions with e.g. the Finite Volume Method. The Finite Volume Method was chosen in this work because of its flexibility and availability in form of the open source CFD toolkit OpenFOAM. Notable alternatives are the Finite Difference and the Finite Element Method, as well as various Lagrangian methods, such as Smoothed Particle Hydrodynamics or Material Point Method (see e.g. references in the introduction of Paper III). A very short introduction into the Finite Volume Method and its most important aspects is given here to facilitate the understanding of this work. For a more detailed introduction, the reader is referred to Ferziger and Perić (2002), Jasak (1996) or Moukalled *et al.* (2016).

The Finite Volume Method is based on the integral form of conservation equations. A general convection-diffusion equation for a conservative property Ψ and its density $\psi\left(\mathbf{x},t\right)$, with convective velocity $\mathbf{u}\left(\mathbf{x},t\right)$, the diffusion coefficient $\Gamma_\psi\left(\mathbf{x},t\right)$ and the source term $S_\psi\left(\mathbf{x},t\right)$,

$$\underbrace{\frac{\partial \psi}{\partial t}}_{\text{temporal derivative}} + \underbrace{\boldsymbol{\nabla}\cdot\left(\mathbf{u}\,\psi\right)}_{\text{convective term}} = \underbrace{\boldsymbol{\nabla}\cdot\left(\Gamma_\psi\,\boldsymbol{\nabla}\,\psi\right)}_{\text{diffusive term}} + \underbrace{S_\psi}_{\text{source term}}, \tag{1.24}$$

is given in integral form as

$$\frac{\partial}{\partial t}\int\limits_{\Omega_{\mathrm{CV}}} \psi\,\mathrm{d}V + \int\limits_{\Omega_{\mathrm{CV}}} \boldsymbol{\nabla}\cdot\left(\mathbf{u}\,\psi\right)\,\mathrm{d}V = \int\limits_{\Omega_{\mathrm{CV}}} \boldsymbol{\nabla}\cdot\left(\Gamma_\psi\,\boldsymbol{\nabla}\,\psi\right)\,\mathrm{d}V + \int\limits_{\Omega_{\mathrm{CV}}} S_\psi\,\mathrm{d}V. \tag{1.25}$$

Using *Gauss' divergence theorem* allows the removal of the divergence operators,

$$\frac{\partial}{\partial t}\int\limits_{\Omega_{\mathrm{CV}}} \psi\,\mathrm{d}V + \oint\limits_{\partial\Omega_{\mathrm{CV}}} \mathbf{n}\cdot\left(\mathbf{u}\,\psi\right)\,\mathrm{d}S = \oint\limits_{\partial\Omega_{\mathrm{CV}}} \mathbf{n}\cdot\left(\Gamma_\psi\,\boldsymbol{\nabla}\,\psi\right)\,\mathrm{d}S + \int\limits_{\Omega_{\mathrm{CV}}} S_\psi\,\mathrm{d}V. \tag{1.26}$$

The spatial domain is discretized by an arbitrary number of finite volume cells as shown in Fig. 1.4 that act as control volumes, i.e. Ω_{CV}. Finite volume cells cover the spatial domain entirely, do not overlap, are convex and bounded

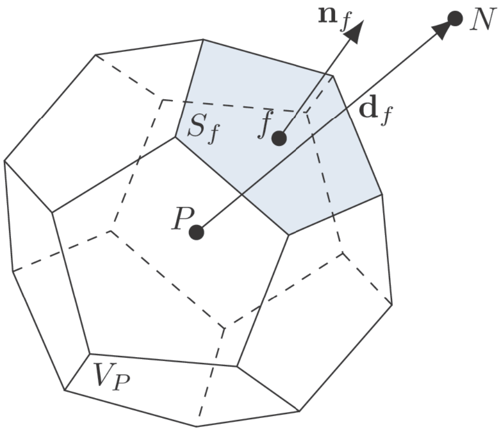

Figure 1.4: The prototype of a finite volume cell. Redrawn after Tuković and Jasak (2012).

by an arbitrary number of flat faces with centre point f and surface area S_f. The cell P has a volume V_P and centre point $\mathbf{x}_P$. Neighbouring cells which share the face f with cell P are notated with N. The sum of all cells is called mesh. A second order accurate approximation of the field ψ within the cell P is given by

$$\psi\left(\mathbf{x}, t\right) = \psi_P(t) + \boldsymbol{\nabla}\,\psi_P(t)\,\left(\mathbf{x} - \mathbf{x}_P\right) \tag{1.27}$$

and the integral over the cell P follows to second order accuracy as

$$\int\limits_{V_P} \psi\left(\mathbf{x}, t\right)\,\mathrm{d}V = \psi_P(t)\,V_P. \tag{1.28}$$

A similar approximation follows for surface integrals which follow as

$$\int\limits_{S_f} \psi\left(\mathbf{x}, t\right)\,\mathrm{d}S = \psi_f(t)\,S_f. \tag{1.29}$$

This allows the replacement of the integrals with sums,

$$\frac{\partial \psi_P}{\partial t} V_P + \sum_f \mathbf{n}_f \cdot \left(\mathbf{u}_f\,\psi_f\right)\,S_f = \sum_f \mathbf{n}_f \cdot \left(\Gamma_{\psi,f}\,(\boldsymbol{\nabla}\,\psi)_f\right)\,S_f + S_{\psi,P}\,V_P. \tag{1.30}$$

Values on faces, e.g. ψ_f can be replaced by a combination of values on centres, ψ_P and ψ_N, using second order accurate interpolations,

$$\psi_f = \psi_P \alpha + \psi_N\,(1 - \alpha). \tag{1.31}$$

The factor α depends on the interpolation rule. Various interpolation rules (second order central, first order upwind) can be found in the literature and the stability of the method is highly dependent on selecting the appropriate rule. Boundary conditions are incorporated by replacing the interpolation rule, Eq. (1.31), with a relation that reflects the boundary condition.

The time is split into an arbitrary number of time steps with duration Δt and the temporal evolution is calculated in a time-marching manner, starting from a known state called initial condition. The temporal derivative can be discretized with a simple integration rule, e.g. backward or forward Euler,

$$\frac{\partial \psi_P}{\partial t} = \frac{\psi_P^i - \psi_P^{i-1}}{\Delta t}, \tag{1.32}$$

with the known old value ψ_P^{i-1} at t^{i-1} and the new unknown value ψ_P^i at $t^i = t^{i-1} + \Delta t$. The scheme is called backward (implicit) Euler if $\psi = \psi^i$ in Eq. (1.30) or forward (explicit) Euler if $\psi = \psi^{i-1}$ in Eq. (1.30). Implicit and explicit higher order schemes can be constructed with minor additional complexity.

The directional derivative in the diffusive term is approximated by

$$\mathbf{n}_f \cdot (\boldsymbol{\nabla}\, \psi)_f = \frac{\psi_N - \psi_P}{d_f}, \tag{1.33}$$

with $d_f = |\mathbf{x}_N - \mathbf{x}_P|$. This approximation is only second order accurate for specific geometries and correction terms have to be applied in practice.

The fully (implicitly) discretized system can be written as

$$\begin{aligned}\frac{\psi_P^i - \psi_P^{i-1}}{\Delta t} V_P + \sum_f \mathbf{n}_f \cdot \mathbf{u}_f^i \, \left(\psi_P^i\, \alpha + \psi_N^i\, (1-\alpha)\right) S_f = \\ \sum_f \frac{\psi_N^i - \psi_P^i}{d_f} \Gamma_{\psi,f}\, S_f + S_{\psi,P}\, V_P,\end{aligned} \tag{1.34}$$

where ψ_P^i and ψ_N^i remain the only unknowns. Factors of unknowns can be collected and the discretized equation can be written as

$$a_P\, \psi_P^i + a_N\, \psi_N^i = b_P^i, \tag{1.35}$$

for all cells P, resulting in as many linear equations as cells. The linear system can be solved by respective algorithms to yield values for ψ_P^i. The full solution of the partial differential equation can be reconstructed with Eq. (1.27).

The convection-diffusion equation is a simple example and we have to deal with additional difficulties for practical applications. Additional complexity can be introduced by coupling with other PDEs and non-linear terms (e.g. the convective term of the momentum conservation equation). In such cases, we have to rely on an explicit or semi-implicit treatment of the respective terms. The incompressible Navier–Stokes Equations represent a very special form of PDE and require specialized algorithms (e.g. PISO) to obtain a solution.

OpenFOAM provides a large range of functionalities with the Finite Volume Method as the central element. Most notably, this includes data structures such as meshes, fields, cells or viscosity models and the respective input- and output routines, an implementation of the Finite Volume Method and linear solver for the resulting system. Many recurring programming tasks are simplified by auxiliary functions or code snippets. A large variety of physical models has been implemented into OpenFOAM and they can be used with no or little modification, as done in Paper III. For other cases, it is sufficient to create a new library that can be loaded by OpenFOAM during runtime, as done in Paper I. Finally, deeper modifications require a new application or modifications to an existing application and this was required for Papers II and IV.

Listing 1.1: Solution of a convection-diffusion equation with OpenFOAM.

```
fvScalarMatrix psiEqn
(
    fvm::ddt(psi)               // temporal derivative
  + fvm::div(u, psi)            // convective term
  ==
  + fvm::laplacian(Gamma, psi)  // diffusive term
    S_psi                       // source term
);

psiEqn.solve();                 // calling the linear algebra solver
```

The implementation of PDEs is very convenient in OpenFOAM. The convection-diffusion conservation equation (1.24) can be implemented as shown in listing 1.1 (the time looping is excluded). The namespace `fvm` refers to Finite Volume Method and contains all methods and classes required for the implicit solution of PDEs. The namespace `fvc`, i.e. Finite Volume Calculus, provides additional functionalities, e.g. calculating derivatives based on known fields, which can be used for explicit solutions or explicit corrections to implicit solutions.

The OpenFOAM models applied in this work are based on the standard models *multiphaseInterFoam* and *multiphaseEulerFoam* of OpenFOAM-v1812. Both solvers implement the Navier–Stokes Equations and a multicomponent- or multiphase-system. *multiphaseInterFoam* implements a sharp interface and a single momentum conservation equation that is shared by all components, *multiphaseEulerFoam* implements a gradual or dispersed interface and a momentum conservation equation for each phase. Further they allow the application of custom viscosity models, i.e. the $\mu(I)$-rheology in case of this thesis. The time step duration algorithm was adapted in both solvers to account for the high viscosity that is found in granular flows (see Lst. A.1). The solver *multiphaseEulerFoam* was further extended to include the granular pressure in the momentum conservation equation (see Paper II and Lst. A.2).

For Paper IV, the solver *multiphaseEulerFoam* was further extended as follows: The momentum conservation equations were changed to account for a variable density of phases (e.g. $\rho\,\partial\mathbf{u}/\partial t \rightarrow \partial(\rho\,\mathbf{u})/\partial t$) (see Lst. A.3). The class `phaseModel` was extended with various functions (e.g. `solveAlphas(...)`, `correct(...)`, `nHatf(...)`) from the class `multiphaseMixture` of *multiphaseInterFoam* to allow a split of phases in various components (see Lst. A.4). The advection of components within `phaseModel` is solved with the MULES algorithm (Multidimensional universal limiter for explicit solution) and corrected by the same counter gradient transport term as applied in *multiphaseInterFoam*. The component-wise volumetric flux as calculated and corrected by the MULES algorithm is further multiplied with the component density and the respective sum over all components is applied in the advection term of the phase momentum conservation equation.

1.6 Summary of Papers

This thesis covers a wide range of areas, from the theoretical model development to the practical implementation and application. The four cumulative chapters lead to the following main conclusions.

Paper I focuses on the implementation of plastic constitutive models into the Navier–Stokes Equations. In particular, it is shown how (almost) arbitrary yield criteria can be expressed as a non-linear viscosity. This allows the simulation of granular flows with computational fluid mechanics frameworks. The relations between plasticity and viscosity were investigated in unprecedented levels of detail and many previous ad-hoc assumptions were formalized and placed on a solid foundation.

Paper II extends the plastic constitutive models from paper I to granular multiphase flows, incorporating pore fluid flow and variations of pore pressure and packing density (porosity). This allows reliable predictions of subaquatic granular flows with minimal fitting of model parameters. The packing density and the related excess pore pressure showed to be the decisive parameter for the mobility of subaquatic granular flows and the source for many flow patterns observed in laboratory experiments and the field.

Paper III demonstrates the ability of the Navier–Stokes Equations and the applied software framework OpenFOAM to simulate the generation and propagation of idealized landslide tsunamis. The landslide consists of water in this study and the exclusion of complex landslide rheologies allowed a thorough study of the simulated waves. It could be shown that the applied framework is capable of reproducing the decisive mechanics of wave generation and propagation. Particular focus was put on the verification of the numerical solution and estimates for the required mesh resolution, the time step resolution and the related errors are given. Further, a large variety of simulations was conducted to empirically investigate the influence of various landslide parameters on the wave generation.

Paper IV combines the granular multiphase model with the tsunami generation model and thus papers III and II. The paper demonstrates the simulation of tsunamis generated by porous granular landslides with good accuracy and reliability. The model is further applied to a full three-dimensional real scale case, the 2014 lake Askja landslide tsunami. This case study proves the scalability and the consistency of the model for a wide range of events and scales.

1.7 Bibliography

S. Abadie, D. Morichon, S. Grilli and S. Glockner, "Numerical simulation of waves generated by landslides using a multiple-fluid Navier–Stokes model," *Coastal Engineering*, vol. 57, no. 9, pp. 779–794, 2010, DOI: 10.1016/j.coastaleng.2010.03.003.

S. Abadie, A. Paris, R. Ata, S. Le Roy, G. Arnaud, A. Poupardin, L. Clous, P. Heinrich, J. Harris, R. Pedreros *et al.*, "La Palma landslide tsunami: calibrated wave source and assessment of impact on French territories," *Natural Hazards and Earth System Sciences*, vol. 20, no. 11, pp. 3019–3038, 2020, DOI: 10.5194/nhess-20-3019-2020.

S. Assier-Rzadkieaicz, P. Heinrich, P. C. Sabatier, B. Savoye and J. F. Bourillet, "Numerical Modelling of a Landslide-generated Tsunami: The 1979 Nice Event," *Pure and Applied Geophysics*, vol. 157, no. 10, pp. 1707–1727, 2000, DOI: 10.1007/PL00001057.

S. Bakkehoi, U. Domaas and K. Lied, "Calculation of snow avalanche runout distance," *Annals of Glaciology*, vol. 4, pp. 24–29, 1983.

T. Barker and J. M. N. T. Gray, "Partial regularisation of the incompressible μ(I)-rheology for granular flow," *Journal of Fluid Mechanics*, vol. 828, pp. 5–32, 2017, DOI: 10.1017/jfm.2017.428.

A. S. Baumgarten and K. Kamrin, "A general fluid–sediment mixture model and constitutive theory validated in many flow regimes," *Journal of Fluid Mechanics*, vol. 861, pp. 721–764, 2019, DOI: 10.1017/jfm.2018.914.

M. J. Berger, D. L. George, R. J. LeVeque and K. T. Mandli, "The GeoClaw software for depth-averaged flows with adaptive refinement," *Advances in Water Resources*, vol. 34, no. 9, pp. 1195–1206, 2011, DOI: 10.1016/j.advwatres.2011.02.016.

C. Biscarini, "Computational fluid dynamics modelling of landslide generated water waves," *Landslides*, vol. 7, no. 2, pp. 117–124, 2010, DOI: 10.1007/s10346-009-0194-z.

S. Bondevik, F. Løvholt, C. Harbitz, J. Mangerud, A. Dawson and J. I. Svendsen, "The Storegga Slide tsunami—comparing field observations with numerical simulations," in *Ormen Lange–an Integrated Study for Safe Field Development in the Storegga Submarine Area*, pp. 195–208, Elsevier, 2005.

F. Bouchut, E. D. Fernández-Nieto, E. H. Koné, A. Mangeney and G. Narbona-Reina, “A two-phase solid-fluid model for dense granular flows including dilatancy effects: comparison with submarine granular collapse experiments,” in *EPJ Web of Conferences - Powders & Grains 2017*, vol. 140, p. 09039, EDP Sciences, 2017, DOI: 10.1051/epjconf/201714009039.

F. Chen, V. Heller and R. Briganti, “Numerical modelling of tsunamis generated by iceberg calving validated with large-scale laboratory experiments,” *Advances in Water Resources*, vol. 142, p. 103647, 2020, DOI: 10.1016/j.advwatres.2020.103647.

M. Christen, J. Kowalski and P. Bartelt, “RAMMS: Numerical simulation of dense snow avalanches in three-dimensional terrain,” *Cold Regions Science and Technology*, vol. 63, no. 1–2, pp. 1–14, 2010, DOI: 10.1016/j.coldregions.2010.04.005.

L. Clous and S. Abadie, “Simulation of energy transfers in waves generated by granular slides,” *Landslides*, vol. 16, no. 9, pp. 1663–1679, 2019, DOI: 10.1007/s10346-019-01180-0.

G. Crosta, S. Imposimato and D. Roddeman, “Numerical modeling of 2-D granular step collapse on erodible and nonerodible surface,” *Journal of Geophysical Research: Earth Surface*, vol. 114, no. F3, 2009, DOI: 10.1029/2008JF001186.

B. Domnik, S. P. Pudasaini, R. Katzenbach and S. A. Miller, “Coupling of full two-dimensional and depth-averaged models for granular flows,” *Journal of Non-Newtonian Fluid Mechanics*, vol. 201, pp. 56–68, 2013, DOI: 10.1016/j.jnnfm.2013.07.005.

S. Dunatunga and K. Kamrin, “Continuum modelling and simulation of granular flows through their many phases,” *Journal of Fluid Mechanics*, vol. 779, pp. 483–513, 2015, DOI: 10.1017/jfm.2015.383.

E. D. Fernández-Nieto, F. Bouchut, D. Bresch, M. C. Diaz and A. Mangeney, “A new Savage–Hutter type model for submarine avalanches and generated tsunami,” *Journal of Computational Physics*, vol. 227, no. 16, pp. 7720–7754, 2008, DOI: 10.1016/j.jcp.2008.04.039.

J. H. Ferziger and M. Perić, *Computational methods for fluid dynamics*, Springer, 3rd edn., 2002.

A. Franco, J. Moernaut, B. Schneider-Muntau, M. Aufleger, M. Strasser and B. Gems, “Lituya Bay 1958 Tsunami – detailed pre-event bathymetry reconstruction and 3D-numerical modelling utilizing the CFD software Flow-3D,” *Natural Hazards and Earth System Sciences Discussions*, vol. 2019, pp. 1–34, 2019, DOI: 10.5194/nhess-2019-285.

H. M. Fritz, “Initial phase of landslide generated impulse waves,” Ph.D. thesis, ETH Zurich, 2002, DOI: 10.3929/ethz-a-004443906.

H. M. Fritz, J. V. Hillaire, E. Molière, Y. Wei and F. Mohammed, “Twin tsunamis triggered by the 12 January 2010 Haiti earthquake,” *Pure and Applied Geophysics*, vol. 170, no. 9-10, pp. 1463–1474, 2013.

D. L. George, R. M. Iverson and C. M. Cannon, “New methodology for computing tsunami generation by subaerial landslides: Application to the 2015 Tyndall Glacier landslide, Alaska,” *Geophysical Research Letters*, vol. 44, no. 14, pp. 7276–7284, 2017, DOI: 10.1002/2017GL074341.

L. Gesenhues, J. J. Camata, A. M. A. Côrtes, F. A. Rochinha and A. L. G. A. Coutinho, “Finite element simulation of complex dense granular flows using a well-posed regularization of the μ(I)-rheology,” *Computers and Fluids*, vol. 188, pp. 102–113, 2019, DOI: 10.1016/j.compfluid.2019.05.012.

G. Gisler, R. Weaver and M. L. Gittings, “SAGE calculations of the tsunami threat from La Palma,” *Science of Tsunami Hazards*, vol. 24, no. 4, pp. 288–312, 2006.

S. S. Grigorian, M. E. Eglit and Y. L. Iakimov, “A new formulation and solution of the problem of snow avalanche motion,” *Trudy Vysokogornogo Geofizicheskogo Instituta*, vol. 12, pp. 104–113, 1967.

S. T. Grilli, D. R. Tappin, S. Carey, S. F. Watt, S. N. Ward, A. R. Grilli, S. L. Engwell, C. Zhang, J. T. Kirby, L. Schambach and M. Muin, “Modelling of the tsunami from the December 22, 2018 lateral collapse of Anak Krakatau volcano in the Sunda Straits, Indonesia.” *Scientific Reports*, vol. 9, no. 1, pp. 11946–11946, 2019, DOI: 10.1038/s41598-019-48327-6.

E. Grimstad, “The Loen Rock Slide – An Analysis of the Stability,” in *Landslides and Avalanches – International Conference and Field Trip on Landslides*, 2006.

Y. Guo and J. S. Curtis, “Discrete element method simulations for complex granular flows,” *Annual Review of Fluid Mechanics*, vol. 47, pp. 21–46, 2015, DOI: 10.1146/annurev-fluid-010814-014644.

C. B. Harbitz, F. Løvholt and H. Bungum, “Submarine landslide tsunamis: how extreme and how likely?” *Natural Hazards*, vol. 72, no. 3, pp. 1341–1374, 2014, DOI: 10.1007/s11069-013-0681-3.

C. B. Harbitz, F. Løvholt, G. Pedersen and D. G. Masson, “Mechanisms of tsunami generation by submarine landslides: a short review.” *Norwegian Journal of Geology/Norsk Geologisk Forening*, vol. 86, no. 3, 2006.

C. B. Harbitz, G. Pedersen and B. Gjevik, “Numerical simulations of large water waves due to landslides,” *Journal of Hydraulic Engineering*, vol. 119, no. 12, pp. 1325–1342, 1993.

P. Heinrich, A. Piatanesi and H. Hebert, “Numerical modelling of tsunami generation and propagation from submarine slumps: the 1998 Papua New Guinea event,” *Geophysical Journal International*, vol. 145, no. 1, pp. 97–111, 2001, DOI: 10.1111/j.1365-246X.2001.00336.x.

V. Heller, “The need for a paradigm shift in subaerial landslide-tsunami research,” *Coastal Engineering Proceedings*, 2020, DOI: 10.9753/icce.v36v.currents.36.

C. W. Hirt and B. D. Nichols, “Volume of fluid (VOF) method for the dynamics of free boundaries,” *Journal of Computational Physics*, vol. 39, no. 1, pp. 201–225, 1981.

J. Horrillo, A. Wood, G.-B. Kim and A. Parambath, “A simplified 3-D Navier-Stokes numerical model for landslide-tsunami: Application to the Gulf of Mexico,” *Journal of Geophysical Research: Oceans*, vol. 118, no. 12, pp. 6934–6950, 2013, DOI: 10.1002/2012JC008689.

O. Hungr, “A model for the runout analysis of rapid flow slides, debris flows, and avalanches,” *Canadian Geotechnical Journal*, vol. 32, no. 4, pp. 610–623, 1995, DOI: 10.1139/t95-063.

O. Hungr, “Simplified models of spreading flow of dry granular material,” *Canadian Geotechnical Journal*, vol. 45, no. 8, pp. 1156–1168, 2008, DOI: 10.1139/T08-059.

O. Iglesias, G. Lastras, M. Canals, M. Olabarrieta, M. Gonzalez, Í. Aniel-Quiroga, L. Otero, R. Duran, D. Amblas, J. L. Casamor *et al.*, “The BIG’95 submarine landslide–generated tsunami: a numerical simulation,” *The Journal of Geology*, vol. 120, no. 1, pp. 31–48, 2012.

I. R. Ionescu, A. Mangeney, F. Bouchut and O. Roche, “Viscoplastic modeling of granular column collapse with pressure-dependent rheology,” *Journal of Non-Newtonian Fluid Mechanics*, vol. 219, pp. 1–18, 2015, DOI: 10.1016/j.jnnfm.2015.02.006.

F. Irgens, *Continuum mechanics*, Springer Science & Business Media, 2008.

H. Jasak, “Error analysis and estimation for the finite volume method with applications to fluid flows,” Ph.D. thesis, Imperial College, University of London, 1996.

P. Jop, Y. Forterre and O. Pouliquen, “A constitutive law for dense granular flows,” *Nature*, vol. 441, no. 7094, p. 727, 2006, DOI: 10.1038/nature04801.

J. Kim, F. Løvholt, D. Issler and C. F. Forsberg, “Landslide material control on tsunami genesis–The Storegga slide and tsunami (8,100 years BP),” *Journal of Geophysical Research*, vol. 124, no. 6, pp. 3607–3627, 2019, DOI: 10.1029/2018JC014893.

J. T. Kirby, G. Wei, Q. Chen, A. B. Kennedy and R. A. Dalrymple, “FUNWAVE 1.0: Fully Nonlinear Boussinesq Wave Model - Documentation and User’s Manual,” Tech. Rep. CACR-98-06, University of Delaware, 1998.

K. Kremer, G. Simpson and S. Girardclos, “Giant Lake Geneva tsunami in ad 563,” *Nature Geoscience*, vol. 5, no. 11, pp. 756–757, 2012, DOI: 10.1038/ngeo1618.

L. Lacaze, J. C. Phillips and R. R. Kerswell, “Planar collapse of a granular column: Experiments and discrete element simulations,” *Physics of Fluids*, vol. 20, no. 6, p. 063302, 2008, DOI: 10.1063/1.2929375.

P.-Y. Lagrée, L. Staron and S. Popinet, “The granular column collapse as a continuum: validity of a two-dimensional Navier–Stokes model with a μ(I)-rheology,” *Journal of Fluid Mechanics*, vol. 686, pp. 378–408, 2011, DOI: 10.1017/jfm.2011.335.

H. Lee, R. Kayen, J. V. Gardner and J. Locat, “Characteristics of several tsunamigenic submarine landslides,” in *Submarine mass movements and their consequences*, pp. 357–366, Springer, 2003.

M. Liingaard, A. Augustesen and P. V. Lade, “Characterization of models for time-dependent behavior of soils,” *International Journal of Geomechanics*, vol. 4, no. 3, pp. 157–177, 2004, DOI: 10.1061/(ASCE)1532-3641(2004)4:3(157).

E. K. Lindstrøm, G. K. Pedersen, A. Jensen and S. Glimsdal, “Experiments on slide generated waves in a 1: 500 scale fjord model,” *Coastal Engineering*, vol. 92, pp. 12–23, 2014.

P. L.-F. Liu, T.-R. Wu, F. Raichlen, C. E. Synolakis and J. C. Borrero, “Runup and rundown generated by three-dimensional sliding masses,” *Journal of Fluid Mechanics*, vol. 536, pp. 107–144, 2005, DOI: 10.1017/S0022112005004799.

F. Løvholt, G. Pedersen and G. Gisler, “Oceanic propagation of a potential tsunami from the La Palma Island,” *Journal of Geophysical Research: Oceans*, vol. 113, no. C9, 2008, DOI: 10.1029/2007JC004603.

F. Løvholt, I. Schulten, D. Mosher, C. Harbitz and S. Krastel, “Modelling the 1929 Grand Banks slump and landslide tsunami,” *Geological Society, London, Special Publications*, vol. 477, no. 1, pp. 315–331, 2019.

G. Ma, J. T. Kirby, T.-J. Hsu and F. Shi, “A two-layer granular landslide model for tsunami wave generation: Theory and computation,” *Ocean Modelling*, vol. 93, pp. 40–55, 2015, DOI: 10.1016/j.ocemod.2015.07.012.

G. Ma, F. Shi and J. T. Kirby, “Shock-capturing non-hydrostatic model for fully dispersive surface wave processes,” *Ocean Modelling*, vol. 43, pp. 22–35, 2012, DOI: 10.1016/j.ocemod.2011.12.002.

A. Mangeney, F. Bouchut, N. Thomas, J.-P. Vilotte and M. Bristeau, “Numerical modeling of self-channeling granular flows and of their levee-channel deposits,” *Journal of Geophysical Research: Earth Surface*, vol. 112, no. F2, 2007, DOI: 10.1029/2006JF000469.

N. Martin, I. R. Ionescu, A. Mangeney, F. Bouchut and M. Farin, “Continuum viscoplastic simulation of a granular column collapse on large slopes: μ(I) rheology and lateral wall effects,” *Physics of Fluids*, vol. 29, no. 1, p. 013301, 2017, DOI: 10.1063/1.4971320.

C. M. Mast, P. Arduino, P. Mackenzie-Helnwein and G. R. Miller, “Simulating granular column collapse using the material point method,” *Acta Geotechnica*, vol. 10, no. 1, pp. 101–116, 2015, DOI: 10.1007/s11440-014-0309-0.

V. Medina, M. Hürlimann and A. Bateman, “Application of FLATModel, a 2D finite volume code, to debris flows in the northeastern part of the Iberian Peninsula,” *Landslides*, vol. 5, no. 1, pp. 127–142, 2008, DOI: 10.1007/s10346-007-0102-3.

M. Mergili, J.-T. Fischer, J. Krenn and S. P. Pudasaini, “r.avaflow v1, an advanced open-source computational framework for the propagation and interaction of two-phase mass flows,” *Geoscientific Model Development*, vol. 10, no. 2, pp. 553–569, 2017, DOI: 10.5194/gmd-10-553-2017.

M. Mergili, K. Schratz, A. Ostermann and W. Fellin, “Physically-based modelling of granular flows with Open Source GIS,” *Natural Hazards and Earth System Sciences*, vol. 12, no. 1, pp. 187–200, 2012, DOI: 10.5194/nhess-12-187-2012.

C. Meruane, A. Tamburrino and O. Roche, “On the role of the ambient fluid on gravitational granular flow dynamics,” *Journal of Fluid Mechanics*, vol. 648, p. 381, 2010, DOI: 10.1017/S0022112009993181.

F. Moukalled, L. Mangani and M. Darwish, *The finite volume method in computational fluid dynamics*, Springer, 2016, DOI: 10.1007/978-3-319-16874-6.

R. P. Mulligan, A. Franci, M. A. Celigueta and W. A. Take, “Simulations of landslide wave generation and propagation using the Particle Finite Element Method,” *Journal of Geophysical Research: Oceans*, vol. 125, p. e2019JC015873, 2020, DOI: 10.1029/2019JC015873.

OpenCFD, “OpenFOAM user guide,” *OpenFOAM Foundation*, 2018, last checked: 11.08.20.

A. Panizzo, P. De Girolamo, M. Di Risio, A. Maistri and A. Petaccia, “Great landslide events in Italian artificial reservoirs,” *Natural Hazards and Earth System Sciences*, vol. 5, pp. 733–740, 2005, DOI: 10.5194/nhess-5-733-2005.

A. Paris, E. A. Okal, C. Guérin, P. Heinrich, F. Schindelé and H. Hébert, “Numerical modeling of the June 17, 2017 landslide and tsunami events in Karrat Fjord, West Greenland,” *Pure and Applied Geophysics*, vol. 176, pp. 3035–3057, 2019, DOI: 10.1007/s00024-019-02123-5.

A. K. Patra, A. C. Bauer, C. C. Nichita, E. B. Pitman, M. F. Sheridan, M. Bursik, B. Rupp, A. Webber, A. J. Stinton, L. M. Namikawa and C. S. Renschler, “Parallel adaptive numerical simulation of dry avalanches over natural terrain,” *Journal of Volcanology and Geothermal Research*, vol. 139, no. 1, pp. 1–21, 2005, DOI: 10.1016/j.jvolgeores.2004.06.014.

C. Peng, W. Wu, H.-s. Yu and C. Wang, “A SPH approach for large deformation analysis with hypoplastic constitutive model,” *Acta Geotechnica*, vol. 10, no. 6, pp. 703–717, 2015, DOI: 10.1007/s11440-015-0399-3.

E. B. Pitman, C. C. Nichita, A. Patra, A. Bauer, M. Sheridan and M. Bursik, “Computing granular avalanches and landslides,” *Physics of Fluids*, vol. 15, no. 12, pp. 3638–3646, 2003, DOI: 10.1063/1.1614253.

S. P. Pudasaini, “A general two-phase debris flow model,” *Journal of Geophysical Research: Earth Surface*, vol. 117, no. F3, 2012, DOI: 10.1029/2011JF002186.

S. P. Pudasaini and K. Hutter, *Avalanche Dynamics: Dynamics of Rapid Flows of Dense Granular Avalanches*, Springer, 2007, DOI: 10.1007/978-3-540-32687-8.

A. B. Rabinovich, R. E. Thomson, E. A. Kulikov, B. D. Bornhold and I. V. Fine, “The landslide-generated tsunami of November 3, 1994 in Skagway Harbor, Alaska: A case study,” *Geophysical Research Letters*, vol. 26, no. 19, pp. 3009–3012, 1999.

M. Rauter, A. Kofler, A. Huber and W. Fellin, “faSavageHutterFOAM 1.0: depth-integrated simulation of dense snow avalanches on natural terrain with OpenFOAM,” *Geoscientific Model Development*, vol. 11, no. 7, pp. 2923–2939, 2018, DOI: 10.5194/gmd-11-2923-2018.

M. Rauter and Ž. Tuković, “A finite area scheme for shallow granular flows on three-dimensional surfaces,” *Computers and Fluids*, vol. 116, pp. 184–199, 2018, DOI: 10.1016/j.compfluid.2018.02.017.

A. Romano, J. L. Lara, G. Barajas, B. Di Paolo, G. Bellotti, M. Di Risio, I. J. Losada and P. De Girolamo, “Tsunamis generated by submerged landslides: numerical analysis of the near-field wave characteristics,” *Journal of Geophysical Research: Oceans*, vol. 125, p. e2020JC016157, 2020, DOI: 10.1029/2020JC016157.

P. Sampl and T. Zwinger, “Avalanche simulation with SAMOS,” *Annals of Glaciology*, vol. 38, no. 1, pp. 393–398, 2004, DOI: 10.3189/172756404781814780.

K. Sassa, K. Dang, H. Yanagisawa and B. He, “A new landslide-induced tsunami simulation model and its application to the 1792 Unzen-Mayuyama landslide-and-tsunami disaster,” *Landslides*, vol. 13, no. 6, pp. 1405–1419, 2016.

S. B. Savage, M. H. Babaei and T. Dabros, “Modeling gravitational collapse of rectangular granular piles in air and water,” *Mechanics Research Communications*, vol. 56, pp. 1–10, 2014, DOI: 10.1016/j.mechrescom.2013.11.001.

S. B. Savage and K. Hutter, “The motion of a finite mass of granular material down a rough incline,” *Journal of Fluid Mechanics*, vol. 199, pp. 177–215, 1989, DOI: 10.1017/S0022112089000340.

S. B. Savage and K. Hutter, “The dynamics of avalanches of granular materials from initiation to runout. Part I: Analysis,” *Acta Mechanica*, vol. 86, no. 1-4, pp. 201–223, 1991, DOI: 10.1007/BF01175958.

D. G. Schaeffer, “Instability in the evolution equations describing incompressible granular flow,” *Journal of Differential Equations*, vol. 66, no. 1, pp. 19–50, 1987, DOI: 10.1016/0022-0396(87)90038-6.

S. A. Sepúlveda and A. Serey, “Tsunamigenic, earthquake-triggered rock slope failures during the April 21, 2007 Aisén earthquake, southern Chile (45.5 S),” *Andean Geology*, vol. 36, no. 1, pp. 131–136, 2009.

T. Shan and J. Zhao, “A coupled CFD-DEM analysis of granular flow impacting on a water reservoir,” *Acta Mechanica*, vol. 225, no. 8, pp. 2449–2470, 2014, DOI: 10.1007/s00707-014-1119-z.

P. Si, H. Shi and X. Yu, “Development of a mathematical model for submarine granular flows,” *Physics of Fluids*, vol. 30, no. 8, p. 083302, 2018a, DOI: 10.1063/1.5030349.

P. Si, H. Shi and X. Yu, “A general numerical model for surface waves generated by granular material intruding into a water body,” *Coastal Engineering*, vol. 142, pp. 42–51, 2018b, DOI: 10.1016/j.coastaleng.2018.09.001.

L. Staron, P.-Y. Lagrée and S. Popinet, “The granular silo as a continuum plastic flow: The hour-glass vs the clepsydra,” *Physics of Fluids*, vol. 24, no. 10, p. 103301, 2012, DOI: 10.1063/1.4757390.

C. E. Synolakis, J.-P. Bardet, J. C. Borrero, H. L. Davies, E. A. Okal, E. A. Silver, S. Sweet and D. R. Tappin, “The slump origin of the 1998 Papua New Guinea tsunami,” *Proceedings of the Royal Society of London. Series A: Mathematical, Physical and Engineering Sciences*, vol. 458, no. 2020, pp. 763–789, 2002.

H. Takagi, M. B. Pratama, S. Kurobe, M. Esteban, R. Aránguiz and B. Ke, “Analysis of generation and arrival time of landslide tsunami to Palu City due to the 2018 Sulawesi earthquake,” *Landslides*, vol. 16, no. 5, pp. 983–991, 2019.

H. Tan, G. Ruffini, V. Heller and S. Chen, “A numerical landslide-tsunami hazard assessment technique applied on hypothetical scenarios at Es Vedrà, offshore Ibiza,” *Journal of Marine Science and Engineering*, vol. 6, no. 4, p. 111, 2018, DOI: 10.3390/jmse6040111.

Ž. Tuković and H. Jasak, “A moving mesh finite volume interface tracking method for surface tension dominated interfacial fluid flow,” *Computers and Fluids*, vol. 55, pp. 70–84, 2012, DOI: 10.1016/j.compfluid.2011.11.003.

A. Voellmy, “Über die Zerstörungskraft von Lawinen.” *Schweizerische Bauzeitung*, vol. 73, no. 12,15,17,19, 1955, DOI: 10.5169/seals-61878.

A. von Boetticher, J. M. Turowski, B. W. McArdell, D. Rickenmann, M. Hürlimann, C. Scheidl and J. W. Kirchner, “DebrisInterMixing-2.3: a finite volume solver for three-dimensional debris-flow simulations with two calibration parameters – Part 2: Model validation with experiments,” *Geoscientific Model Development*, vol. 10, no. 11, pp. 3963–3978, 2017, DOI: 10.5194/gmd-10-3963-2017.

A. von Boetticher, J. M. Turowski, B. W. McArdell, D. Rickenmann and J. W. Kirchner, “DebrisInterMixing-2.3: a finite volume solver for three-dimensional debris-flow simulations with two calibration parameters – Part 1: Model description,” *Geoscientific Model Development*, vol. 9, no. 9, pp. 2909–2923, 2016, DOI: 10.5194/gmd-9-2909-2016.

P. Wallemacq, R. Below and D. McLean, “UNISDR and CRED report: Economic losses, poverty & disasters (1998–2017),” *CRED, Brussels*, 2018.

C. Wang, Y. Wang, C. Peng and X. Meng, “Dilatancy and compaction effects on the submerged granular column collapse,” *Physics of Fluids*, vol. 29, no. 10, p. 103307, 2017a, DOI: 10.1063/1.4986502.

C. Wang, Y. Wang, C. Peng and X. Meng, “Two-fluid smoothed particle hydrodynamics simulation of submerged granular column collapse,” *Mechanics Research Communications*, vol. 79, pp. 15–23, 2017b, DOI: 10.1016/j.mechrescom.2016.12.001.

J. Wang, S. N. Ward and L. Xiao, “Numerical simulation of the December 4, 2007 landslide-generated tsunami in Chehalis Lake, Canada,” *Geophysical Journal International*, vol. 201, no. 1, pp. 372–376, 2015.

S. N. Ward, “Landslide tsunami,” *Journal of Geophysical Research: Solid Earth*, vol. 106, no. B6, pp. 11201–11215, 2001, DOI: 10.1029/2000JB900450.

S. N. Ward and S. Day, “Ritter Island Volcano - lateral collapse and the tsunami of 1888,” *Geophysical Journal International*, vol. 154, no. 3, pp. 891–902, 2003, DOI: 10.1046/j.1365-246X.2003.02016.x.

H. G. Weller, G. Tabor, H. Jasak and C. Fureby, “A tensorial approach to computational continuum mechanics using object-oriented techniques,” *Computers in Physics*, vol. 12, no. 6, pp. 620–631, 1998, DOI: 10.1063/1.168744.

L. Xiao, J. Wang, S. N. Ward and L. Chen, “Numerical modeling of the June 24, 2015, Hongyanzi landslide generated impulse waves in Three Gorges Reservoir, China,” *Landslides*, vol. 15, no. 12, pp. 2385–2398, 2018.

W.-J. Xu, X.-Y. Dong and W.-T. Ding, “Analysis of fluid-particle interaction in granular materials using coupled SPH-DEM method,” *Powder Technology*, vol. 353, pp. 459–472, 2019, DOI: 10.1016/j.powtec.2019.05.052.

S. Yavari-Ramshe and B. Ataie-Ashtiani, “Numerical modeling of subaerial and submarine landslide-generated tsunami waves–recent advances and future challenges,” *Landslides*, vol. 13, no. 6, pp. 1325–1368, 2016, DOI: 10.1007/s10346-016-0734-2.

H. Yeh, F. Imamura, C. Synolakis, Y. Tsuji, P. Liu and S. Shi, “The Flores island tsunamis,” *Eos, Transactions American Geophysical Union*, vol. 74, no. 33, pp. 369–373, 1993.

Y. Yudhicara, P. Bani and A. Darmawan, “Geothermal system as the cause of the 1979 landslide tsunami in Lembata Island, Indonesia,” *Indonesian Journal on Geoscience*, vol. 2, no. 2, pp. 91–99, 2015.

X. Zhang, K. Krabbenhoft and D. Sheng, “Particle finite element analysis of the granular column collapse problem,” *Granular Matter*, vol. 16, no. 4, pp. 609–619, 2014, DOI: 10.1007/s10035-014-0505-5.

Papers

Paper I

Granular viscosity from plastic yield surfaces: the role of the deformation type in granular flows

Matthias Rauter, Thomas Barker, Wolfgang Fellin

Published in *Computers and Geotechnics*, January 2020, volume 122, pp. 103492. DOI: 10.1016/j.compgeo.2020.103492.

Abstract

Numerical simulations of granular flows with Navier–Stokes type models emerged in the last decade, challenging the well established depth-averaged models. The structure of these equations allows for extension to general rheologies based on complex and realistic constitutive models. Substantial effort has been put into describing the effect of the shear rate, i.e. the magnitude of the velocity gradient, on the shear stress. Here we analyse the effect of the deformation type. We apply the theories of Mohr–Coulomb and Matsuoka–Nakai to calculate the stresses under different deformation types and compare results to the theory of Drucker–Prager, which is formulated independently of the deformation type. This model is particularly relevant because it is the basis for many granular rheologies, such as the $\mu(I)$–rheology. All models have been implemented into the open-source toolkit OpenFOAM® for a practical application. We found that, within the context of these models, the deformation type has a large influence on the stress. However, for the geometries considered here, these differences are limited to specific zones which have little influence on the landslide kinematics. Finally we are able to give indicators on when the deformation type should be considered in modelling of landslides and when it can be neglected.

I.1 Introduction

Dense granular flows are substantial parts of many natural hazards, such as avalanches, landslides, debris flows and lahars. A constitutive description of granular materials is important for a deeper understanding and improved prediction of these processes.

The first models for granular materials stem from geotechnics and applications in the soil mechanics community, with the earliest examples of a mathematical description being in the 19th century, when Charles-Augustin de Coulomb formulated his famous friction law (see e.g. Pudasaini and Hutter, 2007), based on the rules found earlier by Guillaume Amontons (see e.g. Holmberg *et al.*, 2012). It relates normal stress σ_n and shear stress τ between two solids and defines the friction angle ϕ as

$$\tan(\phi) = \frac{\tau}{\sigma_\mathrm{n}}. \tag{I.1}$$

This relation is limited to well defined sliding planes and not generally applicable to three-dimensional situations. Christian Otto Mohr generalized Coulomb's law by determining the decisive shear plane in a failing solid with arbitrary stress state. The resulting formulation is known as the Mohr–Coulomb (MC) failure criterion (Yu, 2002). The Mohr–Coulomb failure criterion describes the failure of brittle materials, such as concrete and granular material with good accuracy. In fact, it has been successfully applied to a wide range of problems, especially within elasto-plastic frameworks (Lubliner, 1990). Various extensions have been applied to the original idea, introducing strain hardening and softening or so-called caps, limiting the admissible pressure (Schanz *et al.*, 1999). Matsuoka and Nakai (1974) proposed a smoother version of the Mohr–Coulomb criterion, the Matsuoka–Nakai (MN) failure criterion. It has gained a lot of popularity, as it improved numerical stability as well as physical accuracy. All developments were merged into modern constitutive models for quasi-static granular materials, such as the hardening-soil-model (Schanz *et al.*, 1999), Severn-Trent-sand (Gajo and Wood, 1999), SaniSand (Taiebat and Dafalias, 2008), Hypoplasticity (Kolymbas, 1991; Von Wolffersdorff, 1996) or Barodesy (Kolymbas, 2012; Fellin and Ostermann, 2013; Medicus and Fellin, 2017).

All of the above models assume quasi-static conditions and describe the stresses at failure. The respective extension to dynamic cases has been of interest for a long time. Schaeffer (1987) was the first to combine the two-dimensional Navier–Stokes Equations, with the quasi-static Mohr–Coulomb failure criterion. His work assumed that the Mohr–Coulomb failure stress is valid beyond failure and at any strain rate, an assumption which is consistent with ideal plasticity (Lubliner, 1990), where failure criterion and yield criterion are coinciding. In this sense we will use henceforth the term yield criterion when computing the stress in a flowing material. Schaeffer's theory matches Mohr–Coulomb only for plane strain (i.e. two dimensional deformations) and incompressible flows, i.e. isochoric shear. Although he found some problematic instabilities, his work was highly influential in the granular flow community and his approach was applied for both, plane strain and fully three-dimensional granular flows, first and foremost in chemical engineering (van Wachem, 2000; Passalacqua and Fox, 2011).

Early models assumed that the magnitude of the stress tensor remains constant after failure and independent of the shear rate. This assumption fails to describe various phenomena from physical experiments, e.g. steady flows on inclined planes or roll waves (GDR MiDi, 2004; Pouliquen *et al.*, 2006; Johnson and Gray, 2011; Edwards *et al.*, 2017) and a large amount of research has been attributed to describe the respective correlations. Most notable are the early works of Bagnold (1954, 1966) and Voellmy (1955), both combining Coulomb's friction law and an additional dynamic term. More recent developments have been achieved with kinetic theory (Campbell, 1990; Goldhirsch, 2003) and with the so-called $\mu(I)$–rheology, relating the dimensionless friction coefficient $\mu = \sin(\phi)$ to the dimensionless inertial number I (Pouliquen *et al.*, 2006).

The first generally applicable $\mu(I)$–rheology was introduced by Jop *et al.* (2006), basically following the approach of Schaeffer (1987) but with a shear rate dependent yield criterion. The instabilities found by Schaeffer (1987) are partially present in the model of Jop *et al.* (2006) and addressed, among others, by Barker *et al.* (2015) and Barker and Gray (2017).

Although the success of respective models is impressive, we have to contemplate that Schaeffer's approach is limited to plane, incompressible deformation, i.e. isochoric shear. If his relation is used for arbitrary three-dimensional deformations, one gets what is commonly known as the Drucker–Prager (DP) yield criterion in solid mechanics (Drucker and Prager, 1952). The differences between Mohr–Coulomb and Drucker–Prager are well known (Chen and Liu, 1990) and may be rather large, depending on the induced deformation (Maiolino and Luong, 2009; Wojciechowski, 2018). This yields, for example, remarkable errors in earth pressure calculations (Schweiger, 1994). Furthermore, it has been revealed that the Mohr–Coulomb yield criterion is fulfilled in discrete element simulations to a much better degree than the Drucker–Prager yield criterion (Pähtz *et al.*, 2019).

These circumstances lead to a big gap between Mohr–Coulomb models, and the recent success of the $\mu(I)$–rheology. This gap is what we aim to close with this work. We will extend the approach of Schaeffer (1987) and Jop *et al.* (2006) to different yield criteria. This allows us to implement constitutive models based on Mohr–Coulomb and Matsuoka–Nakai alongside the classic relation of Schaeffer (1987) (i.e. Drucker–Prager) into the CFD-toolkit OpenFOAM® (OpenCFD Ltd., 2004). We are comparing the three relations by inducing three-dimensional deformations in granular flow simulations. We neglect the shear rate dependence of stresses in this work to focus solely on the effect of the yield criterion. However, the $\mu(I)$-scaling is perfectly compatible with all of the presented yield criteria and can be easily reintroduced. To keep computational demand to an acceptable level, we run axisymmetric cases, some of which have been validated with physical experiments (Lube *et al.*, 2004). We are able to draw some conclusions and determine the circumstances for which the widely used Drucker–Prager relation differs from the traditional Mohr–Coulomb relation.

I.2 Method

The incompressible Navier–Stokes Equations are given as

$$\boldsymbol{\nabla}\cdot\mathbf{u} = 0, \tag{I.2}$$

$$\frac{\partial(\rho\,\mathbf{u})}{\partial t} + \boldsymbol{\nabla}\cdot(\rho\,\mathbf{u}\otimes\mathbf{u}) = \boldsymbol{\nabla}\cdot\mathbf{T} + \rho\,\mathbf{g} = \boldsymbol{\nabla}\cdot(2\,\eta\,\mathbf{D}) - \boldsymbol{\nabla}\,p + \rho\,\mathbf{g}, \tag{I.3}$$

with velocity $\mathbf{u}$, density ρ, stress tensor $\mathbf{T} = \mathbf{T}^{\text{dev}} - p\,\mathbf{I}$, strain rate tensor[1] $\mathbf{D}$, pressure $p = -1/3\,\text{tr}\,(\mathbf{T})$ and gravitational acceleration $\mathbf{g}$. In the following, we will assume that pore-pressure is negligibly small and hence that the pressure p is equal to the effective pressure p'.

In order to combine granular rheologies with the Navier–Stokes Equations, it is required to calculate the deviatoric stress tensor $\mathbf{T}^{\text{dev}}$ in terms of the known strain rate tensor,

$$\mathbf{D} = \text{sym}\,(\boldsymbol{\nabla}\,\mathbf{u}) = \frac{1}{2}\left(\boldsymbol{\nabla}\,\mathbf{u} + (\boldsymbol{\nabla}\,\mathbf{u})^T\right), \tag{I.4}$$

and the dynamic viscosity[2] η, or equivalently the kinematic viscosity $\nu = \eta/\rho$ (note the first term on the right-hand side of Eq. (I.3)). Therefore, without substantial modification of the underlying equations, all constitutive modelling is reduced to the scalar viscosity. This introduces some severe limitations, namely alignment between stress and strain rate tensor, which we will illuminate below. The hydrostatic part of the stress tensor, $-p\,\mathbf{I}$ can not be established with a constitutive relation in incompressible flow models (as $\text{tr}(\mathbf{D}) = 0$) and is therefore calculated from the constraint of the continuity equation (I.2) with e.g. the PISO algorithm (Issa, 1986).

I.2.1 A Tensorial Description of Deformation and Stress

The set of all stress tensors, at which yielding occurs forms a surface in stress space, which we define as the yield surface (see Fig. I.4). Admissible stress tensors of static material are located within the yield surface and stress tensors do not exist outside the yield surface (Lubliner, 1990). Vice-versa, a yield surface, in addition with the so called flow rule, is sufficient to describe a perfectly plastic material. As we will show later, the flow rule is required to determine the location on the yield surface and thus the stress tensor.

Many yield surfaces are defined in terms of stress invariants and we will shortly introduce the most important notations and relations. The first invariant is the trace of a tensor,

$$I_1(\mathbf{A}) = \text{tr}(\mathbf{A}) = A_{11} + A_{22} + A_{33}, \tag{I.5}$$

and the trace of the stress tensor is proportional to the pressure

$$I_1(\mathbf{T}) = -3\,p. \tag{I.6}$$

The second invariant is defined as

$$I_2(\mathbf{A}) = \frac{1}{2}\left(\text{tr}(\mathbf{A})^2 - \text{tr}\left(\mathbf{A}^2\right)\right), \tag{I.7}$$

---

[1] Note that the strain rate tensor is called streching tensor in soil mechanics.

[2] The most common symbol for the dynamic viscosity is μ. However, this symbol is reserved for the friction coefficient in granular flows and we will use η instead.

and related to the norm of a tensor, which is defined here as[3]

$$\|\mathbf{A}\| = \sqrt{\frac{1}{2}\operatorname{tr}(\mathbf{A}^2)}. \tag{I.8}$$

For the incompressible strain rate tensor we can thus write

$$I_2(\mathbf{D}) = -\|\mathbf{D}\|^2, \tag{I.9}$$

and the same is the case for the deviatoric stress tensor

$$I_2(\mathbf{T}^{\mathrm{dev}}) = -\|\mathbf{T}^{\mathrm{dev}}\|^2. \tag{I.10}$$

Finally, the third invariant is defined as

$$I_3(\mathbf{A}) = \det(\mathbf{A}), \tag{I.11}$$

and is, in combination with the second invariant, related to the type of deformation. The type of deformation can be described in terms of the Lode-angle (Chen and Han, 2007), defined as

$$\theta = \frac{1}{3}\arcsin\left(\frac{I_3(\mathbf{D})}{2}\left(\frac{3}{-I_2(\mathbf{D})}\right)^{3/2}\right). \tag{I.12}$$

A physical interpretation of the Lode-angle is shown in Fig. I.1. Deformation types can be reduced to three cases for incompressible flows: True triaxial compression is defined by one negative and two positive principal strain rates and characterized by a negative Lode-angle. Isochoric shear is the combination of plane strain (one principal strain rate is zero) and incompressibility, the Lode-angle in this case is zero. Finally, a positive Lode-angle indicates true triaxial extension, which is defined by two negative and one positive principal strain rates. Moreover, the two limiting cases shown in Fig. I.3 are called triaxial compression and extension. Note that in reality, deformation types are much more complicated due to e.g. volumetric deformations.

The Lode-angle as defined by Eq. (I.12) is limited to the interval $[-30°, 30°]$, respectively. For an interpretation in principal stress space as deviatoric polar angle (Fig. I.3), the Lode-angle is located in one of six equal sectors, depending on the order of the principal stresses (Haigh–Westergaard coordinates, Chen and Han, 2007). For isotropic constitutive models this plays no role and Eq. (I.12) can be used throughout all derivations.

The three invariants are sufficient to describe a tensor, except for its orientation in space (i.e. solid body deformation). However, a rigid body deformation is not relevant for isotropic constitutive models. This makes invariants very convenient for defining yield criteria and constitutive models.

---

[3] Note that often the Frobenius norm is used instead, defined as $|\mathbf{A}| = \sqrt{\operatorname{tr}(\mathbf{A}^2)}$ for symmetric tensors.

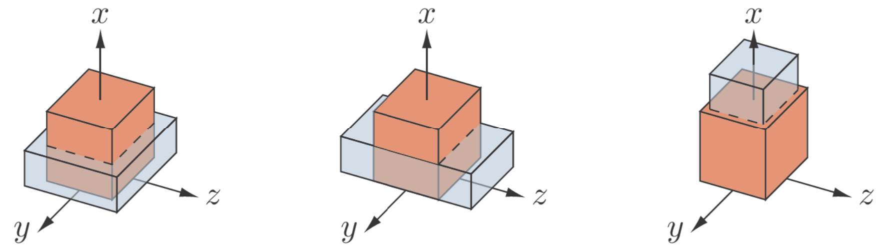

$\theta = -30°$
$D_1 < 0, D_2 = D_3 > 0$
triax. compression

$\theta = 0$
$D_2 = 0$
isochoric shear

$\theta = 30°$
$D_1 > 0, D_2 = D_3 < 0$
triax. extensions

Figure I.1: Deformation types and the respective Lode-angle. The red solid shows the undeformed state, the blue solid shows the deformed state. Three deformation types are compatible with incompressible flows: Triaxial compression, isochoric shear and triaxial extension. True triaxial compression is a mix of triaxial compression and isochoric shearing, true triaxial extension a mix of triaxial extension and isochoric shearing with the respective range of Lode-angles.

I.2.2 Stress Tensor Reconstruction

It is common to assume that the deviatoric stress and strain rate tensors are co-axial, meaning that their eigenvectors are parallel (Schaeffer, 1987; Schranz and Fellin, 2016; Barker *et al.*, 2017),

$$\mathbf{T}_i^{\text{dev}} = \lambda_i \mathbf{D}_i, \tag{I.13}$$

where $\mathbf{T}_i^{\text{dev}}$ and $\mathbf{D}_i$ are the eigenvectors of the respective tensor. This holds at least in steady, critical state (Schofield and Wroth, 1968) and allows for visualisation of the principal stress and strain rate tensors in the same principal-value-space, which is for example utilized in Fig. I.2. However, this assumption is not sufficient to determine the complete stress tensor.

A stricter assumption, which is sufficient to determine the complete stress tensor is alignment between deviatoric stress and strain rate tensor (Jop *et al.*, 2006; Barker *et al.*, 2017). Alignment of tensors implies co-axiality and an equal ratio between eigenvalues. This can be expressed in terms of principal stresses and strain rates as

$$\frac{|\mathbf{T}_1^{\text{dev}}|}{|\mathbf{D}_1|} = \frac{|\mathbf{T}_2^{\text{dev}}|}{|\mathbf{D}_2|} = \frac{|\mathbf{T}_3^{\text{dev}}|}{|\mathbf{D}_3|}, \tag{I.14}$$

or more generally as

$$\frac{T_{ij}^{\text{dev}}}{D_{ij}} = \text{locally constant}. \tag{I.15}$$

This assumption is commonly applied in granular flows, among others by the $\mu(I)$–rheology (Jop *et al.*, 2006). It allows for expression of the deviatoric stress tensor as the product of a scalar and the strain rate tensor and to establish a relation compatible with the Navier–Stokes Equations,

$$\mathbf{T}^{\mathrm{dev}} = 2\,\eta\,\mathbf{D}. \tag{I.16}$$

Note that the viscosity η is not constant and depends on the pressure and the strain rate (we will additionally introduce a dependence on the Lode-angle). Alignment is fundamental for many granular flow theories and its validity is indicated by good experimental agreement (GDR MiDi, 2004; Jop *et al.*, 2006).

The validity of alignment can also be checked with models that include non-alignment between stress and strain tensor. We will use the constitutive soil model Barodesy (Kolymbas, 2012; Medicus and Fellin, 2017) in here, as it has shown to provide a realistic relation between the directions of stresses and strain rates at critical state (Medicus *et al.*, 2016). Note that the intrinsic non-alignment of Barodesy makes it impossible to express it with a scalar viscosity, making it incompatible with the Navier–Stokes Equations. The stress in critical state follows from Barodesy as

$$\mathbf{T} = \frac{3p}{\mathrm{tr}\,(\mathbf{R})}\mathbf{R} \tag{I.17}$$

with

$$\mathbf{R} = -\exp\left(\frac{\alpha}{\sqrt{2}}\frac{\mathbf{D}}{\|\mathbf{D}\|}\right). \tag{I.18}$$

The only constitutive parameter α is usually expressed by the friction angle ϕ but in here used to match Barodesy to the Matsuoka–Nakai criterion,

$$\alpha = \sqrt{\frac{2}{3}}\log\left(\frac{k_{\mathrm{MN}} - 1 - \sqrt{(k_{\mathrm{MN}}-1)\,(k_{\mathrm{MN}}-9)}}{k_{\mathrm{MN}} - 1 + \sqrt{(k_{\mathrm{MN}}-1)\,(k_{\mathrm{MN}}-9)}}\right), \tag{I.19}$$

where k_{MN} is the constitutive parameter of the Matsuoka–Nakai criterion, see Eq. (I.34). Note that the factor $\sqrt{2}$ in Eq. (I.18) is related to the definition of the norm following Eq. (I.8).

Furthermore, plasticity theory allows us to classify the popular approach of alignment in a broader context. The associated flow rule,

$$\mathbf{D} = \lambda\,\frac{\partial f(\mathbf{T})}{\partial \mathbf{T}}, \tag{I.20}$$

states that the plastic strain rate tensor (in here simply $\mathbf{D}$, as we assume ideal plasticity) is oriented normal on the yield surface $f(\mathbf{T})$. This relation follows the principle of maximal plastic dissipation (Lubliner, 1990) but the yield surface $f(\mathbf{T})$ can be replaced with arbitrary plastic potentials $\tilde{f}(\mathbf{T})$ in the flow rule (Eq. (I.20)). In such a case one speaks of a non-associative flow rule. This procedure is applied often, as this matches soil behaviour better (Lade and Musante, 1978; Lade *et al.*, 1987; Desrues *et al.*, 2000).

Inserting the definition for alignment (Eq. (I.16)) into the flow rule (Eq. (I.20)) yields

$$\frac{\mathbf{T}^{\mathrm{dev}}}{2\,\eta} = \lambda \frac{\partial \tilde{f}(\mathbf{T})}{\partial \mathbf{T}}, \tag{I.21}$$

which necessarily leads to a von Mises type surface for the plastic potential,

$$\tilde{f}(\mathbf{T}) = \|\mathbf{T}^{\mathrm{dev}}\|^2 - k_{\mathrm{vM}} = 0, \tag{I.22}$$

with constant k_{vM}. Conveniently, this flow rule is consistent with the continuity equation (I.2). Note, that associated flow rules for Drucker–Prager, Mohr–Coulomb and Matsuoka–Nakai predict volumetric strain, which is contradicting with Eq. (I.2) and experimental observations in critical state. This gives three methods to determine the direction of the stress tensor with respect to the strain rate tensor: Associated flow rule given by Eq. (I.20) and von Mises plastic potential (i.e. alignment), as well as sophisticated soil models, in here Barodesy. All three approaches are presented and compared in Fig. I.2 for the Matsuoka–Nakai yield surface, as this matches Barodesy best (Fellin and Ostermann, 2013). Results overlap in the deviatoric plane for triaxial extension and compression but differ substantially for shear. The ad-hoc assumption of alignment results in strain rate directions close to the associative flow rule and Barodesy, two physically reasonable models. In particular, the alignment assumption fits Barodesy and thus experimental behaviour, better than the associated flow rule.

In the following we will apply a von Mises plastic potential, as this allows simple implementation of various yield surfaces into the Navier–Stokes equations. Moreover, this approach guarantees a well defined stress tensor for all relevant yield surfaces and is compatible with incompressible flows.

I.2.3 Yield Criteria

One of the simplest yield criteria, the von Mises yield surface, has been introduced in Eq. (I.22). It represents basic plastic behaviour and is as such the basis for visco-plastic rheologies like Bingham or Herschel-Bulkley (Gauer *et al.*, 2006). However, it only takes into account the second stress-invariant and is thus not able to cover basic granular behaviour, i.e. pressure-dependent shear strength.

The Drucker–Prager yield criterion is the simplest criterion that takes the frictional character of granular materials into account (Drucker and Prager, 1952). As such, it connects the pressure with the deviatoric part of the stress tensor,

$$f(\mathbf{T}) = \sin(\phi)\, p - \|\mathbf{T}^{\mathrm{dev}}\| = 0, \tag{I.23}$$

with the friction angle ϕ. Note that this is a special parametrisation for a cohesionless material in terms of the friction angle ϕ, such that Drucker–Prager and Mohr–Coulomb match for a Lode-angle $\theta = 0$, i.e. isochoric plane strain

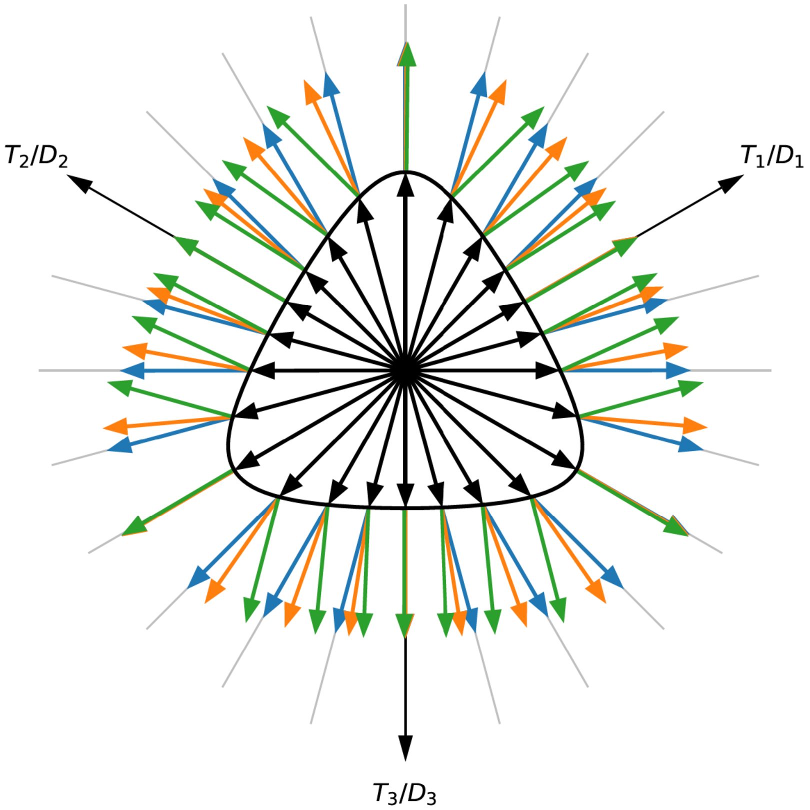

Figure I.2: Matsuoka–Nakai yield surface and the respective principal stresses (black) in the deviatoric plane of principal stress/strain space. The strain rates, which can create these stress states are shown as arrows, attached to the respective stress states: Associated flow rule (green), Barodesy (orange) and von Mises plastic potential (i.e. alignment, blue).

(Schaeffer, 1987). This yield surface allows us, in combination with the von Mises flow rule or equivalently Eq. (I.16), to define the viscosity as

$$\eta = \frac{\sin(\phi)\ p}{2\,\|\mathbf{D}\|}. \tag{I.24}$$

It is also possible to model the friction coefficient $\mu = \sin(\phi)$ as a function of the inertial number I, which leads to the $\mu(I)$–rheology (Jop *et al.*, 2006),

$$\eta \quad = \frac{\mu(I)\,p}{2\,\|\mathbf{D}\|}. \tag{I.25}$$

This shows that the $\mu(I)$–rheology can be classified as a Drucker–Prager yield surface with a von Mises plastic potential, within the framework of plasticity theory.

The Mohr–Coulomb criterion additionally takes into account the deformation type by incorporating both the major and minor principal stresses,

$$f(\mathbf{T}) = \frac{T_1 - T_3}{T_1 + T_3} - \sin(\phi) = 0. \tag{I.26}$$

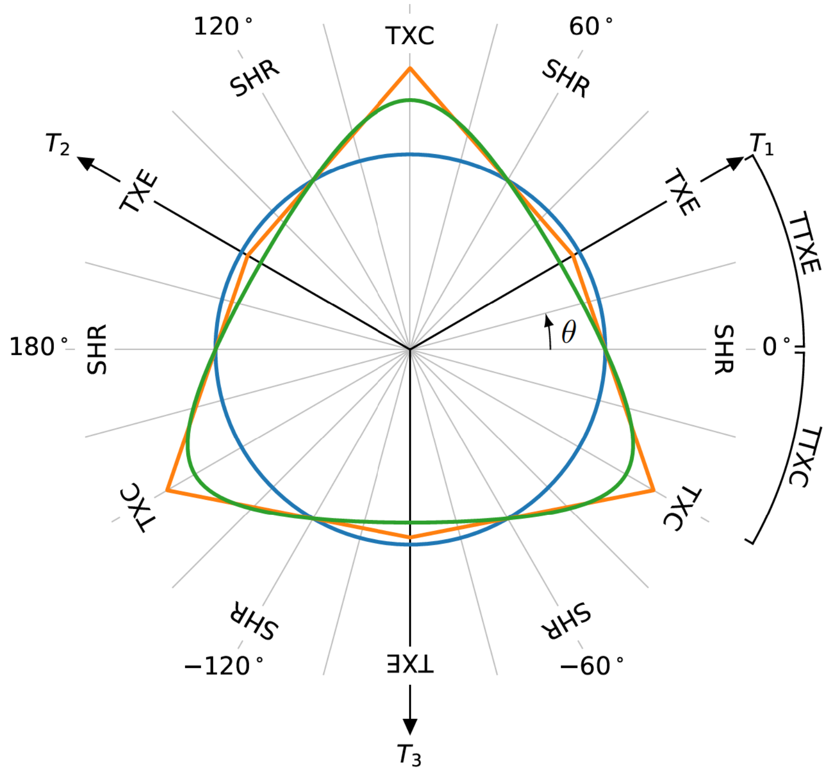

Figure I.3: The yield surfaces in the deviatoric plane: Drucker–Prager (blue), Mohr–Coulomb (orange) and Matsuoka–Nakai (green). The angle enclosed with the horizontal axis is called Lode-angle and its values indicate the type of deformation: triaxial extension (TXE), triaxial compression (TXC) and isochoric shear (SHR). True triaxial extension (TTXE) and true triaxial compression (TTXC) are mixes of respective limiting cases (TXE and TXC) and isochoric shear (SHR).

This relation can be expressed in terms of the Lode-angle and other invariants as (Chen and Han, 2007)

$$f(\mathbf{T}) = \left(\frac{\sin(\theta)}{\sqrt{3}} - \frac{\cos(\theta)}{\sin(\phi)}\right)\sqrt{-I_2(\mathbf{T}^{\mathrm{dev}})} + \frac{1}{3}\,I_1(\mathbf{T}) = 0 \tag{I.27}$$

and the viscosity follows as

$$\eta = \frac{\sin(\phi)\,p}{2\,\|\mathbf{D}\|}\,\frac{\sqrt{3}}{\sqrt{3}\,\cos(\theta) + \sin(\theta)\,\sin(\phi)}. \tag{I.28}$$

Note that for $\theta = 0$, i.e. isochoric shear, Eq. (I.28) reduces to Eq. (I.24).

The Matsuoka–Nakai criterion is similar to the Mohr–Coulomb criterion, however with a continuous, smooth yield surface. It is defined as

$$f(\mathbf{T}) = \frac{I_1(\mathbf{T})\,I_2(\mathbf{T})}{I_3(\mathbf{T})} - k_{\mathrm{MN}} = 0. \tag{I.29}$$

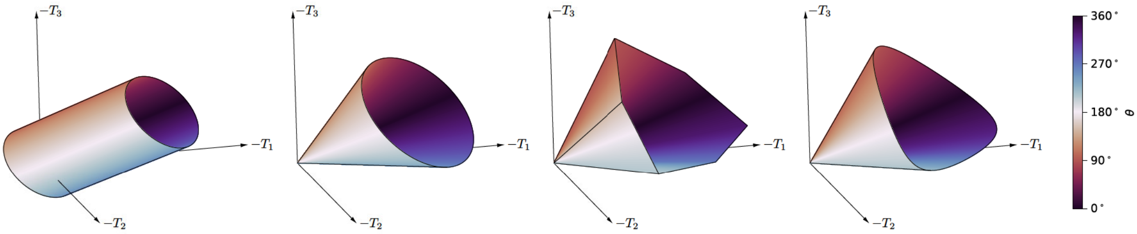

(a) (b) (c) (d)

Figure I.4: Yield surfaces in the three-dimensional principal stress space: von Mises (a), Drucker–Prager (b), Mohr–Coulomb (c) and Matsuoka–Nakai (d). The colour marks the Lode-angle θ.

Introducing Eq. (I.16) into Eq. (I.29) leads to a viscosity that represents this yield surface,

$$\eta = \begin{cases} p\,a\,\dfrac{\cos(\gamma) - \sqrt{3}\,\sin(\gamma) - 1}{6} & \text{for } -30^\circ \leq \theta < 0, \\ p\,a\,\dfrac{2\,\cos(\gamma) - 1}{6} & \text{for } 0 < \theta \leq 30^\circ, \\ \dfrac{p}{2\,\|\mathbf{D}\|}\sqrt{\dfrac{9 - k_{\mathrm{MN}}}{3 - k_{\mathrm{MN}}}} & \text{for } \theta = 0, \end{cases} \tag{I.30}$$

with

$$a = \frac{I_2(\mathbf{D})\,(3 - k_{\mathrm{MN}})}{I_3(\mathbf{D})\,k_{\mathrm{MN}}}, \tag{I.31}$$

$$b = \frac{9 - k_{\mathrm{MN}}}{I_3(\mathbf{D})\,k_{\mathrm{MN}}}, \tag{I.32}$$

$$\gamma = \frac{1}{3}\arctan\left(\frac{-3\sqrt{-3\,(4\,a^3\,b + 27\,b^2)}}{-2\,a^3 - 27\,b}\right). \tag{I.33}$$

The first case in Eq. (I.30) corresponds to true triaxial extension, the second case to true triaxial compression and the last case to isochoric shear, where $I_3(\mathbf{D}) = 0$. The constant k_{MN} is usually chosen such that Matsuoka–Nakai fits the Mohr–Coulomb criterion for triaxial extension and compression, i.e. for $\theta = \pm 30^\circ$. Alternatively, k_{MN} can be chosen such that it fits Mohr–Coulomb and Drucker–Prager for isochoric shear ($\theta = 0$),

$$k_{MN} = \frac{9 - 3\,\sin^2(\phi)}{1 - \sin^2(\phi)}. \tag{I.34}$$

This is more appropriate for granular flows, as we will show later. Note that all three relations contain only a single constitutive parameter, the friction angle ϕ.

I.2.4 Stationary Zones

As mentioned before, stresses lie only on the yield surface (in other words, the yield criterion is fulfilled $f(\mathbf{T}) = 0$), if the respective material is flowing. Otherwise (e.g. in stable zones of the slide, levees and deposition) the stress has to lie within the yield surface. However, this is not included in the presented relations and the viscosity will reach a singularity in stationary zones where $\|\mathbf{D}\| = 0$. To allow deviatoric stresses lower than the deviatoric stresses at yield, we can limit the viscosity to a predefined upper threshold. This way we can simulate quasi-stationary zones - zones with very high viscosity, that will deform very slowly. The viscosity threshold should be chosen high enough such that the deformation is negligible, but low enough to circumvent numerical problems. However, we want to emphasize that this approach is an extreme simplification of quasi-static granular material behaviour and results (e.g. stresses) in static zones are questionable. An elasto-plastic model is more appropriate than the simple visco-plastic model applied in here. The time step in numerical simulations is chosen following the stability criterion (CFL condition) as given by Moukalled *et al.* (2016). Note that the viscosity has to be taken into account in the calculation of the CFL number and that without a limitation of the viscosity, the time step would be very small. This method has been found to be sufficient for the here presented cases.

I.3 Element test

We want to consider three strain rate tensors, representing triaxial compression, extension and isochoric shear as shown in Fig. I.1 and Tab. I.1. The viscosities and stress tensors can be calculated explicitly in terms of the known relations Eqs. (I.24), (I.28) and (I.30). The only parameter is the friction angle ϕ, which was set to 36.5°. Tab. I.1 shows the respective stresses as absolute and relative values in relation to the Drucker–Prager yield surface. All models predict the same stresses for isochoric shear, since they have been calibrated for this case. In comparison to Drucker–Prager, Matsuoka–Nakai and Mohr–Coulomb predict higher deviatoric stresses for triaxial compression and lower deviatoric stresses for triaxial extension, which can be seen in Fig. I.3 as well. The biggest difference, of 44%, can be observed between Drucker–Prager and Mohr–Coulomb for triaxial compression. To yield the high stresses of the Mohr–Coulomb model with Drucker–Prager, a friction angle of 59° would be required, highlighting the considerable discrepancy between models.

I.4 Numerical experiments

For a practical application, the yielding criteria and the respective viscosity models have been implemented into the CFD-toolkit OpenFOAM. OpenFOAM provides a convenient interface for the implementation of custom viscosity models, which can then be used within various solvers (Weller *et al.*, 1998). We chose

Table I.1: Element test.

	Strain				Model	Stress				
	$D_x/\|\mathbf{D}\|$	$D_y/\|\mathbf{D}\|$	$D_z/\|\mathbf{D}\|$	θ		$\eta\,\|\mathbf{D}\|$	$\|\mathbf{T}^{\mathrm{dev}}\|/p$	relative	$\|\mathbf{T}\|/p$	relative
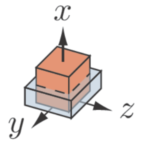	−1.155	0.577	0.577	−30°	DP	0.297	0.595	1	0.721	1
					MC	0.428	0.857	1.44	0.949	1.32
					MN	0.380	0.756	1.27	0.862	1.20
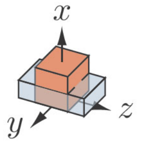	−1	0	1	0°	DP	0.297	0.595	1	0.721	1
					MC	0.297	0.595	1	0.721	1
					MN	0.297	0.595	1	0.721	1
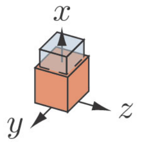	1.155	−0.577	−0.577	30°	DP	0.297	0.595	1	0.721	1
					MC	0.287	0.573	0.96	0.703	0.98
					MN	0.264	0.528	0.89	0.667	0.925

the solver *multiphaseInterFoam* which allows simulation of complex geometries by tracking multiple phases with phase indicator functions. The first phase is representing dry sand and applies the granular viscosity model and a density of $\rho_\mathrm{s} = 1430\,\mathrm{kg\,m^{-3}}$, whereas the second phase represents air. Because of its low viscosity ($\nu_\mathrm{a} = 1.48 \cdot 10^{-5}\,\mathrm{m^2\,s^{-1}}$) and density ($\rho_\mathrm{a} = 1\,\mathrm{kg\,m^{-3}}$), it has neglectable influence on the granular phase. Tracking of the motion of the interface is realized by transporting phase indicator functions α_s (sand) and α_a (air) with the velocity $\mathbf{u}$, which is shared among all phases,

$$\frac{\partial \alpha_i}{\partial t} + \mathbf{u} \cdot \boldsymbol{\nabla}\, \alpha_i = 0. \tag{I.35}$$

With known phase indicator values α_i (i beeing either s or a), the local density ρ and viscosity η can be calculated as the mean of individual phase values, i.e.

$$\rho = \sum_i \alpha_i\, \rho_i, \tag{I.36}$$

$$\eta = \sum_i \alpha_i\, \eta_i. \tag{I.37}$$

This results in a simple model for granular flows with complex geometries and large strain. We apply a friction angle of $\phi = 36.5°$ in all simulations, similar to Savage *et al.* (2014). The viscosity is truncated to the interval $\nu_\mathrm{s} = [10^{-5}, 10^{0}]\,\mathrm{m^2\,s^{-1}}$.

The simplest and most common benchmarks for granular flow models are two-dimensional column collapses, flows on inclined planes and flows down chutes. However, they all lead to isochoric plane strain conditions and are therefore inappropriate for our investigations. As shown with the simple element test, all models will yield the same results in two-dimensional simulations. This behaviour has been confirmed with back-calculations of the experiments by Balmforth and Kerswell (2005). Results are not shown here as they basically match previous results of e.g. Lagrée *et al.* (2011) and Savage *et al.* (2014). It follows that for a meaningful comparison of the proposed rheologies, we need to induce three-dimensional deformations. Axisymmetric simulations are an obvious choice for such a task, as they enforce three-dimensional deformations while keeping the computational expense comparable to a two-dimensional case.

I.4.1 Cylindrical granular collapse

The simplest axisymmetric experiment is the collapse of a granular cylinder (Fig. I.5), which is presented in the following. Physical experiments of such have been conducted by Lube *et al.* (2004). We choose to simulate two cases with different aspect ratios, $h_0/r_0 = 1/2$ and $h_0/r_0 = 2$. The simulations with an aspect ratio of 1/2 have been realized with a cylinder of height $h_0 = 0.1\,\mathrm{m}$ and radius $r_0 = 0.2\,\mathrm{m}$. By exploiting the radial symmetry of the problem, we could apply a two-dimensional wedge-shaped mesh (OpenCFD Ltd., 2004) with size $0.5\,\mathrm{m} \times 0.2\,\mathrm{m}$. The cell size was set to 1.67 mm and a mesh refinement study

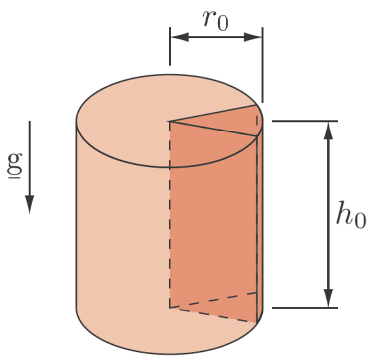

Figure I.5: Cylindrical granular collapse: Only a small wedge with one cell across the wedge thickness, as highlighted in the figure, is simulated. The geometry is described by the aspect ratio r_0/h_0.

(cell sizes 2.5 mm, 1.67 mm, 1.25 mm) indicated that this resolution is sufficient for all practical purposes, with relative errors of less than 1%. The simulation duration was set to 0.5 s, which was sufficient for the duration of the collapse of about 0.35 s. The strict stability criterion following Moukalled *et al.* (2016) and the high viscosity leads to very small time steps of approximately 10^{-6} s, which is more restrictive than the traditional CFL type criterion.

Vertical sections of the granular pile at three different times and for all rheologies are shown in Fig. I.6. In addition, the experimental result of Lube *et al.* (2004) for an aspect ratio of 0.54 is shown, scaled to match the final pile height h_∞ and the final radius r_∞. Figure I.7 highlights the Lode-angle θ and

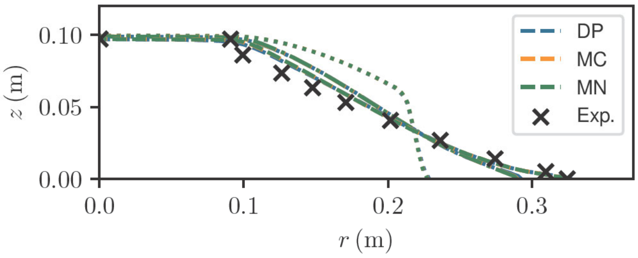

Figure I.6: Cylindrical granular collapse, aspect ratio 1/2, with various yield surfaces at $t = 0.1$ s (dotted line), $t = 0.2$ s (dot-dashed line) and $t = 0.5$ s (dashed line). The grid resolution is 1.67 mm. The colour marks the yield criteria and the black crosses mark the experimental final pile shape (Lube et al., 2004). Results are very similar, overlap almost entirely and differ by not more than 1%.

the strain rate $\|\mathbf{D}\|$, as resulting in the simulation with Matsuoka–Nakai yield surface at $t = 0.2$ s. These fields are widely similar in all three simulations and thus not shown repetitively. The differences in stresses between Mohr–Coulomb, Matsuoka–Nakai and Drucker–Prager are highlighted in Fig. I.8. Stresses differ

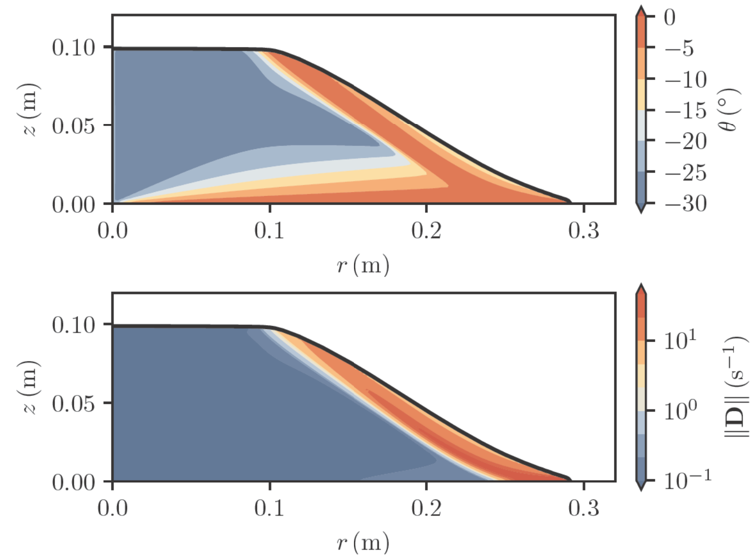

Figure I.7: Cylindrical granular collapse with the Matsuoka–Nakai yield criterion at $t = 0.2\,\mathrm{s}$. The grid resolution is 1.67 mm. The black line marks the free surface of the granular pile, the colour displays the Lode-angle θ (top) and the strain rate $\|\mathbf{D}\|$ (bottom).

up to 40% and 25% for Mohr–Coulomb and Matsuoka–Nakai, respectively, which corresponds approximately to the element test.

Aspect ratio 2 has been realized with a cylinder of height $h_0 = 0.2\,\mathrm{m}$ and radius $r_0 = 0.1\,\mathrm{m}$. The same meshing strategy as before has been applied, however, with a computational domain of size $0.4\,\mathrm{m} \times 0.3\,\mathrm{m}$. Vertical sections of the granular pile are shown in Fig. I.9, for three different times and all rheologies, together with the experiment of Lube *et al.* (2004) for an aspect ratio of 1.81. The Lode-angle θ and the strain rate $\|\mathbf{D}\|$ from the simulation with Matsuoka–Nakai are shown in Fig. I.10 for $t = 0.1\,\mathrm{s}$. The differences in stresses are highlighted in Fig. I.11. Their maximum is similar as in the previous case.

I.4.2 Ring granular collapse

Cylinder collapses show solely negative Lode-angles $\theta = [-30^\circ, 0]$. The full range of the Lode-angle can be shown by the collapse of a ring, as shown in Fig. I.12. Similarly to a cylinder, a ring allows to take advantage of the axisymmetry and only a vertical section has to be simulated. We choose an aspect ratio of $h_0/r_0 = 1$ and an inner radius $r_i = 2.5\,h_0$. Taller rings or rings with smaller inner radii collide at the centre, larger inner radii or smaller rings lead to lower Lode-angles and less visible effect. Indeed, for $r_i \to \infty$ one approaches the two-dimensional granular collapse. Vertical sections of the ring at three time steps are shown in Fig. I.13. Figure I.14 highlights the Lode-angle θ and the strain rate $\|\mathbf{D}\|$. The difference in stresses are highlighted in Fig. I.15.

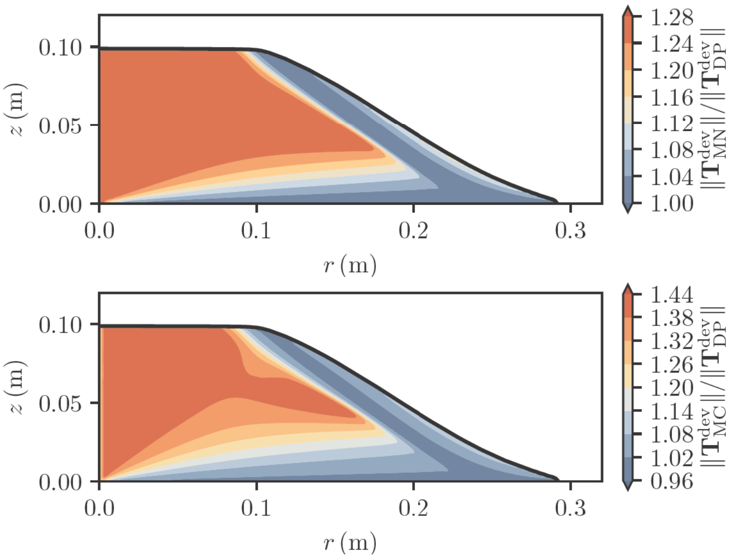

Figure I.8: Cylindrical granular collapse with the Matsuoka–Nakai (top) and Mohr–Coulomb (bottom) yield criterion. The colour displays the ratio between the respective criterion and Drucker–Prager.

I.5 Discussion and conclusions

All conducted simulations show stable and smooth results. Mesh depended instabilities, as predicted by Schaeffer (1987) and observed by others (Martin *et al.*, 2017; Gesenhues *et al.*, 2019) do not show in any of our simulations. We conclude that the applied meshes are too coarse to resolve the small scale features that form the growing instabilities. We expect to see these instabilities in further grid refinements and in such a case the constant friction coefficient $\mu = \sin(\phi)$ in Eqs. (I.24), (I.28), and (I.30) should be replaced with the regularised relation of Barker and Gray (2017). The modification of the yield criteria has no influence on the ill-posedness in two dimensions and isochoric plane strain conditions. Thus, all relations will be at least partially ill-posed in three dimensional cases and the presented yield surfaces will be no replacement for the regularisation of e.g. Barker and Gray (2017).

We choose to keep the constant friction coefficient in favour of simple equations and parameters.

The presented cases share some characteristics, which allows some conclusions on the general behaviour of investigated rheologies. Granular piles are collapsing while most of the deformation is located in a shear-band that encloses an angle of 35°-40° with the horizontal plane, roughly matching the friction angle of the material. This corresponds to the failure mechanism as reported by Lube *et al.* (2004). In fact, experiments of Lube *et al.* (2004) correspond reasonably well to the numerical simulations, as shown in Figs. I.6 and I.9. Material below the shear band is mostly static, leading to a maximum pile inclination similar to the friction angle, roughly matching theoretical predictions (Schranz and

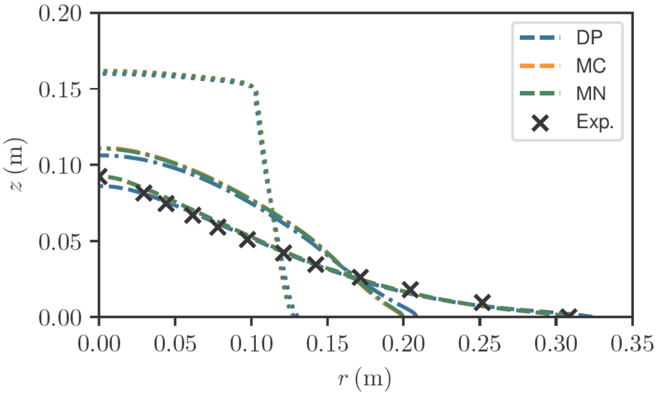

Figure I.9: Cylindrical granular collapse, aspect ratio 2, with various yield surfaces at $t = 0.1\,\mathrm{s}$ (dotted line), $t = 0.2\,\mathrm{s}$ (dot-dashed line) and $t = 0.5\,\mathrm{s}$ (dashed line). The colour marks the yield criteria and the black crosses mark the experimental final pile shape (Lube et al., 2004). The grid resolution is 1.67 mm. The largest difference in geometry is about 5%. Matsuoka-Nakai and Mohr-Coulomb overlap almost entirely while Drucker-Prager is visibly different.

Fellin, 2016). However, most regions are flatter due to the inertia of fast moving material.

Stresses in compressive zones differ substantially between the Mohr–Coulomb criterion and the Drucker–Prager criterion (up to 44%). Differences between the Matsuoka–Nakai and the Drucker–Prager criterion are smaller (up to 28%) but still relevant. However, the runout and the final shapes of the granular piles are little affected by the high variation of stresses. The highest variation in the pile shape is visible in the simulation of the high column with a difference of 5%. In other cases, the difference stays well below 1%.

At first glance, it seems unreasonable that a considerable increase of internal stresses does not affect the kinematics significantly. However, a closer investigation reveals that shear-bands overlap with regions where the Lode-angle is close to 0°. This is at least the case for the low collapses (see Figs. I.16a and I.16b). A Lode-angle close to zero means that stresses have to be similar, as yield surfaces intersect at this point (see Fig. I.3). Regions of large strain rates and a non-zero Lode-angle are basically limited to the tall cylinder (see Fig. I.16c), which also shows the highest differences in the kinematics. It is reasonable to assume that these shear bands control the kinematics and runout of the collapse. The dominance of these zones on the kinematic behaviour can be further investigated by plotting a histogram of the dissipated energy in terms of the Lode-angle, Fig. I.17. All cases show a pronounced peak of dissipated energy at a Lode-angle of 0°. In fact, in the two low cases, almost all the energy is dissipated in the interval $[-5°, 5°]$, leading to the similarities in kinematics. The granular cylinder with high aspect ratio differs from this behaviour, as a considerable amount of energy is dissipated during true triaxial compression.

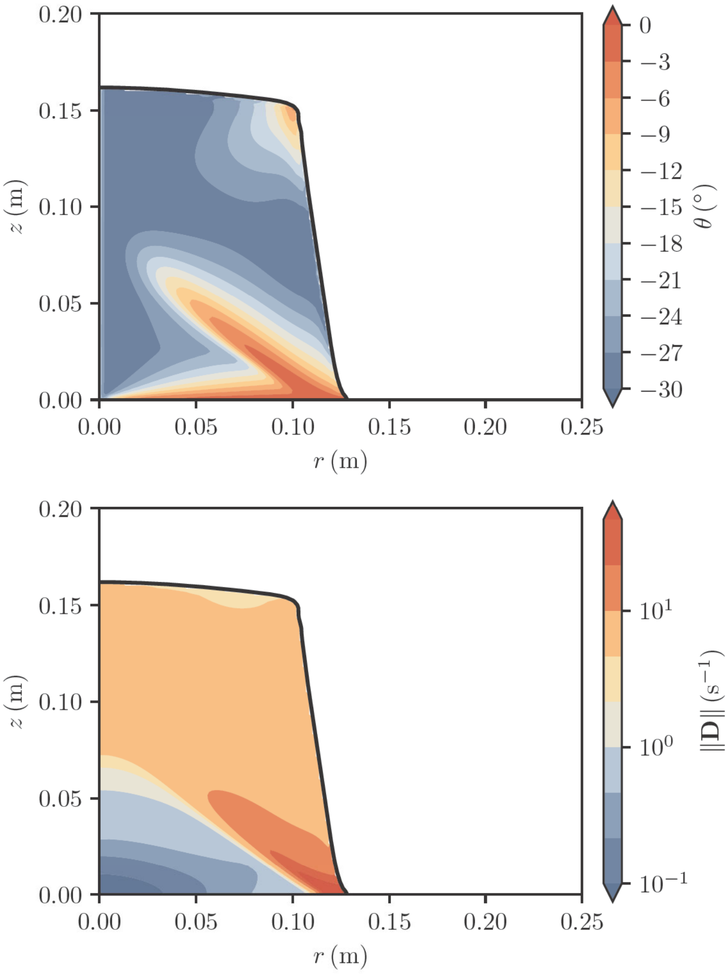

Figure I.10: Cylindrical granular collapse with the Matsuoka–Nakai yield criterion at $t = 0.1\,\mathrm{s}$. The grid resolution is 1.67 mm. The black line marks the free surface of the granular pile, the colour displays the Lode-angle θ (top) and the strain rate $\|\mathbf{D}\|$ (bottom).

This explains the bigger difference in slide kinematics between models in this case.

Finally we can estimate the effect of complex yielding criteria in real case landslides and avalanches. This can be done by introducing the non-dimensional variables, that are usually applied for landslide and avalanche models (Savage and Hutter, 1989; Pudasaini and Hutter, 2007; Johnson and Gray, 2011), see Fig. I.18. These scaling laws are based on the assumption that the typical height of the slide H is much smaller than the typical length L,

$$\frac{H}{L} = \varepsilon \ll 1. \tag{I.38}$$

The non-dimensional coordinates and velocities (marked with a hat) follow as

$$(x, y, z) = L\,(\hat{x}, \hat{y}, \varepsilon\hat{z})\,, \tag{I.39}$$

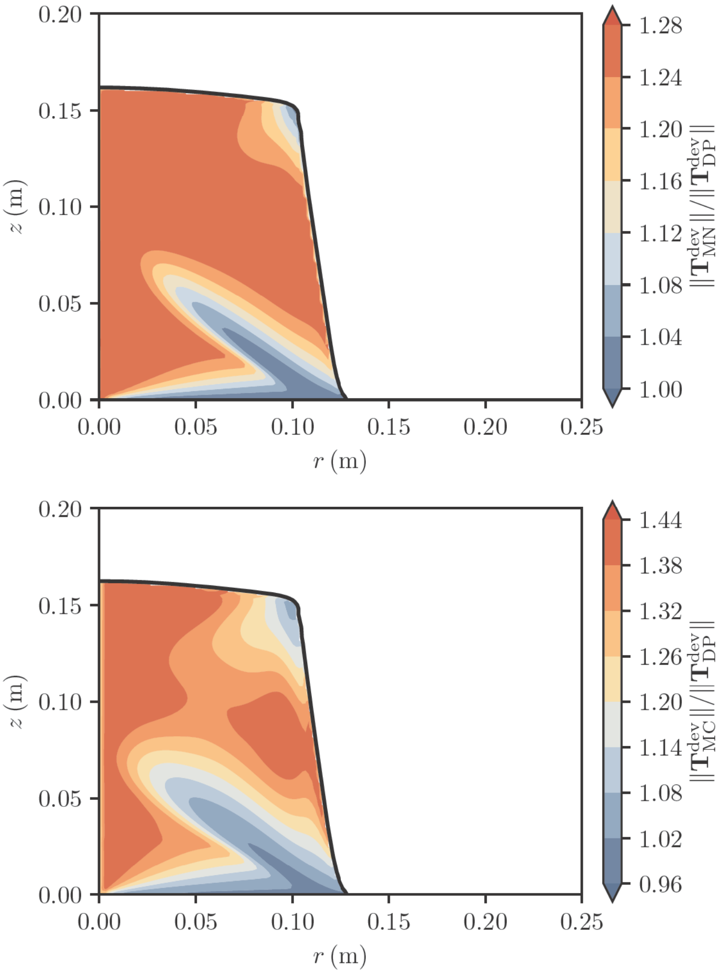

Figure I.11: Cylindrical granular collapse with the Matsuoka–Nakai (top) and Mohr–Coulomb (bottom) yield criterion. The colour displays the ratio between the respective criterion and Drucker–Prager.

$$(u, v, w) = (g\,L)^{1/2}\,(\hat{u}, \hat{v}, \varepsilon\hat{w})\,, \tag{I.40}$$

where x, y are the slope-parallel coordinates (u, v the respective velocities) and z the slope-normal coordinate (w the respective velocity). Assuming continuous shearing along the whole flow depth (i.e. Bagnold-profile), the non-dimensional strain-rate tensor follows as

$$\begin{bmatrix} D_{xx} & D_{xy} & D_{xz} \\ & D_{yy} & D_{yz} \\ & & D_{zz} \end{bmatrix} = \left(\frac{g}{L}\right)^{1/2} \begin{bmatrix} \hat{D}_{xx} & \hat{D}_{xy} & \frac{1}{\varepsilon}\hat{D}_{xz} \\ & \hat{D}_{yy} & \frac{1}{\varepsilon}\hat{D}_{yz} \\ & & \hat{D}_{zz} \end{bmatrix} \tag{I.41}$$

and furthermore the second and third invariants as

$$I_2(\mathbf{D}) = \frac{1}{\varepsilon^2}\left(\frac{g}{L}\right) I_2(\hat{\mathbf{D}}), \tag{I.42}$$

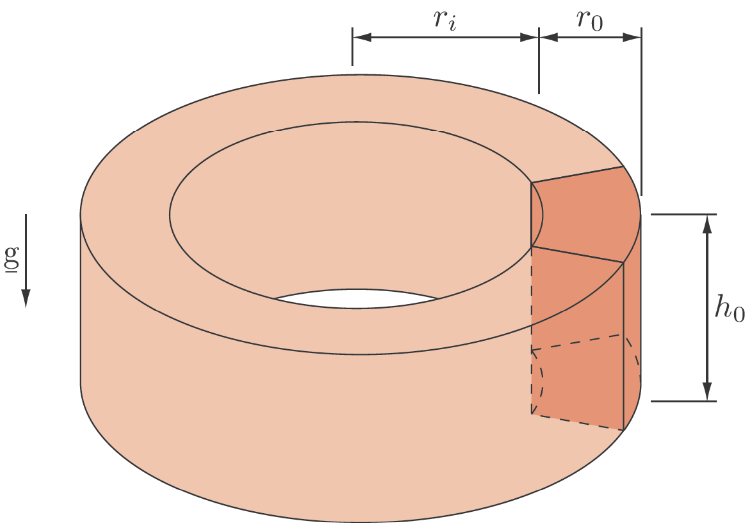

Figure I.12: Ring granular collapse: Only a small wedge with one cell across the wedge thickness is simulated. The geometry is defined by the height h_0, radius r_0 and inner radius r_i.

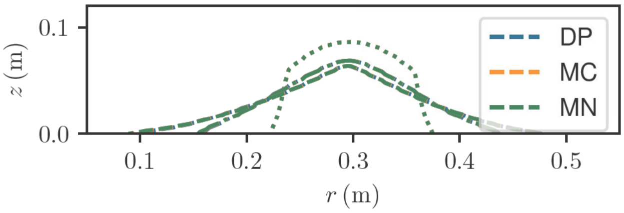

Figure I.13: Ring granular collapse with various yield surfaces (marked by colour) at $t = 0.1\,\mathrm{s}$ (dotted line), $t = 0.2\,\mathrm{s}$ (dot-dashed line) and $t = 0.5\,\mathrm{s}$ (dashed line). The grid resolution is 1.67 mm. Results are very similar, overlap almost entirely and differ by not more than 1%.

$$I_3(\mathbf{D}) = \frac{1}{\varepsilon^2}\left(\frac{g}{L}\right)^{3/2} I_3(\hat{\mathbf{D}}). \tag{I.43}$$

Introducing the dimensionless variables into the Lode-angle yields

$$\theta = \frac{1}{3}\arcsin\left(\varepsilon\,\frac{3^{3/2}}{2}\,I_3(\hat{\mathbf{D}})\left(-I_2(\hat{\mathbf{D}})\right)^{-3/2}\right), \tag{I.44}$$

showing that θ is small since it contains ε and otherwise only dimensionless variables. For small angles θ we can make the approximation $\sin(\theta) \approx \theta$ and get

$$\theta \approx \varepsilon\,\frac{3^{3/2}}{2}\,I_3(\hat{\mathbf{D}})\left(-I_2(\hat{\mathbf{D}})\right)^{-3/2} \ll 1\,\mathrm{rad}. \tag{I.45}$$

This means that in shallow granular flows the Lode-angle is close to zero. The cylinder with an aspect ratio of 1/2 and the ring are avalanching in a relatively

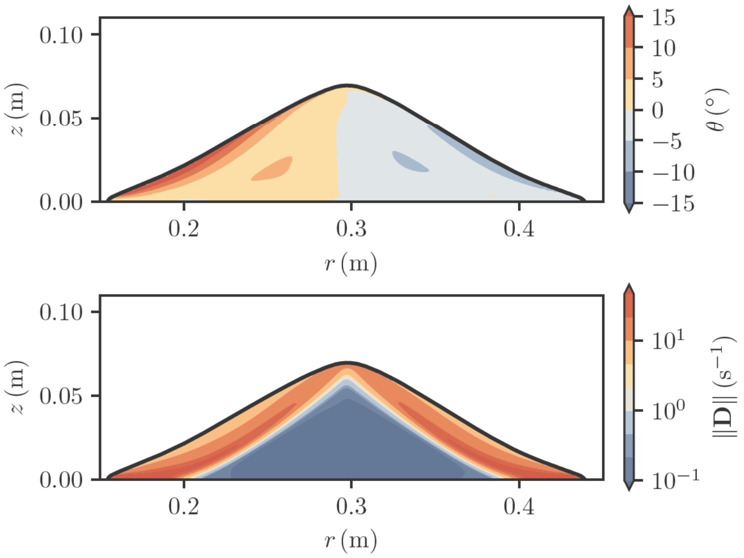

Figure I.14: Ring granular collapse with the Matsuoka–Nakai yield criterion at $t = 0.2$ s. The grid resolution is 1.67 mm. The black line marks the free surface of the granular pile, the colour displays the Lode-angle θ (top) and the strain rate $\|\mathbf{D}\|$ (bottom).

thin layer on top (see Figs. I.7 and I.14) and the shallowness assumption holds. The high cylinder on the other hand collapses completely and the shallowness assumption cannot be applied. Therefore one has to expect a Lode-angle far from zero and thus differences between yield criteria.

I.6 Summary and outlook

Using the approach of Schaeffer (1987), almost arbitrary yield surfaces can be expressed as non-Newtonian viscosities and thus implemented into the incompressible Navier–Stokes Equations. We showed this by implementing three yield surfaces into the open source toolkit OpenFOAM, namely Drucker–Prager, Mohr–Coulomb and Matsuoka–Nakai. All three yield surfaces have been calibrated for isochoric shear. This means that they are equal for two-dimensional and similar for shear dominated flows. For other deformation types differences of up to 44% in internal stresses have to be expected. Numerical simulations of axisymmetric granular collapses revealed such deformation types and the respective differences. Deformation in mobilised zones was mainly characterized by shearing, in contrast to static zones, where triaxial compression was dominant. However, static zones are irrelevant for the kinematics, leading to a good agreement between yield surfaces in terms of runout. The only exception was the tall granular collapse with aspect ratio 2, where triaxial compression dominated the early stage of the rapid collapse.

A scaling analysis based on the shallowness assumption, $H/L \ll 1$ and a Bagnold velocity profile, reveals that deformation in typical landslides and

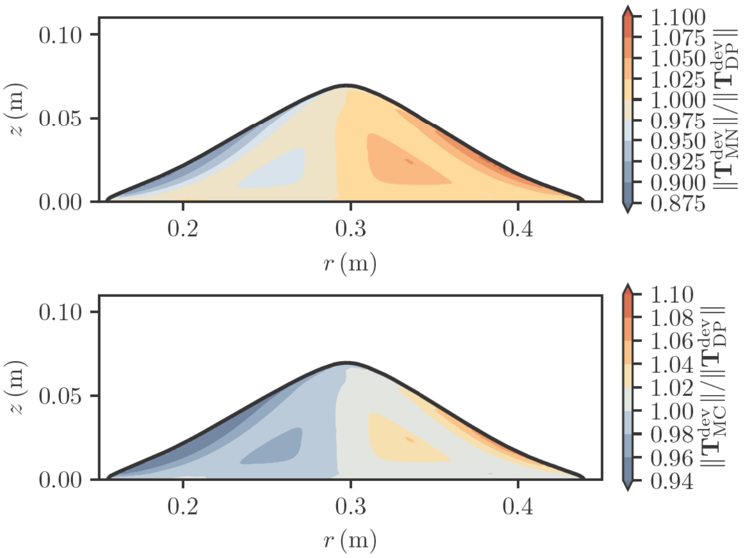

Figure I.15: Ring granular collapse with the Matsuoka–Nakai (top) and Mohr–Coulomb (bottom) yield criterion. The colour displays the ratio between the respective criterion and Drucker–Prager.

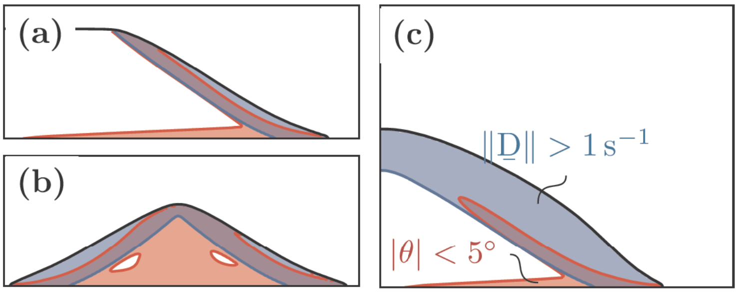

Figure I.16: Shearbands with a shear rate higher than $1\,\mathrm{s}^{-1}$ (blue) and a Lode-angle between $-5°$ and $5°$ (red). Cylindrical collapse with $h_0/r_0 = 1/2$ at $t = 0.2\,\mathrm{s}$ (a), ring collapse at $t = 0.2\,\mathrm{s}$ (b), cylindrical collapse with $h_0/r_0 = 2$ at $t = 0.2\,\mathrm{s}$ (c).

avalanches will be dominated by shearing, indicated by small Lode-angles $\theta \ll 1\,\mathrm{rad}$. However, in cases where the shallowness assumption does not hold, predictions of dynamics and kinematics will be different for the presented models. This is especially the case when dealing with obstacles, as the shear dominated flow pattern will be disturbed. Zones of triaxial compression and extension will emerge and deviatoric stresses will vary, leading to further flow pattern changes and possibly highly varying forces on the obstacles. There is strong evidence that Mohr–Coulomb and Matsuoka–Nakai might be the better choice here (Schweiger, 1994; Maiolino and Luong, 2009; Wojciechowski, 2018; Pähtz *et al.*, 2019). However, a final conclusion can only be drawn with experiments and

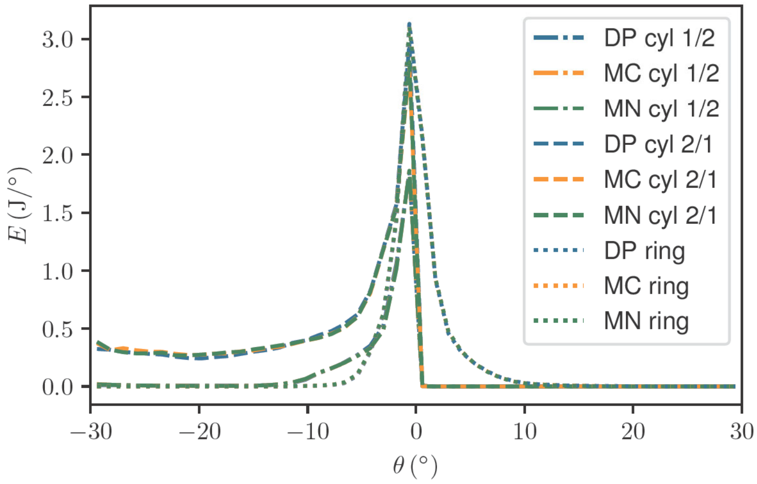

Figure I.17: Dissipated energy as a function of the Lode-angle θ for all simulations. The peak at $\theta = 0°$ indicates that most energy is dissipated during isochoric shearing. The variation due to the rheology is small and lines of the same experiment overlap almost entirely.

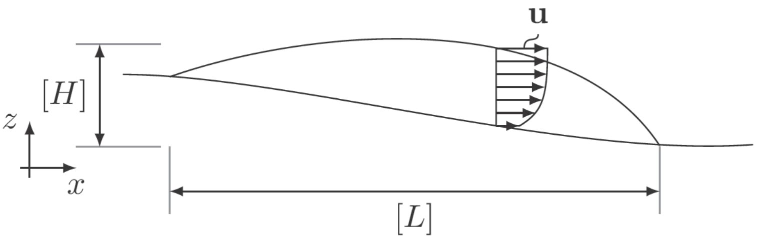

Figure I.18: Typical height H and length L of a landslide as used in the scaling analysis of Savage and Hutter (1989).

respective simulations. The extension of a Drucker–Prager yield criterion to a Mohr–Coulomb yield criterion is straight-forward and can be done by adding an additional factor, solely depending on the Lode-angle and the friction angle (see Eq. (I.28)). For the calculation of the runout and especially in depth-integrated models with complex rheologies (e.g. Baker *et al.*, 2016), the simpler Drucker–Prager model should be sufficient. The here presented methodology can be combined with the popular $\mu(I)$–rheology by introducing the velocity depended friction coefficient into the yield surfaces, $\sin(\phi) \equiv \mu(I)$. Finally we want to note that all statements in this paper are limited to incompressible flows. In compressible flows, even two-dimensional deformations might be characterised with a Lode-angle unequal zero, making the here found similarities invalid.

Acknowledgements

This project has received funding from the European Union's Horizon 2020 research and innovation programme under the Marie Skłodowska-Curie grant agreement No. 721403 (SLATE). The computational results presented have been achieved (in part) using the HPC infrastructure LEO of the University of Innsbruck. We thank Eoin Maguire, Nico Gray, Magdalena Schreter, Finn Løvholt, Geir Pedersen and two anonymous referees for interesting discussions and valuable comments.

I.7 Bibliography

R. A. Bagnold, "Experiments on a gravity-free dispersion of large solid spheres in a Newtonian fluid under shear," in *Proceedings of the Royal Society of London A: Mathematical, Physical and Engineering Sciences*, vol. 225, pp. 49–63, The Royal Society, 1954, DOI: 10.1098/rspa.1954.0186.

R. A. Bagnold, "The shearing and dilatation of dry sand and the 'singing' mechanism," in *Proceedings of the Royal Society of London A: Mathematical, Physical and Engineering Sciences*, vol. 295, pp. 219–232, The Royal Society, 1966, DOI: 10.1098/rspa.1966.0236.

J. L. Baker, T. Barker and J. M. N. T. Gray, "A two-dimensional depth-averaged $\mu(I)$-rheology for dense granular avalanches," *Journal of Fluid Mechanics*, vol. 787, pp. 367–395, 2016, DOI: 10.1017/jfm.2015.684.

N. J. Balmforth and R. R. Kerswell, "Granular collapse in two dimensions," *Journal of Fluid Mechanics*, vol. 538, pp. 399–428, 2005, DOI: 10.1017/S0022112005005537.

T. Barker and J. M. N. T. Gray, "Partial regularisation of the incompressible μ(I)-rheology for granular flow," *Journal of Fluid Mechanics*, vol. 828, pp. 5–32, 2017, DOI: 10.1017/jfm.2017.428.

T. Barker, D. G. Schaeffer, P. Bohorquez and J. M. N. T. Gray, "Well-posed and ill-posed behaviour of the μ(I)-rheology for granular flow," *Journal of Fluid Mechanics*, vol. 779, pp. 794–818, 2015, DOI: 10.1017/jfm.2015.412.

T. Barker, D. G. Schaeffer, M. Shearer and J. M. N. T. Gray, "Well-posed continuum equations for granular flow with compressibility and μ(I)-rheology," *Proceedings of the Royal Society A*, vol. 473, no. 2201, p. 20160846, 2017, DOI: 10.1098/rspa.2016.0846.

C. S. Campbell, "Rapid granular flows," *Annual Review of Fluid Mechanics*, vol. 22, no. 1, pp. 57–90, 1990, DOI: 10.1146/annurev.fl.22.010190.000421.

W.-F. Chen and D.-J. Han, *Plasticity for structural engineers*, J. Ross Publishing, 2007.

W.-F. Chen and X. L. Liu, *Limit analysis in soil mechanics*, vol. 52, Elsevier, 1990.

J. Desrues, B. Zweschper and P. A. Vermeer, "Database for tests on Hostun RF sand," *Publication Series of the Institute of Geotechnik, University Stuttgart*, 2000.

D. C. Drucker and W. Prager, "Soil mechanics and plastic analysis or limit design," *Quarterly of Applied Mathematics*, vol. 10, no. 2, pp. 157–165, 1952.

A. N. Edwards, S. Viroulet, B. P. Kokelaar and J. M. N. T. Gray, "Formation of levees, troughs and elevated channels by avalanches on erodible slopes," *Journal of Fluid Mechanics*, vol. 823, pp. 278–315, 2017, DOI: 10.1017/jfm.2017.309.

W. Fellin and A. Ostermann, "The critical state behaviour of barodesy compared with the Matsuoka–Nakai failure criterion," *International Journal for Numerical and Analytical Methods in Geomechanics*, vol. 37, no. 3, pp. 299–308, 2013, DOI: 10.1002/nag.1111.

A. Gajo and M. Wood, "Severn–Trent sand: a kinematic-hardening constitutive model: the q–p formulation," *Géotechnique*, vol. 49, no. 5, pp. 595–614, 1999, DOI: 10.1680/geot.1999.49.5.595.

P. Gauer, A. Elverhoi, D. Issler and F. V. De Blasio, "On numerical simulations of subaqueous slides: back-calculations of laboratory experiments of clay-rich slides," *Norsk Geologisk Tidsskrift*, vol. 86, no. 3, pp. 295–300, 2006.

GDR MiDi, "On dense granular flows," *The European Physical Journal E*, vol. 14, no. 4, pp. 341–365, 2004, DOI: 10.1140/epje/i2003-10153-0.

L. Gesenhues, J. J. Camata, A. M. A. Côrtes, F. A. Rochinha and A. L. G. A. Coutinho, "Finite element simulation of complex dense granular flows using a well-posed regularization of the μ(I)-rheology," *Computers and Fluids*, vol. 188, pp. 102–113, 2019, DOI: 10.1016/j.compfluid.2019.05.012.

I. Goldhirsch, "Rapid granular flows," *Annual Review of Fluid Mechanics*, vol. 35, no. 1, pp. 267–293, 2003, DOI: 10.1146/annurev.fluid.35.101101.161114.

K. Holmberg, P. Andersson and A. Erdemir, "Global energy consumption due to friction in passenger cars," *Tribology International*, vol. 47, pp. 221–234, 2012, DOI: 10.1016/j.triboint.2011.11.022.

R. I. Issa, "Solution of the implicitly discretised fluid flow equations by operator-splitting," *Journal of Computational Physics*, vol. 62, no. 1, pp. 40–65, 1986, DOI: 10.1016/0021-9991(86)90099-9.

C. G. Johnson and J. M. N. T. Gray, "Granular jets and hydraulic jumps on an inclined plane," *Journal of Fluid Mechanics*, vol. 675, pp. 87–116, 2011, DOI: 10.1017/jfm.2011.2.

P. Jop, Y. Forterre and O. Pouliquen, “A constitutive law for dense granular flows,” *Nature*, vol. 441, no. 7094, p. 727, 2006, DOI: 10.1038/nature04801.

D. Kolymbas, “An outline of hypoplasticity,” *Archive of Applied Mechanics*, vol. 61, no. 3, pp. 143–151, 1991, DOI: 10.1007/BF00788048.

D. Kolymbas, “Barodesy: a new hypoplastic approach,” *International Journal for Numerical and Analytical Methods in Geomechanics*, vol. 36, no. 9, pp. 1220–1240, 2012, DOI: 10.1002/nag.1051.

P. V. Lade and H. M. Musante, “Three-dimensional behavior of remolded clay,” *Journal of the Geotechnical Engineering Division*, vol. 104, no. 2, pp. 193–209, 1978.

P. V. Lade, R. B. Nelson and Y. M. Ito, “Nonassociated flow and stability of granular materials,” *Journal of Engineering Mechanics*, vol. 113, no. 9, pp. 1302–1318, 1987.

P.-Y. Lagrée, L. Staron and S. Popinet, “The granular column collapse as a continuum: validity of a two-dimensional Navier–Stokes model with a μ(I)-rheology,” *Journal of Fluid Mechanics*, vol. 686, pp. 378–408, 2011, DOI: 10.1017/jfm.2011.335.

G. Lube, H. E. Huppert, R. S. J. Sparks and M. A. Hallworth, “Axisymmetric collapses of granular columns,” *Journal of Fluid Mechanics*, vol. 508, pp. 175–199, 2004, DOI: 10.1017/S0022112004009036.

J. Lubliner, *Plasticity theory*, Macmillan, 1990.

S. Maiolino and M. P. Luong, “Measuring discrepancies between Coulomb and other geotechnical criteria: Drucker-Prager and Matsuoka-Nakai,” in *7th Euromech Solid Mechanics Conference, Lisbon, Portugal*, pp. 09–07, 2009.

N. Martin, I. R. Ionescu, A. Mangeney, F. Bouchut and M. Farin, “Continuum viscoplastic simulation of a granular column collapse on large slopes: μ(I) rheology and lateral wall effects,” *Physics of Fluids*, vol. 29, no. 1, p. 013301, 2017, DOI: 10.1063/1.4971320.

H. Matsuoka and T. Nakai, “Stress-deformation and strength characteristics of soil under three different principal stresses,” in *Proceedings of the Japan Society of Civil Engineers*, vol. 1974, pp. 59–70, Japan Society of Civil Engineers, 1974, DOI: 10.2208/jscej1969.1974.232_59.

G. Medicus and W. Fellin, “An improved version of barodesy for clay,” *Acta Geotechnica*, vol. 12, no. 2, pp. 365–376, 2017, DOI: 10.1007/s11440-016-0458-4.

G. Medicus, D. Kolymbas and W. Fellin, “Proportional stress and strain paths in barodesy,” *International Journal for Numerical and Analytical Methods in Geomechanics*, vol. 40, no. 4, pp. 509–522, 2016, DOI: 10.1002/nag.2413.

F. Moukalled, L. Mangani and M. Darwish, *The finite volume method in computational fluid dynamics*, Springer, 2016, DOI: 10.1007/978-3-319-16874-6.

OpenCFD Ltd., *OpenFOAM - The Open Source CFD Toolbox - User Guide*, 2004, last checked: 20.01.2020.

T. Pähtz, O. Durán, D. N. de Klerk, I. Govender and M. Trulsson, "Local rheology relation with variable yield stress ratio across dry, wet, dense, and dilute granular flows," *Physial Review Letters*, vol. 123, p. 048001, 2019, DOI: 10.1103/PhysRevLett.123.048001.

A. Passalacqua and R. O. Fox, "Implementation of an iterative solution procedure for multi-fluid gas–particle flow models on unstructured grids," *Powder Technology*, vol. 213, no. 1, pp. 174–187, 2011, DOI: 10.1016/j.powtec.2011.07.030.

O. Pouliquen, C. Cassar, P. Jop, Y. Forterre and M. Nicolas, "Flow of dense granular material: towards simple constitutive laws," *Journal of Statistical Mechanics: Theory and Experiment*, vol. 2006, no. 07, p. P07020, 2006, DOI: 10.1088/1742-5468/2006/07/P07020.

S. P. Pudasaini and K. Hutter, *Avalanche Dynamics: Dynamics of Rapid Flows of Dense Granular Avalanches*, Springer, 2007, DOI: 10.1007/978-3-540-32687-8.

S. B. Savage, M. H. Babaei and T. Dabros, "Modeling gravitational collapse of rectangular granular piles in air and water," *Mechanics Research Communications*, vol. 56, pp. 1–10, 2014, DOI: 10.1016/j.mechrescom.2013.11.001.

S. B. Savage and K. Hutter, "The motion of a finite mass of granular material down a rough incline," *Journal of Fluid Mechanics*, vol. 199, pp. 177–215, 1989, DOI: 10.1017/S0022112089000340.

D. G. Schaeffer, "Instability in the evolution equations describing incompressible granular flow," *Journal of Differential Equations*, vol. 66, no. 1, pp. 19–50, 1987, DOI: 10.1016/0022-0396(87)90038-6.

T. Schanz, P. Vermeer and P. Bonnier, "The hardening soil model: formulation and verification," in *Beyond 2000 in Computational Geotechnics*, ed. R. B. J. Brinkgreve, pp. 281–296, A. A. Balkema Rotterdam, 1999.

A. Schofield and P. Wroth, *Critical state soil mechanics*, McGraw-Hill London, 1968.

F. Schranz and W. Fellin, "Stability of infinite slopes investigated with elastoplasticity and hypoplasticity," *Geotechnik*, vol. 39, no. 3, pp. 184–194, 2016, DOI: 10.1002/gete.201500021.

H. Schweiger, "On the use of Drucker-Prager failure criteria for earth pressure problems," *Computers and Geotechnics*, vol. 16, no. 3, pp. 223–246, 1994, DOI: 10.1016/0266-352X(94)90003-5.

M. Taiebat and Y. F. Dafalias, “SANISAND: Simple anisotropic sand plasticity model,” *International Journal for Numerical and Analytical Methods in Geomechanics*, vol. 32, no. 8, pp. 915–948, 2008, DOI: 10.1002/nag.651.

B. G. M. van Wachem, “Derivation, implementation, and validation of computer simulation models for gas-solid fluidized beds,” Ph.D. thesis, TU Delft, Delft University of Technology, Delft, Netherlands, 2000, last checked: 11.09.19.

A. Voellmy, “Über die Zerstörungskraft von Lawinen.” *Schweizerische Bauzeitung*, vol. 73, no. 12,15,17,19, 1955, DOI: 10.5169/seals-61878.

P.-A. Von Wolffersdorff, “A hypoplastic relation for granular materials with a predefined limit state surface,” *Mechanics of Cohesive-frictional Materials: An International Journal on Experiments, Modelling and Computation of Materials and Structures*, vol. 1, no. 3, pp. 251–271, 1996, DOI: 10.1002/(SICI)1099-1484(199607)1:3<251::AID-CFM13>3.0.CO;2-3.

H. G. Weller, G. Tabor, H. Jasak and C. Fureby, “A tensorial approach to computational continuum mechanics using object-oriented techniques,” *Computers in Physics*, vol. 12, no. 6, pp. 620–631, 1998, DOI: 10.1063/1.168744.

M. Wojciechowski, “A note on the differences between Drucker-Prager and Mohr-Coulomb shear strength criteria,” *Studia Geotechnica et Mechanica*, vol. 40, no. 3, pp. 163–169, 2018, DOI: 10.2478/sgem-2018-0016.

M.-H. Yu, “Advances in strength theories for materials under complex stress state in the 20th century,” *Applied Mechanics Reviews*, vol. 55, no. 3, pp. 169–218, 2002, DOI: 10.1115/1.1472455.

Authors’ addresses

Matthias Rauter Norwegian Geotechnical Institute, Postboks 3930 Ulleval Stadion, 0806 Oslo, Norway, matthias.rauter@ngi.no

Thomas Barker University of Edinburgh, Alexander Graham Bell building, EH9 3FG Edinburgh, United Kingdom, thomas.barker@ed.ac.uk

Wolfgang Fellin University of Innsbruck, Innrain 52, 6020 Innsbruck, Austria, wolfgang.fellin@uibk.ac.at

Paper II

The compressible granular collapse in a fluid as a continuum: validity of a Navier–Stokes model with $\mu(J)$,$\phi(J)$-rheology

Matthias Rauter

Accepted by *Journal of Fluid Mechanics*

Abstract

The incompressible $\mu(I)$-rheology has been used to study subaerial granular flows with remarkable success. For subaquatic granular flows, drag between grains and the pore fluid is substantially higher and the physical behaviour is more complex. High drag forces constrain the rearrangement of grains and dilatancy, leading to a considerable build-up of pore pressure. Its transient and dynamic description is the key to modelling subaquatic granular flows but out of the scope of incompressible models. In this work, we advance from the incompressible $\mu(I)$-rheology to the compressible $\mu(J)$,$\phi(J)$-rheology to account for pore pressure, dilatancy, and the scaling laws under subaquatic conditions. The model is supplemented with critical state theory to yield the correct properties in the quasi-static limit. The pore fluid is described by an additional set of conservation equations and the interaction with grains is described by a drag model. This new implementation enables us to include most of the physical processes relevant for submerged granular flows in a highly transparent manner. Both, the incompressible and compressible rheologies are implemented into OpenFOAM and various simulations at low and high Stokes numbers are conducted with both frameworks. We found a good agreement of the $\mu(J)$,$\phi(J)$-rheology with low Stokes number experiments, that incompressible models fail to describe. The combination of granular rheology, pore pressure, and drag model leads to complex phenomena such as apparent cohesion, remoulding, hydroplaning, and turbidity currents. The simulations give remarkable insights into these phenomena and increase our understanding of subaquatic mass transports.

II.1 Introduction

Avalanches and landslides, as well as many industrial processes can be classified as granular flows. Substantially improved rheological formulations have given rise to numerous attempts to simulate these phenomena with Navier–Stokes type models. The vast amount of studies relies on the $\mu(I)$-rheology and its derivatives. The core of the $\mu(I)$-rheology is the Drucker–Prager yield criterion (Drucker and Prager, 1952; Rauter *et al.*, 2020) and the recognition that the friction coefficient μ is solely a function of the inertial number I (GDR MiDi, 2004; Jop *et al.*, 2006). Further studies found a similar correlation between the inertial number and the packing density ϕ (Forterre and Pouliquen, 2008).

A similar scaling was found in granular flows with low Stokes numbers St (see Eq. (II.31)). The Stokes number is related to the ratio between inertia and drag force on a particle and thus describes the influence of ambient fluid on the granular flow dynamics (e.g. Finlay, 2001). Small Stokes numbers indicate a strong influence of the pore fluid on the particles, and hence also on the landslide dynamics. In this regime, the viscous number J replaces the inertial number I as a control parameter for the friction coefficient μ and the packing density ϕ, forming the so-called $\mu(J)$,$\phi(J)$-rheology (Boyer *et al.*, 2011). Furthermore, excess pore pressure can be remarkably high under these conditions and it is imperative to explicitly consider it in numerical simulations. High drag forces and respectively small Stokes numbers are usually related to small particles. They are virtually omnipresent in geophysical flows: submarine landslides (Kim *et al.*, 2019), turbidity currents (Heerema *et al.*, 2020), powder snow avalanches (Sovilla *et al.*, 2015), and pyroclastic flows (Druitt, 1998) can be dominated by fine grained components. It follows that a large portion of gravitational mass flows occurs at low Stokes numbers and a deeper understanding of the respective processes is relevant for many researchers.

Incompressible granular flow models have been applied in different forms to various problems in the last decade. Lagrée *et al.* (2011) were the first to conduct numerical simulations of subaerial granular collapses with the $\mu(I)$-rheology and the finite volume method. Staron *et al.* (2012) used the same method to simulate silo outflows, and Domnik *et al.* (2013) used a constant friction coefficient to simulate granular flows on inclined plates. von Boetticher *et al.* (2016, 2017) applied a similar model, based on OpenFOAM, to debris flows and many more examples can be found in the literature. More recently, compressible flow models have been introduced to simulate subaquatic granular flows at low Stokes numbers. The applied methods include, e.g., smoothed particle hydrodynamics (Wang *et al.*, 2017), coupled lattice Boltzmann and discrete element method (Yang *et al.*, 2017), the material point method (Baumgarten and Kamrin, 2019) or the finite volume multiphase framework of OpenFOAM (Si *et al.*, 2018a). Results have often been compared to experiments of Balmforth and Kerswell (2005) (subaerial) and Rondon *et al.* (2011) (subaquatic), two works that gained benchmark character in the granular flow community.

Most of the mentioned applications rely on standard methods from computational fluid dynamics (CFD). This is reasonable, considering the similarity between the hydrodynamic (Navier–Stokes) equations and the granular flow equations. However, the pressure dependent and shear thinning viscosity associated with granular flows introduces considerable conceptual and numerical problems. The unconditional ill-posedness of an incompressible granular flow model with constant friction coefficient was described by Schaeffer (1987) and the partial ill-posedness of the $\mu(I)$-rheology by Barker *et al.* (2015). By carefully tuning the respective relations, Barker and Gray (2017) were able to regularize the $\mu(I)$-rheology for all but very high inertia numbers. Barker *et al.* (2017) described a well-posed compressible rheology, incorporating the $\mu(I)$-rheology as a special case.

Another pitfall of granular rheologies is the concept of effective pressure. When pore pressure is considerably high (i.e. at low Stokes numbers), it is imperative to distinguish between effective pressure and total pressure (first described by Terzaghi, 1925). Effective pressure represents normal forces in the grain skeleton that have a stabilizing effect, in contrast to pore pressure which has no stabilizing effect. This has shown to be a major issue, as pore pressure and consequently the effective pressure, react very sensitively to the packing density and dilatancy (Rondon *et al.*, 2011).

Besides the rheology, tracking of the slide geometry poses a major challenge. Surface tracking is usually implemented in terms of the algebraic volume-of-fluid (VOF) method (e.g. Lagrée *et al.*, 2011; Si *et al.*, 2018a), the level-set method (e.g. Savage *et al.*, 2014), geometric surface tracking methods (e.g. Roenby *et al.*, 2016; Marić *et al.*, 2018), or particles based methods (e.g. Baumgarten and Kamrin, 2019; Wang *et al.*, 2017).

The volume-of-fluid method, which is also used in this work, allows to track the slide as a single component but also as a mixture of multiple phases (grains and pore fluid). Components are defined in here as objects (e.g. the landslide) that completely cover a bounded region in space without mixing with other components (e.g. the ambient fluid), see Fig. II.3. The tracking becomes a purely geometric problem (see e.g. Roenby *et al.*, 2016, for a geometric interpretation). In contrast, phases (e.g. grains) are dispersed and mixed with other phases (e.g. pore fluid) to represent the dynamic bulk of the landslide, see Fig. II.1.

The component-wise tracking is used in various landslide models (e.g. Lagrée *et al.*, 2011; Domnik *et al.*, 2013; Barker and Gray, 2017). Components, i.e. the slide and the surrounding fluid, are immiscible and separated by a sharp interface. Usually, this also implies that the model is incompressible. The phase-wise tracking is commonly applied in chemical engineering (Gidaspow, 1994; van Wachem, 2000; Passalacqua and Fox, 2011) and has lately been introduced to environmental engineering (e.g. Cheng *et al.*, 2017; Chauchat *et al.*, 2017; Si *et al.*, 2018a). This approach allows to describe a variable mixture of grains and pore fluid that merges smoothly into the ambient fluid. The description of the pore fluid as an individual phase enables the model to decouple effective pressure from pore pressure, which is imperative in many flow configurations, e.g. for low Stokes numbers.

In this work, a two-component and a two-phase Navier–Stokes type model are applied to granular flows. Both models are implemented into the open-source toolkit OpenFOAM (Weller *et al.*, 1998; Rusche, 2002; OpenCFD Ltd., 2004), using the volume-of-fluid method for component- and phase-wise tracking (see section II.2). Subaerial (Balmforth and Kerswell, 2005) and subaquatic granular collapses (Rondon *et al.*, 2011) are simulated with both models and results are compared to the respective experiments and with each other.

We apply the $\mu(I)$,$\phi(I)$-rheology to subaerial cases ($St \gtrapprox 1$) and the $\mu(J)$,$\phi(J)$-rheology to subaquatic cases ($St \lessapprox 1$). The two-component model applies simplified rheologies in form of the incompressible $\mu(I)$- and $\mu(J)$-rheologies. The $\phi(I)$- and $\phi(J)$-curves are merged into the particle pressure relation of Johnson and Jackson (1987) to achieve the correct quasi-static limits (Vescovi *et al.*, 2013). This yields reasonable values for the packing density at rest which is imperative for granular collapses with static regions. In contrast to many previous works (e.g. Savage *et al.*, 2014; von Boetticher *et al.*, 2017; Si *et al.*, 2018a), we renounce additional contributions to shear strength (e.g. cohesion) because we do not see any physical justification (e.g. electrostatic forces, capillary forces, cementing) in the investigated cases. We apply a very transparent and simple model, focusing on the relevant physical processes and achieve a remarkable accuracy, especially in comparison to more complex models (e.g. Si *et al.*, 2018a; Baumgarten and Kamrin, 2019). Further, it is shown that various experimental setups with different initial packing densities can be simulated with the same constitutive parameters, whereas many previous attempts required individual parameters for different cases (e.g. Savage *et al.*, 2014; Wang *et al.*, 2017; Si *et al.*, 2018a).

The paper is organised as follows: The multi-phase (section II.2.1) and multi-component (section II.2.2) models are introduced in section II.2, including models for granular viscosity (section II.2.3), granular particle pressure (sections II.2.4 and II.2.5) and drag (section II.2.6). Results are shown and discussed in section II.3 for a subaerial case and in section II.4 for two subaquatic cases. A conclusion is drawn in section II.5 and a summary is given in section II.6. Furthermore, a thorough sensitivity analysis is provided in the appendix.

II.2 Methods

II.2.1 Two-phase landslide-model

The two-phase model is based on the phase momentum and mass conservation equations (see e.g. Rusche, 2002). The governing equations for the continuous fluid phase are given as

$$\frac{\partial \phi_\mathrm{c}}{\partial t} + \boldsymbol{\nabla} \cdot (\phi_\mathrm{c}\, \mathbf{u}_\mathrm{c}) = 0, \tag{II.1}$$

$$\begin{aligned}\frac{\partial \phi_\mathrm{c}\, \rho_\mathrm{c}\, \mathbf{u}_\mathrm{c}}{\partial t} + \boldsymbol{\nabla} \cdot (\phi_\mathrm{c}\, \rho_\mathrm{c}\, \mathbf{u}_\mathrm{c} \otimes \mathbf{u}_\mathrm{c}) = \boldsymbol{\nabla} \cdot (\phi_\mathrm{c}\, \mathbf{T}_\mathrm{c}) - \phi_\mathrm{c}\, \boldsymbol{\nabla}\, p + {}\\ \phi_\mathrm{c}\, \rho_\mathrm{c}\, \mathbf{g} + k_\mathrm{gc}\, (\mathbf{u}_\mathrm{g} - \mathbf{u}_\mathrm{c})\,.\end{aligned} \tag{II.2}$$

and for the grains as

$$\frac{\partial \phi_\mathrm{g}}{\partial t} + \boldsymbol{\nabla} \cdot (\phi_\mathrm{g}\, \mathbf{u}_\mathrm{g}) = 0, \tag{II.3}$$

$$\begin{aligned}\frac{\partial \phi_\mathrm{g}\, \rho_\mathrm{g}\, \mathbf{u}_\mathrm{g}}{\partial t} + \boldsymbol{\nabla} \cdot (\phi_\mathrm{g}\, \rho_\mathrm{g}\, \mathbf{u}_\mathrm{g} \otimes \mathbf{u}_\mathrm{g}) = \boldsymbol{\nabla} \cdot (\phi_\mathrm{g}\, \mathbf{T}_\mathrm{g}) - \boldsymbol{\nabla}\, p_\mathrm{s} - \phi_\mathrm{g}\, \boldsymbol{\nabla}\, p + \\ \phi_\mathrm{g}\, \rho_\mathrm{g}\, \mathbf{g} + k_\mathrm{gc}\, (\mathbf{u}_\mathrm{c} - \mathbf{u}_\mathrm{g}) ,\end{aligned} \tag{II.4}$$

Phase-fraction fields ϕ_g and ϕ_c, i.e. the phase volume over the total volume

$$\phi_i = \frac{V_i}{V}, \tag{II.5}$$

describe the composition of the grain-fluid mixture, see Fig. II.1 (the index i indicates either c or g). The granular phase-fraction is identical with the packing density $\phi = \phi_\mathrm{g}$. Phase-fractions take values between zero and one and the sum of all phase-fractions yields one. The pore fluid is assumed to match the surrounding fluid and the respective phase-fraction ϕ_c is therefore one outside the slide. This way, phase-fraction fields provide not only a mechanism to track the packing density of the slide, but also its geometry. Every phase moves with a unique velocity field $\mathbf{u}_i$, which is not divergence-free. This allows the mixture to change, yielding a variable packing density and thus bulk-compressibility, although phase densities ρ_g and ρ_c are constant. The volume weighted average velocity is divergence free,

$$\boldsymbol{\nabla} \cdot \overline{\mathbf{u}} = \boldsymbol{\nabla} \cdot (\phi_\mathrm{g}\, \mathbf{u}_\mathrm{g} + \phi_\mathrm{c}\, \mathbf{u}_\mathrm{c}) = 0, \tag{II.6}$$

which allows to use numerical methods for incompressible flow.

The pore pressure (or shared pressure) p is acting on all phases equally, while the grain phase experiences additional pressure due to force chains between particles, the so called effective pressure (or particle pressure) p_s, see Fig. II.2. The effective pressure is a function of the packing density in this model and the balance between effective pressure and external pressure (e.g. overburden pressure) ensures realistic packing densities. The total pressure can be assembled as

$$p_\mathrm{tot} = p + p_\mathrm{s}. \tag{II.7}$$

The deviatoric phase stress tensors are expressed as

$$\mathbf{T}_i = 2\, \rho_i\, \nu_i \mathbf{S}_i, \tag{II.8}$$

with phase viscosity ν_i, phase density ρ_i and deviatoric phase strain rate tensor

$$\mathbf{S}_i = \frac{1}{2}\left(\boldsymbol{\nabla}\mathbf{u}_i + (\boldsymbol{\nabla}\mathbf{u}_i)^T\right) - \frac{1}{3}\boldsymbol{\nabla} \cdot \mathbf{u}_i\, \mathbf{I}. \tag{II.9}$$

The viscosity of the pore fluid ν_c is usually constant and the granular viscosity ν_g is following from constitutive models like the $\mu(I)$-rheology (see section II.2.3). The total deviatoric stress tensor can be calculated as

$$\mathbf{T} = \phi_\mathrm{c}\, \mathbf{T}_\mathrm{c} + \phi_\mathrm{g}\, \mathbf{T}_\mathrm{g}. \tag{II.10}$$

The last terms in Eqs. (II.2) and (II.4) represent drag forces between phases and k_{gc} is the drag coefficient of the grains in the pore fluid. Lift and virtual mass forces are neglected in this work, because they play a minor role (Si *et al.*, 2018a).

The granular viscosity ν_{g}, the effective pressure p_{s}, and the drag coefficient k_{gc} represent interfaces to exchangeable sub-models, presented in sections II.2.3-II.2.6.

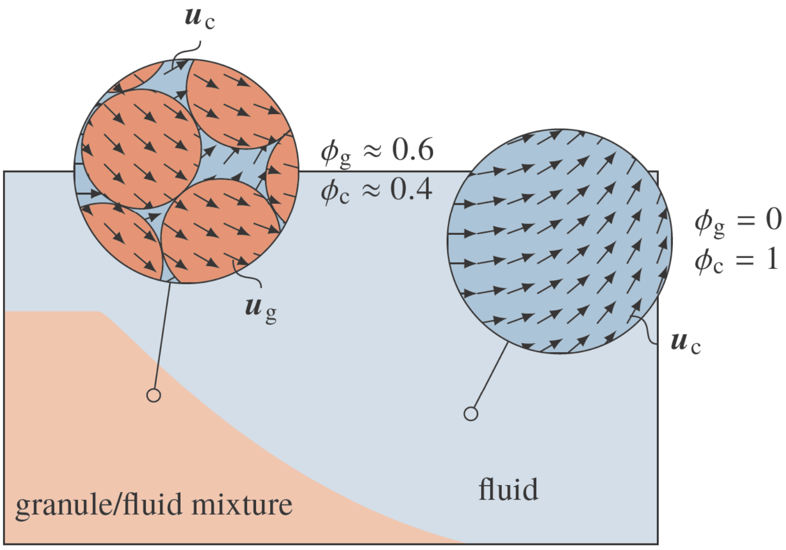

Figure II.1: Definition of phase-fractions ϕ_i and phase velocities $\mathbf{u}_i$ in and outside a dense granular avalanche for the two-phase model. Phase velocities can differ, allowing phase-fractions to change, giving the avalanche compressible properties.

II.2.2 Two-component landslide-model

Many two-phase systems can be substantially simplified by assuming that phases move together, i.e. that phase velocities are equal,

$$\mathbf{u}_i \approx \overline{\mathbf{u}} = \phi_{\mathrm{g}}\,\mathbf{u}_{\mathrm{g}} + \phi_{\mathrm{c}}\,\mathbf{u}_{\mathrm{c}}. \tag{II.11}$$

This fits very well to completely separated phases that are divided by a sharp interface (e.g. surface waves in water, Rauter *et al.*, 2021) but also systems of mixed phases (e.g. grains and fluid) can be handled to some extent (e.g. Lagrée *et al.*, 2011). The phase momentum conservation equations (II.2) and (II.4) can be combined into a single momentum conservation equation and the system takes the form of the ordinary Navier–Stokes Equations with variable fluid properties (see e.g. Rusche, 2002),

$$\frac{\partial \rho\,\overline{\mathbf{u}}}{\partial t} + \boldsymbol{\nabla}\cdot(\rho\,\overline{\mathbf{u}}\otimes\overline{\mathbf{u}}) = \boldsymbol{\nabla}\cdot\mathbf{T} - \boldsymbol{\nabla}\,p_{\mathrm{tot}} + \rho\,\mathbf{g}, \tag{II.12}$$

$$\boldsymbol{\nabla}\cdot\overline{\mathbf{u}} = 0. \tag{II.13}$$

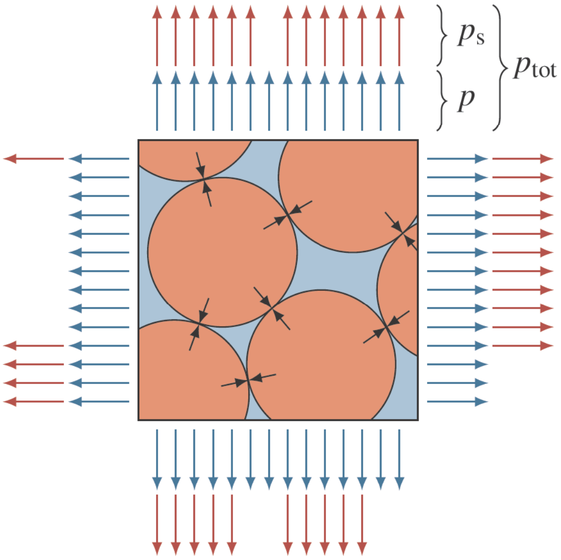

Figure II.2: Representative volume element of a grain-fluid mixture. The effective pressure p_s (red arrows) represents normal forces in the grain skeleton (black arrows). The pore-pressure (blue arrows) represents pressure that is equally shared by pore fluid and grains.

A detailed derivation can be found in appendix II.7. The pressure is denoted as p_tot, indicating that it contains contributions from hydrodynamic and effective pressure.

The phase-fraction fields ϕ_i cannot be recovered after this simplification and the method switches to the tracking of components instead of phases, see Fig. II.3. Components are tracked with so-called component indicator functions α_i (sometimes called phase indicator functions but in here we consequently distinguish phases from components), being either one if component i is present at the respective location or zero otherwise,

$$\alpha_i = \begin{cases} 1 & \text{if component } i \text{ is present} \\ 0 & \text{otherwise} \end{cases} \tag{II.14}$$

Values between zero and one are not intended by this method and only appear due to numerical reasons, i.e. the discretisation of the discontinuous field (see section II.2.7). In here, two component indicator functions are used, one for the ambient fluid component, α_c, and one for the slide component, α_s (see Fig. II.3). Evolution equations for component indicator functions can be derived from mass conservation equations as

$$\frac{\partial \alpha_i}{\partial t} + \boldsymbol{\nabla} \cdot (\alpha_i\, \overline{\mathbf{u}}) = 0. \tag{II.15}$$

The definition of components is straight forward for completely separated phases, where components can be matched with phases, e.g. water and air. The definition of the slide component, on the other hand, is not unambiguous, as it consists of a variable mixture of grains and pore fluid. A boundary of the slide component can, for example, be found by defining a limit for the packing density (e.g. 50% of the average packing density). Further, a constant reference packing density $\overline{\phi}$ has to be determined, which is assigned to the whole slide component. The density of the slide component follows as

$$\rho_\mathrm{s} = \overline{\phi}\rho_\mathrm{g} + (1 - \overline{\phi})\rho_\mathrm{c}, \tag{II.16}$$

and a similar relation can be established for the deviatoric stress tensor (see section II.2.3.1).

The local density ρ and the local deviatoric stress tensor $\mathbf{T}$ can be calculated as

$$\rho = \sum_i \alpha_i\, \rho_i = \alpha_\mathrm{s}\, \rho_\mathrm{s} + \alpha_\mathrm{c}\, \rho_\mathrm{c} \tag{II.17}$$

$$\mathbf{T} = \sum_i \alpha_i\, \mathbf{T}_i = \alpha_\mathrm{s}\, \mathbf{T}_\mathrm{s} + \alpha_\mathrm{c}\, \mathbf{T}_\mathrm{c}, \tag{II.18}$$

using component densities ρ_i, as well as component deviatoric stress tensors $\mathbf{T}_i$. Component deviatoric stress tensors are calculated as

$$\mathbf{T}_i = 2\, \nu_i\, \rho_i\, \mathbf{S}, \tag{II.19}$$

with the component viscosity ν_i and the deviatoric shear rate tensor $\mathbf{S}$. Note that the deviatoric shear rate tensor $\mathbf{S}$ matches the shear rate tensor $\mathbf{D}$, because the volume weighted averaged velocity field is divergence free,

$$\mathbf{S} = \mathbf{D} = \frac{1}{2}\left(\boldsymbol{\nabla}\, \overline{\mathbf{u}} + (\boldsymbol{\nabla}\, \overline{\mathbf{u}})^T\right). \tag{II.20}$$

The viscosity of the ambient fluid ν_c is usually constant and the viscosity of the slide region ν_s is following from granular rheology, see section II.2.3.

II.2.3 Rheology

II.2.3.1 Unifying rheologies

Most granular rheologies (e.g. the $\mu(I)$-rheology) are defined in terms of the total deviatoric stress tensor in the slide component $\mathbf{T}_\mathrm{s}$. This has to be accounted for and corrected in the two-phase model if the same viscosity model is used in both models. Similar to Eq. (II.16), component viscosities can be related to phase viscosities as

$$\mathbf{T}_\mathrm{s} = \overline{\phi}\mathbf{T}_\mathrm{g} + (1 - \overline{\phi})\, \mathbf{T}_\mathrm{c}, \tag{II.21}$$

$$2\, \rho_\mathrm{s}\, \nu_\mathrm{s}\mathbf{S}_\mathrm{s} = 2\, \overline{\phi}\rho_\mathrm{g}\, \nu_\mathrm{g}\, \mathbf{S}_\mathrm{g} + 2\, (1 - \overline{\phi})\rho_\mathrm{c}\, \nu_\mathrm{c}\, \mathbf{S}_\mathrm{c}. \tag{II.22}$$

The contribution of the granular phase to stresses is assumed to be much higher than the contribution of the pore fluid, $\overline{\phi}\rho_\mathrm{g}\, \nu_\mathrm{g}\, \mathbf{S}_\mathrm{g} \gg (1 - \overline{\phi})\rho_\mathrm{c}\, \nu_\mathrm{c}\, \mathbf{S}_\mathrm{c}$. Further,

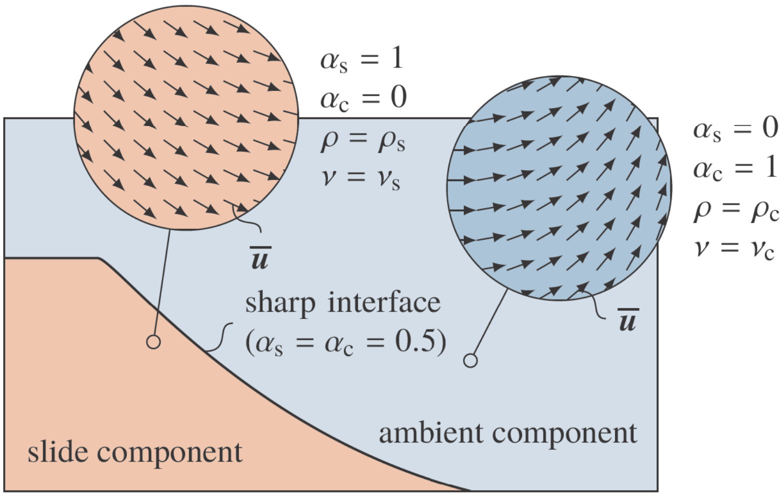

Figure II.3: Definition of component indicator functions α_i and the velocity $\overline{\mathbf{u}}$ in and outside a dense granular avalanche for the two-component model.

by neglecting the mass of the pore fluid, $\rho_s \approx \overline{\phi}\,\rho_g$, it follows that kinematic viscosities have to be similar in both models,

$$\nu_s \approx \nu_g. \tag{II.23}$$

Alternatively, one can match the dynamic viscosities $\nu_s\,\rho_s$ and $\nu_g\,\rho_g$ if the factor ϕ_g is removed from the viscous term in Eq. (II.4). Note, that this assumptions are fairly accurate for subaerial granular flows but questionable for subaquatic granular flows. However, multi-phase and multi-component models differ substantially under subaquatic conditions and a unification is not possible.

II.2.3.2 Drucker–Prager plasticity model

An important characteristic of granular materials is the pressure dependent shear stress, described by the Drucker–Prager yield criterion (Drucker and Prager, 1952). Schaeffer (1987) was the first to include granular friction in the Navier–Stokes equations by expressing the Drucker–Prager yield criterion in terms of the shear rate tensor and the pressure,

$$\mathbf{T}_s = \mu\,p_s\,\frac{\mathbf{S}}{\|\mathbf{S}\|}, \tag{II.24}$$

where the norm of a tensor $\|\mathbf{A}\|$ is defined as

$$\|\mathbf{A}\| = \sqrt{\frac{1}{2}\,\mathrm{tr}\,(\mathbf{A}^2)}. \tag{II.25}$$

The friction coefficient μ is constant and a material parameter in the first model by Schaeffer (1987). The slide component viscosity follows as

$$\nu_s = \frac{\|\mathbf{T}_s\|}{2\,\rho_s\,\|\mathbf{S}\|} = \mu\,\frac{p_s}{2\,\rho_s\|\mathbf{S}\|}. \tag{II.26}$$

This relation has been applied with slight modifications by e.g. Domnik *et al.* (2013), Savage *et al.* (2014) or Rauter *et al.* (2020). Following the findings in section II.2.3.1, the kinematic viscosity of slide and grains have to be similar and the granular phase viscosity follows as

$$\nu_{\mathrm{g}} = \frac{\|\mathbf{T}_{\mathrm{g}}\|}{2\,\rho_{\mathrm{s}}\,\|\mathbf{S}_{\mathrm{g}}\|} = \mu\,\frac{p_{\mathrm{s}}}{2\,\rho_{\mathrm{g}}\overline{\phi}\,\|\mathbf{S}_{\mathrm{g}}\|}. \tag{II.27}$$

The viscosity reaches very high values for $\|\mathbf{S}\| \to 0$ and very small values for $p_{\mathrm{s}} \to 0$ and both limits can lead to numerical problems. To overcome numerically unstable behaviour the viscosity is truncated to an interval $[\nu_{\mathrm{min}}, \nu_{\mathrm{max}}]$. A thoughtful choice of ν_{max} is crucial for the presented method. Small values tend towards unphysical results, because solid-like behaviour can only be simulated by very high viscosities. Big values, on the other hand, tend towards numerical instabilities (see section II.2.7.3). The ideal value for the maximum viscosity depends on the respective case and can be estimated with a scaling and sensitivity analysis (see appendix II.8.1). The relation

$$\nu_{\mathrm{max}} = \frac{1}{10}\,\sqrt{|\mathbf{g}|\,H^3}, \tag{II.28}$$

where H is the characteristic height of the investigated case, was found to give a good estimate for a reasonable viscosity cut-off. Notably, the Drucker–Prager yield surface leads to an ill-posed model (Schaeffer, 1987) and the truncation of the viscosity is not sufficient for a regularization.

Schaeffer (1987) did not distinguish between effective and total pressure in Eq. (II.26), limiting the applications of his model substantially. We will explicitly consider effective pressure in Eqs. (II.26) and (II.27) using Eq. (II.34) or (II.36) in the two-component model and Eq. (II.37), (II.40), or (II.43) in the two-phase model to avoid such limitations.

II.2.3.3 $\mu(I)$-rheology

The $\mu(I)$-rheology (GDR MiDi, 2004; Jop *et al.*, 2006; Forterre and Pouliquen, 2008) states that the friction coefficient μ is not constant in dense, dry, granular flows but rather a function of the inertial number I. The inertial number I is defined as the ratio between the typical time scale for microscopic rearrangements of grains with diameter d, $t_{\mathrm{micro}} = d\,\sqrt{\rho_{\mathrm{g}}/p_{\mathrm{s}}}$, and the macroscopic time scale of the deformation, $t_{\mathrm{macro}} = 1/2\,\|\mathbf{S}\|^{-1}$,

$$I = 2\,d\,\|\mathbf{S}\|\sqrt{\frac{\rho_{\mathrm{g}}}{p_{\mathrm{s}}}}, \tag{II.29}$$

In the two-phase model, the shear rate $\mathbf{S}$ is replaced with the deviatoric shear rate of grains $\mathbf{S}_{\mathrm{g}}$. Various approaches have been proposed for the $\mu(I)$-curve, in here we apply the classic relation, given as

$$\mu(I) = \mu_1 + (\mu_2 - \mu_1)\,\frac{I}{I_0 + I}, \tag{II.30}$$

where μ_1, μ_2 and I_0 are material parameters (Jop *et al.*, 2006). The dynamic friction coefficient $\mu(I)$ is introduced into the Drucker–Prager yield criterion, Eqs. (II.26) or (II.27) to get the respective granular viscosity.

II.2.3.4 $\mu(J)$-rheology

At small Stokes numbers, defined as

$$St = 2\, d^2 \, \|\mathbf{S}\| \, \frac{\rho_\mathrm{g}}{\nu_\mathrm{c}\, \rho_\mathrm{c}}, \tag{II.31}$$

the pore fluid has substantial influence on the rheology and the microscopic time scale is defined by the viscous scaling $t_\mathrm{micro} = \nu_\mathrm{c}\, \rho_\mathrm{c}/p_\mathrm{s}$ (Boyer *et al.*, 2011). The friction coefficient is thus no longer a function of the inertial number I but rather of the viscous number J, defined as

$$J = 2\, \|\mathbf{S}\| \frac{\nu_\mathrm{c}\, \rho_\mathrm{c}}{p_\mathrm{s}}. \tag{II.32}$$

The functional relation of the friction coefficient on the viscous number was described by Boyer *et al.* (2011) as

$$\mu(J) = \mu_1 + (\mu_2 - \mu_1)\, \frac{J}{J_0 + J} + J + \frac{5}{2}\, \phi_\mathrm{m} \sqrt{J}, \tag{II.33}$$

where μ_1, μ_2, J_0 and ϕ_m are material parameters (Boyer *et al.*, 2011). The $\mu(J)$-rheology is taking advantage of the Drucker–Prager yield criterion, similar to the $\mu(I)$-rheology.

Notably, the $\mu(I)$ and $\mu(J)$-rheology can be combined by forming a new dimensionless number $K = J + \alpha\, I^2$ with a constitutive parameter α (Trulsson *et al.*, 2012; Baumgarten and Kamrin, 2019). However, this was not required for the cases presented in this work.

II.2.4 Effective pressure in the two-component model

II.2.4.1 Total pressure assumption

The two-component model is limited in considering pore pressure and dilatancy effects because the packing density is not described by this model. The effective pressure can only be reconstructed from total pressure p_tot and various assumptions. The simplest model assumes that the pore pressure is negligibly small, leading to

$$p_\mathrm{s} \approx p_\mathrm{tot}. \tag{II.34}$$

This assumption is reasonable for subaerial granular flows and has been applied to such by e.g. Lagrée *et al.* (2011) or Savage *et al.* (2014).

II.2.4.2 Hydrostatic pressure assumption

In subaquatic granular flows, the surrounding high-density fluid increases the total pressure substantially and it cannot be neglected. Following Savage *et al.* (2014), improvement can be achieved by calculating the hydrostatic pore pressure as

$$p_{\mathrm{hs}} = \begin{cases} \rho_{\mathrm{c}}\, \mathbf{g} \cdot (\mathbf{x} - \mathbf{x}_0) & \text{for} \quad \mathbf{g} \cdot (\mathbf{x} - \mathbf{x}_0) > 0, \\ 0 & \text{otherwise,} \end{cases} \tag{II.35}$$

and subtracting it from the total pressure,

$$p_{\mathrm{s}} \approx p_{\mathrm{tot}} - p_{\mathrm{hs}}. \tag{II.36}$$

Here, $\mathbf{x}_0$ is the position of the free water surface, where the total pressure is supposed to be zero. For a variable and non-horizontal free water surface, common in e.g. landslide-tsunamis, this concept is complicated substantially, and to the authors knowledge, not applied. Furthermore, excess pore pressure, which is common in low Stokes number flows, is out of the scope for this model.

II.2.5 Effective pressure in the two-phase model

II.2.5.1 Critical state theory

The structure of the two-phase model allows us to include the packing density in the effective pressure equation. Critical state theory (Roscoe *et al.*, 1958; Roscoe, 1970; Schofield and Wroth, 1968) was the first model to describe the relationship between the effective pressure and the packing density. The critical state is defined as a state of constant packing density and constant shear stress, which is reached after a certain amount of shearing of an initially dense or loose sample. The packing density in this state, called critical packing density ϕ_{crit}, is a function of the effective pressure p_{s}. This function can be inverted to get the effective pressure as a function of the critical packing density. It is further assumed that the flow is in its critical state $\phi_{\mathrm{g}} = \phi_{\mathrm{crit}}$ to get a model that is compatible with the governing equations. This assumption is reasonable for avalanches, slides, and other granular flows but questionable for the initial release and deposition. At small deformations, the packing density might be lower (underconsolidated) or higher (overconsolidated) than the critical packing density and the effective pressure model will over- or underestimate the effective pressure.

A popular relation for the effective pressure (the so-called critical state line) has been described by Johnson and Jackson (1987); Johnson *et al.* (1990) as

$$p_{\mathrm{s}} = a\, \frac{\phi_{\mathrm{g}} - \phi_{\mathrm{rlp}}}{\phi_{\mathrm{rcp}} - \phi_{\mathrm{g}}}, \tag{II.37}$$

where ϕ_{rlp} is the random loose packing density in critical state, ϕ_{rcp} the random close packing density in critical state and a a scaling parameter. The scaling parameter a can be interpreted as the effective pressure at the packing density

$\frac{1}{2}(\phi_{\mathrm{rcp}} + \phi_{\mathrm{rlp}})$. Note that we apply a simplified version of the original relation, similar to Vescovi *et al.* (2013). Packing densities above ϕ_{rcp} are not valid and avoided by the asymptote of the effective pressure at ϕ_{rcp}. If packing densities higher or equal ϕ_{rcp} appear in simulations, they should be terminated and restarted with refined numerical parameters (e.g. time step duration).

II.2.5.2 $\phi(I)$-relation

Equation (II.37) is known to hold for slow deformations in critical state (see e.g. Vescovi *et al.*, 2013). However, this relation is not consistent with granular flow experiments. Granular flows show dilatancy with increasing shear rate, expressed by e.g. Forterre and Pouliquen (2008) as a function of the inertia number I,

$$\phi_{\mathrm{g}}(I) = \phi_{\max} - \Delta\phi\, I, \tag{II.38}$$

where $\phi_{\max}$ and $\Delta\phi$ are material parameters. This relation can be transformed into a model for the effective pressure by introducing the inertial number I,

$$p_{\mathrm{s}} = \rho_{\mathrm{s}} \left(2\,\|\mathbf{S}_{\mathrm{g}}\|\, d\, \frac{\Delta\phi}{\phi_{\max} - \phi_{\mathrm{g}}}\right)^2. \tag{II.39}$$

This relation has two substantial problems: For $\|\mathbf{S}_{\mathrm{g}}\| = 0$ it yields $p_{\mathrm{s}} = 0$ and for $\phi_{\mathrm{g}} = 0$ it yields $p_{\mathrm{s}} \neq 0$, which causes numerical problems and unrealistic results. The first problem is addressed by superposing Eq. (II.39) with the quasi-static relation (II.37), similar to Vescovi *et al.* (2013). The second problem is solved by multiplying Eq. (II.39) with the normalized packing density $\phi_{\mathrm{g}}/\overline{\phi}$, which ensures that the pressure vanishes for $\phi_{\mathrm{g}} = 0$. The normalization with the reference packing density $\overline{\phi}$ ensures that parameters ($\phi_{\max}$, $\Delta\phi$) will be similar to the original equation. Further, to reduce the number of material parameters, we set the maximum packing density in the $\phi(I)$-relation equal to the random close packing density ϕ_{rcp}. The final relation reads

$$p_{\mathrm{s}} = a\, \frac{\phi_{\mathrm{g}} - \phi_{\mathrm{rlp}}}{\phi_{\mathrm{rcp}} - \phi_{\mathrm{g}}} + \rho_{\mathrm{g}}\, \frac{\phi_{\mathrm{g}}}{\overline{\phi}} \left(2\,\|\mathbf{S}_{\mathrm{g}}\|\, d\, \frac{\Delta\phi}{\phi_{\mathrm{rcp}} - \phi_{\mathrm{g}}}\right)^2, \tag{II.40}$$

and is shown in Fig. II.4 alongside the original relations of Johnson and Jackson (1987) and Forterre and Pouliquen (2008). Interestingly, this relation contains many features of the extended kinetic theory of Vescovi *et al.* (2013) (compare Fig. II.4b with Fig. 6b in Vescovi *et al.* (2013)). Notably, the inertial number is a function of only the packing density and the shear rate, $I = f(\phi_{\mathrm{g}}, \|\mathbf{S}_{\mathrm{g}}\|)$, because the effective pressure is calculated as function of the packing density. The same follows for the friction coefficient $\mu = f(\phi_{\mathrm{g}}, \|\mathbf{S}_{\mathrm{g}}\|)$ and the deviatoric stress tensor $\|\mathbf{T}_{\mathrm{g}}\| = f(\phi_{\mathrm{g}}, \|\mathbf{S}_{\mathrm{g}}\|)$. This highlights that the two-phase model implements a density-dependent rheology, rather than a pressure-dependent rheology.

It should be noted that there are various possibilities to combine critical state theory and the $\mu(I)$,$\phi(I)$-rheology. An alternative approach including bulk viscosity is provided by e.g. Schaeffer *et al.* (2019).

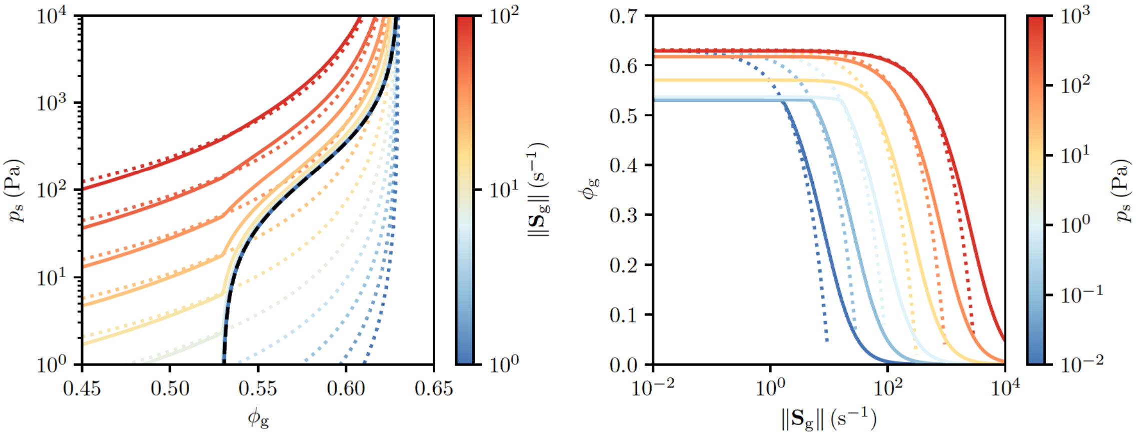

Figure II.4: Left: Effective pressure p_s following the $\phi(I)$-relation as a function of packing density ϕ_g and deviatoric shear rate $\|\mathbf{S}_\mathrm{g}\|$. The dashed lines show the original relation of Forterre and Pouliquen (2008), the continuous coloured lines show the modified relation and the black line the quasi-static limit following Johnson and Jackson (1987). Right: The critical packing density as a function of particle pressure p_s and deviatoric shear rate $\|\mathbf{S}_\mathrm{g}\|$. Dashed lines are following the original $\phi(I)$-relation, continuous lines the modified version. The critical state theory would result in horizontal lines in this plot.

II.2.5.3 $\phi(J)$-relation

The low Stokes number regime requires the replacement of the inertial number I with the viscous number J. The dependence of the packing density on the viscous number was described by Boyer *et al.* (2011) as

$$\phi_\mathrm{g} = \frac{\phi_\mathrm{m}}{1+\sqrt{J}}, \tag{II.41}$$

and we can derive the effective pressure by inserting the viscous number as

$$p_\mathrm{s} = \frac{2\,\nu_\mathrm{c}\,\rho_\mathrm{c}\,\|\mathbf{S}_\mathrm{g}\|}{\left(\frac{\phi_\mathrm{m}}{\phi_\mathrm{g}}-1\right)^2}. \tag{II.42}$$

Notably, Boyer *et al.* (2011) emphasised that ϕ_m is not matching the random close packing density $\phi_\mathrm{rcp} \approx 0.63$ but rather a value close to 0.585. This leads to substantial problems for large values of ϕ_g as the relation is only valid for $\phi_\mathrm{g} < \phi_\mathrm{m} = 0.585$ or $\|\mathbf{S}_\mathrm{g}\| = 0$. In other words, shearing is only possible for $\phi_\mathrm{g} < \phi_\mathrm{m}$. We solve this issue by allowing a creeping shear rate of S_0 at packing densities above ϕ_m. Further and as before, we superpose the relation with the quasi-static relation of Johnson and Jackson (1987) to yield the correct asymptotic values for $\|\mathbf{S}_\mathrm{g}\| \to 0$ known from critical state theory. The final relation reads

$$p_\mathrm{s} = a\,\frac{\phi_\mathrm{g}-\phi_\mathrm{rlp}}{\phi_\mathrm{rcp}-\phi_\mathrm{g}} + \frac{2\,\nu_\mathrm{c}\,\rho_\mathrm{c}\,\|\mathbf{S}_\mathrm{g}\|}{\left(\frac{\hat{\phi}_\mathrm{m}}{\phi_\mathrm{g}}-1\right)^2}, \tag{II.43}$$

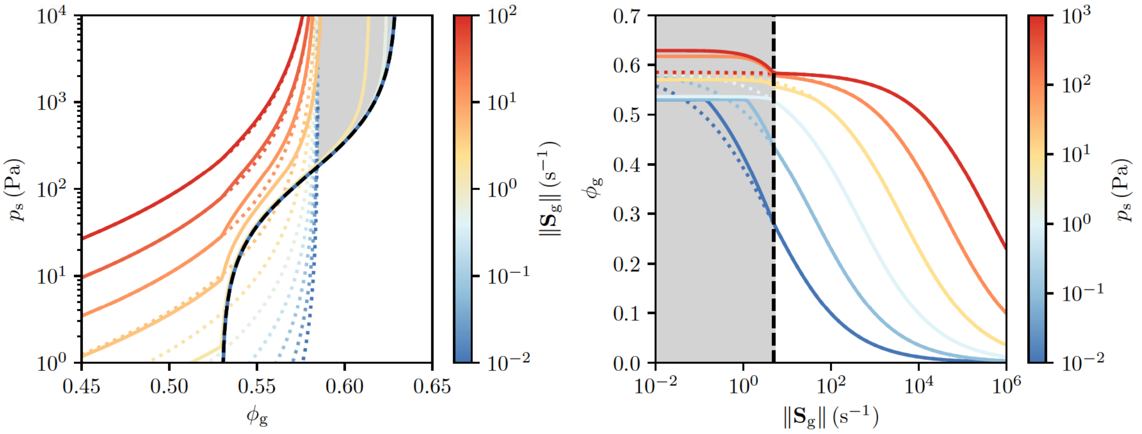

Figure II.5: Left: Particle pressure p_s following the $\phi(J)$-relation as a function of packing density ϕ_g and deviatoric shear rate $\|\mathbf{S}_g\|$. The dashed lines show the original relation of Boyer *et al.* (2011), the continuous coloured lines show the modified relation and the black line the static limit expressed following Johnson and Jackson (1987). Right: The critical packing density as a function of particle pressure p_s and deviatoric shear rate $\|\mathbf{S}_g\|$. Dashed lines are following the original $\phi(J)$-relation, continuous lines the modified version. The grey area shows the region where only creeping shear rates below S_0 are allowed.

with

$$\hat{\phi}_m = \begin{cases} \phi_m + (\phi_{rcp} - \phi_m)\,(S_0 - \|\mathbf{S}\|) & \text{for} \quad S_0 > \|\mathbf{S}\|, \\ \phi_m & \text{else}. \end{cases} \tag{II.44}$$

The respective relation is shown in Fig. II.5 alongside the original relations of Johnson and Jackson (1987) and Boyer *et al.* (2011). States with $\|\mathbf{S}\| \geq S_0$ and $\phi_g \geq \phi_m$ or $\phi_g \geq \phi_{rcp}$ are not intended by this model and simulations should be terminated if such states appear.

II.2.6 Drag and permeability model

The drag model describes the momentum exchange between grains and pore fluid in the two-phase model and widely controls permeability, excess pore pressure relaxation, and the settling velocity of grains. A wide range of drag models for various situations can be found in the literature. In here we stick to the Kozeny–Carman relation as applied by Pailha and Pouliquen (2009),

$$k_{gc} = 150\,\frac{\phi_g^2\,\nu_c\,\rho_c}{\phi_c\,d^2}, \tag{II.45}$$

with the grain diameter d as the only parameter. This relation is supposed to be valid for small relative velocities and densely packed granular material. It has been modified to account for higher relative velocities (Ergun, 1952) and lower packing densities (Gidaspow, 1994), however, which is not relevant for

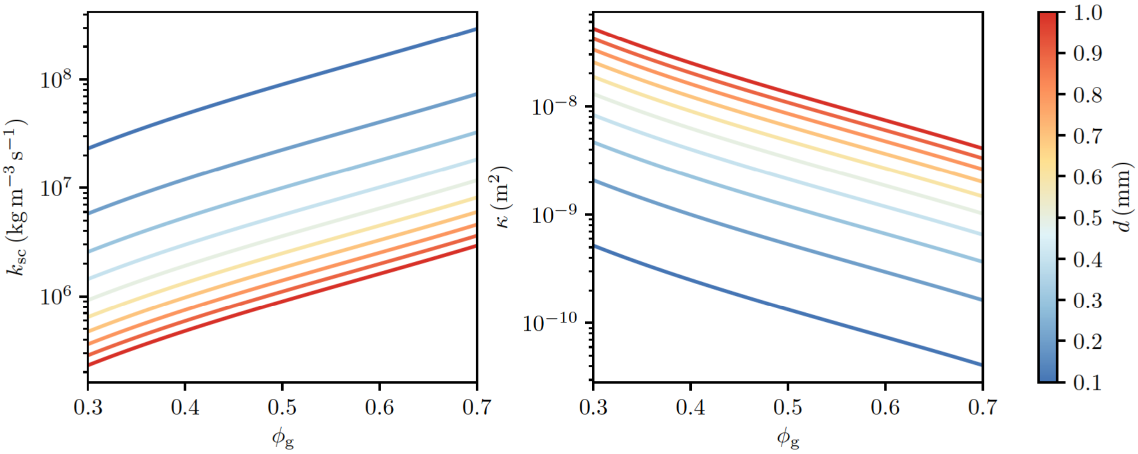

Figure II.6: Drag coefficient k_{gc} (left) and permeability κ (right) following the Kozeny–Carman relation Pailha and Pouliquen (2009) for various grain diameters (colour) and packing densities (x-axis).

the investigated configurations (see Si *et al.* (2018a) for an application of the extended relation). This relation is visualized in Fig. II.6a for various diameters and packing densities.

The drag coefficient can be reformulated into a permeability coefficient as known in soil mechanics and porous media. Comparing Darcy's law (e.g. Bear, 1972) with the equations of motion for the fluid phase, we can calculate the hydraulic conductivity as

$$K = \frac{\rho_{\mathrm{c}} |\mathbf{g}|}{k_{\mathrm{gc}}} \tag{II.46}$$

and furthermore the intrinsic permeability (e.g. Bear, 1972) as

$$\kappa = K \frac{\nu_{\mathrm{c}}}{|\mathbf{g}|} = \frac{\nu_{\mathrm{c}}\, \rho_{\mathrm{c}}}{k_{\mathrm{gc}}} = \frac{\phi_{\mathrm{c}}\, d^2}{150\, \phi_{\mathrm{g}}^2}. \tag{II.47}$$

The permeability is visualized in Fig. II.6b. In a similar manner, the drag coefficient can be calculated as

$$k_{\mathrm{gc}} = \frac{\rho_{\mathrm{c}}\, \nu_{\mathrm{c}}}{\kappa}, \tag{II.48}$$

if the intrinsic permeability of the granular material is known.

II.2.7 Numerical solution and exception handling

All models are implemented into OpenFOAM-v1812 (Weller *et al.*, 1998; OpenCFD Ltd., 2004) and solved with the finite volume method (Jasak, 1996; Rusche, 2002; Moukalled *et al.*, 2016).

II.2.7.1 Two-component landslide-model

The two-component model is based on the solver multiphaseInterFoam, using the PISO-algorithm (Issa, 1986) and interpolations following Rhie and Chow (1983) to solve the coupled system of pressure and velocity. First, an updated velocity field is calculated without the contribution of pressure. The predicted velocity field is later corrected to be divergence-free and the pressure follows from the required correction. Finally, all other fields, e.g. the phase indicator functions, are updated. This procedure is repeated in each time step.

Components (slide and ambient air or water) are divided by an interface which is supposed to be sharp. However, the interface is often smeared by numerical diffusion. To keep the interface between components sharp, the relative velocity between phases $\mathbf{u}_{\mathrm{ij}}$, which was previously eliminated from the system, is reintroduced in Eq. (II.15),

$$\frac{\partial \alpha_i}{\partial t} + \boldsymbol{\nabla} \cdot (\alpha_i \, \overline{\mathbf{u}}) + \boldsymbol{\nabla} \cdot (\alpha_i \, \alpha_j \, \mathbf{u}_{ij}) = 0. \tag{II.49}$$

Eq. (II.49) is finally solved using the MULES algorithm (Multidimensional Universal Limiter with Explicit Solution) (Weller, 2008). This scheme limits the interface compression term (i.e. the term containing $\mathbf{u}_{ij}$) to avoid over- ($\alpha_i > 1$) and undershoots ($\alpha_i < 0$) of the component indicator fields.

There is no conservation equation for the relative velocity in the two-component model and it has to be reconstructed from assumptions. Two methods are known to construct the relative velocity for granular flows. Barker *et al.* (2021) suggest to construct the relative velocity for granular flows from physical effects such as segregation and settling. The relative velocity follows as the terminal velocity of spheres in the surrounding fluid under the influence of gravity. Alternatively, one can construct a velocity field that is normal to the interface and of the same magnitude as the average velocity $\overline{\mathbf{u}}$,

$$\mathbf{u}_{ij} = |\overline{\mathbf{u}}| \frac{\alpha_j \, \boldsymbol{\nabla} \, \alpha_i - \alpha_i \, \boldsymbol{\nabla} \, \alpha_j}{|\alpha_j \, \boldsymbol{\nabla} \, \alpha_i - \alpha_i \, \boldsymbol{\nabla} \, \alpha_j|}. \tag{II.50}$$

This method has a maximum sharpening effect (Weller, 2008) and is thus also applied in this work.

II.2.7.2 Two-phase landslide-model

The two-phase model is based on the solver multiphaseEulerFoam. The system of pressure and average velocity is solved with the same concept as in the two-component solver. The velocity fields for all phases are first predicted without contributions from pore pressure p, but including effective pressure p_{s}. The average velocity is then corrected to be divergence-free and the pore pressure follows from the required correction. In a further step, the velocity correction is applied to phase velocities. The solution procedure is described in depth by Rusche (2002). The interface compression term is not required in this model because settling and segregation is directly simulated and counteracting numerical diffusion. The implementation of the effective pressure term is taken from SedFoam 2.0 (Chauchat *et al.*, 2017).

II.2.7.3 Time stepping

The numerical solution of transport equations is subject to limitations that pose restrictions on the solution method. One of these limitations is known as the Courant-Friedrichs-Lewy (CFL) condition and enforced by limiting the CFL number. In convection dominated problems, the CFL number is defined as the ratio of the time step duration Δt and the cell convection time $\Delta x/u_x$, i.e. the time required for a particle to pass a cell with size Δx,

$$\mathrm{CFL}^{\mathrm{conv}} = \frac{u_x\,\Delta t}{\Delta x}. \tag{II.51}$$

For the stability of e.g. the forward Euler method, it is required, that the convection time is smaller than the time step duration,

$$\mathrm{CFL}^{\mathrm{conv}} \leq 1, \tag{II.52}$$

and similar limits exist for other explicit methods. This limitation has to be enforced by choosing the time step duration Δt according to mesh size and flow velocity.

However, Eq. (II.51) is only valid for convection dominated problems. In the case of granular flows, the viscosity term is dominating over all other terms. Therefore, the viscosity has to be considered in the calculation of the CFL number and the time step duration. The respective definition, ignoring the contribution of convection follows as

$$\mathrm{CFL}^{\mathrm{diff}} = \frac{\nu\,\Delta t}{\Delta x^2}. \tag{II.53}$$

This relation is imperative for stability of explicit and semi-implicit Navier–Stokes solvers when viscous forces are dominating. The squared cell size in the denominator and the high viscosity introduce very strict limitations on the time step, making computations very expensive. Note that simplified relations for the one-dimensional case are given in here. The full multi-dimensional conditions for arbitrary finite volume cells can be found in Rauter *et al.* (2021).

II.3 Subaerial granular collapse

As a first test of the numerical models, we simulate the granular collapse experiments of Balmforth and Kerswell (2005) under subaerial conditions. A sketch of the experiment is shown in Fig. II.7. The experiment was conducted between two parallel, smooth walls and the setup is approximated as a 2D granular collapse. Balmforth and Kerswell (2005) conducted multiple experiments with different geometries, in here we focus on the experiments with an aspect ratio of $H/L = 1/2$, but similar results have been obtained for other aspect ratios. In theory, both, the two-component and the two-phase model should be equally capable of simulating this case because pore pressure plays a minor role. Most parameters, such as density, quasi-static friction coefficient, and particle diameter are reported by Balmforth and Kerswell (2005). The missing parameters are completed with data from the literature. Notably, the experiments are conducted on a smooth surface, which was incorporated in simulations by switching to a constant friction coefficient μ_{wall} at smooth surfaces. This modification is simple in the finite volume method because stresses are calculated on cell faces before their divergence is calculated as a sum over faces.

The Stokes number is estimated to be of order 10^3 (with $\|\mathbf{S}\| = 10\,\mathrm{s}^{-1}$) for this experiments and the $\mu(I)$,$\phi(I)$-rheology is chosen to describe friction and effective pressure. Parameters for the $\mu(I)$ and $\phi(I)$-curves are chosen in the physically reasonable range ($\mu_2 - \mu_1 \approx 0.3$, $I_0 \approx 0.25$, $\Delta\phi = 0.1$) following various references (e.g. Forterre and Pouliquen, 2008) in combination with values reported by Balmforth and Kerswell (2005). A wide range of limiting packing densities can be found in the literature, ϕ_{rlp} varying between 0.5 (Si *et al.*, 2018a) and 0.598 (Vescovi *et al.*, 2013), ϕ_{rcp} varying between 0.619 (Vescovi *et al.*, 2013) and 0.64 (Savage *et al.*, 2014). These parameters are therefore optimized to the subaquatic case (section II.4), where extended measurements are available, and applied to this case without further modification. The average packing density is assumed to be $\overline{\phi} = 0.6$ following the critical state line at this pressure level. The applied pressure equation is visualized in Fig. II.4. From the height $H = 0.1\,\mathrm{m}$ the required viscosity threshold $\nu_{\max}$ can be estimated following Eq. (II.28) to be of order $1\,\mathrm{m}^2\,\mathrm{s}^{-1}$. This estimation was validated with a sensitivity analysis (see appendix II.8.1). The final set of parameters is given in Tab. II.1.

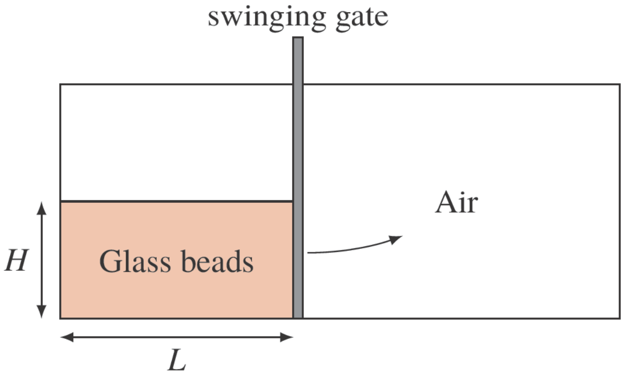

Figure II.7: Experimental column collapse setup of Balmforth and Kerswell (2005). The aspect ration H/L has been varied throughout the experiments. We will focus on the experiment $L = 0.2\,\mathrm{m}$, $H = 0.1\,\mathrm{m}$, similar to Savage *et al.* (2014).

Regular meshes of square cells are used to cover a simulation domain of $0.5 \times 0.2\,\mathrm{m}$, which was sufficient to have no artificial influences from boundaries. Standard boundary conditions are applied at walls (zero velocity, zero pressure

Table II.1: Material parameters for the subaerial granular collapse simulations. Note that not all material parameters are required by all models.

phase / comp.	par.	value	description
air	ρ_c	$1\,\mathrm{kg\,m^{-3}}$	air density
	ν_c	$1.48 \cdot 10^{-5}\,\mathrm{m^2\,s^{-1}}$	air viscosity
slide / grains	d	$10^{-3}\,\mathrm{m}$	particle diameter
	μ_wall	0.317	wall friction coefficient
	μ_1	0.595	quasi-static friction coefficient
	μ_2	0.895	dynamic friction coefficient
	I_0	0.25	reference inertial number
	ν_min	$10^{-4}\,\mathrm{m^2\,s^{-1}}$	lower viscosity threshold
	ν_max	$1\,\mathrm{m^2\,s^{-1}}$	upper viscosity threshold
	$\overline{\phi}$	0.60	assumed mean packing density[3]
	ρ_s	$1\,430\,\mathrm{kg\,m^{-3}}$	slide density[1]
	ρ_g	$2\,600\,\mathrm{kg\,m^{-3}}$	particle density[2]
	ϕ_rlp	0.53	random loose packing density[2]
	ϕ_rcp	0.63	random close packing density[2]
	a	$130\,\mathrm{Pa}$	critical state line parameter[2]
	$\Delta\phi$	0.1	dynamic loosening factor[2]

[1] only two-component model.

[2] only two-phase model.

[3] used to match the kinematic viscosity in the two-phase model following Eq. (II.22).

gradient) and the permeable top (zero velocity gradient, zero pressure). Multiple mesh resolutions were applied to investigate the influence of the grid resolution on the results (see appendix II.8.2). The time stepping was investigated with a similar approach, modifying the limit for $\mathrm{CFL}^\mathrm{diff}_\mathrm{max}$ between 1 and 1000 (depending on model and solver mode, see appendix II.8.3). In the following, the CFL-number is limited to 1 and the cell size set to 0.0017 m, which showed to be sufficient to achieve converged and mesh independent results.

II.3.1 Two-component model

The component indicator for the slide component α_s is initialized to 1 within the square that forms the initial granular column. We assume that hydrostatic pore pressure is negligible ($< 2\,\mathrm{Pa}$) and therefore apply Eq. (II.34) to calculate the effective pressure.

The simulation covering a simulation duration of 0.8 s took 6.9 h on eight cores of LEO4 (High Performance Cluster from the University of Innsbruck, consisting of Intel Xeon (Broadwell) compute cores). The total pressure, which is assumed to match the effective pressure, is shown for three-time steps in Fig. II.8, alongside the final pile in the experiment. The continuous black line shows the sharp free surface, assumed to be located at $\alpha_\mathrm{s} = 0.5$. Furthermore, the velocity field $\overline{\mathbf{u}}$ is shown as arrows. The collapse takes about 0.4 s and the pile remains in its final shape for the rest of the simulation. The two-component model matches the experiment well, however, the volume of the final pile is slightly underestimated. Results are very robust in terms of mesh refinement or coarsening (see appendix II.8.2) and mesh dependent instabilities (as e.g. Martin *et al.*, 2017; Gesenhues *et al.*, 2019) have not been observed.

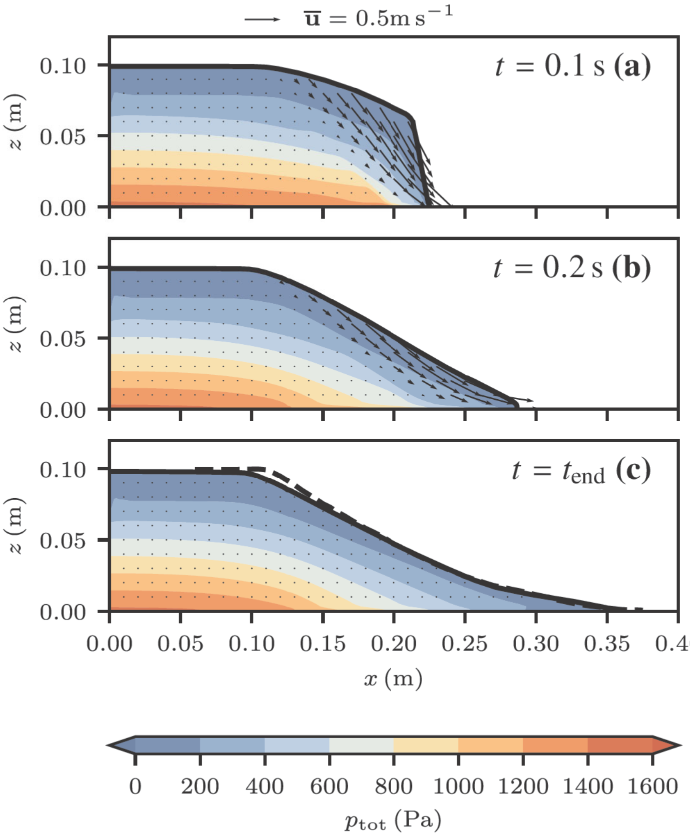

Figure II.8: Total pressure, assumed to match the effective pressure in the two-component model (subaerial case). The black arrows represent the velocity. The continuous black line shows the free surface of the slide ($\alpha_\mathrm{s} = 0.5$), the dashed black line shows the final experimental pile shape of Balmforth and Kerswell (2005).

II.3.2 Two-phase model

The two-phase model uses the same parameters as the two-component model, including numerical parameters, such as viscosity threshold and CFL limit. The phase-fraction ϕ_g was initialized such that effective pressure is in balance with lithostatic vertical stresses, yielding an initial mean phase-fraction of $\overline{\phi_g} = 0.608$. This procedure ensures that there will be no dilatancy or compaction in stable regions of the pile.

The simulation took 9.1 h under the same conditions as the two-component simulation. A stronger mesh dependency is observed for this model, however, the runout is converging for fine meshes (see appendix II.8.2). The pore pressure and the effective pressure following the extended $\phi(I)$-theory are shown for three time steps in Fig. II.9, alongside the final pile shape in the experiment. The continuous black line indicates the position of the free surface, assumed to be located at $\phi_s = 0.25$. The average velocity is shown as arrows in Figs. II.9a-c, the relative velocity of air with respect to grains in Figs. II.9d-f. The relative velocity in the initial phase is considerably high, indicating an inflow of air into the bulk and thus dilatancy. The two-phase model matches the experiment exceptionally well and the dilatancy in the experiment is matched by the simulation to a high degree. Note that the effective pressure at rest is directly linked to the packing density which can be qualitatively estimated from Fig. II.9f.

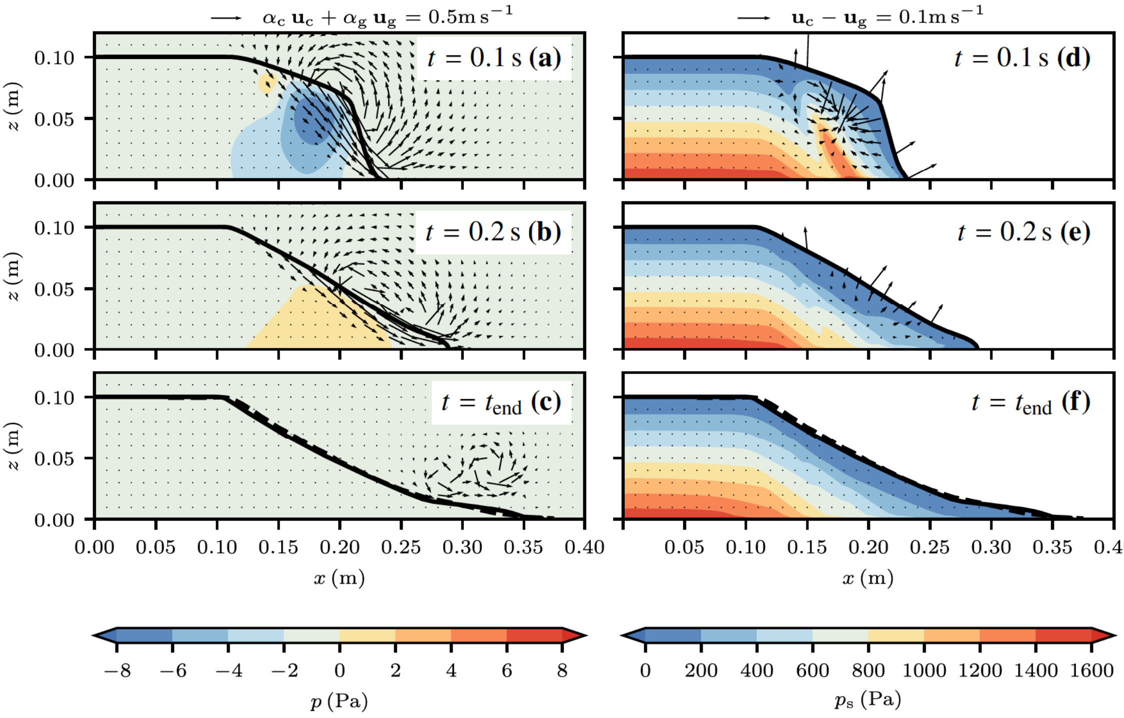

Figure II.9: Pore pressure (a-c) and effective pressure (d-f) in the two-phase model (subaerial case). The arrows show the average velocity (a-c) and the relative velocity (d-f). The continuous black line shows the free surface of the slide ($\phi_g = 0.25$), the dashed black line shows the final experimental pile shape of Balmforth and Kerswell (2005).

II.3.3 Discussion and comparison

Both models performed well at simulating the subaerial granular collapse. This is in line with previous results of e.g. Lagrée *et al.* (2011) or Savage *et al.* (2014). The effective pressure and the total pressure are fairly similar, because excess pore pressure is dissipating quickly through dilatancy or compaction. The magnitude of pore pressure in the two-phase model is smaller than 8 Pa and thus less than 1 % of the effective pressure, validating the assumption of neglectable pore pressure.

The runout is similar in both models, the front is slightly elongated in the two-phase model. Further, the two-phase model shows a better match with the experiment at the upper end of the final slope. Both of these minor differences can be attributed to dilatancy effects. The two-component model is intrinsically not able to capture this process. Two mechanisms for dilatancy can be observed in the two-phase model. Firstly, the average effective pressure in the slide is reduced as it is spreading out and the packing density decreases proportionally to the effective pressure, as prescribed by the critical state line. Secondly, shearing can reduce the packing density well below its critical packing density due to the dynamic contribution of the $\phi(I)$-theory to effective pressure. The loosely packed slide will not return to the critical packing density after shearing but remain in a loose state, forming a hysteresis. The granular material is able to remain in a loose state because the deviatoric stress tensor counteracts one-dimensional settling deformations (known as oedometric compression in soil mechanics). Furthermore, the granular column may have been overconsolidated in the experiment, however, this was not incorporated in the model due to the initialisation in critical state.

Dilatancy is rather unimportant under subaerial conditions, as it does not imply changes in rheology or flow dynamics. Therefore, the two-component model is well suited for subaerial granular collapses, where pore pressure is negligibly small and the Stokes number is well above one.

The reduced friction at the smooth basal surface has a small but noticeable effect on the final pile shape. The runout is longer when incorporating the smooth surface and matches the experiment better. Previous works (e.g. Savage *et al.*, 2014) ignored the smooth bottom of the experiment and still obtained accurate final pile shapes by using a constant friction coefficient. The increased friction of the $\mu(I)$-rheology (in comparison to a constant quasi-static friction coefficient) compensates for the reduced basal friction quite exactly (see appendix II.8.4).

The two-component model is less sensitive to grid resolution than the two-phase model (see appendix II.8.2) but more sensitive to the time step duration (see appendix II.8.3). At the same resolution, both models require roughly the same computational resources and no model shows a substantial advantage in this regard.

It is important to carefully choose the time step duration, as it can have drastic influences on simulation results. Generally, $\mathrm{CFL}^{\mathrm{diff}}$ has to be limited to one to guarantee satisfying results, while some cases and solver settings allow higher $\mathrm{CFL}^{\mathrm{diff}}$ numbers. This limitation is much stronger than the traditional

CFL criterion and CFL$^{\mathrm{conv}}$ is roughly 0.001. Notably, the time step duration is constant in simulations, $\Delta t \approx 3 \cdot 10^{-6}\,\mathrm{s}$, because the constant maximum viscosity $\nu_{\max}$ in stable regions and the constant cell size Δx controlled the time stepping.

II.4 Subaqueous granular collapse

The granular collapse experiments of Rondon *et al.* (2011) are conducted under subaquatic conditions and the Stokes number was estimated to be of order 10^{-1} (at $\|\mathbf{S}\| = 10\,\mathrm{s}^{-1}$). Pore pressure, packing density, and permeability play an important role under these conditions and the complexity increases substantially. Experiments accounted for the increased complexity by varying the average initial packing density in experiments between 0.55 and 0.61. The pore pressure was recorded by a sensor in the bottom plate, approximately below the centre of the column at $x = 0.02\,\mathrm{m}$ (see Fig. II.10). This sensor showed strong variations of the pore pressure in dense and loose experiments, indicating its important role for subaquatic slides.

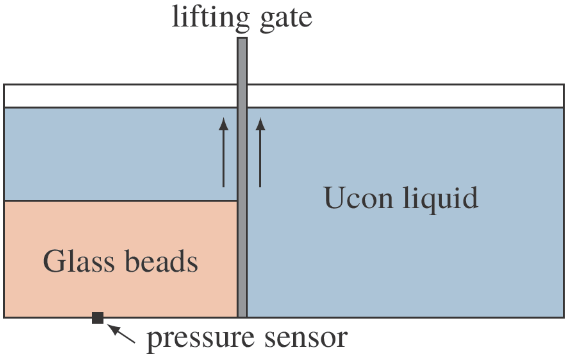

Figure II.10: Experimental column collapse setup of Rondon *et al.* (2011). The packing density and the aspect ratio have been varied in the experiment. We will focus on a densely and a loosely packed case, similar to Savage *et al.* (2014).

A loose or underconsolidated ($\overline{\phi_{\mathrm{g}}} = 0.55$, $L = 0.06\,\mathrm{m}$, $H = 0.048\,\mathrm{m}$) and a dense or overconsolidated ($\overline{\phi_{\mathrm{g}}} = 0.6$, $L = 0.06\,\mathrm{m}$, $H = 0.042\,\mathrm{m}$) simulation are conducted in this work to investigate the sensitivity of the model. As before, the experiments were conducted between two parallel, smooth walls and the setup is approximated with 2D simulations. Most material parameters are reported by Rondon *et al.* (2011), parameters for the $\mu(J)$ and $\phi(J)$-curves are supplemented with data from Boyer *et al.* (2011). The quasi-static friction coefficient μ_1 is taken from Si *et al.* (2018a). The particles have a diameter of $d = 0.225\,\mathrm{mm}$ and are immersed into a Ucon solution (for details, see Rondon *et al.*, 2011) with a viscosity of $\nu_{\mathrm{c}} = 1.2 \cdot 10^{-5}\,\mathrm{m}^2\,\mathrm{s}^{-1}$ (about 10 times higher than water), leading to a very low permeability of $\kappa \approx 10^{-10}\mathrm{m}^2$ following Eq. (II.47). Early tests revealed that the two-phase model reacts very sensitively to the critical state line parameters ϕ_{rlp}, ϕ_{rcp}, and a. Parameters from the literature (e.g. the critical state line applied by Si *et al.*, 2018a) lead to unrealistic granular pressures at

Table II.2: Material parameters for the subaquatic granular collapse simulations. Note that not all material parameters are required by all models.

phase	par.	value	description
ucon mix	ρ_c	$1\,000\,\mathrm{kg\,m^{-3}}$	ucon mix density
	ν_c	$1.2 \cdot 10^{-5}\,\mathrm{m^2\,s^{-1}}$	ucon mix viscosity
slide	d	$2.25 \cdot 10^{-4}\,\mathrm{m}$	particle diameter
	μ_1	0.340	quasi-static friction coefficient
	μ_2	0.740	dynamic friction coefficient
	J_0	0.005	reference viscous number
	ν_min	$10^{-4}\,\mathrm{m^2\,s^{-1}}$	lower viscosity threshold
	ν_max	$1\,\mathrm{m^2\,s^{-1}}$	upper viscosity threshold
	$\overline{\phi}$	0.60	assumed mean packing density[3]
	ρ_s	$1\,900\,\mathrm{kg\,m^{-3}}$	slide density[1]
	ρ_g	$2\,500\,\mathrm{kg\,m^{-3}}$	particle density[2]
	ϕ_rlp	0.53	random loose packing density[2]
	ϕ_rcp	0.63	random close packing density[2]
	a	$130\,\mathrm{Pa}$	critical state line parameter[2]
	ϕ_m	0.585	dynamic reference packing density[2]
	S_0	$5\,\mathrm{s^{-1}}$	maximum creep shearing[2]

[1] only two-component model.
[2] only two-phase model.
[3] used to match the kinematic viscosity in the two-phase model following Eq. (II.22).

$\phi_\mathrm{g} = 0.60$ and could thus not be applied. We set the limiting packing densities to $\phi_\mathrm{rlp} = 0.53$ and $\phi_\mathrm{rcp} = 0.63$ to allow initial average packing densities between 0.55 and 0.61. The scaling variable a was found by matching the peak pore pressure in the dense simulation with the respective measurement (see Fig. II.14). The total set of parameters used for both cases is shown in Tab. II.2.

Regular meshes of square cells with size 0.0005 m are applied, covering a simulation domain of $0.15\,\mathrm{m} \times 0.105\,\mathrm{m}$ (dense case) and $0.25\,\mathrm{m} \times 0.105\,\mathrm{m}$ (loose case). The CFL number $\mathrm{CFL}^\mathrm{diff}$ is limited to 10 in order to keep computation times to a reasonable level. A sensitivity study was conducted to proof convergence at this grid size (see appendix II.8.2) and $\mathrm{CFL}^\mathrm{diff}$ number (see appendix II.8.3).

II.4.1 Two-component model - dense case

The hydrostatic pore pressure is high under subaquatic conditions and the two-component model applies Eq. (II.36) to consider its influence on the effective pressure. All parameters are taken from Tab. II.2. The evolution of the slide geometry, the effective pressure and the velocity $\overline{\mathbf{u}}$ are shown in Fig. II.11, alongside the final experimental pile shape. The final pile shape of the model corresponds roughly to the experiment. The velocity, on the other hand, is roughly corresponding to the loose case, and the collapse is completed after 1 s, whereas the dense experiment took more than 30 s. The simulation and its failure mechanism are similar to the subaerial case where the free unsupported side of the pile is collapsing until reaching a stable slope inclination. Notably, neither the dense nor the loose experiment showed such a failure mechanism (see Fig. II.15). No excess pore pressure is included in this model and a hypothetical pressure sensor at the bottom of the column would measure constantly 0 Pa as indicated in Fig. II.14.

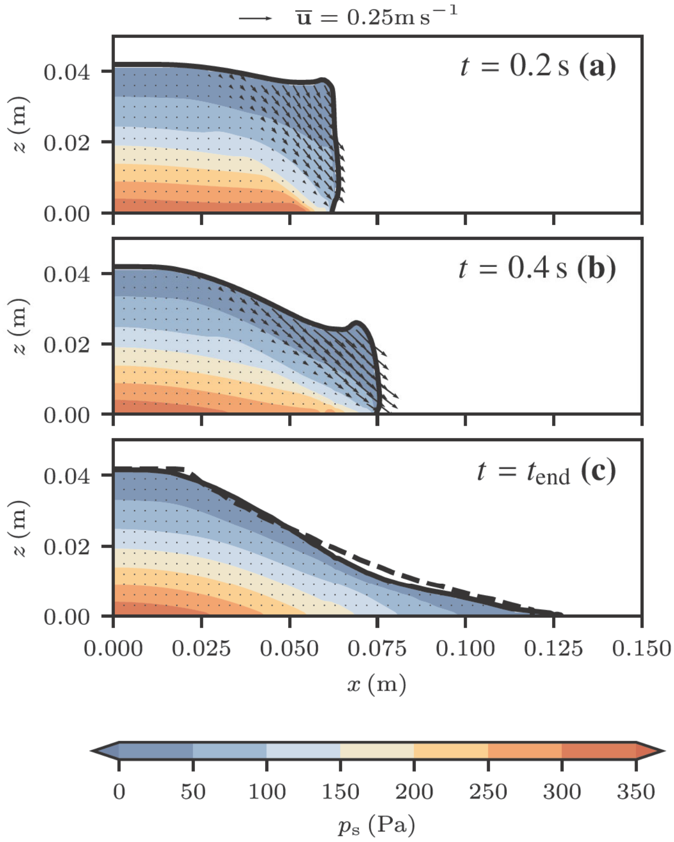

Figure II.11: Effective pressure at $t = 0.2\,\mathrm{s}$ (a), $t = 0.4\,\mathrm{s}$ (b) and $t = 1.0\,\mathrm{s}$ (c) in the two-component model (subaquatic dense case). The black arrows represent the velocity. The continuous black line shows the free surface of the slide ($\alpha_{\mathrm{s}} = 0.5$), the dashed black line shows the final experimental pile shape of Rondon *et al.* (2011).

II.4.2 Two-component model - loose case

The two-component model provides only a few and ineffective possibilities to consider variations of the packing density. To simulate the loose granular collapse with this model, the average packing density is changed to $\overline{\phi} = 0.55$ and the bulk density correspondingly to $\rho_\mathrm{s} = 1825\,\mathrm{kg\,m^3}$. Further, the initial column geometry is changed as reported by Rondon *et al.* (2011). All other parameters match the dense case. Changing rheology parameters, e.g. μ_1 or μ_2 (as e.g. Wang *et al.*, 2017) is technically possible but does not help in understanding the physical process or the influence of packing density.

The difference to the dense simulation is very small and thus not shown in here (see, e.g. Bouchut *et al.*, 2017, for similar results). As before, the final pile shape is close to the dense experiment while the simulated velocity is close to the loose experiment. The runout is slightly longer as in the dense simulation because the loose column is slightly taller.

II.4.3 Two-phase model - dense case

The two-phase model allows us to explicitly consider variations in the initial packing density. The dense case is initialized with a homogeneous packing density of 0.60. The evolution of the dense granular column as simulated with the two-phase model is shown in Fig. II.12, alongside three states of the experiment at $t = 3\,\mathrm{s}$, $6\,\mathrm{s}$ and $30\,\mathrm{s}$. The simulation covering a duration of $10\,\mathrm{s}$, took $240\,\mathrm{h}$ on 8 cores of LEO4. The dense case is dominated by negative excess pore pressure (Fig. II.12a-e), meaning that pore pressure within the slide is lower than outside. The effective pressure (Fig. II.12f-j) is respectively higher, which increases the shear strength of the column. Initially, the shear strength is high enough to delay the collapse and to keep the column mostly stable. The pore pressure gradient leads to the suction of fluid into the column (Fig. II.12g-h) and the granular material is dilating. Dilation reduces the effective pressure and allows the column to collapse. This happens first near the free surface on the unsupported side of the column, leading to a breaching-like flow of grains (Fig. II.12g-h). Grains mix with fluid at the breaching edge, reducing packing density, effective pressure, and thus friction to very low values. The resulting mixture behaves like a small turbidity current and reaches long run-outs with shallow slopes, as visible in Fig. II.12i-j. The zone of low particle pressure extends towards the centre of the column with time and further mobilisation occurs. At $t = 0.5\,\mathrm{s}$, we can see the formation of a shear band. The grains above the shear band slide off, first as a triangular cohesive block (note the uniform velocity field in Fig. II.12b), which disintegrates between $t = 1\,\mathrm{s}$ and $t = 3\,\mathrm{s}$ (Fig. II.12i). The overall process is finished (i.e. t_end) in the simulation after roughly $10\,\mathrm{s}$, while the experiment took about $30\,\mathrm{s}$. The final pile form and the failure mechanism match the experiment very well, which can be seen best in a comparison with the videos provided by Rondon *et al.* (2011), see Fig. II.15. Further, a good match with the measured excess pore pressure is achieved, as shown in Fig. II.14. The time scale and velocity of the collapse, on the other hand, differ substantially between simulation and experiment. Notably, pore pressure p and effective pressure p_s do not sum up to the total vertical load, as a considerable fraction of the vertical load is transferred to the ground by viscous stresses.

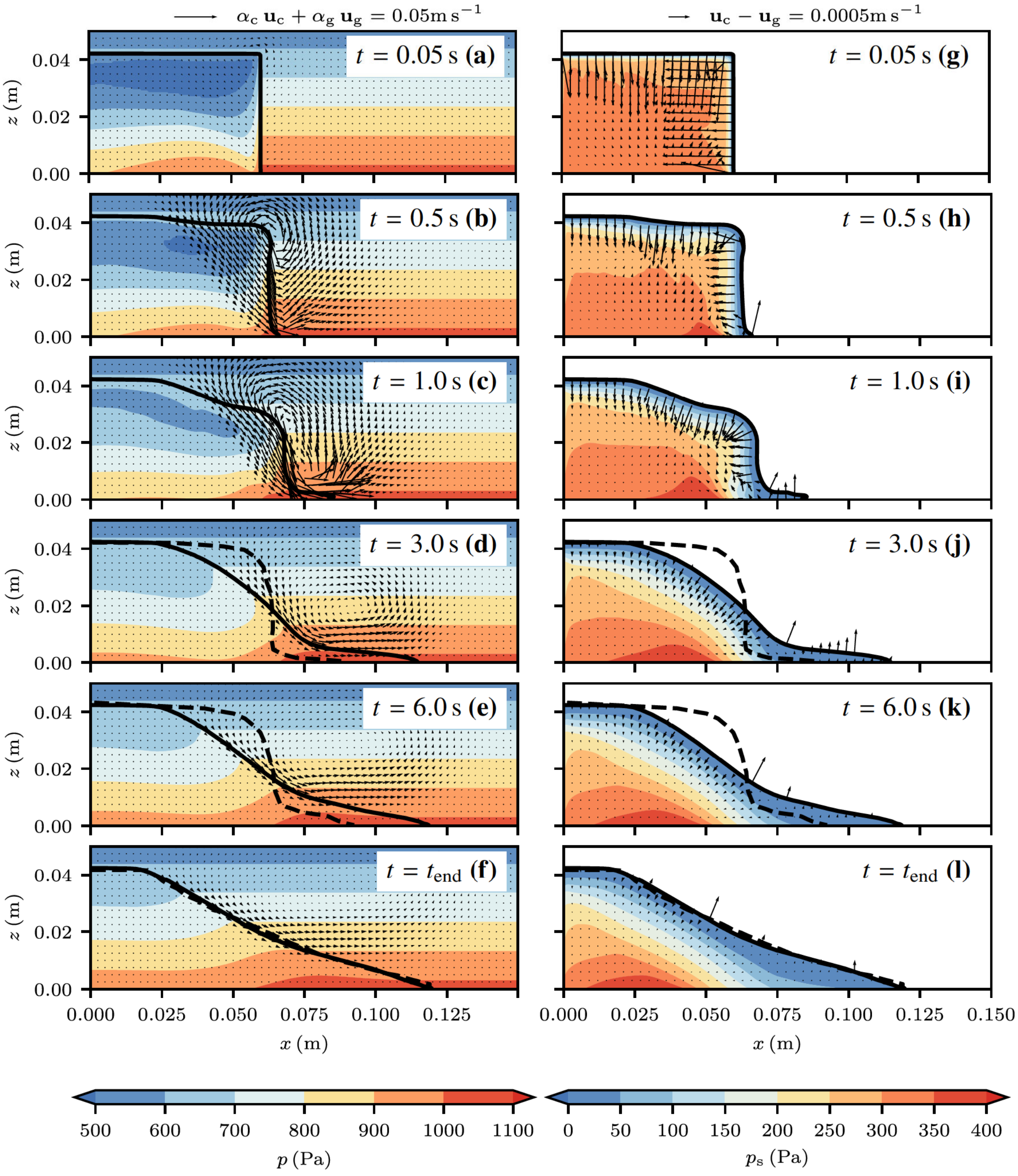

Figure II.12: Pore pressure (a-f) and effective pressure (g-l) at $t = 0.05\,\mathrm{s}$ (a, g), $t = 0.5\,\mathrm{s}$ (b, h), $t = 1\,\mathrm{s}$ (c, i), $t = 3\,\mathrm{s}$ (d, j), $t = 6\,\mathrm{s}$ (e, k) and the final state (f,l) using the two-phase model (subaquatic dense case). The black arrows represent the average velocity (a-f) and the relative velocity (g-l). The final state (t_{end}) is reached at $t = 10\,\mathrm{s}$ in the simulation (small velocities remain) but $t = 30\,\mathrm{s}$ in the experiment. The black line shows the free surface of the slide, assumed at $\phi_s = 0.25$. The free surface of the experiment is shown for comparison as a black dashed line.

II.4.4 Two-phase model - loose case

The simulation of the loose granular column uses the same parameters as the dense simulation. The packing density in the column is initialized homogeneously to $\phi = 0.55$ and its height is increased as reported by Rondon *et al.* (2011). The simulation covering a duration of 6 s took 213 h on 8 cores of LEO4. As a result of the very loose packing, the effective shear strength is low and the column collapses rapidly and entirely, without any static regions. The pore pressure has to support the majority of the weight and is respectively high (Fig. II.13a). The effective pressure increases at the rapidly flowing front, at $t = 0.25\,\mathrm{s}$ (Fig. II.13g) due to the dynamic increase of effective pressure following the $\phi(J)$-theory. The increase in effective pressure leads to a proportional increase in friction and the front is slowed down, Fig. II.13h-i. Although the effective pressure is low in comparison to the dense case (four times lower), the friction is sufficient to bring the slide to a stop. The final slope inclination is shallow and the low quasi-static particle pressure is sufficient to support the slope, Fig. II.13j. The packing density increases slightly during the collapse but the stability is mostly gained by reducing the slope inclination. The final pile shape matches the experiment very well, only a small amount of granular material forms a turbidity current that exceeds the runout of the experiment. The simulated velocity is higher than in the experiment but the difference is less severe than in the dense case. The simulated excess pore pressure differs remarkably from the measured excess pore pressure as shown in Fig. II.14. Two stages can be observed in the simulated excess pore pressure history. First, the simulation shows a high peak of excess pore pressure, exceeding the highest experimental pore pressure by a factor of two. The peak dissipates quickly, as the slide and thus overburden pressure leave the region where the pore pressure sensor is installed. This first peak is not appearing in the experiment, where the highest pore pressure is reached in a flatter peak at a later point in time. In a second phase, starting at $t = 1\,\mathrm{s}$, the pore pressure dissipates much slower. In this phase, the pore pressure dissipation is driven by compaction of the granular material and slightly underestimated by the model.

II.4.5 Discussion and comparison

The subaqueous granular collapse clearly exceeds the capabilities of the two-component model. The high sensitivity to the initial packing density can not be explained with this model and the loose and dense simulation are virtually similar. Results of the two-component model lie between the two extreme cases of the loose and dense experiment, matching the velocity of the loose and the run-out of the dense experiment. This is reasonable, considering that the missing excess pore pressure is stabilizing the dense column and destabilizing the loose column. This model is not sufficient for a practical application, as the runout is substantially underestimated in the loose case. Extremely long run-outs on slopes with 2° inclination have been observed in nature (e.g. Bryn *et al.*, 2005) and they can not be explained with a granular two-component model.

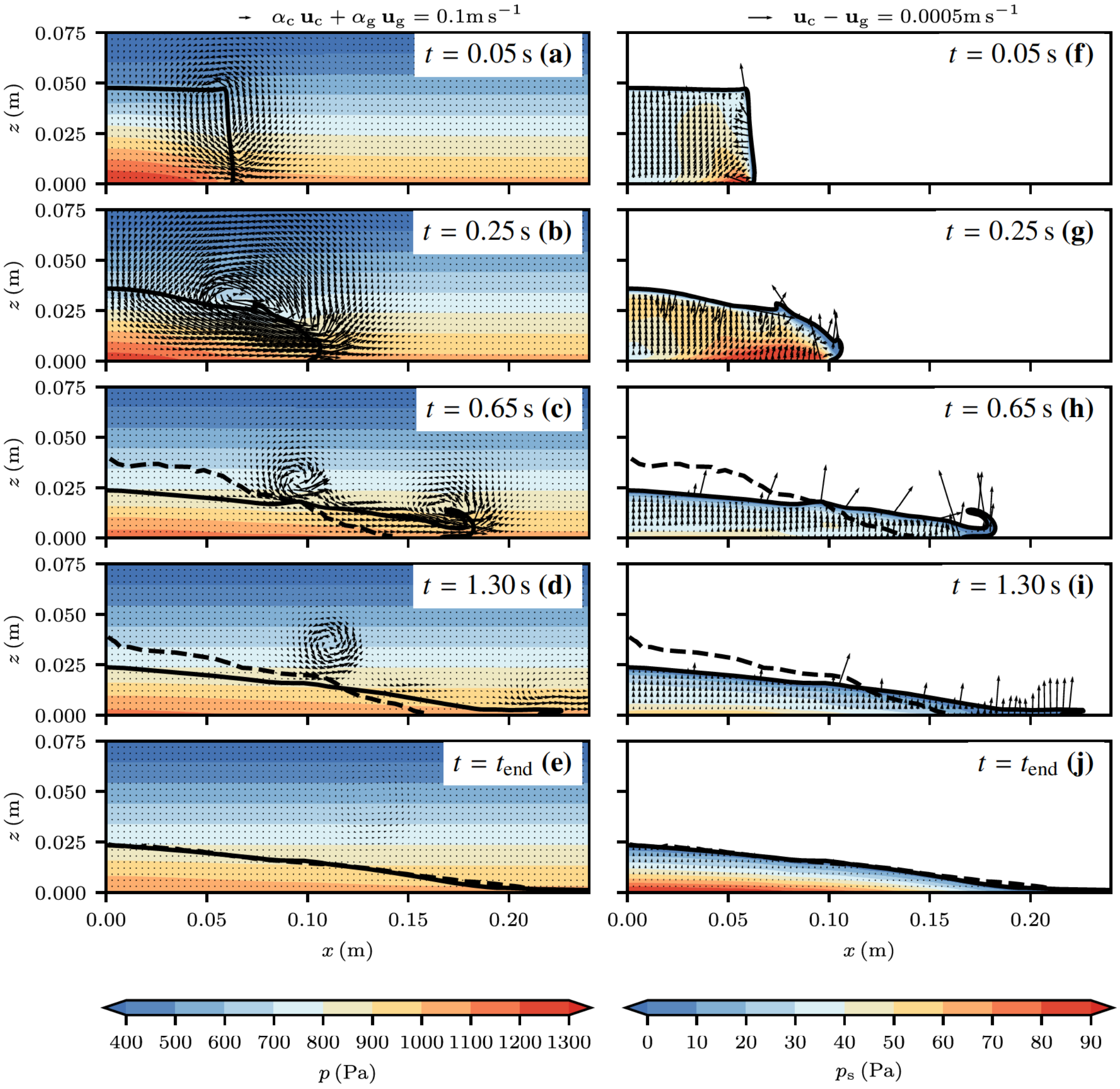

Figure II.13: Pore pressure (a-e) and effective pressure (f-j) at $t = 0.05\,\mathrm{s}$ (a, f), $t = 0.25\,\mathrm{s}$ (b, g) , $t = 0.65\,\mathrm{s}$ (c, h), $t = 1.30\,\mathrm{s}$ (d, i) and the final state ($t_{\mathrm{end}} = 6.0\,\mathrm{s}$) (e, j) using the two-phase model (subaquatic loose case). The black arrows represent the average velocity (a-e) and the relative velocity (f-j). The black line shows the free surface of the slide, assumed at $\phi_s = 0.25$. The free surface of the experiment is shown for comparison as a black dashed line.

The two-phase model can take advantage of its ability to capture excess pore pressure. It outperforms the two-component model by showing the correct final pile shapes (Figs II.12f and II.13e) and a consistent sensitivity to pore pressure and initial packing density (Fig. II.14). The failure mechanism of both, the dense and the loose experiment, are successfully simulated (see Fig. II.15), indicating that the two-phase model captures the most important physical phenomena. The model fails in two aspects, as the pore pressure peak in the loose case and the time scale in the dense case differ by a factor of 2 and 3, respectively.

It should be noted that no exhausting parameter fitting was required for

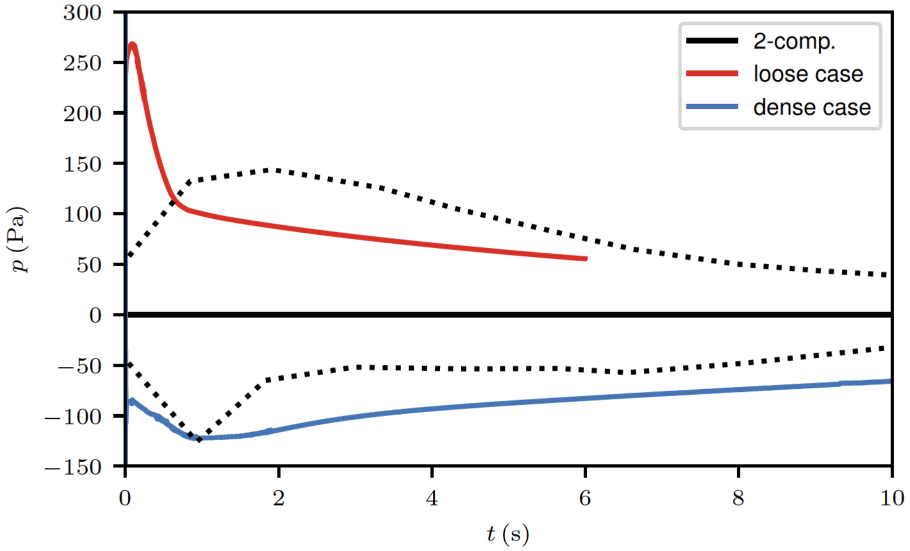

Figure II.14: The excess pore pressure as a function of time for the subaquatic granular collapses. The loose simulation (red) shows a strong peak of excess pore pressure that exceeds the experimental measurement (upper black dashed line). The dense simulation (blue) fits the experimental measurement (lower black dashed line) well. The two-component simulation forms a horizontal line at $p = 0\,\mathrm{Pa}$ as it neglects excess pore pressure.

these results. Solely the critical state line is optimized to yield the correct pore pressure, all other parameters were selected a priori following Rondon *et al.* (2011), Savage *et al.* (2014), and Boyer *et al.* (2011). Notably, some of the issues, e.g. the overestimated velocity of the loose collapse, might be resolvable with fitting parameters. Furthermore, the model allows us to simulate both cases with the same set of parameters with good accuracy. This distinguishes this work from earlier attempts (e.g. Savage *et al.*, 2014; Wang *et al.*, 2017; Si *et al.*, 2018a), where some parameters were fitted individually to the dense and loose case.

The excess pore pressure plays an important role in subaquatic experiments because it controls shear strength and friction. Dilatancy, compaction, and the dynamic particle pressure further influence friction and thus the kinematics of the slide. The dense column is only able to collapse after decreasing its packing density and thus its effective shear strength. The column is dilating until reaching the limiting packing density ϕ_m. Before this packing density is reached, the shear rate is limited to the creeping shear rate S_0. A relatively high value was used for this parameter and a lower creeping limit would be desirable, especially considering the error of the time scale in the dense simulation (see appendix II.8.5). However, strong oscillations were observed when choosing lower values for S_0 because the shear rate often exceeded S_0 before dilating sufficiently.

The bottom of the dense column is further compacting in the simulation, up to a packing density of 0.604. This is reasonable as the initial particle pressure

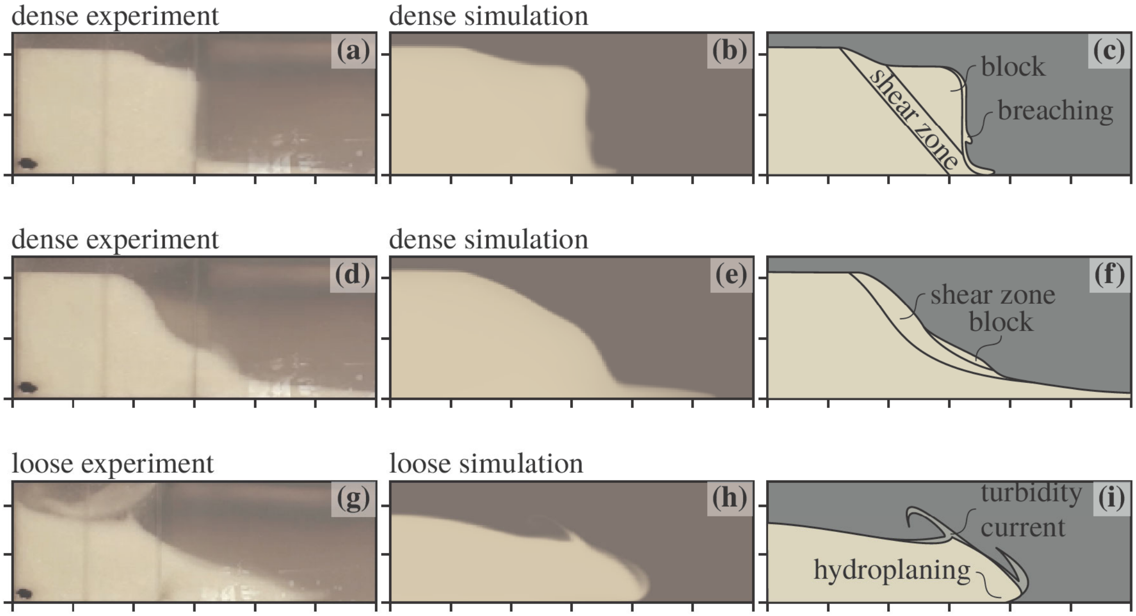

Figure II.15: Selected snapshots of the experiments from Rondon *et al.* (2011) (a,d,g), the simulations (b,e,h) and corresponding sketches (c,f,i). The distance between marks on the axes is 0.02 m. The snapshots highlight the gliding of a cohesive block and breaching (a,b,c), the remoulding of the block due to shearing (d,e,f) and the formation of hydroplaning and turbidity currents (g,h,i) at the loose front.

of 303.3 Pa at $\phi = 0.60$ is below the overburden pressure of 370.8 Pa of the pile. At the same time, negative excess pore pressure can be observed at the bottom of the column. Compaction and negative excess pore pressure seem to contradict each other at first glance. However, the negative excess pore pressure in the upper parts of the column is so strong, that fluid is flowing upwards from the bottom of the column. This can be seen in the relative velocity field (Fig. II.12h), but also the gradient of pore pressure (Fig. II.12b) indicates that pore liquid will flow upwards.

The front speed of the loose collapse is entirely controlled by the dynamic contribution of the $\mu(J)$,$\phi(J)$-rheology to effective pressure and friction. Simulations with critical state theory (constant friction coefficient μ and the quasi-static effective pressure model of Johnson and Jackson (1987)) exceed the experimental runout by far (see Appendix II.8.4). This is a strong contrast to the subaerial case where acceptable results could be achieved with critical state theory.

The dynamic contribution to particle pressure and friction plays also an important role in the dense case, although this pile collapses very slow. The thin layers of grains that are breaching from the unsupported column flank reach packing densities far below $\phi_{\mathrm{rlp}} = 0.53$ due to mixing with the ambient fluid. At this packing density, the quasi-static contribution to effective pressure vanishes, and the runout of these particles is entirely controlled by dynamic particle pressure and friction. The runout of the breaching flank could not be controlled in simulations with critical state theory (see appendix II.8.4).

The pore pressure in the loose case differs qualitatively and quantitatively from the measurement. Within the applied model, it seems reasonable that a high initial peak decreases quickly, as substantial amounts of grains and thus overburden pressure leave the region of the pressure sensor. Similar results with an early, short, and strong peak and a slow further dissipation, close to the measurement, have been obtained with other frameworks, e.g. by Bouchut *et al.* (2017) or Baumgarten and Kamrin (2019).

The dilatancy of the dense column is substantially faster in the numerical model than in the experiment, although the permeability is underestimated following the comparison of the pore pressure. Therefore it is unlikely that permeability is the cause for this discrepancy and we assume that inaccuracies in the rheology are responsible. The $\mu(J)$,$\phi(J)$-rheology describes the steady shearing of a fluid-grain mixture very well (Boyer *et al.*, 2011). However, the transient transition towards the steady packing density at a certain effective pressure is not described. This transition depends on the permeability of the granular material but also on its viscosity (shear and bulk viscosity). As mentioned before, the high value for the creeping shear rate S_0 could be responsible for this issue but it might also be related to the missing bulk viscosity or a mismatch of constitutive parameters. Bulk viscosity could delay the dilatancy in the early stage of the dense collapse, bringing the time scale of the collapse in the simulation closer to the experiment. Bulk viscosity could further help to decrease the pore pressure peak in the loose case, as some of the pore pressure could be transformed into viscous pressure. Schaeffer *et al.* (2019) suggests a form for the bulk viscosity which has the potential to improve these aspects.

Savage *et al.* (2014) and Si *et al.* (2018a) include a cohesive shear strength into their model to correct some of these problems and to fit results to the experiment. However, there is no evidence for cohesive forces in a fully submerged granular flow. Neither electrostatic forces nor cementing have been reported by Rondon *et al.* (2011). Apparent cohesion can be traced back to negative excess pore pressure, which is directly simulated by the numerical model. Notably, Si *et al.* (2018a) are able to control the slide velocity very well. However, this is achieved by fitting the cohesion to the respective case and by a strong overestimation of the negative excess pore pressure, reaching values around $500\,\mathrm{Pa}$ at the pressure sensor at $t = 3\,\mathrm{s}$ (see Fig. 5 by Si *et al.*, 2018a).

Baumgarten and Kamrin (2019) applied a similar model (elasto-plastic multiphase model with $\mu(K)$,$\phi(K)$-scaling) to the same cases. The results show similar problems, i.e. an overestimation of the pore pressure in the loose case and an overestimation of the collapse velocity in the dense case. Notably, we achieve similar results in these test cases with a substantially simpler model.

II.5 Conclusions

The Navier–Stokes Equations can be an adequate tool for accurate simulations of granular flows when they are complemented with the correct rheologies. Substantial progress has been made in recent years with the $\mu(I)$-rheology and its extensions to compressible flows and low Stokes number flows. The incompressible $\mu(I)$-rheology fits well into the multi-component framework of OpenFOAM and the compressible $\mu(I)$,$\phi(I)$-rheology fits well into the multi-phase framework, as previously shown by e.g. Chauchat *et al.* (2017). We apply, for the first time, the compressible $\mu(I)$,$\phi(I)$-rheology to granular collapses and avalanching flows. The superposition with the critical state theory is imperative to get realistic packing densities at rest and a stable solver. For subaerial, i.e. high Stokes number flows, dilatancy plays a minor role and results of the compressible model are similar to the incompressible model. However, the dilatancy predicted by the compressible model is able to close the gap between the experiments and the incompressible model. Further, the compressible model should be well-posed (Barker *et al.*, 2017; Heyman *et al.*, 2017; Schaeffer *et al.*, 2019), in contrast to many incompressible granular flow models (Barker *et al.*, 2015). Note that bulk viscosity, which is imperative for a well-posed rheology (e.g. Schaeffer *et al.*, 2019), was not considered in this study. However, the coupling of the granular phase to the pore fluid has a similar effect as bulk viscosity and might be able to restore a well-posed system. For a guaranteed well-posed compressible rheology that collapses to the $\mu(I)$,$\phi(I)$-rheology in steady state, the reader is referred to Schaeffer *et al.* (2019).

The upsides of the compressible two-phase model come at the cost of more parameters and a stronger mesh dependence. Furthermore, code and case setup are more complicated with the two-phase model and simulations are more prone to failure if initial conditions or parameters are not well suited for the case. Therefore, the incompressible model might be better suited for some flows at high Stokes numbers, especially considering regularized rheologies that are well-posed for a wide range of flow regimes (e.g Barker and Gray, 2017). Notably, we did not encounter any problems with the partial ill-posedness of the $\mu(I)$-rheology, which could be related to relatively coarse grids, high numerical diffusion, the short simulation duration or the truncation of the viscosity.

The extension to low Stokes number flows is made possible by the $\mu(J)$,$\phi(J)$-rheology. At low Stokes numbers, it is imperative to consider excess pore pressure and a two-phase model is required. Therefore, the incompressible $\mu(J)$-rheology is rather impractical and becomes only applicable after supplementing it with the $\phi(J)$-curve to the compressible $\mu(J)$,$\phi(J)$-rheology. The dynamic growth of pressure and friction is substantial for accurate results, highlighting the value of the $\mu(J)$,$\phi(J)$-rheology. The fitting of parameters was reduced to a minimum and only the critical state line had to be optimized to the experiments. It should be noted that these parameters could be determined by measuring the critical packing density at a few pressure levels, making the simulations free of any fitted parameter. The compressible two-phase model reacts sensitive to the packing density, recreating the final runout, pile shape, and failure mechanism of the experiments very well. The model still lacks in some aspects, e.g. the time scale and the velocity of the dense collapse and the pore pressure peak in the loose collapse.

It was shown that the incompressible two-component model can be derived from the compressible two-phase model by neglecting the relative velocity between phases. This simplification yields reasonable results for subaerial granular flows at high Stokes numbers but fails to describe the subaquatic granular flows at low Stokes numbers. This seems to be contradictory, as the relative velocity (which was neglected in the incompressible model) is very small in the subaquatic case (see Figs. II.12 and II.13) but considerable high in the subaerial case (see Fig. II.9). This apparent paradox can be resolved by the fact that unhindered density changes have no notable influence on the flow dynamics. However, if changes in packing density are constrained, pore pressure will build up and the rheology of the material will change drastically. Thus, pore pressure, rather than compressibility is the key factor that allows the two-phase model to accurately capture the flow mechanics. The two-phase model provides many other upsides aside from the inclusion of pore pressure. The continuous transition from dense granular material to pure ambient fluid should be useful for the simulation of granular free streams (Viroulet *et al.*, 2017), turbidity currents (Heerema *et al.*, 2020) and powder snow avalanches (e.g. Sovilla *et al.*, 2015). Other studies showed that the two-phase model is useful for sediment transport (Chauchat *et al.*, 2017) and other dilute particle-fluid mixtures (e.g. Passalacqua and Fox, 2011).

OpenFOAM provides a good platform to evaluate concepts (e.g. the multi-component and multi-phase methodology) and models (e.g. $\mu(I)$,$\phi(I)$ and $\mu(J)$,$\phi(J)$-rheologies). The implemented rheologies can be further coupled with segregation (Barker *et al.*, 2021) or tsunami simulations (e.g. Si *et al.*, 2018b). However, the segregated semi-implicit solver strategy of OpenFOAM sets limits to models and execution velocity, as (part of the) viscous terms and the particle pressure are included explicitly. This showed to be problematic and a fully implicit solver, that solves all equations simultaneously, might be superior in this regard.

The model can help to understand the extreme outruns of submarine landslides, such as the Storegga landslide (e.g. Bryn *et al.*, 2005) and the big variation in tsunamigenic potentials (e.g. Løvholt *et al.*, 2017). Theories, such as hydroplaning and remoulding (e.g. De Blasio *et al.*, 2004) can be quantitatively described by the critical state theory and its dynamic extension in form of the $\mu(J)$,$\phi(J)$-rheology. Hydroplaning, formerly described as the flowing of sediment on a thin layer of liquid can be interpreted as a region of low or even zero packing density and vanishing effective pressure. This can be observed in Fig. II.15g-i, where the front of the loose slide is lifted by pressure in the surrounding fluid. Remoulding can similarly be explained with critical state theory as an overconsolidated sample that is dilating during shearing (see Fig. II.15a-f). The two-phase model and its capability to describe various and realistic failure mechanisms with different time scales are particularly valuable for understanding the tsunamigenic potential of submarine landslides and the respective slopes.

The dense column collapses very slowly, reaching velocities of up to $0.1\,\mathrm{m\,s^{-1}}$ in small layers near the surface. The loose column collapses entirely with velocities up to $0.4\,\mathrm{m\,s^{-1}}$. The tsunamigenic potential of a landslide scales with initial acceleration and the mobilized volume (e.g. Løvholt *et al.*, 2017) and a substantial difference in tsunamigenic potential follows for the dense and the loose slide. This shows that packing density, excess pore pressure and permeability are key parameters in controlling stability, failure mechanism, slide acceleration, and tsunamigenic potential.

Many full-scale subaquatic landslide simulations are based on Bingham fluids, a visco-plastic rheology independent of the pressure (e.g. Kim *et al.*, 2019). This seems to stand in strong contradiction to the model applied here. However, the simulation of the loose case shows that packing density changes are small. For a nearly constant packing density, the effective pressure decouples from overburden pressure because the weight is absorbed entirely by pore pressure. As a consequence, overburden pressure and friction will decouple and the microscopic granular friction will appear as cohesion on a macroscopic scale. The macroscopic description as a Bingham fluid is therefore surprisingly consistent with the findings in this work, especially for fine grained marine sediments with low permeabilities.

II.6 Summary

This work highlights a path to extend the incompressible $\mu(I)$-rheology for subaerial granular flows to the compressible $\mu(J)$,$\phi(J)$-rheology for subaquatic granular flows. The implementation of the $\mu(I)$,$\phi(I)$-rheology in a multiphase framework and the $\mu(I)$-rheology in a multi-component framework allows us to conduct subaerial granular collapses with two different models. The application shows consistency between the incompressible $\mu(I)$-rheology (e.g. Lagrée *et al.*, 2011) and the compressible $\mu(I)$,$\phi(I)$-rheology. Notably, substantial modifications to the $\phi(I)$-curve are required for a practical application of the rheology. The simulations show that compressibility and dilatancy have a small influence on high Stokes number flows because excess pore pressure is negligibly small.

The implementation of the $\mu(J)$,$\phi(J)$-rheology extends possible applications to low Stokes number flows, e.g. subaquatic granular collapses. The incompressible model reaches its limitations under these conditions and the compressible model is required for an accurate simulation. Other than previous attempts, we applied the exact same set of parameters to an initially dense and loose granular collapse with satisfying results. Notably, the application of the $\mu(J)$,$\phi(J)$-rheology does not require an extensive fitting of constitutive parameters. The comparison between the compressible model and experiments uncovered discrepancies in the time scale and the pore pressure. These could be indicators for issues in the rheology, e.g. a missing bulk viscosity or issues with the creeping regime that had to be introduced for numerical stability. The well-posedness of the proposed model is not guaranteed and should be investigated in the future.

The compressible two-phase model has a wide range of applications and the results have implications on many problems in geoscience. Applications to sediment transport and scouring (Cheng *et al.*, 2017) have been shown with a similar model. We further expect the applicability to turbidity currents and all other gravitational mass flows with low and high Stokes numbers. Furthermore, Si *et al.* (2018b) showed the applicability of a similar model to landslide tsunami simulations by incorporating the free water surface.

Acknowledgements

The author gratefully acknowledges the support from Wolfgang Fellin and the research area scientific computing of the University of Innsbruck. The author thanks Gertraud Medicus, Thomas Barker, Finn Løvholt and Geir Pedersen for helpful comments and Pascale Aussillous for authorizing the use of pictures of the experiment. Further, the author thanks the editor and two referees for their helpful comments and support in publishing this work.

This project has received funding from the European Union's Horizon 2020 research and innovation programme under the Marie Skłodowska-Curie grant agreement No. 721403 (SLATE). The computational results presented have been achieved (in part) using the HPC infrastructure LEO of the University of Innsbruck.

II.7 Appendix: Derivation of the two-component model

The two-component model can be derived from the two-phase model by summing up the mass and momentum conservation equations. The sum of the mass conservation equations (II.1) and (II.3) yields

$$\frac{\partial \phi_\mathrm{c} + \phi_\mathrm{g}}{\partial t} + \boldsymbol{\nabla} \cdot \left(\phi_\mathrm{c}\, \mathbf{u}_\mathrm{c} + \phi_\mathrm{g}\, \mathbf{u}_\mathrm{g}\right) = 0 \tag{II.54}$$

and with the definitions $\phi_\mathrm{c} + \phi_\mathrm{g} = 1$ and $\overline{\mathbf{u}} = \phi_\mathrm{c}\, \mathbf{u}_\mathrm{c} + \phi_\mathrm{g}\, \mathbf{u}_\mathrm{g}$ we can derive the continuity equation of the two-component model, Eq. (II.13).

The sum of the momentum conservation equations (II.2) and (II.4) is slightly more complex and approximations are required due to non-linearities. Therefore, we will cover each term individually in the following. The sum of the time derivatives of Eqs. (II.2) and (II.4) can be simplified with the definition of the volume averaged velocity $\overline{\mathbf{u}}$, the local density $\rho = \phi_\mathrm{c}\, \rho_\mathrm{c} + \phi_\mathrm{g}\, \rho_\mathrm{g}$ and the relative velocity $\mathbf{u}_\mathrm{r} = \mathbf{u}_\mathrm{g} - \mathbf{u}_\mathrm{c}$ to

$$\begin{aligned}\frac{\partial}{\partial t}\left(\phi_\mathrm{c}\, \rho_\mathrm{c}\, \mathbf{u}_\mathrm{c} + \phi_\mathrm{g}\, \rho_\mathrm{g}\, \mathbf{u}_\mathrm{g}\right) = \frac{\partial}{\partial t}\left(\phi_\mathrm{c}\, \rho_\mathrm{c}\, \left(\overline{\mathbf{u}} - \phi_\mathrm{g} \mathbf{u}_\mathrm{r}\right) + \phi_\mathrm{g}\, \rho_\mathrm{g}\, \left(\overline{\mathbf{u}} + \phi_\mathrm{c}\, \mathbf{u}_\mathrm{r}\right)\right) = \\ \frac{\partial \rho\, \overline{\mathbf{u}}}{\partial t} + \frac{\partial}{\partial t}\left(\phi_\mathrm{g}\, \phi_\mathrm{c}\, \mathbf{u}_\mathrm{r}\, \left(\rho_\mathrm{g} - \rho_\mathrm{c}\right)\right) \approx \frac{\partial \rho\, \overline{\mathbf{u}}}{\partial t}.\end{aligned} \tag{II.55}$$

The second term in Eq. (II.55) vanishes if the relative velocity is zero or if the phase densities are equal. The two-component model assumes that phase velocities are equal (Eq. II.11) and the second term can be neglected. The error in the momentum conservation is expected to be small in relation to limitations of the incompressible rheology.

The sum of the convective fluxes follows a similar pattern,

$$\begin{aligned}
&\boldsymbol{\nabla}\cdot(\phi_\mathrm{c}\,\rho_\mathrm{c}\,\mathbf{u}_\mathrm{c}\otimes\mathbf{u}_\mathrm{c}+\phi_\mathrm{g}\,\rho_\mathrm{g}\,\mathbf{u}_\mathrm{g}\otimes\mathbf{u}_\mathrm{g})=\\
&\boldsymbol{\nabla}\cdot(\phi_\mathrm{c}\,\rho_\mathrm{c}\,(\overline{\mathbf{u}}-\phi_\mathrm{g}\,\mathbf{u}_\mathrm{r})\otimes(\overline{\mathbf{u}}-\phi_\mathrm{g}\,\mathbf{u}_\mathrm{r})+\phi_\mathrm{g}\,\rho_\mathrm{g}\,(\overline{\mathbf{u}}+\phi_\mathrm{c}\,\mathbf{u}_\mathrm{r})\otimes(\overline{\mathbf{u}}+\phi_\mathrm{c}\,\mathbf{u}_\mathrm{r}))=\\
&\boldsymbol{\nabla}\cdot(\rho\,\overline{\mathbf{u}}\otimes\overline{\mathbf{u}})+\boldsymbol{\nabla}\cdot(\phi_\mathrm{c}\,\phi_\mathrm{g}\,(\overline{\mathbf{u}}\otimes\mathbf{u}_\mathrm{r}+\mathbf{u}_\mathrm{r}\otimes\overline{\mathbf{u}})\,(\rho_\mathrm{g}-\rho_\mathrm{c}))+\\
&\boldsymbol{\nabla}\cdot(\phi_\mathrm{c}\,\phi_\mathrm{g}\,\mathbf{u}_\mathrm{r}\otimes\mathbf{u}_\mathrm{r}\,(\phi_\mathrm{g}\,\rho_\mathrm{c}+\phi_\mathrm{c}\,\rho_\mathrm{g}))\approx\boldsymbol{\nabla}\cdot(\rho\,\overline{\mathbf{u}}\otimes\overline{\mathbf{u}})\,.
\end{aligned}\tag{II.56}$$

The second and third term vanish if the relative velocity is zero. Notably, only the second term vanishes if the phase densities are equal due to the non-linearity in the convection term. For the approximation of the two-component model, it is sufficient to recover the first term, as the relative velocity is neglected.

The terms on the left hand side of Eqs. (II.2) and (II.4), can be summed up without further assumptions,

$$\boldsymbol{\nabla}\cdot(\phi_\mathrm{c}\,\mathbf{T}_\mathrm{c}+\phi_\mathrm{g}\,\mathbf{T}_\mathrm{g})=\boldsymbol{\nabla}\cdot\mathbf{T},\tag{II.57}$$

$$\phi_\mathrm{c}\,\boldsymbol{\nabla}\,p+\phi_\mathrm{g}\,\boldsymbol{\nabla}\,p+\boldsymbol{\nabla}\,p_\mathrm{s}=\boldsymbol{\nabla}p_\mathrm{tot},\tag{II.58}$$

$$\phi_\mathrm{c}\,\rho_\mathrm{c}\,\mathbf{g}+\phi_\mathrm{g}\,\rho_\mathrm{g}\,\mathbf{g}=\rho\,\mathbf{g},\tag{II.59}$$

$$k_\mathrm{gc}\,(\mathbf{u}_\mathrm{g}-\mathbf{u}_\mathrm{c})+k_\mathrm{gc}\,(\mathbf{u}_\mathrm{c}-\mathbf{u}_\mathrm{g})=0,\tag{II.60}$$

and the momentum-conservation equation of the two-component model, Eq. (II.12) can be assembled.

II.8 Appendix: Sensitivity study

The numerical models require a wide range of parameters. Most parameters are physical and can be derived from experiments and literature. However, some parameters are purely numerical and their values can not be derived from experiments. The following parameter study was used to derive numerical parameters that have been applied in simulations. The most influential numerical parameters are the grid size Δx, the maximum Courant number $\mathrm{CFL}^\mathrm{diff}$, related to the time step Δt, and the maximum viscosity ν_max. Furthermore, the effect of dynamic friction, i.e. the difference between a constant friction coefficient μ and the $\mu(I)$ or $\mu(J)$-rheology is investigated. The applied model and the flow regime (subaerial or subaquatic, dense or loose) are shown for each figure in the upper left edge.

II.8.1 Influence of the maximum viscosity

The maximum viscosity is one of the most influential numerical parameters in the applied model. It should be reasonably high to mimic solid behaviour, but as small as possible to improve numerical stability and to keep computational expense low. A reasonable limit can be found by investigating the dimensionless governing equations, in which the respective scales are isolated. The momentum conservation of the Navier–Stokes Equations can be written as

$$\frac{\partial \mathbf{u}}{\partial t} + \boldsymbol{\nabla} \cdot (\mathbf{u} \otimes \mathbf{u}) = -\frac{1}{\rho} \boldsymbol{\nabla} p + \frac{1}{2} \nu \boldsymbol{\nabla}^2 \mathbf{u} + \mathbf{g} \tag{II.61}$$

for a single incompressible Newtonian fluid with density ρ and constant viscosity ν. By scaling space with the height of the slide H, the velocity with the respective free fall velocity $\sqrt{|\mathbf{g}|\, H}$, the time with the free fall time $\sqrt{H/|\mathbf{g}|}$, and the pressure with the respective hydrostatic pressure $\rho\, |\mathbf{g}|\, H$, the dimensionless variables (marked with a hat) can be established as

$$\mathbf{x} = H\, \hat{\mathbf{x}}, \tag{II.62}$$

$$\boldsymbol{\nabla} = \frac{1}{H} \hat{\boldsymbol{\nabla}} = \frac{1}{H} \left(\frac{\partial}{\partial \hat{\mathbf{x}}}, \frac{\partial}{\partial \hat{\mathbf{y}}}, \frac{\partial}{\partial \hat{\mathbf{z}}} \right)^T, \tag{II.63}$$

$$\mathbf{u} = \sqrt{|\mathbf{g}|\, H}\, \hat{\mathbf{u}}, \tag{II.64}$$

$$t = \sqrt{\frac{H}{|\mathbf{g}|}}\, \hat{t}, \tag{II.65}$$

$$p = \rho\, |\mathbf{g}|\, H\, \hat{p}. \tag{II.66}$$

Introducing the dimensionless variables into the momentum conservation equation and dividing by $|\mathbf{g}|$ yields

$$\frac{\partial \hat{\mathbf{u}}}{\partial \hat{t}} + \hat{\boldsymbol{\nabla}} \cdot (\hat{\mathbf{u}} \otimes \hat{\mathbf{u}}) = -\hat{\boldsymbol{\nabla}}\, \hat{p} + \sqrt{\frac{1}{|\mathbf{g}|\, H^3}} \nu\, \hat{\boldsymbol{\nabla}}^2\, \hat{\mathbf{u}} + \frac{\mathbf{g}}{|\mathbf{g}|}. \tag{II.67}$$

In the case of a solid-like behaviour, the viscous term should be dominating over all other terms. All terms, except for the viscous term, are of order one and we can deduce that the inequality

$$\sqrt{\frac{1}{|\mathbf{g}|\, H^3}} \nu_{\max} > \frac{1}{\varepsilon} \tag{II.68}$$

should be fulfilled to simulate the behaviour of a solid. ε is a small dimensionless number, indicating the magnitude of viscous stresses over other terms. The viscosity which is required for a solid-like behaviour can be calculated as

$$\nu_{\max} > \frac{1}{\varepsilon} \sqrt{|\mathbf{g}|\, H^3}, \tag{II.69}$$

as a function of respective scales by choosing the magnitude of viscous stresses over other terms, ε. The required magnitude for ε can be estimated by conducting a numerical sensitivity analysis.

Variations of $\nu_{\max}$ (and thus ε) are presented in Fig. II.16 for the subaerial case at $t = 0.8\,\mathrm{s}$, using the two-component model. The value of $\nu_{\max} = 1\,\mathrm{m}^2\,\mathrm{s}^{-1}$ is adequate for this example and the left side of the pile stays nearly static as it is the case in the experiment. The respective value for the dimensionless scaling factor ε follows as 0.1 ($H = 0.1\,\mathrm{m}$, $|\mathbf{g}| \approx 10\,\mathrm{m\,s}^2$), indicating that viscous forces have to be about 10 times higher than all other contributions to the momentum conservation equation. For lower viscosities, the pile is notably deformed and shows no stable regions and no granular characteristics. Rather, the pile shows the characteristics of a visco-plastic fluid (see rheology comparisons by Lagrée *et al.*, 2011), which indicates that the viscosity threshold was dominating the simulation. Notably, cases with high maximum viscosity are stable after $t = 0.4\,\mathrm{s}$ while cases with low maximum viscosity keep flowing beyond $t = 0.8\,\mathrm{s}$. For an application of granular rheologies in OpenFOAM, we suggest a maximum viscosity following Eq. (II.28) with $\varepsilon = 1/10$.

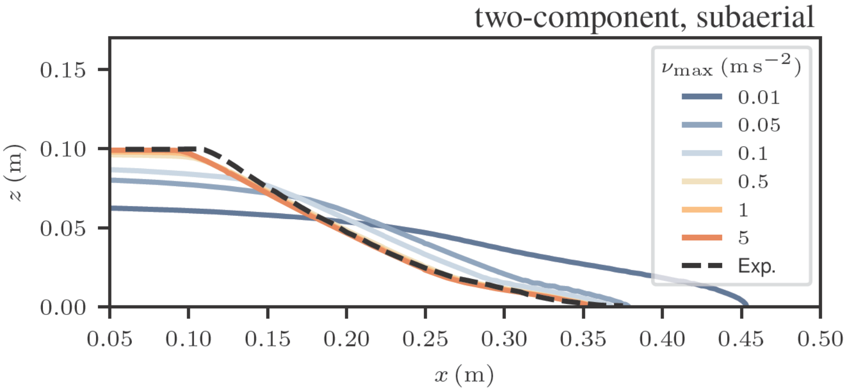

Figure II.16: Pile shape at $t = 0.8\,\mathrm{s}$ of the subaerial granular collapse with various values for $\nu_{\max}$ using the two-component model. The high influence of this numerical parameter and the unphysical effect of low values is clearly visible. The dashed black line shows the final pile shape of the experiment for comparison. The two-phase model behaves similarly.

II.8.2 Grid sensitivity

The grid sensitivity is an important issue for complex flow models and we provide a full grid sensitivity analysis for the multi-component and the multi-phase model. The grid sensitivity study for the multi-component model is solely conducted for the subaerial case because the mechanics of this model is similar in all cases. The final pile shape of the investigated case is shown in Fig. II.17 for various grid resolutions. This model reacts very robustly to coarse grids and 30 cells along the pile height are sufficient to get accurate results for the final pile shape.

The two-phase model is more complex in terms of grid sensitivity. Three different failure mechanisms of the granular column can be observed in the simulations with the two-phase model. The three mechanisms react differently to a variation of the grid resolution. In some cases, the model reacts very sensitively to coarse grids and a grid refinement study should always be performed when applying this model. Fig. II.18 shows the grid convergence analysis for the

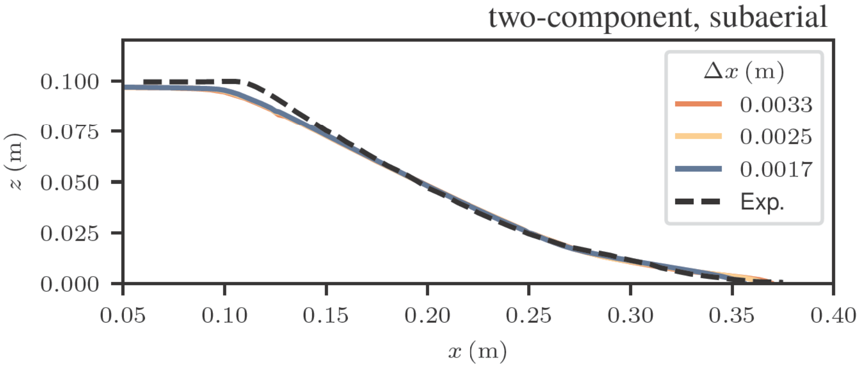

Figure II.17: Grid sensitivity of the two-component model for the subaerial case. The model behaves similarly in the subaquatic cases. The black dashed line shows the experimental final pile shape for reference.

subaerial, the subaquatic dense, and subaquatic loose case. The two-phase model is slightly more sensitive to coarse girds than the two-component model in the subaerial case, see Fig. II.18a. The problematic area is the thin flow front and the issue is probably related to the mixed role of the phase-fraction field.

The two-phase model is very sensitive to coarse grids in the subaquatic dense case, see Fig. II.18b. Breaching of a thin layer of grains on the unsupported side of the column leads to a reduced phase-fraction in cells that contain the slide surface. This reduces the effective pressure in all of those cells and further the shear strength, accelerating the collapse. The result is a mesh dependency of the final pile shape and the collapse velocity. The mesh had to be refined down to a cell size of 0.0005 m, to achieve accurate results. Notably, the difference between the smallest two cell sizes is still remarkably at the front of the collapse. An additional refinement step would be desirable, but this would have exhausted the available computational resources.

The loose subaquatic case can be simulated with good accuracy on a relatively coarse mesh as shown in Fig. II.18c. This is not surprising as the failure mechanism and flow pattern is much simpler. In particular, the effective pressure discontinuity at the free surface is weaker than in the dense case and thus requires a smaller grid resolution.

II.8.3 Time step duration sensitivity

The time step duration is investigated similarly as the grid resolution. The time step duration is not fixed but adapted to velocity ($\mathrm{CFL}^{\mathrm{conv}}$) and viscosity ($\mathrm{CFL}^{\mathrm{diff}}$), relative to the grid size. The viscous contribution to the CFL number is always much bigger in the investigated cases and the time step sensitivity study was conducted based on this value. Notably, stability can be guaranteed only for $\mathrm{CFL}^{\mathrm{diff}} < 1$. However, the $\mathrm{CFL}^{\mathrm{diff}}$ number allows only an estimation of the stability and in some cases larger time steps are possible.

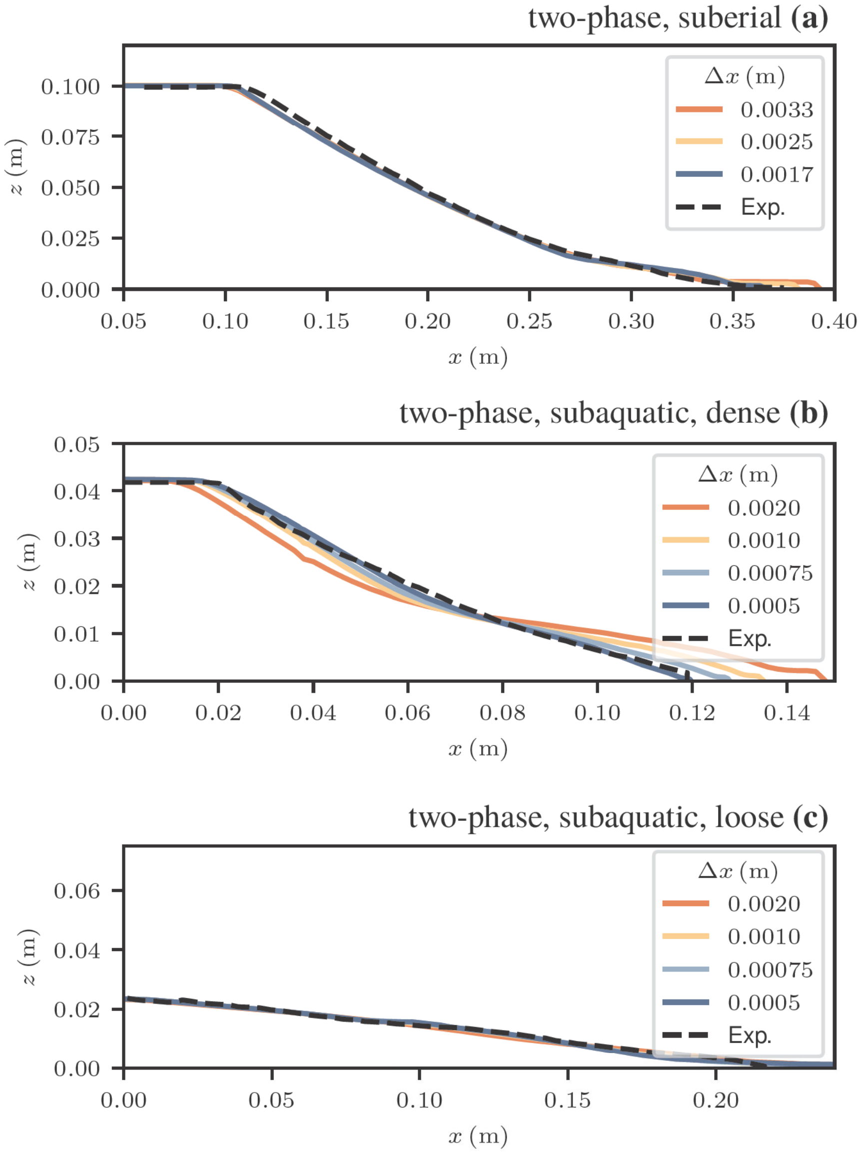

Figure II.18: Grid sensitivity of the two-phase model for the subaerial case (a), the dense subaquatic case (b) and the subaquatic loose case (c). The black dashed lines show the experimental final pile shapes for reference.

The two-component solver can operate in two modes, using a full momentum predictor step or a reduced momentum predictor step. The full momentum predictor step solves the full linearised system of the discretized momentum conservation equation. The reduced momentum predictor step calculates an explicit prediction of the velocity field based on the velocity field of the last time step. This has a substantial influence on the stability when viscous stresses are dominating.

Fig. II.19a shows the final pile shape for various time step durations and the full momentum predictor step in the two-component model. Notably oscillations in pressure can already be seen at $\mathrm{CFL}^{\mathrm{diff}} = 2$ (not shown) and they grow substantially for higher $\mathrm{CFL}^{\mathrm{diff}}$ numbers. The pressure oscillations start to influence the pile shape at $\mathrm{CFL}^{\mathrm{diff}} = 10$ and the pile is completely distorted for $\mathrm{CFL}^{\mathrm{diff}} = 100$.

The two-component model is more robust to larger time steps when operating with the reduced momentum predictor step, see Fig. II.19b. Pressure oscillations start approximately at $\mathrm{CFL}^{\mathrm{diff}} = 100$ and the first influence on the slide geometry can be observed at $\mathrm{CFL}^{\mathrm{diff}} = 1000$. Anyway, it is recommended to run the two-component model with small enough time steps to prevent pressure oscillations, ideally at $\mathrm{CFL}^{\mathrm{diff}} = 1$, as done in this work.

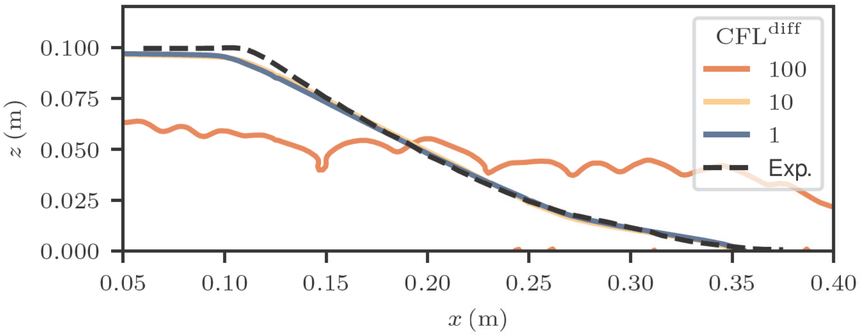
two-component, suberial, full momentum predictor **(a)**

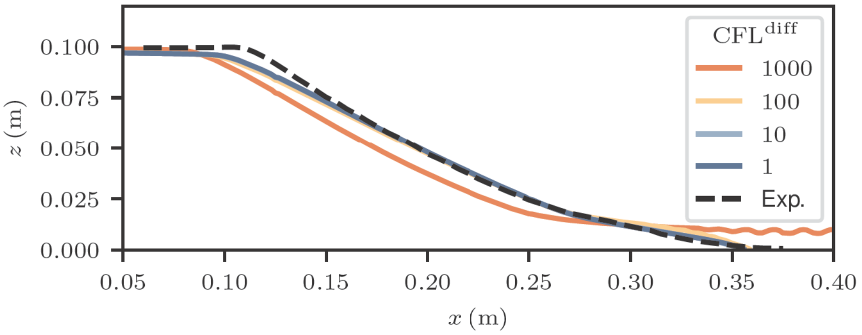
two-component, suberial, reduced momentum predictor **(b)**

Figure II.19: Sensitivity of the two-component model on the time step duration, expressed by the viscous CFL number. The solver was operated with the full momentum predictor (a) and the reduced momentum predictor (b).

The two-phase model reacts less sensitive to large time step durations. In fact, simulations were stable up to $\mathrm{CFL}^{\mathrm{diff}} = 1000$. No pressure oscillations could be observed and the final pile shape is nearly unaffected for all cases, see Fig. II.20. However, the accuracy got worse for large time step durations and we observed a slower initial acceleration for $\mathrm{CFL}^{\mathrm{diff}} = 1000$. No subaquatic simulations with the two-phase model and $\mathrm{CFL}^{\mathrm{diff}} = 1$ have been conducted, as this would have exhausted the computational resources.

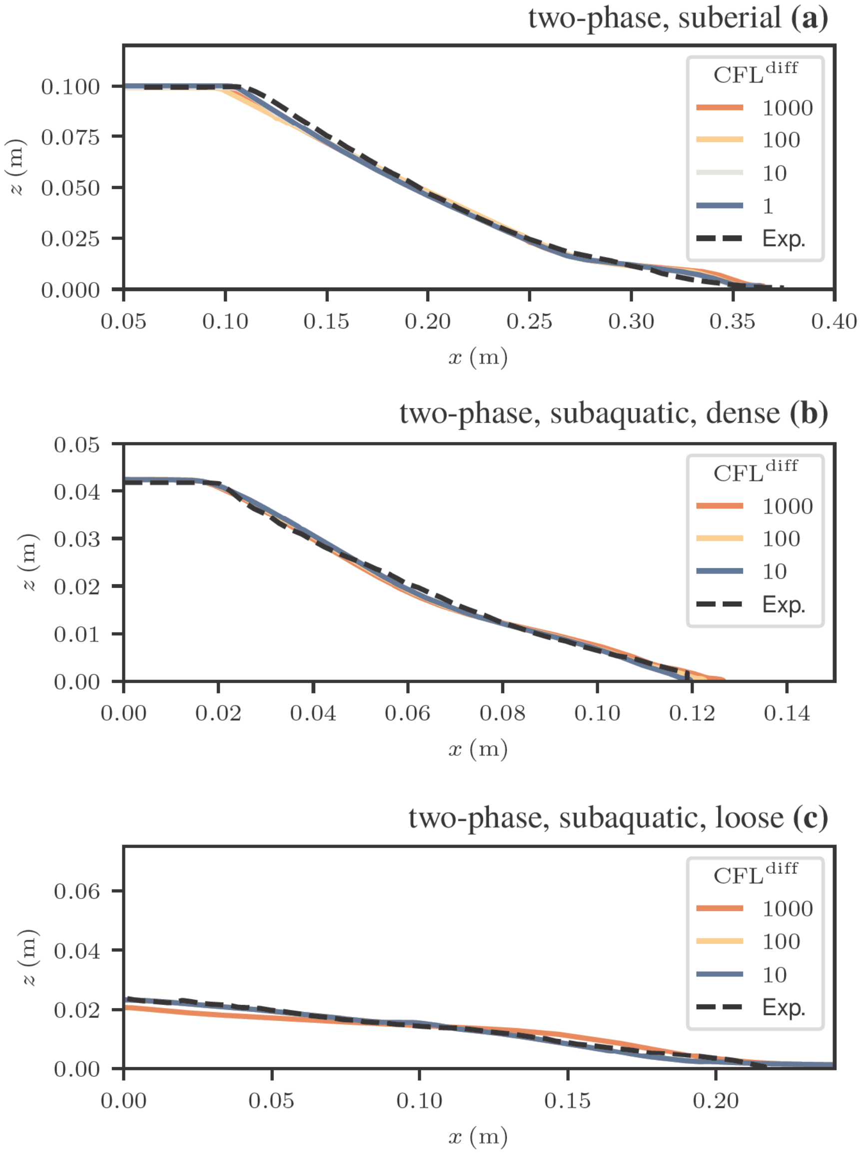

Figure II.20: Sensitivity of the two-phase model on the time step duration, expressed by the viscous CFL in the subaerial case (a), the subaquatic, dense case (b) and the subaquatic, loose case (c).

II.8.4 Influence of dynamic friction and wall friction

The effect of the dynamic increase of friction following the $\mu(I)$-rheology and the effect of the reduced wall friction were investigated with both models. Results are shown in Fig. II.21a for the two-component model and in Fig. II.21b for the two-phase model. The models do not react sensitively to the variation of the friction model and the basal friction coefficient. The runout is slightly underestimated in simulations with the $\mu(I)$-rheology on a rough surface. However, the introduction of the smooth surface elongates the runout and the simulations fit the experiment well. Simulations with a constant friction coefficient on a rough surface fit the experiment also well, simulations with constant friction coefficient on a smooth surface overestimate the runout.

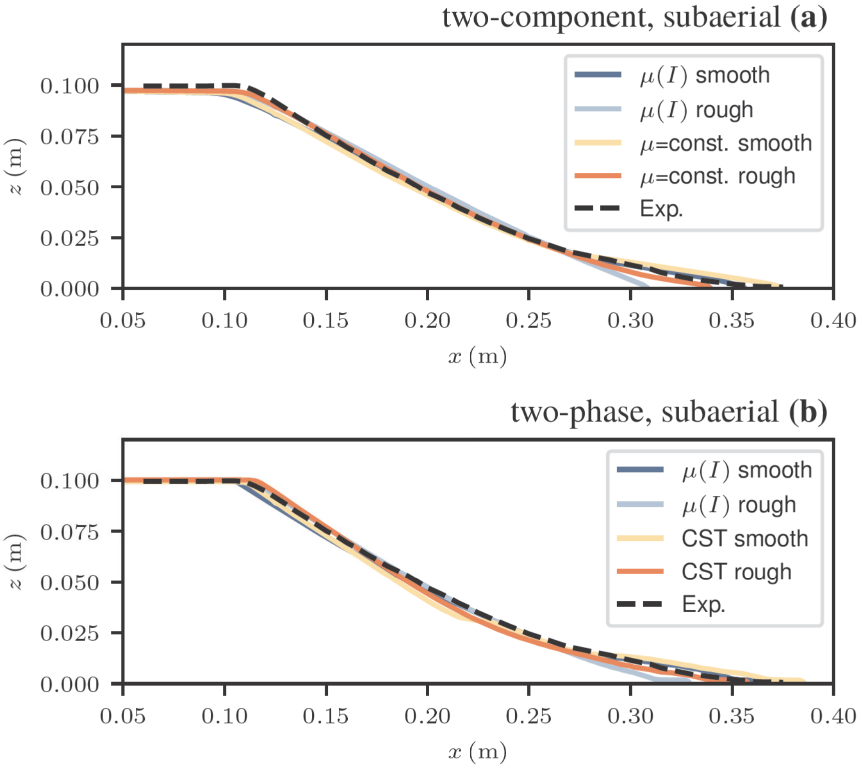

Figure II.21: Influence of dynamic friction, dynamic effective pressure and wall friction on the final pile shape in the two-component model (a) and the two-phase model (b).

The dynamic contribution to effective pressure and friction is imperative for simulations at low Stokes numbers. Fig. II.22 shows the dense and loose subaquatic two-phase simulations with critical state theory and $\mu(J)$,$\phi(J)$-theory. The outrun cannot be controlled without the dynamic contributions of the $\mu(J)$,$\phi(J)$-theory and exceeds the final runout very quickly.

II.8.5 Influence of the creep shear rate

The influence of the creep shear rate S_0 is shown in Fig. II.23 for the subaquatic dense case. This figure shows an early time step at $t = 1.0\,\mathrm{s}$ and the final pile shape at $t = 10\,\mathrm{s}$. A reduction of the creeping shear rate from $5\,\mathrm{s}^{-1}$ to $1\,\mathrm{s}^{-1}$ leads to a slower initial collapse of the column. The delayed collapse is desirable and brings the simulation closer to the experiment. However, the low value for S_0 leads to oscillations in the particle pressure because the simulation accelerates and reaches shear rates beyond S_0 too quickly. The simulation with $S_0 = 5\,\mathrm{s}^{-1}$ shows no oscillations and has thus been utilized in the main part of this work. Notably, a smaller time step duration will allow smaller values for S_0, however

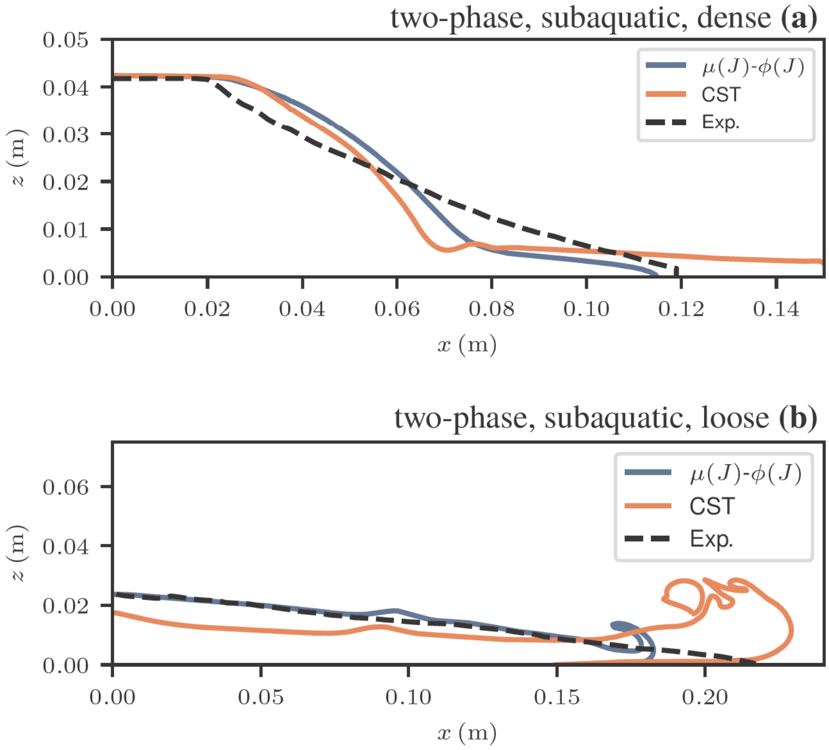

Figure II.22: The dense granular collapse at $t = 6.0\,\mathrm{s}$ (a) and the loose granular collapse at $t = 0.65\,\mathrm{s}$ (b), simulated with critical state theory and $\mu(J)$,$\phi(J)$-rheology. The dashed black line shows the final experimental pile shape. The simulations with critical state theory clearly exceed the experiment early in the simulation.

for an increased computational cost. The final pile shape is barley affected by the change in S_0.

II.9 Bibliography

N. J. Balmforth and R. R. Kerswell, “Granular collapse in two dimensions,” *Journal of Fluid Mechanics*, vol. 538, pp. 399–428, 2005, DOI: 10.1017/S0022112005005537.

T. Barker and J. M. N. T. Gray, “Partial regularisation of the incompressible μ(I)-rheology for granular flow,” *Journal of Fluid Mechanics*, vol. 828, pp. 5–32, 2017, DOI: 10.1017/jfm.2017.428.

T. Barker, M. Rauter, E. S. F. Maguire, C. G. Johnson and J. M. N. T. Gray, “Coupling rheology and segregation in granular flows,” *Journal of Fluid Mechanics*, vol. 909, p. A22, 2021, DOI: 10.1017/jfm.2020.973.

T. Barker, D. G. Schaeffer, P. Bohorquez and J. M. N. T. Gray, “Well-posed and

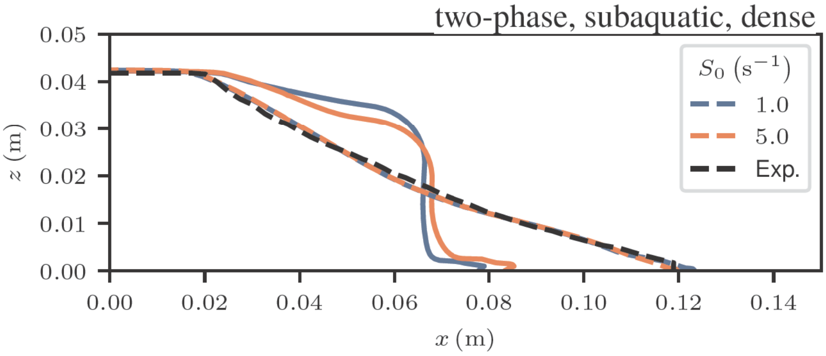

Figure II.23: Influence of the creep shear rate S_0 on the pile shape. Two time steps are shown, $t = 1\,\mathrm{s}$ (continuous) and $t = 10\,\mathrm{s}$ (dashed). The black dashed line shows the final experimental pile shape.

ill-posed behaviour of the μ(I)-rheology for granular flow," *Journal of Fluid Mechanics*, vol. 779, pp. 794–818, 2015, DOI: 10.1017/jfm.2015.412.

T. Barker, D. G. Schaeffer, M. Shearer and J. M. N. T. Gray, "Well-posed continuum equations for granular flow with compressibility and μ(I)-rheology," *Proceedings of the Royal Society A*, vol. 473, no. 2201, p. 20160846, 2017, DOI: 10.1098/rspa.2016.0846.

A. S. Baumgarten and K. Kamrin, "A general fluid–sediment mixture model and constitutive theory validated in many flow regimes," *Journal of Fluid Mechanics*, vol. 861, pp. 721–764, 2019, DOI: 10.1017/jfm.2018.914.

J. Bear, *Dynamics of fluids in porous media*, Courier Corporation, 1972.

F. Bouchut, E. D. Fernández-Nieto, E. H. Koné, A. Mangeney and G. Narbona-Reina, "A two-phase solid-fluid model for dense granular flows including dilatancy effects: comparison with submarine granular collapse experiments," in *EPJ Web of Conferences - Powders & Grains 2017*, vol. 140, p. 09039, EDP Sciences, 2017, DOI: 10.1051/epjconf/201714009039.

F. Boyer, É. Guazzelli and O. Pouliquen, "Unifying suspension and granular rheology," *Physical Review Letters*, vol. 107, no. 18, p. 188301, 2011, DOI: 10.1103/PhysRevLett.107.188301.

P. Bryn, K. Berg, C. F. Forsberg, A. Solheim and T. J. Kvalstad, "Explaining the Storegga slide," *Marine and Petroleum Geology*, vol. 22, no. 1-2, pp. 11–19, 2005, DOI: 10.1016/j.marpetgeo.2004.12.003.

J. Chauchat, Z. Cheng, T. Nagel, C. Bonamy and T.-J. Hsu, "SedFoam-2.0: a 3-D two-phase flow numerical model for sediment transport," *Geoscientific Model Development*, vol. 10, no. 12, p. 4367, 2017, DOI: 10.5194/gmd-10-4367-2017.

Z. Cheng, T.-J. Hsu and J. Calantoni, “SedFoam: A multi-dimensional Eulerian two-phase model for sediment transport and its application to momentary bed failure,” *Coastal Engineering*, vol. 119, pp. 32–50, 2017, DOI: 10.1016/j.coastaleng.2016.08.007.

F. V. De Blasio, L. Engvik, C. B. Harbitz and A. Elverhøi, “Hydroplaning and submarine debris flows,” *Journal of Geophysical Research*, vol. 109, no. C1, 2004, DOI: 10.1029/2002JC001714.

B. Domnik, S. P. Pudasaini, R. Katzenbach and S. A. Miller, “Coupling of full two-dimensional and depth-averaged models for granular flows,” *Journal of Non-Newtonian Fluid Mechanics*, vol. 201, pp. 56–68, 2013, DOI: 10.1016/j.jnnfm.2013.07.005.

D. C. Drucker and W. Prager, “Soil mechanics and plastic analysis or limit design,” *Quarterly of Applied Mathematics*, vol. 10, no. 2, pp. 157–165, 1952.

T. H. Druitt, “Pyroclastic density currents,” *Geological Society, London, Special Publications*, vol. 145, no. 1, pp. 145–182, 1998, DOI: 10.1144/GSL.SP.1996.145.01.08.

S. Ergun, “Fluid flow through packed columns,” *Industrial and Engineering Chemistry*, vol. 48, pp. 89–94, 1952.

W. H. Finlay, *The mechanics of inhaled pharmaceutical aerosols: an introduction*, Academic press, 2001.

Y. Forterre and O. Pouliquen, “Flows of Dense Granular Media,” *Annual Review of Fluid Mechanics*, vol. 40, pp. 1–24, 2008, DOI: 10.1146/annurev.fluid.40.111406.102142.

GDR MiDi, “On dense granular flows,” *The European Physical Journal E*, vol. 14, no. 4, pp. 341–365, 2004, DOI: 10.1140/epje/i2003-10153-0.

L. Gesenhues, J. J. Camata, A. M. A. Côrtes, F. A. Rochinha and A. L. G. A. Coutinho, “Finite element simulation of complex dense granular flows using a well-posed regularization of the μ(I)-rheology,” *Computers and Fluids*, vol. 188, pp. 102–113, 2019, DOI: 10.1016/j.compfluid.2019.05.012.

D. Gidaspow, *Multiphase flow and fluidization: continuum and kinetic theory descriptions*, Academic press, 1994.

C. J. Heerema, P. J. Talling, M. J. Cartigny, C. K. Paull, L. Bailey, S. M. Simmons, D. R. Parsons, M. A. Clare, R. Gwiazda, E. Lundsten, K. Anderson, K. L. Maier, J. P. Xu, E. J. Sumner, K. Rosenberger, J. Gales, M. McGann, L. Carter and E. Pope, “What determines the downstream evolution of turbidity currents?” *Earth and Planetary Science Letters*, vol. 532, p. 116023, 2020, DOI: 10.1016/j.epsl.2019.116023.

J. Heyman, R. Delannay, H. Tabuteau and A. Valance, “Compressibility regularizes the $\mu(I)$-rheology for dense granular flows,” *Journal of Fluid Mechanics*, vol. 830, pp. 553–568, 2017, DOI: 10.1017/jfm.2017.612.

R. I. Issa, “Solution of the implicitly discretised fluid flow equations by operator-splitting,” *Journal of Computational Physics*, vol. 62, no. 1, pp. 40–65, 1986, DOI: 10.1016/0021-9991(86)90099-9.

H. Jasak, “Error analysis and estimation for the finite volume method with applications to fluid flows,” Ph.D. thesis, Imperial College, University of London, 1996.

P. C. Johnson and R. Jackson, “Frictional–collisional constitutive relations for granular materials, with application to plane shearing,” *Journal of Fluid Mechanics*, vol. 176, pp. 67–93, 1987, DOI: 10.1017/S0022112087000570.

P. C. Johnson, P. Nott and R. Jackson, “Frictional–collisional equations of motion for participate flows and their application to chutes,” *Journal of Fluid Mechanics*, vol. 210, pp. 501–535, 1990, DOI: 10.1017/S0022112090001380.

P. Jop, Y. Forterre and O. Pouliquen, “A constitutive law for dense granular flows,” *Nature*, vol. 441, no. 7094, p. 727, 2006, DOI: 10.1038/nature04801.

J. Kim, F. Løvholt, D. Issler and C. F. Forsberg, “Landslide material control on tsunami genesis–The Storegga slide and tsunami (8,100 years BP),” *Journal of Geophysical Research*, vol. 124, no. 6, pp. 3607–3627, 2019, DOI: 10.1029/2018JC014893.

P.-Y. Lagrée, L. Staron and S. Popinet, “The granular column collapse as a continuum: validity of a two-dimensional Navier–Stokes model with a μ(I)-rheology,” *Journal of Fluid Mechanics*, vol. 686, pp. 378–408, 2011, DOI: 10.1017/jfm.2011.335.

F. Løvholt, S. Bondevik, J. S. Laberg, J. Kim and N. Boylan, “Some giant submarine landslides do not produce large tsunamis,” *Geophysical Research Letters*, vol. 44, no. 16, pp. 8463–8472, 2017, DOI: 10.1002/2017GL074062.

T. Marić, H. Marschall and D. Bothe, “An enhanced un-split face-vertex flux-based VoF method,” *Journal of Computational Physics*, vol. 371, pp. 967–993, 2018, DOI: 10.1016/j.jcp.2018.03.048.

N. Martin, I. R. Ionescu, A. Mangeney, F. Bouchut and M. Farin, “Continuum viscoplastic simulation of a granular column collapse on large slopes: μ(I) rheology and lateral wall effects,” *Physics of Fluids*, vol. 29, no. 1, p. 013301, 2017, DOI: 10.1063/1.4971320.

F. Moukalled, L. Mangani and M. Darwish, *The finite volume method in computational fluid dynamics*, Springer, 2016, DOI: 10.1007/978-3-319-16874-6.

OpenCFD Ltd., *OpenFOAM - The Open Source CFD Toolbox - User Guide*, 2004, last checked: 20.01.2020.

M. Pailha and O. Pouliquen, “A two-phase flow description of the initiation of underwater granular avalanches,” *Journal of Fluid Mechanics*, vol. 633, pp. 115–135, 2009, DOI: 10.1017/S0022112009007460.

A. Passalacqua and R. O. Fox, “Implementation of an iterative solution procedure for multi-fluid gas–particle flow models on unstructured grids,” *Powder Technology*, vol. 213, no. 1, pp. 174–187, 2011, DOI: 10.1016/j.powtec.2011.07.030.

M. Rauter, T. Barker and W. Fellin, “Granular viscosity from plastic yield surfaces: The role of the deformation type in granular flows,” *Computers and Geotechnics*, vol. 122, p. 103492, 2020, DOI: 10.1016/j.compgeo.2020.103492.

M. Rauter, L. Hoße, R. Mulligan, A. W. Take and F. Løvholt, “Numerical simulation of impulse wave generation by idealized landslides with OpenFOAM,” *Coastal Engineering*, vol. 165, p. 103815, 2021, DOI: 10.1016/j.coastaleng.2020.103815.

C. M. Rhie and W. L. Chow, “Numerical study of the turbulent flow past an airfoil with trailing edge separation,” *AIAA Journal*, vol. 21, no. 11, pp. 1525–1532, 1983.

J. Roenby, H. Bredmose and H. Jasak, “A computational method for sharp interface advection,” *Royal Society Open Science*, vol. 3, no. 11, p. 160405, 2016, DOI: 10.1098/rsos.160405.

L. Rondon, O. Pouliquen and P. Aussillous, “Granular collapse in a fluid: Role of the initial volume fraction,” *Physics of Fluids*, vol. 23, no. 7, p. 073301, 2011, DOI: 10.1063/1.3594200.

K. H. Roscoe, “The influence of strains in soil mechanics,” *Géotechnique*, vol. 20, no. 2, pp. 129–170, 1970, DOI: 10.1680/geot.1970.20.2.129.

K. H. Roscoe, A. N. Schofield and C. P. Wroth, “On the yielding of soils,” *Géotechnique*, vol. 8, no. 1, pp. 22–53, 1958, DOI: 10.1680/geot.1958.8.1.22.

H. Rusche, “Computational fluid dynamics of dispersed two-phase flows at high phase fractions,” Ph.D. thesis, Imperial College London (University of London), 2002.

S. B. Savage, M. H. Babaei and T. Dabros, “Modeling gravitational collapse of rectangular granular piles in air and water,” *Mechanics Research Communications*, vol. 56, pp. 1–10, 2014, DOI: 10.1016/j.mechrescom.2013.11.001.

D. G. Schaeffer, “Instability in the evolution equations describing incompressible granular flow,” *Journal of Differential Equations*, vol. 66, no. 1, pp. 19–50, 1987, DOI: 10.1016/0022-0396(87)90038-6.

D. G. Schaeffer, T. Barker, D. Tsuji, P. Gremaud, M. Shearer and J. M. N. T. Gray, “Constitutive relations for compressible granular flow in the inertial regime,” *Journal of Fluid Mechanics*, vol. 874, pp. 926–951, 2019, DOI: 10.1017/jfm.2019.476.

A. Schofield and P. Wroth, *Critical state soil mechanics*, McGraw-Hill London, 1968.

P. Si, H. Shi and X. Yu, “Development of a mathematical model for submarine granular flows,” *Physics of Fluids*, vol. 30, no. 8, p. 083302, 2018a, DOI: 10.1063/1.5030349.

P. Si, H. Shi and X. Yu, “A general numerical model for surface waves generated by granular material intruding into a water body,” *Coastal Engineering*, vol. 142, pp. 42–51, 2018b, DOI: 10.1016/j.coastaleng.2018.09.001.

B. Sovilla, J. N. McElwaine and M. Y. Louge, “The structure of powder snow avalanches,” *Comptes Rendus Physique*, vol. 16, no. 1, pp. 97–104, 2015, DOI: 10.1016/j.crhy.2014.11.005.

L. Staron, P.-Y. Lagrée and S. Popinet, “The granular silo as a continuum plastic flow: The hour-glass vs the clepsydra,” *Physics of Fluids*, vol. 24, no. 10, p. 103301, 2012, DOI: 10.1063/1.4757390.

K. Terzaghi, “Erdbaumechanik auf bodenphysikalischer Grundlage,” , 1925.

M. Trulsson, B. Andreotti and P. Claudin, “Transition from the viscous to inertial regime in dense suspensions,” *Physical Review Letters*, vol. 109, no. 11, p. 118305, 2012, DOI: 10.1103/PhysRevLett.109.118305.

B. G. M. van Wachem, “Derivation, implementation, and validation of computer simulation models for gas-solid fluidized beds,” Ph.D. thesis, TU Delft, Delft University of Technology, Delft, Netherlands, 2000, last checked: 11.09.19.

D. Vescovi, C. di Prisco and D. Berzi, “From solid to granular gases: the steady state for granular materials,” *International Journal for Numerical and Analytical Methods in Geomechanics*, vol. 37, no. 17, pp. 2937–2951, 2013, DOI: 10.1002/nag.2169.

S. Viroulet, J. L. Baker, A. N. Edwards, C. G. Johnson, C. Gjaltema, P. Clavel and J. M. N. T. Gray, “Multiple solutions for granular flow over a smooth two-dimensional bump,” *Journal of Fluid Mechanics*, vol. 815, pp. 77–116, 2017, DOI: 10.1017/jfm.2017.41.

A. von Boetticher, J. M. Turowski, B. W. McArdell, D. Rickenmann, M. Hürlimann, C. Scheidl and J. W. Kirchner, “DebrisInterMixing-2.3: a finite volume solver for three-dimensional debris-flow simulations with two calibration parameters – Part 2: Model validation with experiments,” *Geoscientific Model Development*, vol. 10, no. 11, pp. 3963–3978, 2017, DOI: 10.5194/gmd-10-3963-2017.

A. von Boetticher, J. M. Turowski, B. W. McArdell, D. Rickenmann and J. W. Kirchner, “DebrisInterMixing-2.3: a finite volume solver for three-dimensional debris-flow simulations with two calibration parameters – Part 1: Model description,” *Geoscientific Model Development*, vol. 9, no. 9, pp. 2909–2923, 2016, DOI: 10.5194/gmd-9-2909-2016.

C. Wang, Y. Wang, C. Peng and X. Meng, “Two-fluid smoothed particle hydrodynamics simulation of submerged granular column collapse,” *Mechanics Research Communications*, vol. 79, pp. 15–23, 2017, DOI: 10.1016/j.mechrescom.2016.12.001.

H. G. Weller, “A new approach to VOF-based interface capturing methods for incompressible and compressible flow,” Technical Report TR/HGW/06, Nabla Ltd., London, UK, 2008.

H. G. Weller, G. Tabor, H. Jasak and C. Fureby, “A tensorial approach to computational continuum mechanics using object-oriented techniques,” *Computers in Physics*, vol. 12, no. 6, pp. 620–631, 1998, DOI: 10.1063/1.168744.

G. C. Yang, C. Y. Kwok and Y. D. Sobral, “The role of fluid viscosity in an immersed granular collapse,” in *EPJ Web of Conferences - Powders & Grains 2017*, vol. 140, p. 09037, EDP Sciences, 2017, DOI: 10.1051/epjconf/201714009037.

Authors’ addresses

Matthias Rauter University of Oslo, Postboks 1337 Blindern, 0316 Oslo, Norway, matthias.rauter@uio.no

Paper III

Numerical simulation of impulse wave generation by idealized landslides with OpenFOAM

Matthias Rauter, Luisa Hoße, Ryan P. Mulligan, W. Andy Take, Finn Løvholt

Published in *Coastal Engineering*, April 2021, volume 165, pp. 103815. DOI: 10.1016/j.coastaleng.2020.103815.

Abstract

Landslide tsunamis and impulse waves are hazardous events with severe socioeconomic impacts. A long standing problem with simulations of these events is the generation stage, where landslides and water interact. Depth-averaged models like the Saint-Venant or Boussinesq Equations lose their validity for such applications. Therefore, we have to rely on a full treatment of the hydrodynamics, for instance by applying the Navier–Stokes Equations and Computational Fluid Dynamics (CFD). However, applications of fully three-dimensional methods to landslide tsunamis are sparse, and have often been outperformed by depth averaged models when compared to experimental data. In this work, we evaluate the multiphase Navier–Stokes Equations as implemented in OpenFOAM® in terms of impulse wave generation. We focus on a simplified two-dimensional setup where the landslide consists of water, in order to circumvent additional complexities due to treatment of landslide rheologies. We conduct a thorough grid refinement study and compare results to experiments to investigate model convergence, stability, and accuracy. The simulations display good agreement with the experimental data if the Courant-Friedrichs-Lewy (CFL) condition, is modified to account for the specific properties of the multiphase system. Further, we use the validated model for sensitivity studies and to review various scaling relations for landslide generated tsunamis. The application of numerical models allows us to perform broad parametric tests and dissect the underlying physics of these predictive equations systematically. We found that the first wave crest may be well estimated by solely the landslide mass in our setting. Including additional properties related to landslide momentum can improve the predictive skill, while other parameters lead to no substantial improvement.

III.1 Introduction

Landslides are the second most frequent tsunami source (Harbitz *et al.*, 2014). Recently, the 2018 Anak Krakatoa landslide induced tsunami caused several hundred fatalities (e.g. Grilli *et al.*, 2019). Several other landslide events of the last decade generated impulse waves with run-up heights of up to 150 m (e.g. Gylfadóttir *et al.*, 2017; George *et al.*, 2017; Paris *et al.*, 2019). Landslide tsunamis have traditionally been modelled through depth-integrated (i.e., two-dimensional) models, reducing the complexity and improving the accuracy in comparison to fully three-dimensional models (e.g. Lovholt *et al.*, 2015; Yavari-Ramshe and Ataie-Ashtiani, 2016). The assumptions of depth-integrated models fit well with the propagation stage of tsunamis and for some cases (e.g. submarine landslides, earthquakes) also to the generation stage. However, the generation can be influenced by a highly rotational and depth-varying velocity field, a complex water surface (e.g. breaking waves) and other processes that stand in strong contrast to the assumptions of depth-integrated and potential flow models. This is especially the case for tsunamis generated by subaerial landslides that impact the water reservoir, such as the Vajont landslide (e.g. Panizzo *et al.*, 2005), the Ritter volcano eruption (e.g. Ward and Day, 2003) or the hypothetical La Palma island collapse (e.g. Gisler *et al.*, 2006; Løvholt *et al.*, 2008; Abadie *et al.*, 2012). Moreover, depth averaged models have shown to face difficulties related to strong non-linearities (e.g. Løvholt *et al.*, 2013) and steep topographies (Løvholt and Pedersen, 2009). For such cases, the most appropriate approach requires a minimum degree of simplification, which implies solving full three-dimensional continuum mechanical models, i.e. the Navier–Stokes Equations. Some studies couple three-dimensional models with depth-averaged models, either for landslides (Domnik *et al.*, 2013), impulse waves (Løvholt *et al.*, 2008) or other large scale flows, which are too extensive for a complete three-dimensional treatment (Mintgen and Manhart, 2018). For a comprehensive comparison the reader is refereed to these publications. Notably, a wide range of alternative and mixed methods was investigated: Savage-Hutter model coupled with Navier–Stokes Equations (e.g. Ma *et al.*, 2015), discrete element method coupled with Navier–Stokes Equations (e.g. Shan and Zhao, 2014), smoothed particle hydrodynamics (e.g. Pastor *et al.*, 2008; Heller *et al.*, 2016) or particle finite element method (e.g. Mulligan *et al.*, 2020) are a few of the promising approaches.

Modelling landslide tsunamis with the Navier–Stokes Equations implies solving a multiphase system. At least two phases, water and air, are required to simulate surface water waves. In addition, the landslide should be treated as an individual phase, to take into account the respective properties. Turbulence, that cannot be resolved with the numerical method must be taken into account by the mathematical model. This issue is usually tackled with turbulence models, and especially the Reynolds-averaged Navier–Stokes (RANS) Equations in combination with the k-ϵ-model have become popular for practical applications (Launder and Spalding, 1974). In addition, the complex rheology of the granular and porous landslide must be adequately described. Various rheologies have been suggested (e.g. Jop *et al.*, 2006; Boyer *et al.*, 2011; Savage *et al.*, 2014; Barker *et al.*, 2017; Si *et al.*, 2018a), however, a unified description of partially and fully water-saturated landslides is still too complex and too poorly understood for many applications. Furthermore, the porosity of granular materials leads to dynamic bulk density changes and excess pore pressure, substantially influencing the rheology (e.g. Ilstad *et al.*, 2004; Rondon *et al.*, 2011). Indeed, most studies with Navier–Stokes Equations rely on simplified rheologies (e.g. Newtonian or Herschel-Bulkley fluids) that do not consider the granular character and the porosity of landslides (e.g. Gisler *et al.*, 2006; Abadie *et al.*, 2010, 2012; Viroulet *et al.*, 2013, 2016; Gabl *et al.*, 2015; Kim *et al.*, 2019). Others use rigid bodies to simulate landslides and similar objects (e.g. Heinrich, 1992; Liu *et al.*, 2005; Chen *et al.*, 2020; Romano *et al.*, 2020). Si *et al.* (2018b) is one of the few examples of combining a surface wave model and granular flows in terms of Navier–Stokes Equations.

In the present numerical study, we will omit the complex nature of the landslide to focus solely on the tsunami generation and propagation. This way we avoid possible shortcomings in the treatment of the landslide, artificially impacting the wave generation and leading to a less transparent analysis. We are guided by the experiments of Bullard *et al.* (2019), where the landslide was pure water in contrast to many other experiments, where granular materials were used (e.g. Viroulet *et al.*, 2013; Fritz, 2002). The rheology of the landslide is hence described fairly well by a simple Newtonian fluid in combination with the turbulence model.

The goal of this work is to verify and validate the multiphase solver of the open source CFD toolkit OpenFOAM® (OpenCFD, 2018) in terms of impulse wave generation and propagation. In particular, we are able to demonstrate that the criterion for adaptive time stepping in OpenFOAM, known as Courant-Friedrichs-Lewy (CFL) condition (see section III.2.2), is insufficient for the presented cases and we introduce a better performing extension. We compare results to the experimental observations of Bullard *et al.* (2019), showing that the numerical model is able to reproduce the experimental results without any parameter fitting.

In a further step, the verified and validated model is applied for a sensitivity and scaling analysis that goes beyond the experimental results. Numerical simulations allow a high degree of automation and even the tank geometry can be modified with little effort. This enables us to investigate a large variety of still water depths and impact angles. We test a wide range of semi-empirical and theoretical scaling relations (Fritz, 2002; Heller and Hager, 2010; Zitti *et al.*, 2015; Mulligan and Take, 2017; Bullard *et al.*, 2019) and use basic statistical methods in an attempt to find the most influential landslide properties for this particular setting. Combined, we present 16 simulations for verification, 16 simulations for validation and 112 simulations for the scaling analysis. All simulations are conducted in a two-dimensional domain (a vertical slice of the tank), although the mathematical model is capable of fully three-dimensional simulations.

The paper is organised as follows: In section III.2, we will introduce the multiphase Navier–Stokes Equations as implemented in OpenFOAM and an improved stability criterion for the time step duration that allows us to achieve the required accuracy in tsunami simulations. Further, we introduce dimensionless landslide and tsunami properties and scaling relations from the literature. We verify and validate the method in section III.3 in terms of the experiments of Bullard *et al.* (2019). Section III.4 extends the parameter space of simulations for a comprehensive sensitivity and scaling analysis, followed by a discussion in section III.5. Finally, we give a summary and an outlook in section III.6.

III.2 Methods

III.2.1 Mathematical model

We apply the unsteady multiphase RANS Equations to simulate a system of multiple fluids (in here water and air), given as

$$\nabla \cdot \mathbf{u} = 0, \tag{III.1}$$

$$\frac{\partial \rho\, \mathbf{u}}{\partial t} + \nabla \cdot (\rho\, \mathbf{u} \otimes \mathbf{u}) = -\nabla\, p + \nabla \cdot (2\,(\mu + \mu_t)\, \mathbf{D}) + \rho\, \mathbf{g}. \tag{III.2}$$

$$\frac{\partial \alpha_i}{\partial t} + \nabla \cdot (\alpha_i\, \mathbf{u}) + \sum_j \nabla \cdot (\alpha_i\, \alpha_j\, \mathbf{u}_{\mathrm{r},ij}) = 0. \tag{III.3}$$

Phase indicator functions α_i are defined as

$$\alpha_i(\mathbf{x}, t) = \begin{cases} 1 & \text{phase } i \text{ present at } \mathbf{x}, t, \\ 0 & \text{otherwise,} \end{cases} \tag{III.4}$$

and allow tracking of the various phases. Numerical diffusion is counteracted by the third term in Eq. (III.3) using the relative velocity between phases $\mathbf{u}_{\mathrm{r},ij}$, which is constructed to ensure sharp interfaces (Rusche, 2002; Weller, 2008; Marschall *et al.*, 2012). The local fluid density $\rho(\mathbf{x}, t)$ and molecular dynamic viscosity $\mu(\mathbf{x}, t)$ follow from present phases and the respective densities ρ_i and viscosities μ_i,

$$\rho = \sum_i \alpha_i(\mathbf{x}, t)\, \rho_i, \tag{III.5}$$

$$\mu = \sum_i \alpha_i(\mathbf{x}, t)\, \mu_i. \tag{III.6}$$

We assume constant fluid densities and viscosities in the following, as this describes water and air reasonably well. All phases advect with the velocity $\mathbf{u}(\mathbf{x}, t)$ and the strain rate tensor $\mathbf{D}$ is defined in terms of its gradient as

$$\mathbf{D} = \frac{1}{2} \left(\nabla\, \mathbf{u} + (\nabla\, \mathbf{u})^T \right). \tag{III.7}$$

The gravitational acceleration is $\mathbf{g}$ and $p(\mathbf{x}, t)$ is the pressure field. The eddy viscosity $\mu_t(\mathbf{x}, t)$ is supposed to consider effects of turbulence that is not resolved by the numerical discretisation and is calculated with the k-ϵ-model (Launder and Spalding, 1974) as

$$\mu_t = \rho\, C_\mu \frac{k^2}{\epsilon}. \tag{III.8}$$

The turbulent kinetic energy $k(\mathbf{x}, t)$ and rate of dissipation $\epsilon(\mathbf{x}, t)$ follow as

$$\begin{aligned} &\frac{\partial \rho\, k}{\partial t} + \nabla \cdot (\rho\, k\, \mathbf{u}) = \\ &\nabla \cdot \left(\left(\frac{\mu_t}{\sigma_k} + \mu \right) \nabla\, k \right) + \mu_t\, (2\, \mathbf{D}) : \nabla\, \mathbf{u} - \rho\, \epsilon, \end{aligned} \tag{III.9}$$

$$\begin{aligned} &\frac{\partial \rho\, \epsilon}{\partial t} + \nabla \cdot (\rho\, \epsilon\, \mathbf{u}) = \\ &\nabla \cdot \left(\left(\frac{\mu_t}{\sigma_\epsilon} + \mu \right) \nabla\, \epsilon \right) + \frac{C_1\, \mu_t\, \epsilon}{k} (2\, \mathbf{D}) : \nabla\, \mathbf{u} - C_2\, \rho \frac{\epsilon^2}{k}. \end{aligned} \tag{III.10}$$

Standard parameters, $C_\mu = 0.09$, $\sigma_k = 1.0$, $\sigma_\epsilon = 1.3$, $C_1 = 1.44$, $C_2 = 1.92$ (Versteeg and Malalasekera, 2007), have been applied in early model tests and the achieved accuracy required no adjustment.

III.2.2 Numerical solution and stability

The computational domain (in time and space) is discretized to solve the governing equations (III.1) to (III.10). The spatial domain is divided into a finite number of polyhedra and the finite volume method (e.g. Weller *et al.*, 1998; Jasak, 1996; Moukalled *et al.*, 2016) is applied to discretize all spatial derivatives. The temporal domain (i.e., the simulation time) is split into a finite number of time steps, and the equations are solved in a time-marching manner. Pressure-velocity coupling is conducted with a semi-implicit method, similar to the PISO algorithm (Issa, 1986) and the governing equations are solved sequentially. Temporal derivatives are discretized with a semi-implicit Euler scheme. The govering equations for phase indicator functions are solved with the MULES algorithm (multi-dimensional limiter for explicit solution, Weller, 2006).

A sequential solution implies that components of the velocity are solved independently and only coupled through explicit terms. This gives rise to stability criteria that limit the time step duration Δt, known as CFL condition (Courant *et al.*, 1928). For convection dominated cases (and uniform grid size Δx), the CFL number is given as

$$\mathrm{CFL}^{\mathrm{conv}} = \frac{|\mathbf{u}|\, \Delta t}{\Delta x}, \tag{III.11}$$

and has to be limited to a value that is characteristic for the time integration scheme (e.g. 1 for explicit Euler). This is done by choosing the time step duration Δt accordingly. High viscosity in the transient convection diffusion equation

(III.3) leads to a stronger constraint of the time step duration (see appendix III.7 for an in-depth discussion) and the CFL number for such a case is given as

$$\mathrm{CFL}^{\mathrm{diff}} = \frac{\mu\,\Delta t}{\rho\,\Delta x^2}. \tag{III.12}$$

As we will show in the following, criterion Eq. (III.12) is imperative for convergence, stability and reliability in our applications, which will often lead to a stricter time step constraint than Eq. (III.11).

III.2.3 Dimensionless properties and scaling relations

We compare numerical simulations and physical experiments with several past experiments from literature. The comparison is based on semi-empirical relations for the near field wave amplitude a_m, that are derived from respective experiments. These relations are defined in terms of standardized dimensionless parameters, encoding the average landslide velocity $\overline{v}_\mathrm{s}$, the average landslide thickness $\overline{s}$, the landslide width b, the landslide mass m_s, the landslide density ρ_s, the total landslide duration Δt_s, the water reservoir density ρ_w and the water reservoir depth h_0, see Fig. III.1. All landslide parameters are averaged over the duration of the impact ($\Delta t_{75\%}$, see section III.3.2) in this work, however, some previous works apply the respective peak values (e.g. Heller and Hager, 2010). The derivation of these properties from simulation and experiment is specific to the case setup and thus explained in the respective section. The dimensionless slide mass is defined as

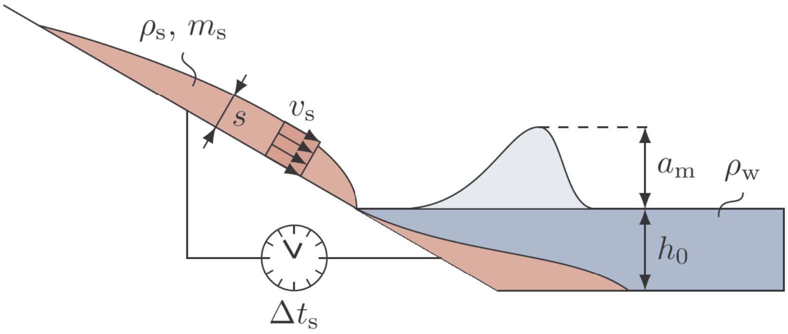

Figure III.1: Landslide (shown in red) and wave (shown in blue) properties. Note that the definition of the averaged velocity and landslide thickness depends on the respective setup and is not generally applicable.

$$M = \frac{m_\mathrm{s}}{\rho_\mathrm{s}\, b\, h_0^2}, \tag{III.13}$$

the dimensionless slide thickness as

$$S = \frac{\overline{s}}{h_0}, \tag{III.14}$$

and the slide Froude number as

$$\mathrm{F} = \frac{\overline{v}_\mathrm{s}}{\sqrt{g\,h_0}}. \tag{III.15}$$

We note that the slide Froude number in principle defines regions of subcritical ($\mathrm{F} < 1$, wave runs away from the landslide), critical ($\mathrm{F} = 1$), and supercritical ($\mathrm{F} > 1$, wave remains in the generation region) flow. However, as F is based on the terminal water depth h_0, some supercritical flow will always take place near the shoreline. Further, the dimensionless landslide impact duration is defined as

$$\Delta T = \Delta t_\mathrm{s} \sqrt{\frac{g}{h_0}}, \tag{III.16}$$

and the relative slide density as the ratio between slide and reservoir densities,

$$R = \frac{\rho_\mathrm{s}}{\rho_\mathrm{w}}. \tag{III.17}$$

However, R is unity throughout this work, as $\rho_\mathrm{s} = \rho_\mathrm{w}$. Furthermore, the cosine of the impact angle α is used in some scaling relations.

The dimensionless near field wave amplitude is defined as

$$A_\mathrm{m} = \frac{a_\mathrm{m}}{h_0}. \tag{III.18}$$

Five scaling relations for this important wave parameter,

$$A_\mathrm{m,SR} = A_\mathrm{m,SR}\left(M, \mathrm{F}, S, \Delta T, R, \cos(\alpha)\right), \tag{III.19}$$

were experimentally evaluated by Bullard *et al.* (2019) and the test is repeated here with the numerical results. The first relation is given by Heller and Hager (2010) for granular slides as

$$A_\mathrm{m,HH10} = \frac{4}{9}\,\mathrm{F}^{4/5}\,S^{2/5}\,M^{1/5}\,\cos\left(\frac{6}{7}\alpha\right)^{2/5}. \tag{III.20}$$

Zitti *et al.* (2015) found

$$A_\mathrm{m,Z15} = \frac{1}{5}\,\mathrm{F}^{1/5}\,S^{3/20}\,M^{9/20}\,\cos(\alpha)^{7/20}, \tag{III.21}$$

and

$$A_{\mathrm{m,Z}\Delta t} = \frac{1}{2}\,\mathrm{F}^{1/5}\,M^{4/5}\,\Delta T^{-1/5}\,\cos(\alpha)^{7/10}. \tag{III.22}$$

for buoyant slides, e.g. snow avalanches. Mulligan and Take (2017) derived an approximation based on physical principles,

$$A_\mathrm{m,q} = \sqrt{1 + R\,S\,\mathrm{F}^2\,\cos(\alpha)^2} - 1, \tag{III.23}$$

and Bullard *et al.* (2019) corrected it for high mobility slides to

$$A_{\mathrm{m,q,max}} = \sqrt{1 + 2\,R\,S\,\mathrm{F}^2\,\cos(\alpha)^2} - 1. \tag{III.24}$$

In addition, we will test the scaling relation of Fritz (2002) for granular landslides, given as

$$A_{\mathrm{m,F02}} = \frac{1}{4}\,\mathrm{F}^{7/5}\,S^{4/5}. \tag{III.25}$$

Note that some of these relations address different systems than investigated in here, e.g. granular material ($A_{\mathrm{m,F02}}$, $A_{\mathrm{m,HH10}}$) and buoyant slides ($A_{\mathrm{m,Z15}}$, $A_{\mathrm{m,Z\Delta}t}$). Further, definitions for the slide parameters can vary, e.g. by applying averaged or peak landslide parameters. An overview over respective parameter ranges can be found in Tab. III.1. It should not be expected that they are applicable without modification. Therefore, we will systematically evaluate and optimize the respective structures for our conditions in section III.4. We also stress that the experimental setups have been different, ranging from gravity driven liquid slides to piston-accelerated granular slide. This has to be taken into account when the scaling relations are compared with the outcome of the present simulations. Furthermore, some of the experiments might be influenced by scaling effects, expected at reservoir depths of $h = 0.2\,\mathrm{m}$ or less (Heller *et al.*, 2008).

Table III.1: Parameter ranges of experiments on which the semi-empirical scaling relations are based on.

Parameter	this study	Bullard *et al.* (2019)	Fritz (2002)	Heller and Hager (2010)	Zitti *et al.* (2015)
material	liquid	liquid	granular	granular	granular
porosity	0	≈ 0–0.3	≈ 0.5	≈ 0.4	≈ 0.5
F	0.041–3.5	2.1–5.4	1.1–4.7	0.86–6.8	0.84-1.9
S	0.017-.0.4	0.04–0.36	0.076–0.66	0.09–1.6	0.026-0.31
M	0.025–5.3	0.077–6.3	0.12–2.4	0.11–10.0	0.029-0.53
R	1	1	1.7	0.59-1.7	≈ 0.5
α	10° – 60°	30°	45°	30° – 90°	30°

III.3 Validation simulations

III.3.1 Simulation setup

For the verification of the numerical method and the validation of the mathematical model, we first aim to reproduce the physical experiments of Bullard *et al.* (2019). The landslide is represented by an elevated water reservoir having a volume V_0. It is released from rest and accelerates due to gravity along the sliding plane inclined with an angle $\alpha = 30°$, finally reaching the water reservoir with a still water depth h_0 (Figs. III.2 and III.3). We used the solver *multiphaseInterFoam* (v1812) that implements Eqs. (III.1)-(III.10) and we extended it to consider the viscous contribution to the CFL criterion (Eq. (III.12)). We make use of two phases in the simulation, namely water

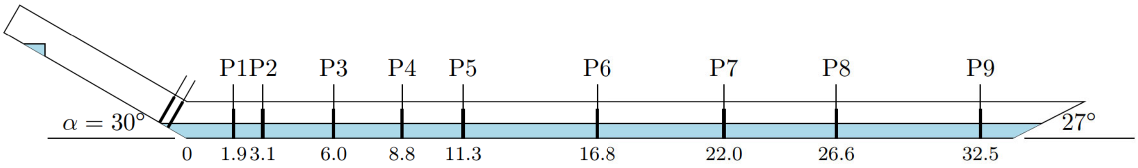

Figure III.2: Overview over the simulation setup following the physical experiments of Bullard *et al.* (2019). Nine gauges are registering the wave amplitude at P1-9. Distances are shown in meters.

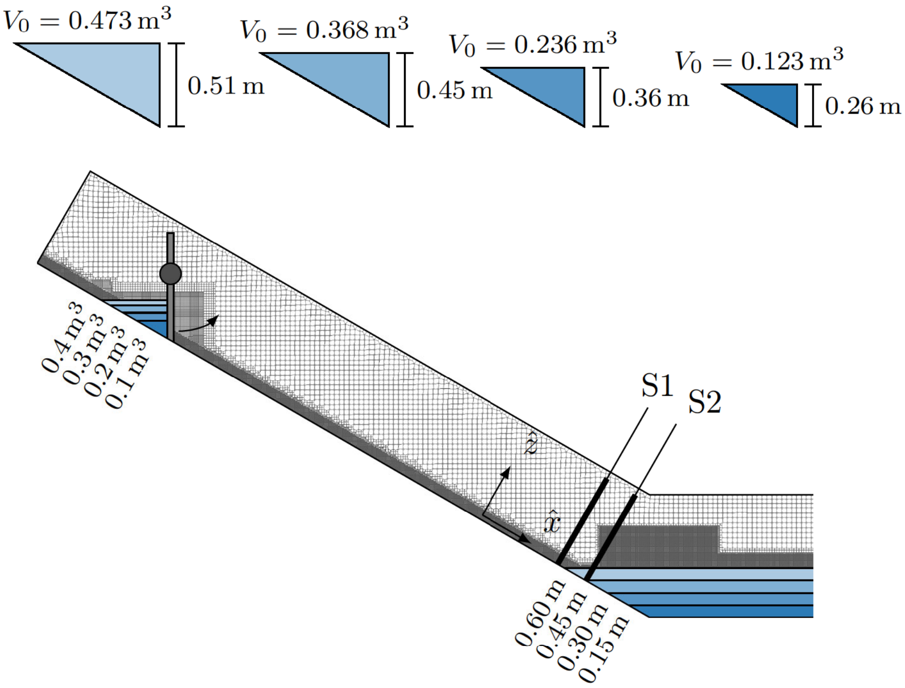

Figure III.3: Close-up of the ramp: the initial volume V_0 and the still water depth h_0 has been varied between $0.1\,\mathrm{m}^3$ and $0.4\,\mathrm{m}^3$ and 0.15 m and 0.60 m, respectively. The coarsest mesh is shown in grey in the background. The slide velocity $v_\mathrm{s}(t)$ and thickness $s(t)$ are measured up at S1 in the numerical simulations (moved up from S2 where it is measured in the experiments).

($\rho_\mathrm{w} = 1\,000\,\mathrm{kg\,m^{-3}}$, $\mu_\mathrm{w} = 10^{-3}\,\mathrm{kg\,m^{-1}\,s^{-1}}$), represented by the phase indicator α_w and air ($\rho_\mathrm{a} = 1\,\mathrm{kg\,m^{-3}}$, $\mu_\mathrm{a} = 1.48 \cdot 10^{-5}\,\mathrm{kg\,m^{-1}\,s^{-1}}$), represented by the phase indicator α_a. Note also that different phases for the landslide and the water reservoir are possible with the applied method, enabling different rheologies and densities in the landslide. However, this was not required for the investigated cases, as the water phase is used to represent both the reservoir water body and the sliding material.

The experiment was conducted in a tank with width $b = 2.1\,\mathrm{m}$. The reservoir that initially holds the landslide is restricted to a width of 1.7 m for constructive reasons related to the release mechanism. We approximate the experimental setup with a two-dimensional numerical setup that corresponds to a tank with constant width b. The reduced width of the landslide reservoir cannot be modelled directly with a two-dimensional setup and we approximate this geometry with a decreased fill height, keeping the landslide volume V_0 constant. The respective volume equivalent fill heights are shown in Fig. III.3. The error related to this simplification is expected to be small in comparison to other modelling uncertainties. All boundaries are modelled as impenetrable walls ($\mathbf{u} = \mathbf{0}$, $\mathbf{n} \cdot \nabla p = 0$, with the boundary normal vector $\mathbf{n}$), except the horizontal top boundary of the tank, which is modelled as a free outlet ($\mathbf{n} \cdot \nabla \mathbf{u} = \mathbf{0}$, $p = 0$, $\mathbf{n} \cdot \nabla \alpha_\mathrm{w} = 0$ for outward pointing velocity and $\alpha_\mathrm{w} = 0$ for inward pointing velocity). The initial conditions for α_w and α_a are defined by the landslide volume V_0 and the still water depth h_0, the velocity is initially zero. We use four different landslide volumes (roughly $0.1\,\mathrm{m}^3 - 0.4\,\mathrm{m}^3$, see Tab. III.2) and four still water depths ($0.15\,\mathrm{m} - 0.60\,\mathrm{m}$, see Fig. III.3) leading to overall 16 different cases that have been simulated for validation. Simulations and experimental measurements are synchronised with the arrival time of the landslide at the water basin (i.e. arrival of the landslide front at point S1), which we define as $t = 0\,\mathrm{s}$.

The experimental slope and tank geometry is covered by a body fitted mesh with a height of 1.5 m, as shown in Fig. III.2. For the exact geometry we refer to Bullard *et al.* (2019). The mesh was generated using *cartesian2DMesh*, a mesh generator of the cfMesh toolbox (Juretić, 2015). The mesh is dominated by hexagons with aspect ratio one and the faces align with the horizontal water surface. This circumvents numerical artefacts of the free surface at rest. The meshed tank is sufficiently tall to cover the highest waves and to keep enough distance from the boundary to prevent potential influences. Local mesh refinements were applied to the landslide slope, the impact area and the location of the free water surface, reducing the mesh size locally by a factor of four (see Fig. III.3). The total simulation duration was set to 20 s which is sufficient to cover the full wave propagation through the tank for most cases, except very shallow ones.

A mesh refinement study (cell sizes and cell numbers in Tab. III.3) was conducted for the case with $h_0 = 0.3\,\mathrm{m}$ and $V_0 = 0.4\,\mathrm{m}^3$. Additional investigations with other configurations (not shown) provided similar findings. The mesh refinement study was repeated with four different time step durations (defined by CFL criteria, see Tab. III.3), leading to overall 16 simulations that were executed for verification. The time step duration is dynamically adapted following the CFL criterion and its average lies between $10^{-4}\,\mathrm{s}$ and $10^{-3}\,\mathrm{s}$, the smallest time step with $\Delta t \approx 10^{-5}\,\mathrm{s}$ is found in the sliding phase. In the initial simulations we observed severe convergence problems with the conventional (i.e. convective) CFL condition (Eq. (III.11)), independent of the chosen limit. We found an appropriate time stepping method limited by $\mathrm{CFL}^\mathrm{diff} < 1.0$ and $\mathrm{CFL}^\mathrm{conv} < 0.5$ and an appropriate mesh size of 0.01 m that have been used for all simulations if not stated otherwise. This simulation is presented in form of a time sequence in Fig. III.4, showing landslide release ($t = -1.2\,\mathrm{s}$), wave generation

Table III.2: Volumetric discharge, timings of the slide and mean slide properties. The discharged volume V is calculated by integrating the product of slide thickness and slide velocity at the measurement point (S1 or S2).

Case	discharge V	slide dur. Δt_s	gen. dur. $\Delta t_{75\%}$	slide vel. $\overline{v}_\mathrm{s}$	slide thickness $\overline{s}$
Experiment					
$V_0 = 0.123\,\mathrm{m}^3$	$0.122\,\mathrm{m}^3$	$0.97\,\mathrm{s}$	$0.38\,\mathrm{s}$	$5.10\,\mathrm{m\,s^{-1}}$	$0.022\,\mathrm{m}$
$V_0 = 0.236\,\mathrm{m}^3$	$0.223\,\mathrm{m}^3$	$1.13\,\mathrm{s}$	$0.50\,\mathrm{s}$	$5.11\,\mathrm{m\,s^{-1}}$	$0.031\,\mathrm{m}$
$V_0 = 0.368\,\mathrm{m}^3$	$0.360\,\mathrm{m}^3$	$1.10\,\mathrm{s}$	$0.57\,\mathrm{s}$	$5.41\,\mathrm{m\,s^{-1}}$	$0.042\,\mathrm{m}$
$V_0 = 0.473\,\mathrm{m}^3$	$0.627\,\mathrm{m}^3$	$1.17\,\mathrm{s}$	$0.62\,\mathrm{s}$	$6.53\,\mathrm{m\,s^{-1}}$	$0.055\,\mathrm{m}$
Numerics					
$V_0 = 0.123\,\mathrm{m}^3$	$0.118\,\mathrm{m}^3$	$1.20\,\mathrm{s}$	$0.59\,\mathrm{s}$	$5.03\,\mathrm{m\,s^{-1}}$	$0.014\,\mathrm{m}$
$V_0 = 0.236\,\mathrm{m}^3$	$0.227\,\mathrm{m}^3$	$1.43\,\mathrm{s}$	$0.63\,\mathrm{s}$	$5.83\,\mathrm{m\,s^{-1}}$	$0.023\,\mathrm{m}$
$V_0 = 0.368\,\mathrm{m}^3$	$0.356\,\mathrm{m}^3$	$1.60\,\mathrm{s}$	$0.68\,\mathrm{s}$	$6.34\,\mathrm{m\,s^{-1}}$	$0.030\,\mathrm{m}$
$V_0 = 0.473\,\mathrm{m}^3$	$0.460\,\mathrm{m}^3$	$1.69\,\mathrm{s}$	$0.71\,\mathrm{s}$	$6.61\,\mathrm{m\,s^{-1}}$	$0.036\,\mathrm{m}$

($t = 0 - 1.25\,\mathrm{s}$), wave propagation ($t = 1.25 - 12.5\,\mathrm{s}$), inundation ($t = 15\,\mathrm{s}$) and wave reflection ($t = 17.5\,\mathrm{s}$). Different stages of the impulse wave are highlighted in Fig. III.5. The impact and wave generation is shown in Fig. III.5c and III.5d alongside a fotograph of the experiment in Fig. III.5a and III.5b. Notably, a large bubble of air gets trapped by the plunging wave. A similar pattern can be observed in the experiment, however, the air is dispersed by turbulence into small bubbles. The propagating wave is highlighted in Fig. III.5d and the inundation in Fig. III.5e.

Table III.3: Difference in first wave crest at Gauge P9 between experiment and simulation for various meshes and time step settings.

	$\Delta x = 0.015\,\mathrm{m}$ $N = 0.48\,\mathrm{M}$	$\Delta x = 0.0125\,\mathrm{m}$ $N = 0.69\,\mathrm{M}$	$\Delta x = 0.01\,\mathrm{m}$ $N = 1.08\,\mathrm{M}$	$\Delta x = 0.0075\,\mathrm{m}$ $N = 1.88\,\mathrm{M}$
$\mathrm{CFL}^\mathrm{conv} < 0.5$	0.027 m (14%)	0.014 m (8%)	0.196 m (105%)	0.150 m (81%)
$\mathrm{CFL}^\mathrm{conv} < 0.1$	0.020 m (11%)	0.014 m (7%)	0.020 m (11%)	0.038 m (20%)
$\mathrm{CFL}^\mathrm{conv} < 0.05$	0.031 m (16%)	0.009 m (5%)	0.025 m (14%)	0.051 m (28%)
$\mathrm{CFL}^\mathrm{diff} < 1.0$	0.025 m (13%)	0.014 m (8%)	0.001 m (1%)	0.001 m (1%)

III.3.2 Derivation of landslide metrics from simulations

All landslide parameters are extracted from the simulation with a line probe at S1, as shown in Figs. III.2 and III.3. Bullard *et al.* (2019) used cameras with view centre point S2 to extract the same parameters from the experiments. We changed the position from S2 to S1 to simplifying the postprocessing, because the original position was partially submerged in some cases. Differences between position S1 and S2 are small (maximum difference in velocity $\approx 0.2\,\mathrm{m\,s^{-1}}$, maximum difference in thickness $\approx 0.003\,\mathrm{m}$) and can be neglected. The slide thickness $s(t)$ is calculated as the highest point at S1 in a slope parallel coordinate

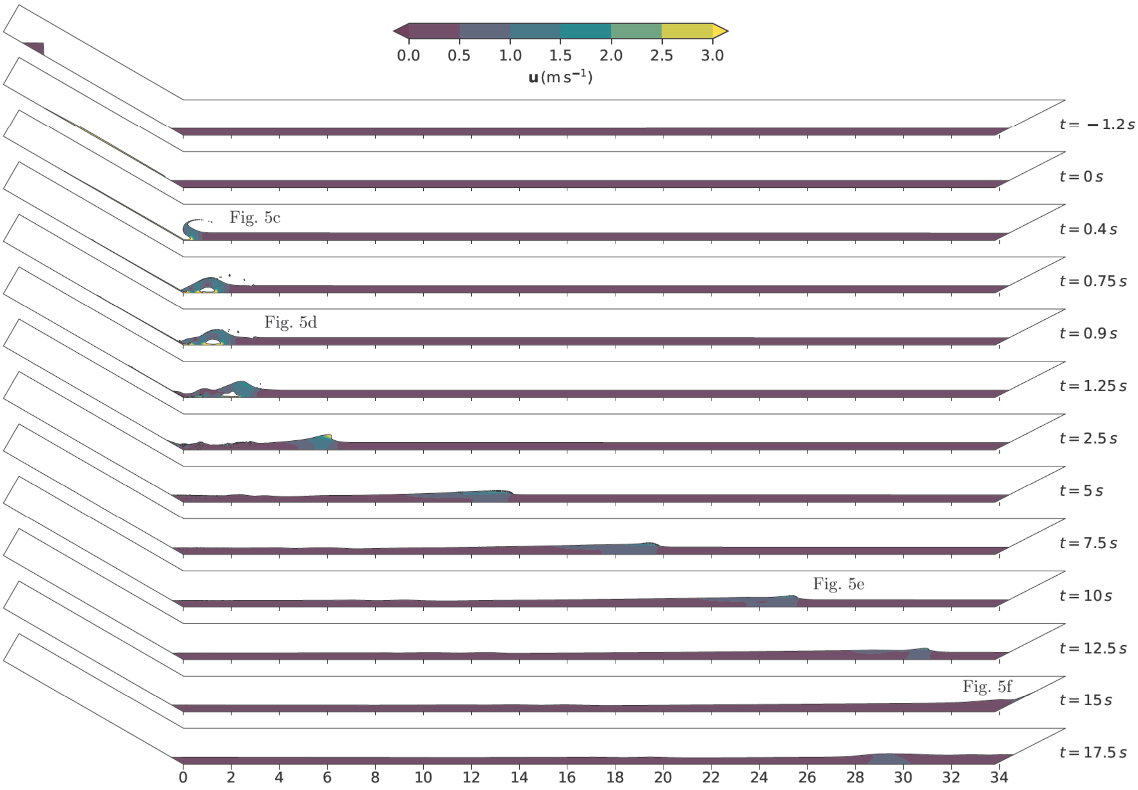

Figure III.4: Time sequence of the simulation with $V_0 = 0.4\,\mathrm{m}^3$, $h_0 = 0.3\,\mathrm{m}$, $\mathrm{CFL}^{\mathrm{diff}} < 1$ and $\Delta x = 0.01\,\mathrm{m}$.

system where α_w exceeds 0.5,

$$s(t) = \max(\hat{z}|_{\alpha_\mathrm{w}(\hat{z},t)>0.5}), \tag{III.26}$$

with the slope local coordinate $\hat{\mathbf{x}} = (\hat{x}, \hat{z})^T$ as shown in Fig. III.3. The depth-averaged slide velocity at S1 is calculated by averaging over the water phase,

$$v_\mathrm{s}(t) = \frac{\int\limits_0^\infty \alpha_\mathrm{w}(\hat{z},t)\,|\mathbf{u}(\hat{z},t)|\,\mathrm{d}\hat{z}}{\int\limits_0^\infty \alpha_\mathrm{w}(\hat{z},t)\,\mathrm{d}\hat{z}}. \tag{III.27}$$

The slide thickness and velocity are presented and compared with the physical experiment in Fig. III.6 for all four slide volumes V_0. The mean slide thickness

$$\overline{s} = \frac{1}{\Delta t_{75\%}} \int\limits_0^{\Delta t_{75\%}} s(t)\,\mathrm{d}t \tag{III.28}$$

and mean slide velocity

$$\overline{v}_\mathrm{s} = \frac{1}{\Delta t_{75\%}} \int\limits_0^{\Delta t_{75\%}} v_\mathrm{s}(t)\,\mathrm{d}t \tag{III.29}$$

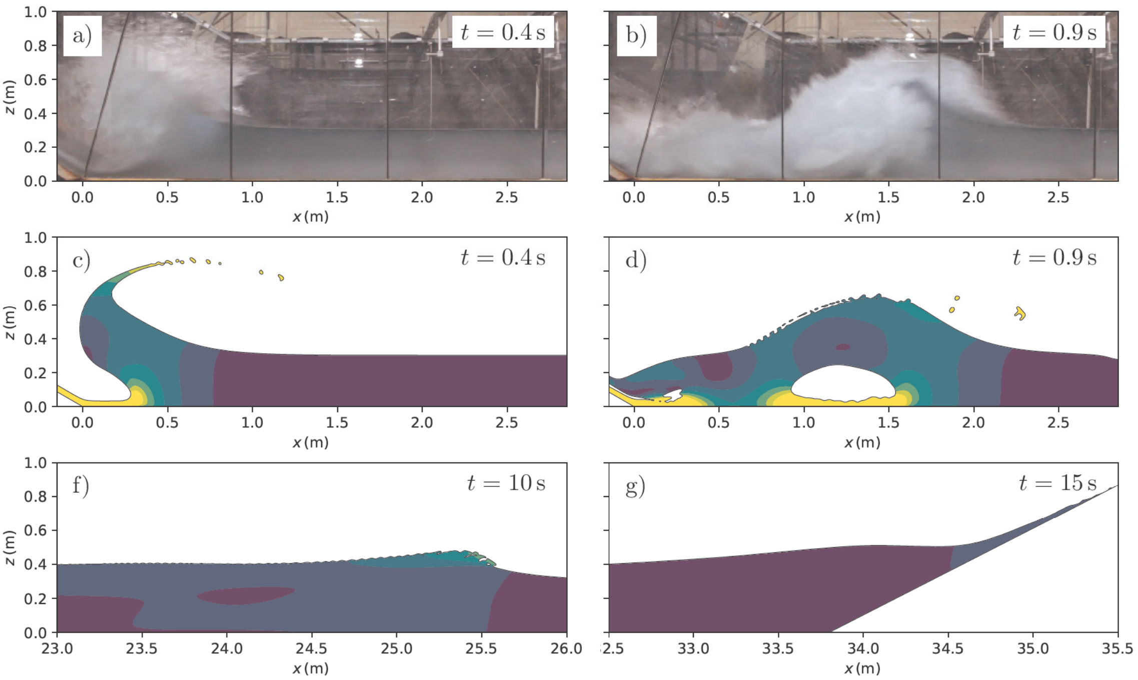

Figure III.5: Stages of the landslide tsunami in detail and in comparison with the experiment: (a, c) the early impact and the plunging wave, (b, d) the formation of a shallow wave, (e) propagation of the wave and (f) indentation and reflection of the wave on the counter slope. The parameter and colour scale are as in Fig. III.4.

are calculated as averages over the time period $\Delta t_{75\%}$, which is the time during which 75% of the volume passes the point. The total landslide duration Δt_{s} is defined as the time period during which the slide height $s(t)$ continuously exceeds 0.0008 m (in accordance with Bullard *et al.* (2019)). The total mass is calculated as

$$m_{\mathrm{s}} = \int_0^\infty \int_0^\infty b\, \rho_{\mathrm{w}}\, \alpha_{\mathrm{w}}(\hat{z}, t)\, |\mathbf{u}(\hat{z}, t)|\, \mathrm{d}\hat{z}\, \mathrm{d}t, \tag{III.30}$$

with the width of the tank $b = 2.10\,\mathrm{m}$. Timings and averaged properties of the slide are presented and compared with the physical experiment in Tab. III.2.

III.3.3 Derivation of wave metrics from simulations

The wave properties are measured at nine virtual gauges (i.e. line probes) that are positioned as in the experiments, see Fig. III.2. The free surface elevation $\eta_i(t)$ at the i-th wave gauge is calculated as

$$\eta_i(t) = \max(z|_{\alpha_{\mathrm{w}}(z,t)>0.5}) - h_0. \tag{III.31}$$

Single droplets, which are recognized as short and high peaks in $\eta_i(t)$, are excluded. The resulting free surface elevation time series η_i is shown in Fig. III.7

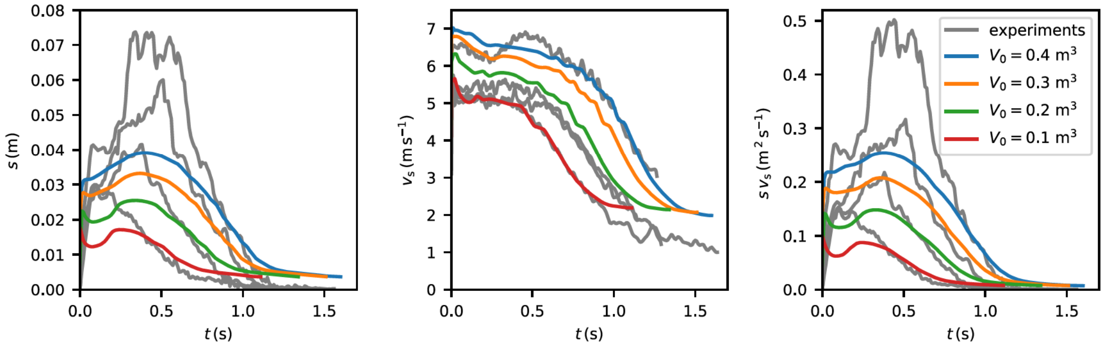

Figure III.6: Simulated slide thickness (coloured lines, left) and depth-averaged slide velocity (coloured lines, middle) and landslide momentum (coloured lines, right). For comparison the experimental data is shown in grey.

for different cell sizes and time step durations. The full set of results, with all combinations of V_0 and h_0, is shown in appendix III.8. The first wave crest at gauge i, $a_{\mathrm{m},i}$ is identified as the first local maximum within an interval of 0.4 s that exceeds the minimum value within this interval for 0.04 m. The time that corresponds to the first local maximum is defined as arrival time. The first wave crest is shown as a function of the still water depth for all gauges and all simulations in Fig. III.8 to investigate the wave crest limit $a_{\mathrm{m},i} \rightarrow 0.6\,h_0$, that was found by Bullard *et al.* (2019). The near field wave amplitude as used in scaling relations is defined as the first wave crest at gauge P1 (Bullard *et al.*, 2019), $a_{\mathrm{m}} = a_{\mathrm{m},1}$.

Table III.4: Errors at selected gauges for the converged ($\Delta x = 0.01$ m, CFL$^{\mathrm{diff}} < 1.0$) simulation with $V_0 = 0.4\,\mathrm{m}^3$, $h_0 = 0.3$ m.

before breaking:	P1	P3
$\Delta a_{\mathrm{m},i}$	0.032 m (8%)	0.088 m (36%)
$\Delta t_{\mathrm{m},i}$	0.13 s (14%)	0.26 s (12%)
after breaking:	P5	P9
$\Delta a_{\mathrm{m},i}$	0.013 m (6%)	0.001 m (1%)
$\Delta t_{\mathrm{m},i}$	0.14 s (3%)	0.37 s (3%)

III.3.4 Verification

We verify the numerical method by ensuring convergence through grid refinement. Considering the early stage of the wave generation, all time stepping criteria perform well. It can be seen in Fig. III.7 that the convective CFL criterion is stricter than the diffusive CFL criterion until $t = 0.5$ s. In other words, the flow is convection dominated (CFL$^{\mathrm{diff}} <$ CFL$^{\mathrm{conv}}$) until the impact because of the fast

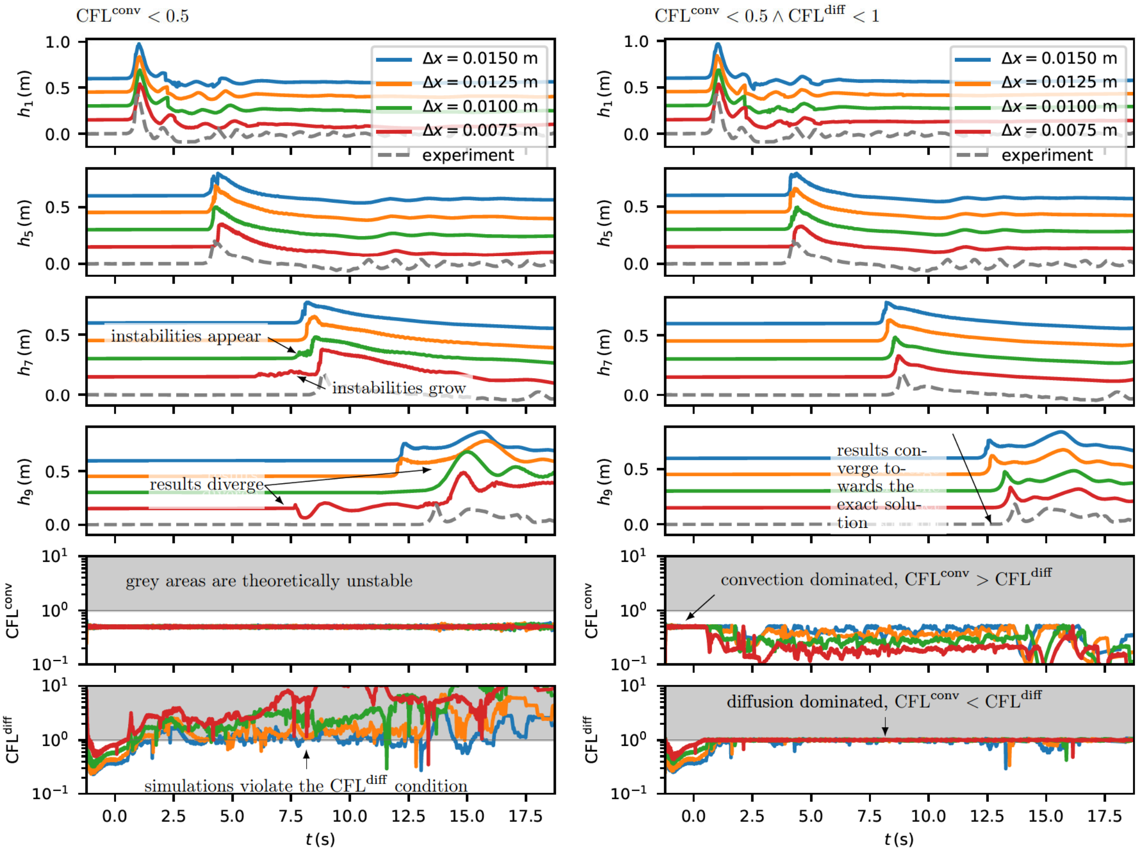

Figure III.7: Wave gauges of experiments with a landslide volume of $V_0 = 0.4\,\mathrm{m}^3$ and water height $h_0 = 0.3\,\mathrm{m}$. Results of different meshes are shown and offset vertically by 0.15 m for the sake of clearness. Conventional time stepping (left) with CFL$^{\mathrm{conv}} < 0.5$ and improved time stepping with CFL$^{\mathrm{conv}} < 0.5$ and CFL$^{\mathrm{diff}} < 1$. Results with the conventional time stepping criterion are affected by instabilities and diverge from the exact solution with mesh refinement. Results with the improved time stepping are reasonable and converge towards the exact solution for finer meshes. The last two columns show the CFL-numbers. It is clear that unphysical behaviour is related to CFL$^{\mathrm{diff}} > 1$ (left). The first wave crest at gauge P9 is also highlighted in Tab. III.3.

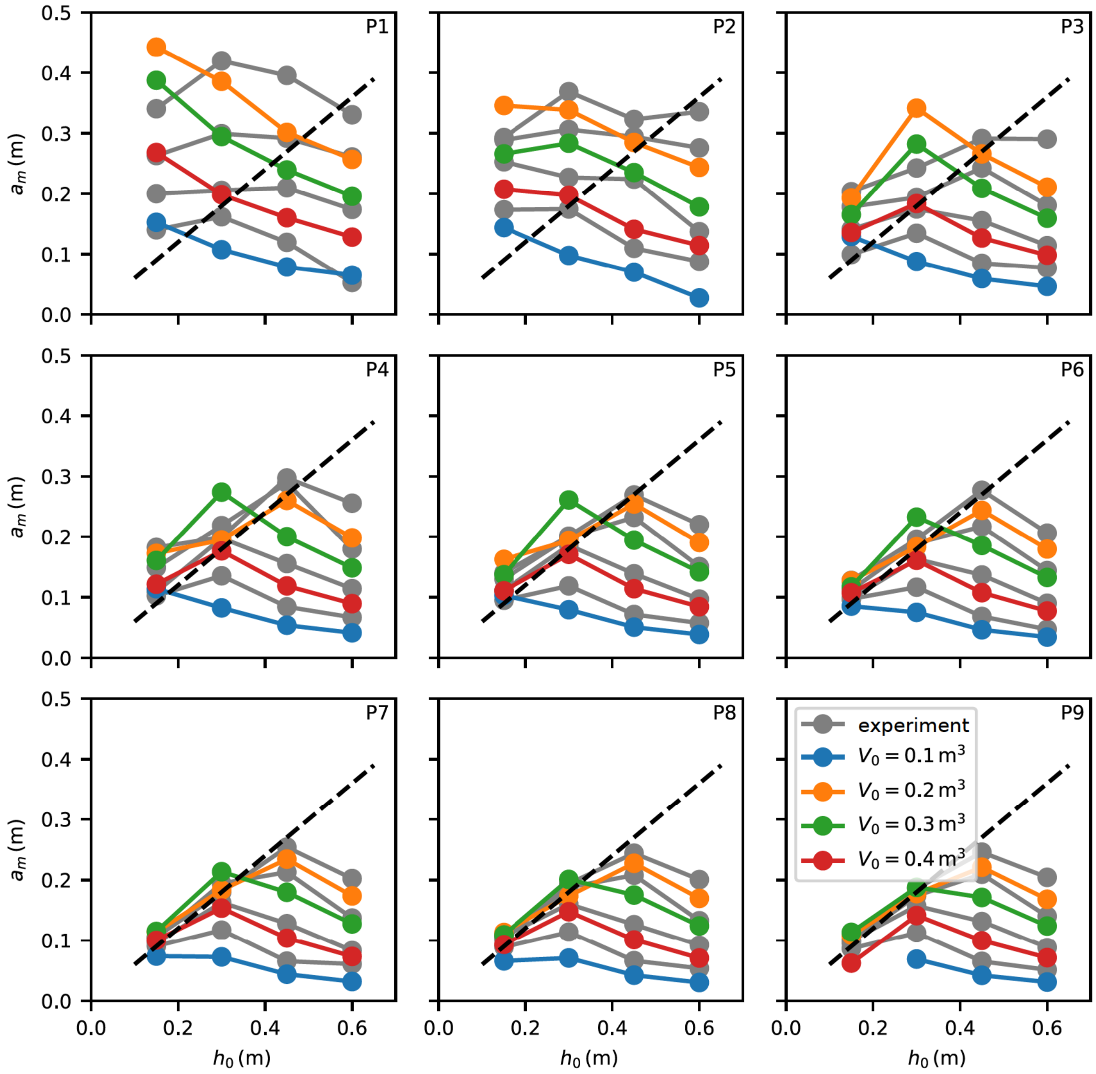

Figure III.8: The first wave crest at Gauges P1-9 for all 16 simulations as a function of the still water depth h_0. The colour marks the landslide volume. Coloured lines represent simulations, grey lines the respective experiments by Bullard *et al.* (2019). The black dashed line marks the found limit of $a_\mathrm{m} \rightarrow 0.6\,h_0$.

travelling landslide and the assumption of the traditional CFL criterion holds. The model behaviour changes drastically during wave propagation which can be seen best at the last gauge P9. The traditional time stepping criterion becomes unstable and the numerical method diverges for finer meshes. The contribution of the viscous term to the CFL number, $\mathrm{CFL}^{\mathrm{diff}}$, reaches values 50 times higher than $\mathrm{CFL}^{\mathrm{conv}}$. This shows that the momentum transfer is dominated by viscous stresses at the later stages of the simulations. This issue could only be solved with the modified (i.e. diffusive) condition, Eq. (III.12) and both, the wave crest (Tab. III.3) and the arrival time converge towards the exact solution. Further, we found with this analysis that results show a numerical uncertainty (Roache, 1997) of a few percent at a mesh resolution of $\Delta x = 0.01\,\mathrm{m}$. This mesh size was hence used in all simulations. The case with $\Delta x = 0.01\,\mathrm{m}$, $h_0 = 0.3\,\mathrm{m}$ and $V_0 = 0.4\,\mathrm{m}^3$ requires an execution time of roughly 24 h on 20 cores of an Intel Xeon E5-2690 v4 CPU. The same simulation with $\Delta x = 0.0075\,\mathrm{m}$ takes roughly 70 h, while changes in h_0 and V_0 have little influence on the execution time. This shows that further refinement is problematic due to the inverse quadratic scaling of $\mathrm{CFL}^{\mathrm{diff}}$ with the cell size Δx.

III.3.5 Validation

III.3.5.1 Landslide

The slide, represented in terms of the landslide thickness $s(t)$ and landslide velocity $v_\mathrm{s}(t)$ at S1 is compared with the physical experiment (at S2) in Fig. III.6. The landslide velocity v_s matches the experiment fairly well. Interestingly, the smallest landslide ($V_0 = 0.1\,\mathrm{m}^3$) and the largest landslide ($V_0 = 0.4\,\mathrm{m}^3$) fit best, with differences in mean velocity of less then $0.1\,\mathrm{m\,s}^{-1}$ (1%). On the other hand, the two mid-sized landslides display mean velocity differences up to $0.83\,\mathrm{m\,s}^{-1}$ (15%), as the velocity in simulations increases steadily with landslide volume while experiments show a jump between 0.3 and $0.4\,\mathrm{m}^3$. The landslide velocity is close to the free fall velocity that follows from this drop height ($v_\mathrm{max} = 7.5\,\mathrm{m\,s}^{-1}$) and it is safe to assume that basal friction played a minor role in these experiments. The landslide thickness s differs more strongly in all cases. The maximum slide thickness is underestimated by the numerical method, especially for the largest landslide, where a difference in mean slide thickness of 35% can be observed (the difference in the peak is higher). The tail is stretched out and is thicker in the simulations, compensating the reduced volume flux in the front of the landslide, leading to an overall similar volume in experiments and simulations (see Tab. III.2). Only the largest landslide differs substantially from this observation and the experiment shows an apparent discharge of $0.627\,\mathrm{m}^3$ that exceeds the initial landslide volume ($0.473\,\mathrm{m}^3$) by 33%. It should be noted that the thickness of the tail is below the cell size of $\Delta x \approx 0.01\,\mathrm{m}$ and that the numerical model cannot resolve such small length scales. The smallest resolvable length scale can be identified in Fig. III.6a as $0.005\,\mathrm{m}$ which roughly corresponds to half of the cell size.

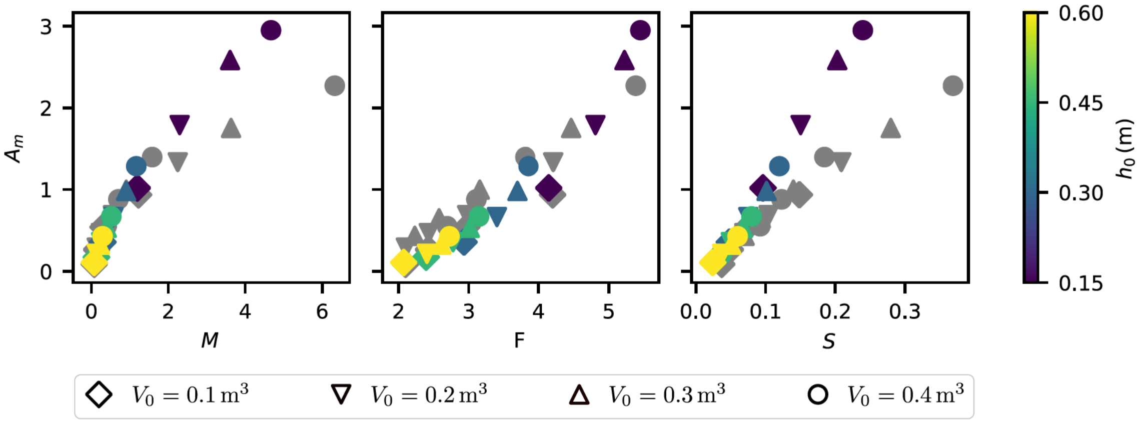

Figure III.9: Dimensionless mean properties of the landslides, the dimensionless landslide mass M, the landslide Froude number F and the dimensionless landslide thickness S, plotted against the dimensionless wave amplitude A_m. The grey circles represent experimental results of Bullard *et al.* (2019), the coloured marks represent numerical results, coloured after the water depth h_0, and the marks indicate the landslide volume V_0.

III.3.5.2 Wave

The simulated wave is compared to the experiment in terms of the first wave crest and the arrival time. A direct comparison of the wave gauge data ($\eta_i(t)$) is not practical, as a small error in arrival time can lead to a large apparent error. The respective difference is shown in Tab. III.4 for selected wave gauges of the case $V_0 = 0.4\,\mathrm{m}^3$, $h_0 = 0.3\,\mathrm{m}$ and lies between 1% and 36%, depending on the position of the gauge. The difference is larger in the near field and reaches its peak in the region where the wave is likely breaking while it reduces substantially in the far field. The wave crest amplitude is shown for all configurations and all gauges in Fig. III.8 with similar differences. Furthermore this figure highlights the breaking of waves, which eventually leads to a wave amplitude limit of $a_{\mathrm{m},i} \to 0.6\,h_0$ in physical experiments and numerical simulations. The trailing waves that are present in experimental results, especially in the case $V_0 = 0.1\,\mathrm{m}^3$, $h_0 = 0.6\,\mathrm{m}$, can also be found in the numerical simulations (see Fig. III.16), however they are substantially lower. Finally, the wave is reflected by the slope at the far end of the flume and the simulation is able to describe this process reasonably well in most cases.

III.3.6 Scaling relations

The range of dimensionless properties from simulations and experiments is shown in Fig. III.9, alongside the dimensionless near field wave amplitudes. Scaling relations are compared to the wave crest as extracted from simulations and from physical experiments in Fig. III.10. Moreover, it shows the relative difference, defined as

$$\delta_{\mathrm{SR}} = \frac{A_{\mathrm{m,SR}} - A_{\mathrm{m}}}{A_{\mathrm{m}}}, \tag{III.32}$$

with $A_{\mathrm{m,SR}}$ being predicted with one of Eqs. (III.20)-(III.25) and A_{m} the corresponding numerical or experimental result. Note that input data for the semi-empirical relation $A_{\mathrm{m,SR}}$ was chosen in correspondence to A_{m}, either from the experiment or the numerical simulation. Further, it should be noted that a positive difference indicates that the semi-empirical relation overestimates the wave amplitude.

The best fitting relation in terms of experimental results is given by $A_{\mathrm{m,q,max}}$ (Eq. (III.24)) with an average relative difference of 25%, while the largest difference was given by A_{Z15} (Eq. (III.21)) with 79%. The same was observed with respect to numerical results with average relative differences of 29% and 79%, respectively. This had to be expected as $A_{\mathrm{m,q,max}}$ was developed for these high mobility flows while A_{Z15} aims to describe buoyant landslides. Interestingly, the relative difference of A_{F02} (Eq. (III.25)) collapses to a single line, indicating a good fit but a mismatch of a constant factor. These preliminary results on scaling relations are valuable and interesting but show several problems, such as the narrow parameter space and the high correlation between the different landslide parameters. Furthermore, scaling relations have not been adjusted to the characteristics of the presented cases. The extended scaling and sensitivity analysis below aims to resolve some of these problems.

III.4 Sensitivity and scaling analysis

The concept of a gravity driven, naturally developing landslide is not very convenient for a well defined sensitivity analysis of slide parameters S, F, M, ΔT and basin parameters h_0 and α. Parameters cannot be explicitly controlled and we have to rely on initial conditions to manipulate landslide parameters. Moreover, parameters are widely correlated in such a case (see Fig. III.9). In this section, the gravity driven landslide as used in section III.3 is therefore replaced with a well controlled boundary condition near to the point of impact as shown in Fig. III.11. Natural events span over a wide range of parameters, from slow cliff collapses to fast slides that accelerated on long slopes and we aim to cover this wide range with the modified simulation setup. This concept is similar to the experiments of Fritz (2002), however, with water instead of granules as slide material. With this concept we can lock the slide thickness $s(t) = \overline{s}$, the slide velocity $v_{\mathrm{s}}(t) = \overline{v}_{\mathrm{s}}$ and the landslide duration Δt_{s} to predefined values. The landslide mass

$$m_{\mathrm{s}} = \rho_{\mathrm{s}}\, b\, \overline{s}\, \overline{v}_{\mathrm{s}}\, \Delta t_{\mathrm{s}} \tag{III.33}$$

is correlated to these parameters and the landslide density ρ_{s}. Geometrical properties such as the slope angle α and the still water depth h_0 can be set during geometry generation and simulation initialisation. Note that a variation

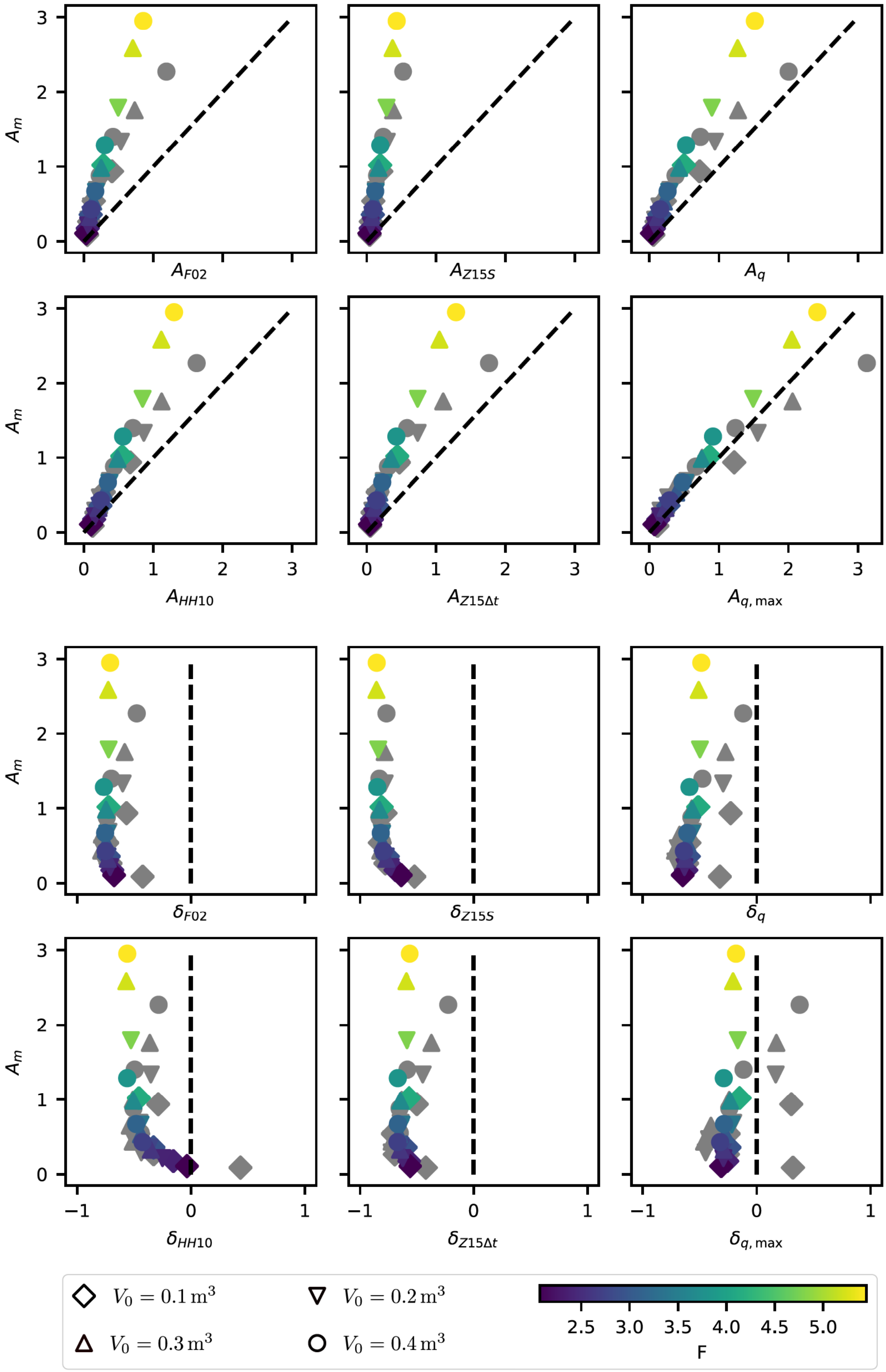

Figure III.10: Semi-empirical models for the first wave crest, A_{F02}, A_{HH10}, A_{Z15S}, $A_{\mathrm{Z15\Delta t}}$, A_{q} and $A_{\mathrm{q\ max}}$ compared to the measured first wave crest in the experiments (grey marks) and the numerical results (coloured marks). The respective differences are shown below. The colour represents the slide Froude number F and the form represents the landslide volume V_0. The black dashed line indicates a perfect fit.

of the geometry leads to different impact positions (i.e. the point where landslide and reservoir touch first, see Fig. III.11) in relation to the position of the first gauge. However, we estimate that the influence of this variation on the wave generation is small, considering the small change of the wave amplitude between P1 and P2 in the verification cases. Another benefit of the modified case setup is the reduced computation time as the landslide slope and the time before slide impact are not simulated. Moreover, the simulation duration and tank extension are reduced to 10 m and 5 s, respectively, and we focus on the first wave gauge P1.

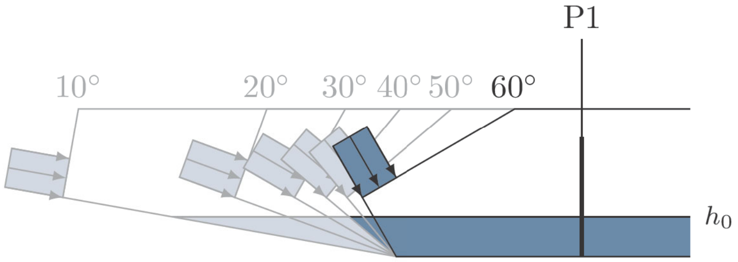

Figure III.11: Modified simulation setup for the sensitivity analysis. Four geometries for four impact angles are shown. The inlet boundary condition, indicated by the arrows, prescribes the velocity $\overline{u}$ over the slide thickness $\overline{s}$ for a duration of Δt. The wave is recorded as before at P1. The geometry is automatically generated and the position of the inlet follows from the still water depth h_0.

Table III.5: Slide parameters in the sensitivity analysis. Underlined parameters are combined with all other parameters, non-underlined parameters are combined only with underlined parameters.

slide duration Δt_s	slide velocity $\overline{v}_\mathrm{s}$	slide thickness $\overline{s}$	angle α	depth h_0
0.25 s	$1\,\mathrm{m\,s^{-1}}$	0.01 m	10°	0.15 m
0.50 s	$2\,\mathrm{m\,s^{-1}}$	0.02 m	20°	0.30 m
1.00 s	$3\,\mathrm{m\,s^{-1}}$	0.04 m	30°	0.45 m
1.50 s	$4\,\mathrm{m\,s^{-1}}$	0.06 m	40°	0.60 m
	$6\,\mathrm{m\,s^{-1}}$	0.08 m	50°	0.75 m
			60°	0.90 m

We choose parameters as presented in Tab. III.5 to extend the coverage of the parameter space in comparison to section III.3. In particular, we are interested in lower Froude numbers to investigate the regime change between subcritical ($\mathrm{F} < 1$) and supercritical ($\mathrm{F} > 1$) wave generation. To reduce the number of required simulations, only selected parameters (underlined in Tab. III.5) are combined with all other parameters. This way, we reduce the number of simulations to 112, without influencing the parameter resolution significantly. Each parameter is applied in at least four simulations. All simulations with the simplified case setup have been executed on a high performance cluster within 24 hours, using about 400 Intel Xeon E5-2690 v4 cores.

The relationship between the simulated dimensionless slide parameters and the first wave crest is presented in Fig. III.12. It can be seen that we achieve a wide range of slide parameters and that they are not as correlated as before. The results of the scaling relations and the respective differences are presented in Fig. III.13 (see also Tab. III.6). The best fitting relation for this setup is $A_{15\Delta t}$ with an average relative difference of 23%, followed by A_{HH10} with a relative difference of 27%. As before, the difference of relation A_{F02} (Eq. (III.25)) collapses to a line and the respective difference is similar with roughly 70%. This fact is very interesting and hints towards a strong predictive power of this relation.

A simple statistical analysis gives a good overview over the significant correlations between landslide parameters and the wave amplitude. The correlation between wave amplitude and landslide parameters is given in terms of correlation coefficients as $R(M, A_{\mathrm{m}}) = 0.88$, $R(\mathrm{F}, A_{\mathrm{m}}) = 0.74$, $R(S, A_{\mathrm{m}}) = 0.78$, and $R(\Delta T, A_{\mathrm{m}}) = 0.32$. The correlation between the wave amplitude A_{m} and the slope angle α is very low, $R(\cos(\alpha), A_{\mathrm{m}}) = 0.06$.

Further, a multiple regression was conducted to derive multiple scaling relations with increasing numbers of parameters. Inspired by the high single parameter correlation of landslide mass M with wave amplitude A_{m}, we first tested a scaling relation solely based on this parameter. The two free parameters were optimized to fit the numerical results, leading to

$$A_{\mathrm{M},1} = 0.45\, M^{0.83}. \tag{III.34}$$

The wave amplitude is predicted by this relation with an average relative error of 26% and the correlation (R-value) between the relation and simulation is 0.91. A second scaling relation (two parameter relation), inspired by Fritz (2002), is based on Froude number F and slide thickness S,

$$A_{\mathrm{M},2} = 1.3\, \mathrm{F}^{1.25}\, S^{0.97} \tag{III.35}$$

and yields an average relative difference of 20%. The correlation between predicted and simulated amplitude is 0.95. Powers of F and S are very similar to values reported by Fritz (2002) but the constant factor is about 5 times higher. This was already indicated by Fig. III.13, where the difference of relation (III.25) was appearing as a line. Other relations based on two parameters show a similar performance, e.g.,

$$A_{\mathrm{M},2.2} = 1.0\, M^{0.99}\, \Delta T^{-0.58}, \tag{III.36}$$

based on landslide mass M and landslide duration ΔT (average difference 18% and R-value 0.94). Taking into consideration three parameters,

$$A_{\mathrm{M},3} = 0.83\, \mathrm{F}^{0.76}\, S^{0.52}\, M^{0.40}, \tag{III.37}$$

reduces the average relative difference to 16% (R-value 0.95). Adding the impact angle α (four parameters),

$$A_{\mathrm{M},4} = 0.89\,\mathrm{F}^{0.80}\,S^{0.50}\,M^{0.38}\,\cos(\alpha)^{0.57}, \tag{III.38}$$

improves results slightly (difference 14%, R-value 0.95). Note that with the present setup, all these parameters and the dimensionless landslide duration ΔT are related through (see also Eq. (III.33))

$$M = S\,\mathrm{F}\,\Delta T \tag{III.39}$$

and they can be exchanged respectively in Eqs. (III.37) and (III.38). Three selected scaling relations ($A_{\mathrm{M},1}$, $A_{\mathrm{M},2}$, $A_{\mathrm{M},3}$) are compared with simulation results in Fig. III.14 alongside the relative difference.

Notably, not all relations perform similar if they are applied to the cases of Bullard *et al.* (2019). As shown in Tab. III.6, especially relations involving the total landslide mass M perform poorly. $A_{\mathrm{M},2}$, based on A_{F02}, performs best in such a scenario.

Table III.6: Average difference between scaling relations when compared to experiments and numerical simulations. The first block shows relations from literature, the second block shows relations optimized to the inlet driven simulations. They are compared to experiment and the gravity driven simulations (grey numbers) without further optimization.

	Scaling rel.	optimized for	Experiment	gravity driven	inlet driven
literature	A_{F02}	granular slides	68%	73%	71%
	A_{HH10}	granular slides	43%	40%	29%
	A_{Z15S}	buoyant slides	79%	79%	55%
	A_{Z15DT}	buoyant slides	59%	62%	25%
	A_{q}	granular slides	50%	58%	72%
	$A_{\mathrm{q,max}}$	liquid slides	29%	25%	47%
optimized	$A_{\mathrm{M},1}$	simulations	55%	52%	26%
	$A_{\mathrm{M},2}$	simulations	24%	15%	20%
	$A_{\mathrm{M},2.2}$	simulations	72%	64%	18%
	$A_{\mathrm{M},3}$	simulations	31%	20%	16%
	$A_{\mathrm{M},4}$	simulations	26%	16%	14%

III.5 Discussion

III.5.1 Verification

We observed severe problems with the convective CFL condition (Eq. (III.11)). A reduction of the limit on $\mathrm{CFL}^{\mathrm{conv}}$ (as done from 0.5 to 0.1 and further to 0.05)

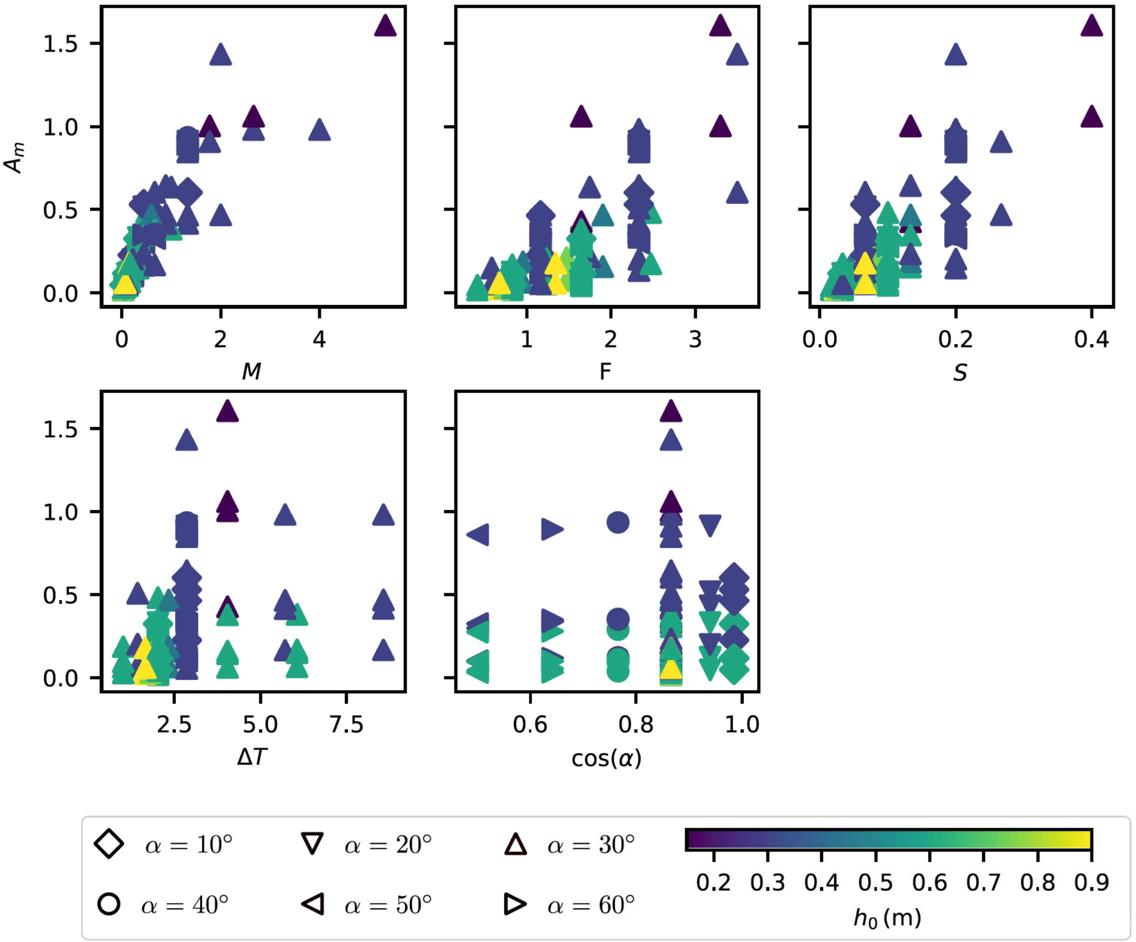

Figure III.12: Dimensionless mean properties of the landslides in the modified and extended simulation setup. The dimensionless landslide mass M, the landslide Froude number F, the dimensionless landslide thickness S, the dimensionless landslide duration ΔT and the cosine of the impact angle cos(α) are plotted against the dimensionless wave amplitude A_{m}. The colour represents the still water depth h_0, the mark represents the impact angle α.

helps to some regard, however, a reliable convergence can only be achieved with the full CFL criterion, including the viscous contributions $\mathrm{CFL}^{\mathrm{diff}}$. This can be traced back to the fact that the momentum conservation equation is dominated by viscous stresses. The diffusive term of the partial differential equation has to be taken into account in stability considerations, as already shown by Courant *et al.* (1928) (see also Ferziger and Perić, 2002; Moukalled *et al.*, 2016, for a more specific interpretation in terms of Navier–Stokes Equations). The domination of viscous stresses can have many reasons, in our cases it can be related to the small scale of the experiment and the respectively small cell size (compare scaling of Eq. (III.11) with Eq. (III.12)) while the viscosity itself is not exceptionally high. Furthermore, the jump of the viscosity at the free surface might be problematic.

Most numerical results converge well with the correct time stepping criterion and we estimated a numerical uncertainty of a few percent. Some gauges (P2

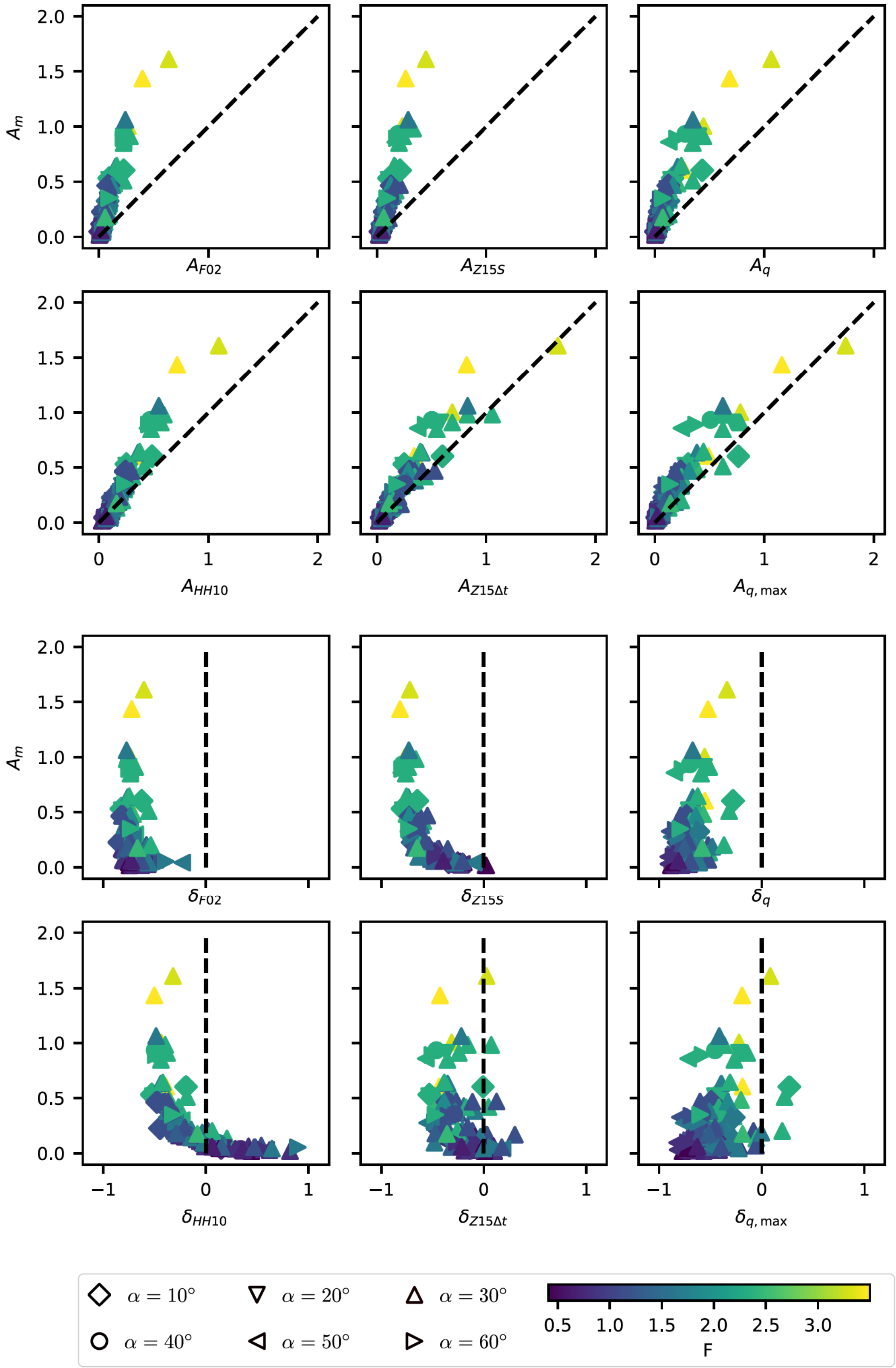

Figure III.13: Semi-empirical models for the first wave crest A_{HH10}, A_{Z15S}, $A_{\mathrm{Z15\Delta t}}$, A_q, $A_{\mathrm{q\,max}}$ and A_{F02} compared with the numerical results. The respective differences to simulations are shown below. The colour represents the slide Froude number F, the mark represents the impact angle α. The black dashed line indicates a perfect fit.

to P5) differ from this trend, but these deviations can likely be linked to wave breaking. This issue could probably be addressed by fine-tuning the parameters of the turbulence model, but investigating this is beyond the scope of this paper.

Generally, as reported by Roenby *et al.* (2017), 10 to 20 cells along the wave crest are required in OpenFOAM with MULES for accurate results of non-breaking waves. This was confirmed by our results which also contain breaking waves. The applied mesh size of $\Delta x = 0.01\,\mathrm{m}$ was sufficient for most waves, although small waves with $a_\mathrm{m} < 0.1\,\mathrm{m}$ appear too diffusive in simulations (find the full set of simulations in appendix III.8). This is especially the case for the trailing wave train following the first wave crest. This confirms once more that at least 10 cells along the wave crest should be used in OpenFOAM. Results appear very accurate with 20 cells along the wave crest and we expect no further improvement with finer meshes as results converge rapidly towards the exact solution. Moreover, further refinement is very expensive for a long tank as used in here, as the numerical cost grows quickly (with $1/\Delta x^4$) due to the strict stability criterion. It should be noted that this issue might not be equally severe for real scale cases. The length scale will be substantially bigger in real scale cases while the viscosity will be similar (depending on landslide rheology). This scaling behaviour will allow comparably large time steps and lower execution times for larger cases.

III.5.2 Validation

Aside from numerical accuracy, the applied mathematical model was tested for physical accuracy, i.e. if it is appropriate for the considered problem. This is achieved by a comparison of the slide thickness, the slide velocity, the first wave crest amplitude and the arrival time of the wave in simulations and experiments. We want to stress that it is important to only use converged results with low numerical uncertainty in such a comparison.

The simulated landslide velocity fits reasonably well to the experiments with two outliers ($V_0 = 0.2\,\mathrm{m}^3$ and $V_0 = 0.3\,\mathrm{m}^3$). The reason for this discrepancy could not be conclusively explained. However, we assume that the difference remains within the uncertainty of the experiments and we found the numerical results to be reasonable. The error in the slide thickness is substantially higher. The numerical method is not able to resolve the thin tale of the landslide and it appears with a thickness of $0.005\,\mathrm{m}$ in simulations (see Fig. III.6). An unrealistic amount of fluid is accumulated in the tail. This volume is missing in the front and middle region of the slide where the thickness is respectively underestimated. Finally, a droplet forms from all the fluid that was left on the slope and that could not be resolved by the numerical method.

This behaviour was observed with all mesh sizes during verification. This might indicate that a substantially finer mesh is required or that the method is not suitable to resolve the thin tale of the fluid landslide. Depth-integrated flow models are not affected by such problems and will perform better in this situation. This issue does not affect the inlet driven simulations for the scaling analysis as the landslide entered the simulation domain close to the impact area with constant and resolvable thickness. The relative error in the maximum slide thickness is roughly 30% for the three small landslides but almost 50% for the largest landslide. The higher error for the largest slide is related to the increased discharge in the experiment (133% of initial landslide volume). The additional volume in the experimental landslide can probably be traced back to entrainment of air into the turbulent slide which is not represented by the numerical model.

Notably, the boundary layer of the slope has not been resolved either. This layer is of high importance for the basal friction and thus the velocity of the landslide. However, basal friction seems not important in the investigated setup and the velocity is not affected by this issue. This might change for other materials such as granular slides, where the friction is substantially higher and depending on a well resolved boundary layer.

The simulated wave amplitude and the arrival time compare generally well to the experiment. We observe that the error diminishes in the far field. This indicates that the turbulent generation stage and wave breaking is the most challenging problem, while wave propagation and the prediction of the limit $a_{\mathrm{m},i} \to 0.6\, h_0$ is remarkably accurate. Note, that the limit found in experiments and numerical simulations is considerably lower than the breaking limit for solitary waves close to 0.8 times the water depth.

The highest relative error in the verification case appears at P3 (36%). This difference is likely related to the breaking of the wave, which takes place before P3 in the experiment but after P4 in the numerical simulation. Accordingly, the error at P5 is small (6%) and the far field error at the last gauge, P9, is even smaller (1%). In fact, breaking of waves and the amplitude thereafter is predicted well by the numerical method, compare Fig. III.8. However, the timing is very sensitive to diffusive processes in the flow and the exact onset is hence hard to predict with the numerical method. This leads to large errors and partially diverting results at Gauges P2 to P5.

Extending the validation to cases beyond the verification case $V_0 = 0.4\,\mathrm{m}^3$, $h_0 = 0.3\,\mathrm{m}$, we found that experimental and numerical near field amplitudes match generally well, with only a few cases giving larger errors (above 25%). The same is the case for far field amplitudes, however, where the error increases for lower wave amplitudes and thus lower landslides volumes to $\Delta a_{\mathrm{m},9} = 0.014\,\mathrm{m}$ for $V_0 = 0.3\,\mathrm{m}^3$ and $\Delta a_{\mathrm{m},9} = 0.016\,\mathrm{m}$ for $V_0 = 0.2\,\mathrm{m}^3$. This most likely corresponds to the numerical uncertainty, which is related to the number of cells across the wave crest.

III.5.3 Scaling relations

The six semi-empirical scaling relations have been compared to the experimental measurements of Bullard *et al.* (2019) and the respective numerical results in Fig. III.10 and Tab. III.6. Further, we extended the parameter space substantially with a simplified setup. In particular, we aimed to cover the more subcritical wave generation indicated by $\mathrm{F} < 1$, different impact angles and higher reservoir depths. The simple statistical analysis showed that the total landslide mass M is the most reliable and most influential landslide parameter for this setting.

Moreover, F and S are second most important when used as single correlation parameters. According to our simulations, the impact angle α plays no relevant role for the wave amplitude. However, it should be noted that these results are limited to almost frictionless landslides with density ratio $R = 1$ and that the impact angle might play a role in buoyant or granular slides.

The multiple regression gives us further insight into the wave generation mechanism. The scaling relation with landslide mass M yields an average relative error of 25% in relation to the simulations. Taking into account the velocity of the landslide at impact can reduce the average relative error to 17%. Both of these relations perform exceptionally good considering their simple structure and the wide range of parameters. In fact, the scaling with F and S ($A_{\mathrm{M},2}$, Eq. (III.35)) yields consistently good results in all simulations as well as in experiments of Bullard *et al.* (2019) and Fritz (2002). The difference found in the constant factor of this relation might be related to the relative density R and a respective extension might further improve the predictive skills of this relation.

$A_{\mathrm{M},1}$ (Eq. (III.34)) and $A_{\mathrm{M},2.2}$ (Eq. (III.36)) including the landslide mass M describe the inlet driven simulations well but the predictions can not be transferred to the setup of Bullard *et al.* (2019), where they perform poorly. We conclude that the landslide mass is transferred into wave energy more efficiently in the inlet driven simulations. This is most likely related to the shape of the landslide and the low energy tail of the naturally evolving landslide which does not contribute to tsunami genesis. The shape of the landslide might be an important factor in real case landslide tsunamis and different failure mechanisms (e.g. cliff collapses with short travel distances (Viroulet *et al.*, 2013)) might require different scaling relations and parametrisations. Equation (III.35), based on F and S, is not affected by these issues as F and S are estimated from the highly energetic front and middle part of the landslide that actually contribute to tsunami genesis (compare tsunami generation duration $\Delta t_{75\%}$). This shows the limits of scaling relations and that they cannot be transferred to different situations without substantial uncertainties. Properties of the landslide that are not described by mean parameters can have a significant impact on the wave generation and scaling relations are not able to cover these influences. This also highlights the added value of numerical simulations which are able to describe various situations with a single set of parameters.

Interestingly, the simulations allow an estimation of the tsunami generation duration. Fig. III.12 shows that the wave amplitude remains constant after the landslide duration reaches a value of approximately $\Delta T = 4$. Further simulations with landslide durations up to $\Delta T = 15$ (not shown) confirmed this conjecture and we estimate the tsunami generation duration to be not longer than

$$\Delta t_{\mathrm{gen,max}} \approx 4 \sqrt{\frac{h_0}{g}}. \tag{III.40}$$

The landslide mass impacting the reservoir within this duration can be transferred into the tsunami while the remaining mass has no first order effect on the near field wave amplitude.

In the setting investigated here, the basin and especially the impact area are very shallow, which means that the landslide is displacing the water mass horizontally during the impact, mimicking a collisional process. Our findings suggest that the landslide mass M (or volume) has a first order effect on the tsunami generation and that the displaced water volume in the basin is the primary factor controlling the tsunami generation. Further, the scaling can be improved by including the Froude number F, indicating that the momentum transfer between the landslide and the water reservoir plays a secondary but still notable role. We anticipate that non-linear effects in the generation phase are also the reason for the non-linear best fit relationship. Combining more than two parameters does not improve the predictive skill of the semi-empirical relations substantially in our case. We further note that there is no substantial difference between sub-critical ($\mathrm{F} < 1$) and critical ($\mathrm{F} > 1$) landslides (see Fig. III.14a). A possible reason is that the present configuration resembles a horizontal displacement or pushing rather than a changing bottom topography that moves independently from the wave, such as for submarine landslides (e.g. Lovholt *et al.*, 2015). Moreover, all of the simulations involve supercritical generation in the shallow region of the impact near the shoreline, which implies that the definition of the Froude number in terms of the terminal depth is somewhat artificial. Finally, it should be noted that these observations are limited to idealized water slides and that granular or buoyant slides might behave different.

III.6 Conclusion and outlook

The experiments of Bullard *et al.* (2019) allowed us to verify and validate OpenFOAM for landslide tsunamis. The landslide was represented in an idealized manner by water, allowing us to ignore granular rheology and porosity of the landslide. Furthermore, we ignored variations across the tank width to reduce the experiments to a two-dimensional problem. The multiphase solver of OpenFOAM is well suited to simulate the process, if the correct Courant-Friedrichs-Lewy criterion is considered. However, the CFL criterion is often used in a simplified form, which we found to be insufficient for impulse wave simulations. The strict stability criterion that we applied leads to a substantial increase in computational cost, especially for fine meshes. The applied CFL criterion can be further refined by taking into account that a part of the viscous term is included implicitly. In the long term, an implicitly block-coupled solver (e.g. Uroić *et al.*, 2019), not limited by such a stability condition, is desired to solve these performance issues. In real scale cases this stability criterion might be less problematic due to its scaling with cell size and viscosity. This indicates that the numerical cost of real scale impulse wave cases (as conducted with other tools before, see e.g. Gisler *et al.*, 2006; Gabl *et al.*, 2015) with OpenFOAM might be manageable. The cell size at the free surface should be smaller than 1/10 of the expected wave amplitude (see also Roenby *et al.*, 2017). Geometric interface convection schemes (see e.g. Marschall *et al.*, 2012; Roenby *et al.*, 2017) might achieve the

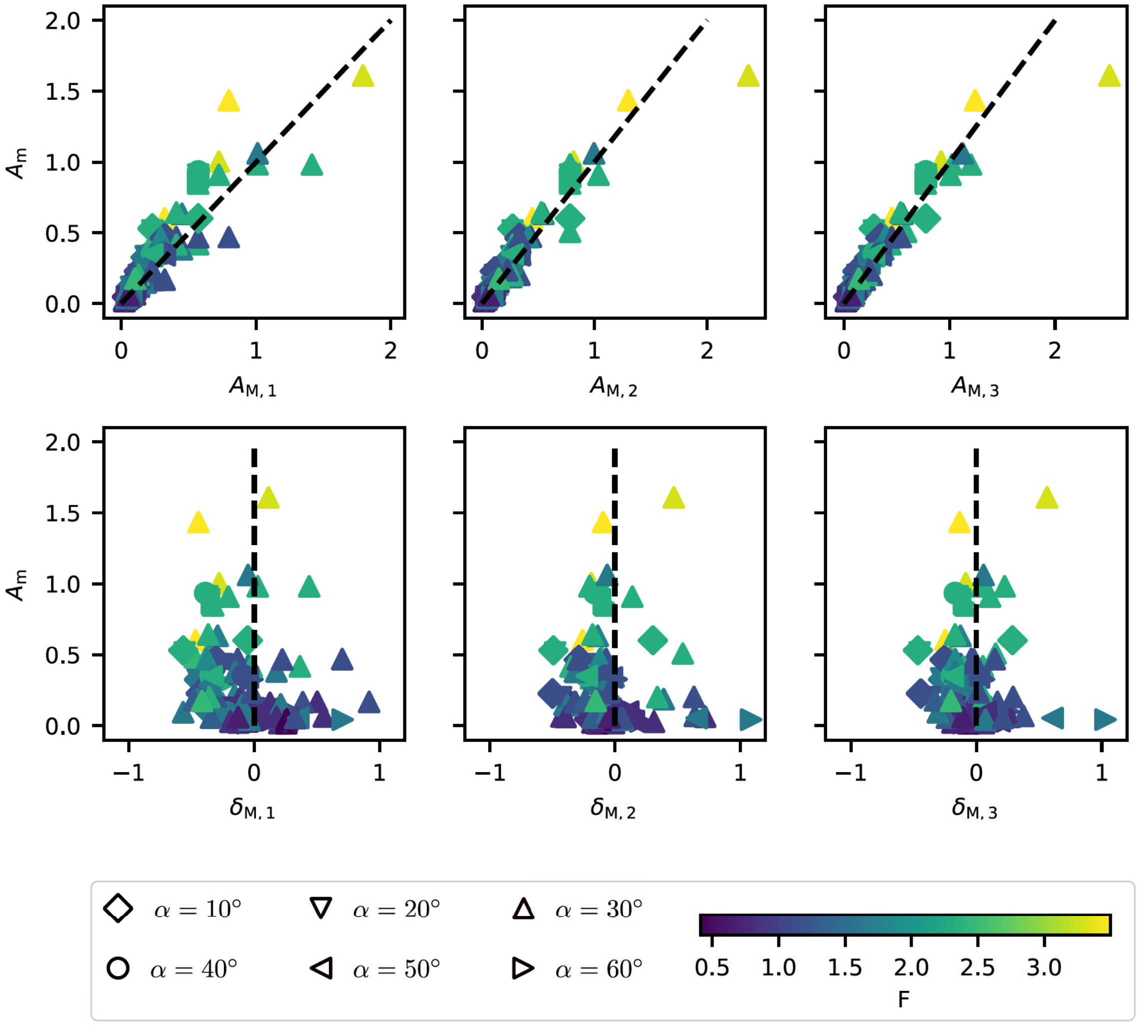

Figure III.14: Optimized relations for the first wave crest with (left to right) 1 parameter ($A_{\mathrm{M},1}$), 2 parameters ($A_{\mathrm{M},2}$) and 3 parameters ($A_{\mathrm{M},3}$) compared to the numerical results. The respective differences are shown below. The colour represents the slide Froude number F and the mark represents the impact angle α. The black dashed line indicates a perfect fit.

same accuracy with less cells. The required grid resolution is achievable for impulse waves with relatively high wave amplitudes (in relation to the simulation domain). However, tsunamis with small amplitude in relation to the simulation domain are out of the scope of this method and depth-integrated models should be applied. The landslide and especially its thin tail and its bottom boundary layer could not be properly resolved in this study, leading to an underestimation of the flow thickness in the tsunamigenic part of the landslide. The slide velocity was not affected, presumably because the boundary layer and basal friction played a minor role in the investigated setup. A more realistic representation of the landslide with complex rheologies might require a substantially higher resolution of the landslide slope.

We executed a sensitivity and scaling analysis in order to evaluate the predictive power of semi-empirical scaling relations. We found that a simple scaling relation involving solely the landslide mass or volume performs surprisingly well. This can be traced back to the wave generation process which relies to leading order on the displacement of water in the basin. The sensitivity study revealed an upper limit of the tsunami generation duration, after which the first wave crest cannot be influenced by the landslide. In most cases the landslide duration is not sufficient for the wave to run away and the Froude number, quantifying this effect, has less influence compared to submarine landslides. Including the Froude number and thus the landslide velocity into the semi-empirical relation gives a slightly better correlation, which implies a second order effect of momentum transfer from the landslide into the water reservoir. Furthermore, multi-parameter scaling relations involving three or more landslide parameters did not notably improve the predictive power of the semi-empirical relations. However, this observation is limited to the simplified model applied in here and might not translate to granular and buoyant slides. We noticed that scaling relations based on the total landslide mass cannot easily be transferred between our two simulation setups, which we relate to a more efficient wave generation in the second setup. The scaling relation based on the Froude number and the slide thickness performed better in this regard and achieved good results in both setups with a single set of parameters. However, Froude number and slide thickness are significantly harder to identify and to predict than the total landslide mass.

The applied numerical method is flexible and allows a wide range of further studies. Three dimensional cases and real scale cases are in the range of possibilities with high performance computing. Dynamic mesh refinement and load balancing might further increase the efficiency (Rettenmaier *et al.*, 2019). Granular and other visco-plastic rheologies can be included in a simple way by introducing a non-Newtonian viscosity relation (e.g. Rauter *et al.*, 2020). Porosity and pore fluid effects, on the other hand, require deeper modification of the numerical method (e.g. Cheng *et al.*, 2017; Si *et al.*, 2018b). Natural terrain can be included in simulation with complex body-fitted meshes (Rauter *et al.*, 2018).

III.7 Appendix: Stability and time stepping

Hyperbolic equations (III.2)-(III.3) introduce characteristic velocities at which disturbances are propagated and the numerical method has to account for this properties. The elliptical pressure equation derived from Eq. (III.1) is exempted as it is solved implicitly. The characteristic velocity of the momentum conservation equation (III.3) is usually the highest and introduces the strongest limitations in terms of time step duration. We will show in the following the derivation of the maximum time step duration at which stability can be guaranteed. For the presented simulations, it was imperative to consider the exact limit and not the approximation that is usually applied in OpenFOAM. Equation (III.3) can be written in a simplified partially discretized form as (see, e.g., Moukalled *et al.*, 2016)

$$
\begin{aligned}
V_p\,\rho_P^{i-1}\,\frac{\mathbf{u}_P^{i}-\mathbf{u}_P^{i-1}}{\Delta t} + \underbrace{\sum_{\forall f}\left(\rho_f^{i-1}\,S_f\,\mathbf{n}_f\cdot\mathbf{u}_f^{i-1}\right)\mathbf{u}_f^{i-1}}_{\text{convective term}} = \\
\underbrace{\sum_{\forall f}\mu_f\,\frac{\mathbf{u}_N^{i-1}-\mathbf{u}_P^{i-1}}{d_{PN}}S_f + V_P\left(\nabla\cdot\left(\mu\,\left(\nabla\,\mathbf{u}\right)^{T}\right)\right)_P}_{\text{diffusive term}} \\
-V_P\,\left(\nabla p\right)_P + V_P\,\rho_P^{i-1}\,\mathbf{g}+, \qquad \text{(III.41)}
\end{aligned}
$$

where the index f indicates values on a face f which is located between cells P and N (see Fig. III.15). Face values are calculated by interpolating values on cell centres P and N. The contributions of molecular and turbulent viscosity have been combined into the viscosity μ as their effect on stability is similar. The velocity at the face $\mathbf{u}_f$ is in the following approximated with the upwind scheme for an outward pointing velocity vector as $\mathbf{u}_f = \mathbf{u}_P$. It can be shown that this is the worst case in terms of transient stability and thus an upper limit for the stability criterion. $\mathbf{n}_f$ is the outward pointing (from P to N) face normal vector and S_f the face area. V_P is the cell volume of cell P and d_{PN} is the distance between cell centres P and N.

The index i indicates fields at the unknown time step t^i, the index $i-1$ at the last known time step $t^{i-1} = t^i - \Delta t$, where Δt is the time step duration (see Fig. III.15). Discretization of the pressure gradient term is not required at this point. Furthermore, the transposed component of the viscous term is ignored for simplicity (note that this would be accurate for constant viscosity) and it is assumed that its magnitude matches its non-transposed part, which can be written as a diffusion term. It is further assumed that the diffusion term is included explicitly, although only the transposed component of the viscous term is included explicitly in OpenFOAM. This way, we can estimate the limitation introduced by the transposed component. The stability of transient cases depends on the coefficients of $\mathbf{u}_P^i$ and $\mathbf{u}_P^{i-1}$ in this equation, which are collected and written as a_P^i and a_P^{i-1}. For the solution to be stable and converging, it is required that a_P^i and a_P^{i-1}, i.e. coefficients of temporal neighbours, have different

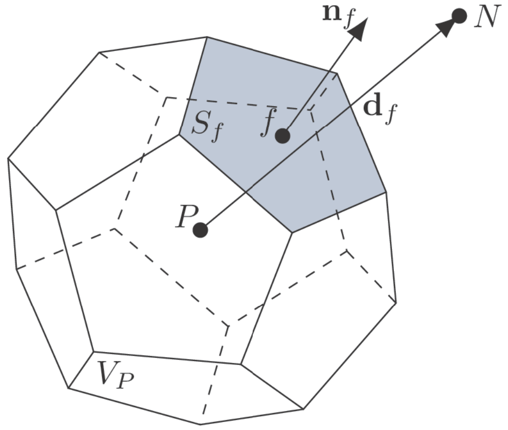

space domain

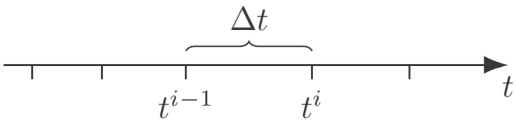

time domain

Figure III.15: Discretisation of space is conducted with finite volume cells, the time is split into a finite number of time steps.

signs (opposite signs rule, see e.g. Moukalled *et al.*, 2016). All coefficients of $\mathbf{u}_P^i$,

$$a_P^i = \frac{V_P\,\rho_P^{i-1}}{\Delta t} > 0, \tag{III.42}$$

are strictly positive, implying that coefficients of $\mathbf{u}_P^{i-1}$

$$a_P^{i-1} = \quad \frac{V_P\,\rho_P^{i-1}}{\Delta t} - \sum_{\forall f}\left(\rho_f^{i-1}\,S_f\,\mathbf{n}_f\cdot\mathbf{u}_f^{i-1}\right) - \sum_{\forall f}\mu_f\,\frac{S_f}{d_{PN}} \leq 0 \tag{III.43}$$

have to be negative for a stable solution. This imposes a restriction on the time step duration Δt,

$$\Delta t \leq \frac{V_P\,\rho_P^{i-1}}{\sum\limits_{\forall f}\left(\rho_f^{i-1}\,S_f\,\mathbf{n}_f\cdot\mathbf{u}_f^{i-1} + \mu_f\,\dfrac{S_f}{d_{PN}}\right)}, \tag{III.44}$$

which is generally known as the CFL condition (after Courant *et al.*, 1928). The Courant-number for equation (III.41) is defined as

$$\mathrm{CFL} = \frac{\Delta t\,\sum\limits_{\forall f}\left(\rho_f^{i-1}\,S_f\,\mathbf{n}_f\cdot\mathbf{u}_f^{i-1} + \mu_f\,\dfrac{S_f}{d_{PN}}\right)}{V_P\,\rho_P^{i-1}}, \tag{III.45}$$

and limited to a specific value for stability, in case of the forward Euler scheme, CFL ≤ 1 (Moukalled *et al.*, 2016). Contributions of diffusion or viscosity (containing μ) and convection (containing $\mathbf{u}$) are simple to identify and two limit cases of neglectable viscosity

$$\mathrm{CFL}^{\mathrm{conv}} = \frac{\Delta t \sum\limits_{\forall f} \left(\rho_f^{i-1} \, S_f \, \mathbf{n}_f \cdot \mathbf{u}_f^{i-1} \right)}{V_P \, \rho_P^{i-1}}, \tag{III.46}$$

and neglectable convection

$$\mathrm{CFL}^{\mathrm{diff}} = \frac{\Delta t \sum\limits_{\forall f} \left(\mu_f \, \dfrac{S_f}{d_{PN}} \right)}{V_P \, \rho_P^{i-1}}, \tag{III.47}$$

can be found. The latter is similar to the Fourier number in heat conduction problems (Incropera *et al.*, 2007). Equations can be simplified for one-dimensional equidistant (Δx) grids ($V_P = \Delta x \, \Delta y \, \Delta z$, $S_f = \Delta y \, \Delta z$, $d_{PN} = \Delta x$) and constant fields to Eqs. (III.11) and (III.12), which are commonly known and simpler to interpret. However, it should be noted that neither of those should be called Courant-number of Eq. (III.41), as they only cover respective parts or limit cases. If the viscosity μ is constant, it is possible to implicitly consider the respective term in a segregated solving routine, and only the non-linear convective term has to be considered in the stability criterion (Eq. (III.46)). Furthermore, assuming flowing water with a velocity of $10\,\mathrm{m\,s^{-1}}$, the contribution of viscosity would only be relevant for very fine meshes with grid size $\Delta x < 10^{-6}\,\mathrm{m}$. Therefore, the contribution of viscosity is often neglected, which is also the case in OpenFOAM. However, considering high viscosity flows (e.g. landslides) or flows with low particle velocities (e.g. surface waves), this leads to instabilities with devastating consequences for results. The here investigated flows have a remarkably high turbulent viscosity and a relatively low convection (velocity) in the later stages of wave propagation. Furthermore, small cells are required to describe the free surface waves. All these circumstances lead to a notable contribution of viscosity to the CFL-number and the full relation has to be considered.

III.8 Appendix: Validation simulations

In the following, we will provide the wave gauge data of all 16 simulations, that have been conducted for validation of the numerical routine. These simulations give a good overview over accuracy of the mathematical model and the numerical solution in various situations. This wave gauge data has been summarized in Fig. III.8 in form of the first wave crest.

Acknowledgements

We thank Wolfgang Fellin for his support, Gemma Bullard for performing the lab experiments, Johan Roenby, Mikael Mortensen, Geir Pedersen and

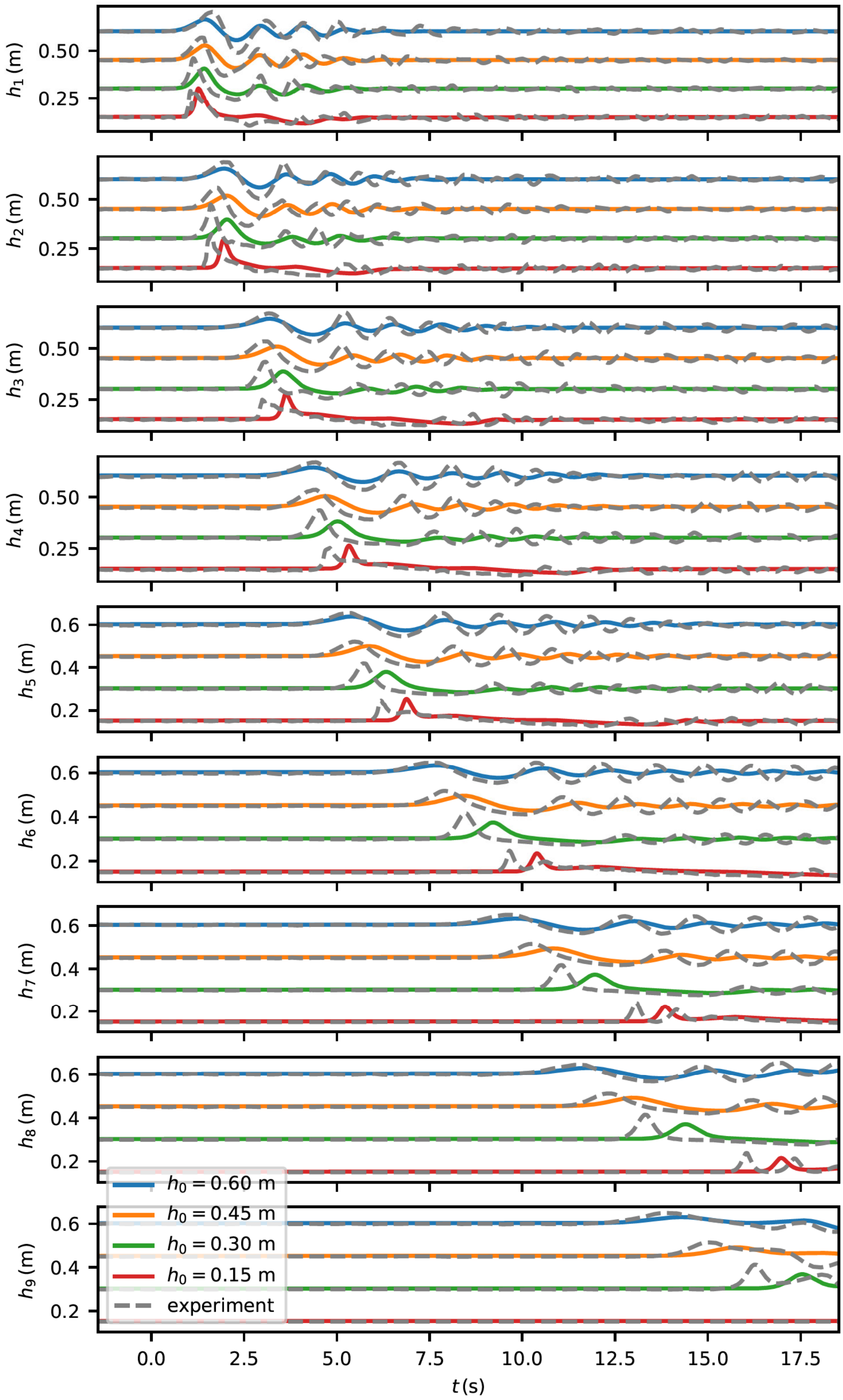

Figure III.16: Wave at gauges in simulations (colour) and experiments (grey) with a landslide volume of $V_0 = 0.1\,\mathrm{m}^3$.

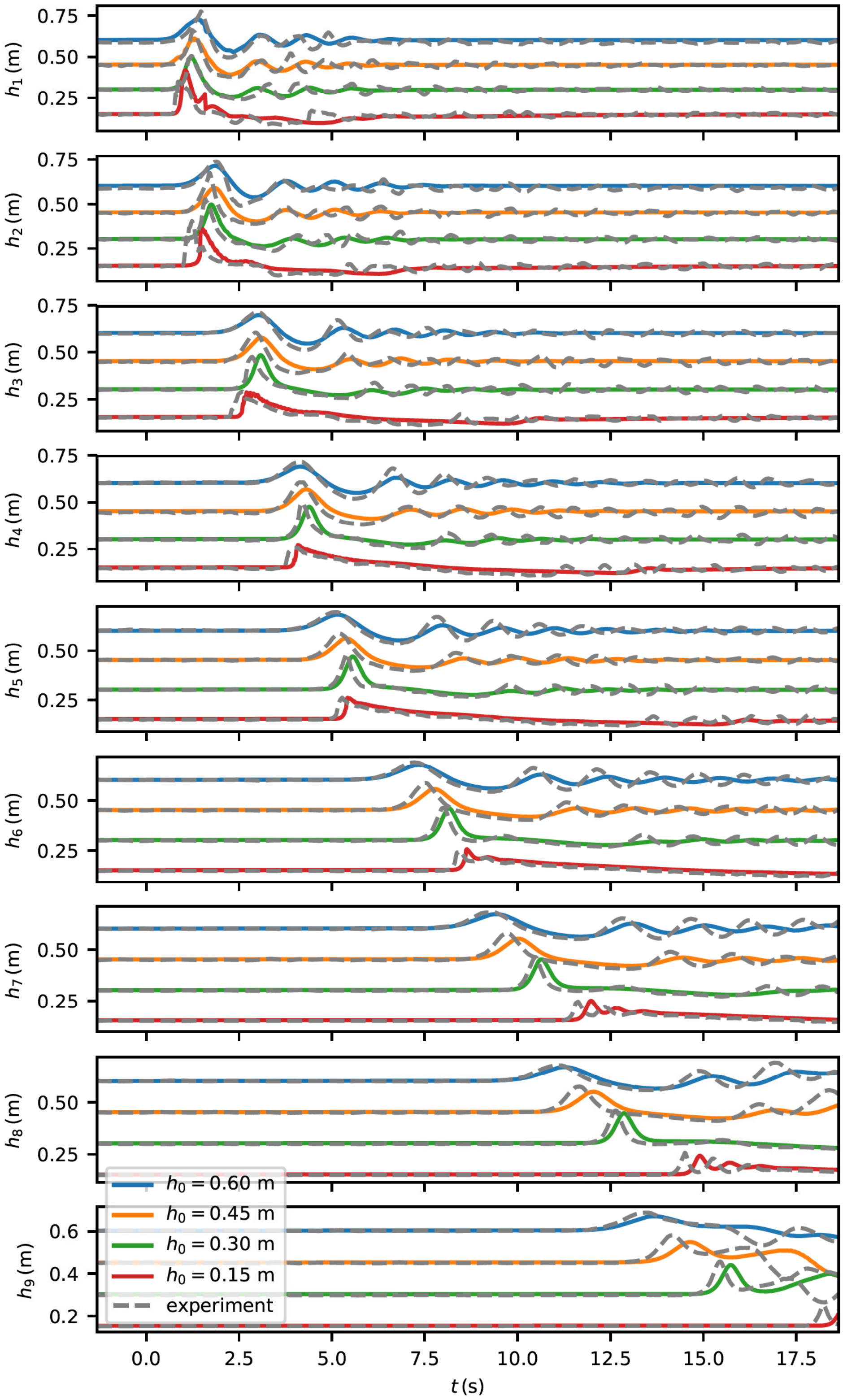

Figure III.17: Wave at gauges in simulations (colour) and experiments (grey) with a landslide volume of $V_0 = 0.2\,\mathrm{m}^3$.

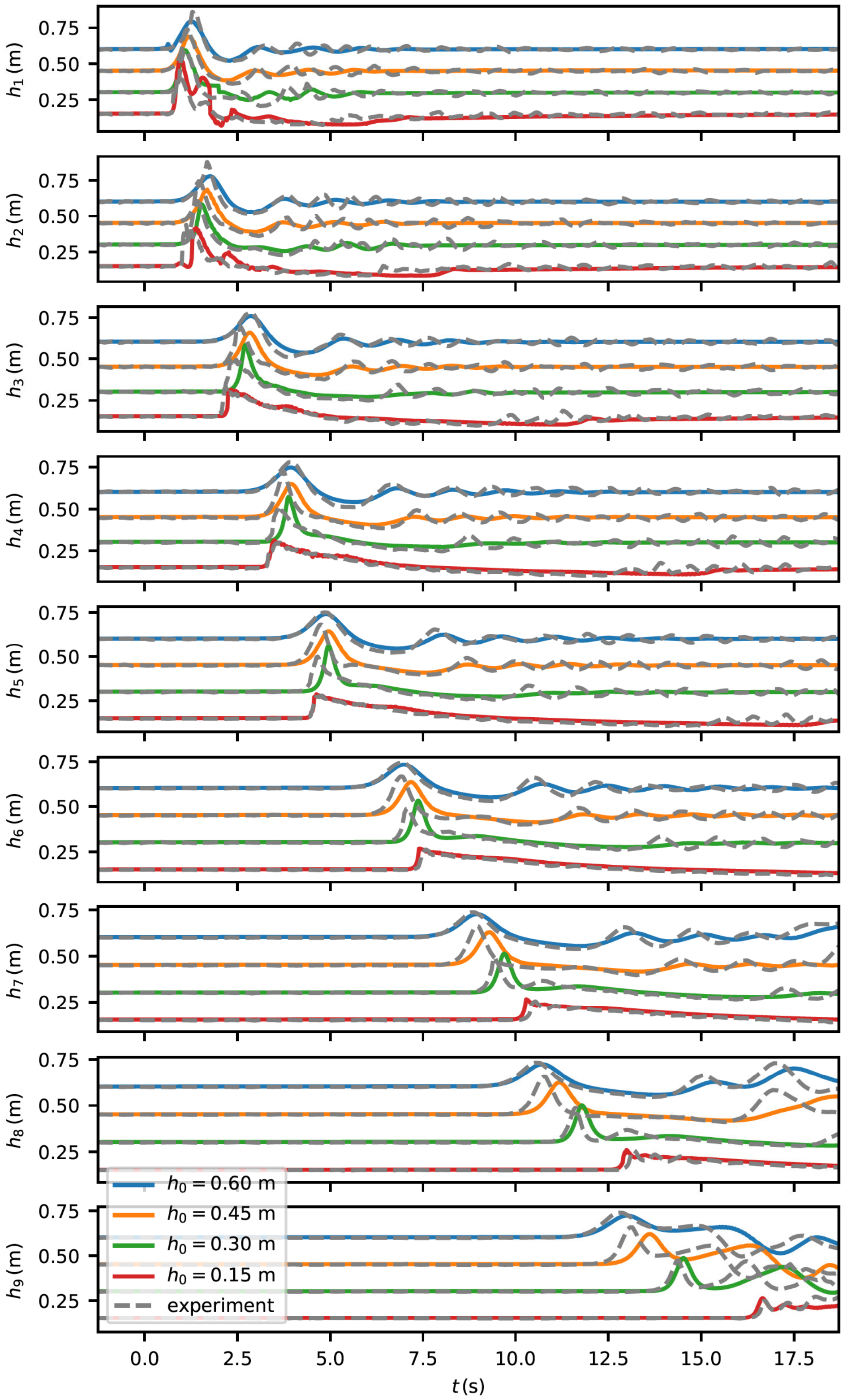

Figure III.18: Wave at gauges in simulations (colour) and experiments (grey) with a landslide volume of $V_0 = 0.3\,\mathrm{m}^3$.

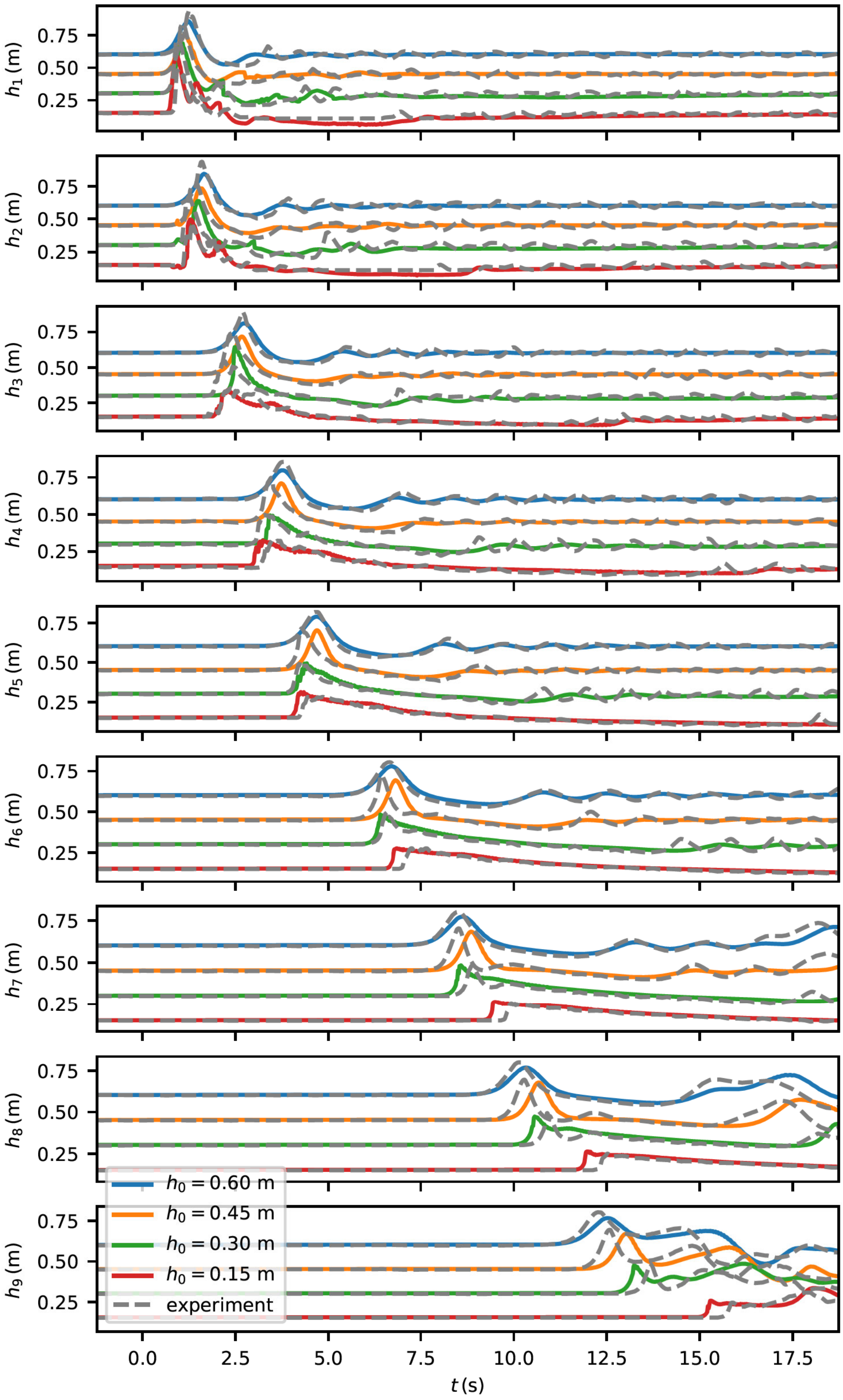

Figure III.19: Wave at gauges in simulations (colour) and experiments (grey) with a landslide volume of $V = 0.4\,\mathrm{m}$.

Oliver Korup for interesting discussions and valuable comments. We thank 2 anonymous referees for constructive criticism that helped improve the quality of the manuscript. This project has received funding from the European Union's Horizon 2020 research and innovation programme under the Marie Skłodowska-Curie grant agreement No. 721403 (SLATE). The computational results presented have been achieved (in part) using the HPC infrastructure LEO of the University of Innsbruck.

III.9 Bibliography

S. Abadie, J. C. Harris, S. T. Grilli and R. Fabre, "Numerical modeling of tsunami waves generated by the flank collapse of the Cumbre Vieja Volcano (La Palma, Canary Islands): Tsunami source and near field effects," *Journal of Geophysical Research*, vol. 117, no. C05030, 2012, DOI: 10.1029/2011JC007646.

S. Abadie, D. Morichon, S. Grilli and S. Glockner, "Numerical simulation of waves generated by landslides using a multiple-fluid Navier–Stokes model," *Coastal Engineering*, vol. 57, no. 9, pp. 779–794, 2010, DOI: 10.1016/j.coastaleng.2010.03.003.

T. Barker, D. G. Schaeffer, M. Shearer and J. M. N. T. Gray, "Well-posed continuum equations for granular flow with compressibility and μ(I)-rheology," *Proceedings of the Royal Society A*, vol. 473, no. 2201, p. 20160846, 2017, DOI: 10.1098/rspa.2016.0846.

F. Boyer, É. Guazzelli and O. Pouliquen, "Unifying suspension and granular rheology," *Physical Review Letters*, vol. 107, no. 18, p. 188301, 2011, DOI: 10.1103/PhysRevLett.107.188301.

G. K. Bullard, R. P. Mulligan, A. Carreira and W. A. Take, "Experimental analysis of tsunamis generated by the impact of landslides with high mobility," *Coastal Engineering*, vol. 152, p. 103538, 2019, DOI: 10.1016/j.coastaleng.2019.103538.

F. Chen, V. Heller and R. Briganti, "Numerical modelling of tsunamis generated by iceberg calving validated with large-scale laboratory experiments," *Advances in Water Resources*, vol. 142, p. 103647, 2020, DOI: 10.1016/j.advwatres.2020.103647.

Z. Cheng, T.-J. Hsu and J. Calantoni, "SedFoam: A multi-dimensional Eulerian two-phase model for sediment transport and its application to momentary bed failure," *Coastal Engineering*, vol. 119, pp. 32–50, 2017, DOI: 10.1016/j.coastaleng.2016.08.007.

R. Courant, K. Friedrichs and H. Lewy, "Über die partiellen Differenzengleichungen der mathematischen Physik," *Mathematische Annalen*, vol. 100, no. 1, pp. 32–74, 1928.

B. Domnik, S. P. Pudasaini, R. Katzenbach and S. A. Miller, “Coupling of full two-dimensional and depth-averaged models for granular flows,” *Journal of Non-Newtonian Fluid Mechanics*, vol. 201, pp. 56–68, 2013, DOI: 10.1016/j.jnnfm.2013.07.005.

J. H. Ferziger and M. Perić, *Computational methods for fluid dynamics*, Springer, 3rd edn., 2002.

H. M. Fritz, “Initial phase of landslide generated impulse waves,” Ph.D. thesis, ETH Zurich, 2002, DOI: 10.3929/ethz-a-004443906.

R. Gabl, J. Seibl, B. Gems and M. Aufleger, “3-D numerical approach to simulate the overtopping volume caused by an impulse wave comparable to avalanche impact in a reservoir,” *Natural Hazards and Earth System Sciences*, vol. 15, no. 12, pp. 2617–2630, 2015, DOI: 10.5194/nhess-15-2617-2015.

D. L. George, R. M. Iverson and C. M. Cannon, “New methodology for computing tsunami generation by subaerial landslides: Application to the 2015 Tyndall Glacier landslide, Alaska,” *Geophysical Research Letters*, vol. 44, no. 14, pp. 7276–7284, 2017, DOI: 10.1002/2017GL074341.

G. Gisler, R. Weaver and M. L. Gittings, “SAGE calculations of the tsunami threat from La Palma,” *Science of Tsunami Hazards*, vol. 24, no. 4, pp. 288–312, 2006.

S. T. Grilli, D. R. Tappin, S. Carey, S. F. Watt, S. N. Ward, A. R. Grilli, S. L. Engwell, C. Zhang, J. T. Kirby, L. Schambach and M. Muin, “Modelling of the tsunami from the December 22, 2018 lateral collapse of Anak Krakatau volcano in the Sunda Straits, Indonesia.” *Scientific Reports*, vol. 9, no. 1, pp. 11946–11946, 2019, DOI: 10.1038/s41598-019-48327-6.

S. S. Gylfadóttir, J. Kim, J. K. Helgason, S. Brynjólfsson, Á. Höskuldsson, T. Jóhannesson, C. B. Harbitz and F. Løvholt, “The 2014 L ake A skja rockslide-induced tsunami: Optimization of numerical tsunami model using observed data,” *Journal of Geophysical Research: Oceans*, vol. 122, no. 5, pp. 4110–4122, 2017, DOI: 10.1002/2016JC012496.

C. B. Harbitz, F. Løvholt and H. Bungum, “Submarine landslide tsunamis: how extreme and how likely?” *Natural Hazards*, vol. 72, no. 3, pp. 1341–1374, 2014, DOI: 10.1007/s11069-013-0681-3.

P. Heinrich, “Nonlinear water waves generated by submarine and aerial landslides,” *Journal of Waterway, Port, Coastal, and Ocean Engineering*, vol. 118, no. 3, pp. 249–266, 1992, DOI: 10.1061/(ASCE)0733-950X(1992)118:3(249).

V. Heller, M. Bruggemann, J. Spinneken and B. D. Rogers, “Composite modelling of subaerial landslide–tsunamis in different water body geometries and novel insight into slide and wave kinematics,” *Coastal Engineering*, vol. 109, pp. 20–41, 2016, DOI: 10.1016/j.coastaleng.2015.12.004.

V. Heller and W. H. Hager, “Impulse product parameter in landslide generated impulse waves,” *Journal of Waterway, Port, Coastal, and Ocean Engineering*, vol. 136, no. 3, pp. 145–155, 2010, DOI: 10.1061/(ASCE)WW.1943-5460.0000037.

V. Heller, W. H. Hager and H.-E. Minor, “Scale effects in subaerial landslide generated impulse waves,” *Experiments in Fluids*, vol. 44, no. 5, pp. 691–703, 2008, DOI: 10.1007/s00348-007-0427-7.

T. Ilstad, J. G. Marr, A. Elverhøi and C. B. Harbitz, “Laboratory studies of subaqueous debris flows by measurements of pore-fluid pressure and total stress,” *Marine Geology*, vol. 213, no. 1-4, pp. 403–414, 2004, DOI: 10.1016/j.margeo.2004.10.016.

F. P. Incropera, A. S. Lavine, T. L. Bergman and D. P. DeWitt, *Fundamentals of heat and mass transfer*, Wiley, 2007.

R. I. Issa, “Solution of the implicitly discretised fluid flow equations by operator-splitting,” *Journal of Computational Physics*, vol. 62, no. 1, pp. 40–65, 1986, DOI: 10.1016/0021-9991(86)90099-9.

H. Jasak, “Error analysis and estimation for the finite volume method with applications to fluid flows,” Ph.D. thesis, Imperial College, University of London, 1996.

P. Jop, Y. Forterre and O. Pouliquen, “A constitutive law for dense granular flows,” *Nature*, vol. 441, no. 7094, p. 727, 2006, DOI: 10.1038/nature04801.

F. Juretić, “cfMesh user guide,” Tech. rep., Creative Fields, Zagreb, 2015.

G.-B. Kim, W. Cheng, R. C. Sunny, J. J. Horrillo, B. C. McFall, F. Mohammed, H. M. Fritz, J. Beget and Z. Kowalik, “Three Dimensional Landslide Generated Tsunamis: Numerical and Physical Model Comparisons,” *Landslides*, pp. 1–17, 2019, DOI: 10.1007/s10346-019-01308-2.

B. E. Launder and D. B. Spalding, “The numerical computation of turbulent flows,” *Computer Methods in Applied Mechanics and Engineering*, vol. 3, pp. 269–289, 1974, DOI: 10.1016/0045-7825(74)90029-2.

P. L.-F. Liu, T.-R. Wu, F. Raichlen, C. E. Synolakis and J. C. Borrero, “Runup and rundown generated by three-dimensional sliding masses,” *Journal of Fluid Mechanics*, vol. 536, pp. 107–144, 2005, DOI: 10.1017/S0022112005004799.

F. Løvholt, P. Lynett and G. Pedersen, “Simulating run-up on steep slopes with operational Boussinesq models; capabilities, spurious effects and instabilities,” *Nonlinear Processes in Geophysics*, vol. 20, no. 3, pp. 379–395, 2013, DOI: 10.5194/npg-20-379-2013.

F. Løvholt and G. Pedersen, “Instabilities of Boussinesq models in non-uniform depth,” *International Journal for Numerical Methods in Fluids*, vol. 61, no. 6, pp. 606–637, 2009, DOI: 10.1002/fld.1968.

F. Løvholt, G. Pedersen and G. Gisler, “Oceanic propagation of a potential tsunami from the La Palma Island,” *Journal of Geophysical Research: Oceans*, vol. 113, no. C9, 2008, DOI: 10.1029/2007JC004603.

F. Lovholt, G. Pedersen, C. B. Harbitz, S. Glimsdal and J. Kim, “On the characteristics of landslide tsunamis,” *Philosophical Transactions of the Royal Society A*, vol. 373, no. 2053, p. 20140376, 2015, DOI: 10.1098/rsta.2014.0376.

G. Ma, J. T. Kirby, T.-J. Hsu and F. Shi, “A two-layer granular landslide model for tsunami wave generation: Theory and computation,” *Ocean Modelling*, vol. 93, pp. 40–55, 2015, DOI: 10.1016/j.ocemod.2015.07.012.

H. Marschall, K. Hinterberger, C. Schüler, F. Habla and O. Hinrichsen, “Numerical simulation of species transfer across fluid interfaces in free-surface flows using OpenFOAM,” *Chemical Engineering Science*, vol. 78, pp. 111–127, 2012, DOI: 10.1016/j.ces.2012.02.034.

F. Mintgen and M. Manhart, “A bi-directional coupling of 2D shallow water and 3D Reynolds-averaged Navier–Stokes models,” *Journal of Hydraulic Research*, vol. 56, pp. 771–785, 2018, DOI: 10.1080/00221686.2017.1419989.

F. Moukalled, L. Mangani and M. Darwish, *The finite volume method in computational fluid dynamics*, Springer, 2016, DOI: 10.1007/978-3-319-16874-6.

R. P. Mulligan, A. Franci, M. A. Celigueta and W. A. Take, “Simulations of landslide wave generation and propagation using the Particle Finite Element Method,” *Journal of Geophysical Research: Oceans*, vol. 125, p. e2019JC015873, 2020, DOI: 10.1029/2019JC015873.

R. P. Mulligan and W. A. Take, “On the transfer of momentum from a granular landslide to a water wave,” *Coastal Engineering*, vol. 125, pp. 16–22, 2017, DOI: 10.1016/j.coastaleng.2017.04.001.

OpenCFD, “OpenFOAM user guide,” *OpenFOAM Foundation*, 2018, last checked: 11.08.20.

A. Panizzo, P. De Girolamo, M. Di Risio, A. Maistri and A. Petaccia, “Great landslide events in Italian artificial reservoirs,” *Natural Hazards and Earth System Sciences*, vol. 5, pp. 733–740, 2005, DOI: 10.5194/nhess-5-733-2005.

A. Paris, E. A. Okal, C. Guérin, P. Heinrich, F. Schindelé and H. Hébert, “Numerical modeling of the June 17, 2017 landslide and tsunami events in Karrat Fjord, West Greenland,” *Pure and Applied Geophysics*, vol. 176, pp. 3035–3057, 2019, DOI: 10.1007/s00024-019-02123-5.

M. Pastor, I. Herreros, J. F. Merodo, P. Mira, B. Haddad, M. Quecedo, E. González, C. Alvarez-Cedrón and V. Drempetic, “Modelling of fast catastrophic landslides and impulse waves induced by them in fjords, lakes and reservoirs,” *Engineering Geology*, vol. 109, no. 1-2, pp. 124–134, 2008, DOI: 10.1016/j.enggeo.2008.10.006.

M. Rauter, T. Barker and W. Fellin, “Granular viscosity from plastic yield surfaces: The role of the deformation type in granular flows,” *Computers and Geotechnics*, vol. 122, p. 103492, 2020, DOI: 10.1016/j.compgeo.2020.103492.

M. Rauter, A. Kofler, A. Huber and W. Fellin, “faSavageHutterFOAM 1.0: depth-integrated simulation of dense snow avalanches on natural terrain with OpenFOAM,” *Geoscientific Model Development*, vol. 11, no. 7, pp. 2923–2939, 2018, DOI: 10.5194/gmd-11-2923-2018.

D. Rettenmaier, D. Deising, Y. Ouedraogo, E. Gjonaj, H. De Gersem, D. Bothe, C. Tropea and H. Marschall, “Load balanced 2D and 3D adaptive mesh refinement in OpenFOAM,” *SoftwareX*, vol. 10, p. 100317, 2019, DOI: 10.1016/j.softx.2019.100317.

P. J. Roache, “Quantification of uncertainty in computational fluid dynamics,” *Annual Review of Fluid Mechanics*, vol. 29, pp. 123–160, 1997, DOI: 10.1146/annurev.fluid.29.1.123.

J. Roenby, B. E. Larsen, H. Bredmose and H. Jasak, “A new volume-of-fluid method in OpenFOAM,” in *VII International Conference on Computational Methods in Marine Engineering. Nantes: International Center for Numerical Methods in Engineering*, 2017.

A. Romano, J. L. Lara, G. Barajas, B. Di Paolo, G. Bellotti, M. Di Risio, I. J. Losada and P. De Girolamo, “Tsunamis generated by submerged landslides: numerical analysis of the near-field wave characteristics,” *Journal of Geophysical Research: Oceans*, vol. 125, p. e2020JC016157, 2020, DOI: 10.1029/2020JC016157.

L. Rondon, O. Pouliquen and P. Aussillous, “Granular collapse in a fluid: Role of the initial volume fraction,” *Physics of Fluids*, vol. 23, no. 7, p. 073301, 2011, DOI: 10.1063/1.3594200.

H. Rusche, “Computational fluid dynamics of dispersed two-phase flows at high phase fractions,” Ph.D. thesis, Imperial College London (University of London), 2002.

S. B. Savage, M. H. Babaei and T. Dabros, “Modeling gravitational collapse of rectangular granular piles in air and water,” *Mechanics Research Communications*, vol. 56, pp. 1–10, 2014, DOI: 10.1016/j.mechrescom.2013.11.001.

T. Shan and J. Zhao, “A coupled CFD-DEM analysis of granular flow impacting on a water reservoir,” *Acta Mechanica*, vol. 225, no. 8, pp. 2449–2470, 2014, DOI: 10.1007/s00707-014-1119-z.

P. Si, H. Shi and X. Yu, “Development of a mathematical model for submarine granular flows,” *Physics of Fluids*, vol. 30, no. 8, p. 083302, 2018a, DOI: 10.1063/1.5030349.

P. Si, H. Shi and X. Yu, “A general numerical model for surface waves generated by granular material intruding into a water body,” *Coastal Engineering*, vol. 142, pp. 42–51, 2018b, DOI: 10.1016/j.coastaleng.2018.09.001.

T. Uroić, H. Jasak and H. Rusche, “Implicitly coupled pressure-velocity solver,” in *OpenFOAM® Selected Papers of the 11th Workshop*, pp. 249–267, Springer, 2019, DOI: 10.1007/978-3-319-60846-4_19.

H. K. Versteeg and W. Malalasekera, *An introduction to computational fluid dynamics: the finite volume method*, Pearson education, 2007.

S. Viroulet, A. Sauret, O. Kimmoun and C. Kharif, “Granular collapse into water: toward tsunami landslides,” *Journal of Visualization*, vol. 16, no. 3, pp. 189–191, 2013, DOI: 10.1007/s12650-013-0171-4.

S. Viroulet, A. Sauret, O. Kimmoun and C. Kharif, “Tsunami waves generated by cliff collapse: comparison between experiments and triphasic simulations,” in *Extreme Ocean Waves*, pp. 173–190, Springer, 2016, DOI: 10.1007/978-3-319-21575-4_10.

S. N. Ward and S. Day, “Ritter Island Volcano - lateral collapse and the tsunami of 1888,” *Geophysical Journal International*, vol. 154, no. 3, pp. 891–902, 2003, DOI: 10.1046/j.1365-246X.2003.02016.x.

H. G. Weller, “Bounded explicit and implicit second-order schemes for scalar transport,” Technical Report TR/HGW/06, Nabla Ltd., London, UK, 2006.

H. G. Weller, “A new approach to VOF-based interface capturing methods for incompressible and compressible flow,” Technical Report TR/HGW/06, Nabla Ltd., London, UK, 2008.

H. G. Weller, G. Tabor, H. Jasak and C. Fureby, “A tensorial approach to computational continuum mechanics using object-oriented techniques,” *Computers in Physics*, vol. 12, no. 6, pp. 620–631, 1998, DOI: 10.1063/1.168744.

S. Yavari-Ramshe and B. Ataie-Ashtiani, “Numerical modeling of subaerial and submarine landslide-generated tsunami waves–recent advances and future challenges,” *Landslides*, vol. 13, no. 6, pp. 1325–1368, 2016, DOI: 10.1007/s10346-016-0734-2.

G. Zitti, C. Ancey, M. Postacchini and M. Brocchini, “Impulse waves generated by snow avalanches falling into lakes,” in *Proceedings of the 36th IAHR World Congress, The Hague, The Netherlands*, vol. 28, 2015.

Authors’ addresses

Matthias Rauter Norwegian Geotechnical Institute, Postboks 3930 Ulleval Stadion, 0806 Oslo, Norway, matthias.rauter@ngi.no

Luisa Hoße University of Potsdam, Potsdam, Germany, lhosse@uni-potsdam.de

Ryan P. Mulligan Queen's University, Kingston, Canada, ryan.mulligan@queensu.ca

W. Andy Take Queen's University, Kingston, Canada, andy.take@queensu.ca

Finn Løvholt Norwegian Geotechnical Institute, Postboks 3930 Ulleval Stadion, 0806 Oslo, Norway finn.lovholt@ngi.no

Chapter 2

Summary and outlook

This thesis spans over a very broad topic, from granular landslides, their rheology and the role of pore fluid to their interaction with water bodies and tsunamis. All developments and investigations were carried out for the goal of a unified simulation of landslides and tsunamis within a single framework. The Navier–Stokes Equations and non-Newtonian rheologies like the $\mu(I)$-rheology made this possible while keeping the complexity to a reasonable level. The models that were developed and applied in this thesis have been implemented in the open source toolkit OpenFOAM. This did not only simplify and accelerate the task but also ensure that the models are usable by other scientists and engineers in the future. Papers I and II established the required rheologies and their implementation into OpenFOAM. Paper III investigated the capabilities of OpenFOAM to predict landslide generated tsunamis, their propagation and breaking mechanisms and paper IV combined the first three works into a unified simulation of granular landslides and tsunamis. It should be noted that paper IV is still in preparation and results might still change.

The work focused on the establishment of the basic three-dimensional model and leading order effects, such as granular rheology and permeability. Many effects are not included and there are vast opportunities to improve and extend the presented model. Most notably, the applied granular rheology is still a very strong simplification of the complex behaviour of granular materials, the critical state theory is not fully implemented and scale effects that can be observed in nature are not fully reproduced. The implementation of the full critical state theory might be especially valuable for the initial phase and quasi-static regions of landslides. At the current stage, this regime is not handled sufficiently and the initialisation and release volume has to be established with other soil models or observations. Further, the interaction with water bodies can be improved by including surface tension, capillary forces, a turbulence model or a better interface tracking algorithm, just to name a few examples. Nevertheless, the model provides a good baseline for further model developments but also for the investigation and prediction of landslide tsunamis. The model parameters and their determination, especially a priori or without extensive knowledge of an event are still problematic, although the presented model provides new insights and some upsides in comparison to traditional depth-integrated models.

The full three-dimensional model is computationally more expensive than simplified depth-integrated two-dimensional models. Further, numerical diffusion of the wave has to be expected if the computational resolution is not sufficiently fine. These are strong drawbacks, however they are balanced by substantial upsides, such as a direct simulation of the interaction between slide and water body, breaking waves and inundations. There might be cases where the increased insights of the three-dimensional model are worth the high numerical expense, especially for real cases with suspected high socio-economic impact. Growing computational resources might make the full three-dimensional model more affordable and practically applicable in the future. There are various other ways to exploit the upsides of the presented method, either by learning to improve simplified methods or by some sort of coupling.

Appendices

Appendix A

Selected examples of code

The following section provides some code examples that have been instrumental for the presented computations. The code is not complete but provides all important information to achieve a consistent implementation to reproduce the results, although own effort will be required for a working implementation.

A.1 Extension of time step duration algorithm to high viscosity

The code in Lst. A.1 was executed in *multiphaseEulerFoam* alongside the existing calculation of the Courant number. The time step is then chosen such that all Courant numbers remain under pre-defined limits. A similar calculation was added to *multiphaseInterFoam*, however adapted to the specific solver.

Listing A.1: Calculation of the viscous Courant number in *multiphaseEulerFoam*.

```
scalar viscosityCoNum = 0.0;
//iterating over all phases
forAllIter(PtrDictionary<granularPhaseModel>, fluid.phases(), iter)
{
    granularPhaseModel& phase = iter();
    volScalarField nuEff(turbulence->nut() + phase.nu()); //effective viscosity

    //Calculate the maximum face momentum flux due to viscosity
    scalarField sumPhi
    (
        fvc::surfaceSum
        (
            0.5*mag(fvc::interpolate(phase*nuEff)*mesh.magSf()*
            mesh.surfaceInterpolation::deltaCoeffs())
        )().primitiveField()
    );
    //the global maximum of the viscosity Courant number
    scalar vCoNumPhase = gMax(sumPhi/mesh.V().field())*runTime.deltaTValue();
    //the maximum viscosity Courant number for all phases
    viscosityCoNum = max(viscosityCoNum, vCoNumPhase);
}
```

A.2 Implementation of particle pressure

The code in Lst. A.2 was added to *multiphaseEulerFoam* for Paper II.

Listing A.2: Implementation of particle pressure in `pEqn.H` of *multiphaseEulerFoam*.

```
// getting the pressure form the granular pressure model
```

```
volScalarField pp(phase.granularPressure());
// limiting the granular pressure to a predefined value to avoid blowups
pp = min(pp, phase.psModel().pmax());
//explicit calculation of the momentum flux on a face due to granular pressure
surfaceScalarField gradPpf = fvc::snGrad(pp)*mesh.magSf();

//remove granular pressure on zero-gradient pressure boundaries (e.g. walls)
forAll(p_rgh.boundaryField(), patchi)
{
    if (isA<zeroGradientFvPatchScalarField>(p_rgh.boundaryField()[patchi]))
        gradPpf.boundaryFieldRef()[patchi] = 0.0;
}

//Contribution of the particle pressure to H/A-flux
phiHbyAs[phasei] += - fvc::interpolate(rAUs[phasei])*gradPpf/phase.rho();
//Contribution of the particle pressure to H/A
HbyAs[phasei] += - rAUs[phasei]*fvc::reconstruct(gradPpf)/phase.rho();
```

A.3 Changes to include components (i.e. subPhases) in multiphaseEulerFoam

The following code is a selection of the modifications to *multiphaseEulerFoam* that was required for Paper IV. In particular, the momentum conservation equation was modified to allow a variable phase density (Lst. A.3) and to allow a split of phases in components (called subphases in the code, Lst. A.4).

Listing A.3: The new phase momentum conservation equation in `UEqn.H` to account for variable phase densities. The residual phase fraction avoided the complete vanishing of phase fractions and improved stability. This change enforces other changes (multiplications with `rho`) in `pEqn.H`.

```
//The residual phase fraction is a small number (about 1e-4) that avoids
//division by zero and a singular system of equations
const volScalarField alpha0 = max(alpha, phase.residualPhaseFraction());

new fvVectorMatrix
(
    fvm::ddt(alpha, phase.rho(), U)              // transient term +
  + (alpha0-alpha)*fvm::ddt(phase.rho(), U)      // residual phase fraction
  + fvm::div(             // convection term (alphaRhoPhi comes from MULES)
             phase.alphaRhoPhi(),
             U
             )
  - fvm::laplacian(alpha0*phase.rho()*nuEff, U) // visocus stress laplacian
  - fvc::div                    // visocus stress, transposed gradient part
    (
        alpha0*phase.rho()*
        nuEff*dev2(T(fvc::grad(U))),       // dev(...) changed to dev2(...)
        "div(Rc)"
    )
);
// the remaining contributions, g, grad(p), drag are added in pEqn.H
```

Listing A.4: The new phase model to account for the additional handling of subPhases or components

```
//This function is evoked in each step to advance the convection of components
//and update the advective momentum flux of the phase alphaRhoPhi_, which is
//used in the momentum equation. cAlpha is the counter gradient transport
//factor (phase parameter), alphaPhi_ is the volume flux of the phase (all
//components). Large parts of the code is taken from multiphaseSystem.C of
//multiphaseInterFoam.
void Foam::phaseModel::solveAlphas(const scalar cAlpha)
{
    //If there are is only 1 component/subphase return
    //without solving but set alphaRhoPhi_
    if (subPhases_.size() < 2)
    {
        alphaRhoPhi_ = alphaPhi_*fvc::interpolate(rho());
        return;
    }

    word alphaScheme("div(phi,alpha)");
    word alpharScheme("div(phirb,alpha)");

    surfaceScalarField alphaPhiRel = alphaPhi_;
    //magnitude of compressive flux
    surfaceScalarField phic(mag(alphaPhiRel/U_.mesh().magSf()));
    phic = Foam::min(cAlpha*phic, Foam::max(phic));

    //solve the advection of all subphases/components
    PtrList<surfaceScalarField> alphaPhiCorrs(subPhases_.size());
    int phasei = 0;
    forAllIter(PtrDictionary<subPhase>, subPhases_, iter)
    {
        subPhase& alpha = iter();
        alphaPhiCorrs.set
        (
            phasei,
            new surfaceScalarField
            (
                "phi" + alpha.name() + "Corr",
                fvc::flux(alphaPhiRel, alpha, alphaScheme)
            )
        );

        //the flux is corrected by the CGT with all other components
        surfaceScalarField& alphaPhiCorr = alphaPhiCorrs[phasei];
        forAllIter(PtrDictionary<subPhase>, subPhases_, iter2)
        {
            subPhase& alpha2 = iter2();
            if (&alpha2 == &alpha) continue;

            //CGT flux of magnitude phic and direction nHatf
            //nHatf is the surface normal on interface, interpolated to cell faces
            surfaceScalarField phir(phic*nHatf(alpha, alpha2));

            alphaPhiCorr += fvc::flux
            (
                -fvc::flux(-phir, alpha2, alpharScheme),
                alpha,
```

```
                alpharScheme
            );
        }

        MULES::limit
        (
            1.0/U_.mesh().time().deltaT().value(), //rDeltaT = 1/DeltaT
            *this, //account for limited available phase volume/porosity
            alpha, //the subphase/component to solve
            alphaPhiRel, //normal flux
            alphaPhiCorr, //compressed flux
            zeroField(),  //Source (exp) = 0
            zeroField(),  //Source (inp) = 0
            1, //component indicator maximum
            0, //component indicator minimum
            true //return correction on alphaPhiCorr
        );
        phasei++;
    }

    MULES::limitSum(alphaPhiCorrs);

    alphaRhoPhi_ = dimensionedScalar(dimensionSet(1, 0, -1, 0, 0), Zero);

    phasei = 0;
    forAllIter(PtrDictionary<subPhase>, subPhases_, iter)
    {
        subPhase& alpha = iter();

        surfaceScalarField& phi = alphaPhiCorrs[phasei];
        phi += upwind<scalar>(U_.mesh(), alphaPhiRel).flux(alpha);

        MULES::explicitSolve
        (
            *this, //account for limited available phase volume/porosity
            alpha, //the subphase/component to solve
            phi,  //MULES limited flux
            zeroField(), //Source (exp) = 0
            zeroField()  //Source (inp) = 0
        );

        //Multiply component flux with component density and add it
        //to phase momentum flux that is then used in UEqn.H
        alphaRhoPhi_ += phi*alpha.rho();
        phasei++;
    }
}

//Calculation of interface normals for the Counter Gradient Transport Term
Foam::tmp<Foam::surfaceVectorField> Foam::phaseModel::nHatfv
(
    const volScalarField& alpha1, const volScalarField& alpha2
) const
{
    surfaceVectorField gradAlphaf
    (
        fvc::interpolate(alpha2)*fvc::interpolate(fvc::grad(alpha1))
```

```
      - fvc::interpolate(alpha1)*fvc::interpolate(fvc::grad(alpha2))
    );
    return gradAlphaf/(mag(gradAlphaf) + deltaN_);
}

Foam::tmp<Foam::surfaceScalarField> Foam::phaseModel::nHatf
(
    const volScalarField& alpha1, const volScalarField& alpha2
) const
{
    return nHatfv(alpha1, alpha2) & U_.mesh().Sf();
}

//Update of density and viscosity after advecting the subphases
void Foam::phaseModel::correct()
{
    //Iterate over all subphases/components and update the viscosity
    forAllIter(PtrDictionary<subPhase>, subPhases_, iter)
        iter().correct();

    //Calculate the phase density depending on present subPhases/components
    PtrDictionary<subPhase>::const_iterator iter = subPhases_.begin();
    rho_ = iter()*iter().rho();
    for (++iter; iter != subPhases_.end(); ++iter)
        rho_ += iter()*iter().rho();

    //Calculate the phase viscosity depending on present subPhases/components
    iter = subPhases_.begin();
    mu_ = iter()*iter().rho()*iter().nu();
    for (++iter; iter != subPhases_.end(); ++iter)
        mu_ += iter()*iter().rho()*iter().nu();

    nu_ = mu_/rho_;
}
```